



HAL
open science

Modeling of the optoelectronic properties of colloidal nanocrystals for infrared imaging purposes

Bilal Chehaibou

► **To cite this version:**

Bilal Chehaibou. Modeling of the optoelectronic properties of colloidal nanocrystals for infrared imaging purposes. Micro and nanotechnologies/Microelectronics. Université de Lille, 2023. English. NNT : 2023ULILN026 . tel-04428163

HAL Id: tel-04428163

<https://theses.hal.science/tel-04428163>

Submitted on 31 Jan 2024

HAL is a multi-disciplinary open access archive for the deposit and dissemination of scientific research documents, whether they are published or not. The documents may come from teaching and research institutions in France or abroad, or from public or private research centers.

L'archive ouverte pluridisciplinaire **HAL**, est destinée au dépôt et à la diffusion de documents scientifiques de niveau recherche, publiés ou non, émanant des établissements d'enseignement et de recherche français ou étrangers, des laboratoires publics ou privés.

Thèse pour obtenir le titre de

Docteur en Sciences

à l'Université de Lille

Spécialité: Electronique, microélectronique, nanoélectronique et
micro-ondes

Présenté par

Bilal Chehaibou

Modeling of the optoelectronic properties of colloidal nanocrystals for infrared imaging purposes

Modélisation des propriétés optoélectroniques de nanocristaux colloïdaux
pour la conception d'imageurs infrarouges

Thèse dirigée par Christophe Delerue (directeur), Peter Reiss
(co-directeur), Arthur Arnaud et Gabriel Mugny (encadrants)

et soutenue le 17/10/2023, devant le jury composé de:

Hervé Rinnert	Professeur des universités (IJL, Nancy)	Rapporteur/Président de jury
Mathieu Luisier	Professeur (ETH, Zürich)	Rapporteur
Soline Boyer-Richard	Maîtresse de conférence (INSA, Rennes)	Examinatrice
Christophe Delerue	Directeur de recherche (IEMN, Lille)	Directeur
Peter Reiss	Chercheur, chef de laboratoire (CEA, Grenoble)	Co-directeur
Arthur Arnaud	Docteur (STMicronics, Crolles)	Co-encadrant
Gabriel Mugny	Docteur (STMicronics, Grenoble)	Co-encadrant
Emmanuel Lhuillier	Chargé de recherche (INSP, Paris)	Invité

Contents

Abstract	i
Résumé en français	i
Remerciements	iii
List of acronyms and abbreviations	iv
Context of the thesis	1
1 Colloidal PbS nanocrystals: synthesis and characterization	5
1.1 Introduction	5
1.2 Characterization methods	5
1.3 General considerations about colloidal synthesis	10
1.3.1 Nucleation and Growth (NG) mechanisms	10
1.3.2 State of art about PbS colloidal syntheses	12
1.4 What we know about surfaces	14
1.4.1 Model tools for surfaces analysis	15
1.4.2 PbS: a story of surface	16
1.4.3 Ligand exchange	18
1.5 Results on NC colloidal formation	21
1.5.1 Syntheses	21
1.5.2 Characterization	22
1.5.3 Ligand exchange	28
1.6 Conclusion	31
2 Bulk to nanocrystals: electronic structure	33
2.1 Introduction	33
2.2 Numerical methods	33
2.3 Lead sulfide	42
2.3.1 Bulk: a peculiar semiconductor	42
2.3.2 Nanocrystal: size and shape	44
2.4 Mercury telluride	46
2.5 Conclusion	50
3 Bulk to nanocrystals: optical and dielectric properties	51
3.1 Introduction	51
3.2 Optical indices	51
3.3 Lead sulfide	56
3.4 Mercury telluride	62
3.5 Conclusion	67

4	Layer of nanocrystals: optical properties	69
4.1	Introduction	69
4.2	Determination of the complex dielectric function in a NC layer	70
4.3	Lead sulfide: size and ligand effects	72
4.3.1	Synthesis and characterization	72
4.3.2	ETBM-EMA model	73
4.3.3	Device simulations	77
4.4	Mercury telluride: shape effect	78
4.4.1	Synthesis and characterization	78
4.4.2	ETBM-EMA model	79
4.5	Conclusion	82
5	Optical performances: material comparison	84
5.1	Introduction	84
5.2	Single nanocrystal performances	85
5.3	Nanocrystal layer performances	90
5.4	Photodiode performances	97
5.5	Conclusion	99
6	Work function for device application	100
6.1	Introduction	100
6.2	State of art	101
6.2.1	Experimental measurements	101
6.2.2	Theoretical calculations	104
6.3	Simulation methodology and results	106
6.4	Conclusion	116
A	Appendix	119
A.1	Bond polarization model	119
A.2	DFT, drop of potential	121
	Bibliography	122

List of Figures

1	Scheme of CMOS image sensor including an array of pixels, vertical and horizontal circuitry, and readout circuitry. Reproduced from [1].	2
2	Photodiode array based on NC layers integrated on top of CMOS readout. From left to right are decomposed the different elements. Reproduced from [2].	3
1.1	(a) Illustration of Bragg's law. (b) Scheme of powder diffraction pattern and the different information that could be obtained: a) the peak positions, b) the peak intensities, c) the peak shapes, d) the resultant. See Figure 1.2 in complementary. (a) and (b) reproduces from [3].	6
1.2	Information from a powder diffraction pattern. Reproduced from [3].	7
1.3	Representation of Stokes shift by Jablonski energy diagram. Reproduced from [4].	8
1.4	Scheme illustrating the different signals that can be detected by TEM. Reproduced from [5].	9
1.5	Typical signals obtained from TGA. Adapted from [6].	10
1.6	(a) The bulk energy term (red) and surface energy term (blue) contribute to the Gibbs free energy change (black) as a function of nucleus size. A critical radius (r_c) exists at which newly formed nuclei enter the nucleation-growth stage if $r > r_c$, otherwise redissolved. Reproduced from [7]. (b) The diagram of the LaMer features the monomer generation (I), burst nucleation (II), and growth (III). A faster monomer generation rate induces a larger number of nuclei that grow toward a smaller NC size (red curve). Reproduced from Ref [7].	12
1.7	Illustration of the hot injection for PbS NC synthesis. Reproduced from [8].	12
1.8	Zhang synthesis. Absorption spectra of PbS NC (left panel), and variation of the first absorption peak with the grams of OA (right panel). Reproduced from [9].	13
1.9	Illustration of the non-hot-injection synthetic route adapted from Cademartiri [10] by Zhang et al. [11]. Reproduced from [11].	14
1.10	A NC concentration and final NC size according to the rate constant of PbS NC formation (k_{obs}) for different sulfur precursors. B , C , and D give the TEM images of three NC syntheses. Reproduced from [12].	14

1.11	(a) Carrier mobility as a function of ligand length for PbSe NC layers. Reproduced from [13]. (b) Positions of the valence band maximum (VBM), conduction band minimum (CBM), and Fermi energy E_F of PbS NCs passivated with different thiophenol ligand molecules. Reproduced from [14].	15
1.12	Wulff construction for PbS rocksalt NC. Top panel: 2D scheme of the planes (100) and (111) drawn according to the Wulff ratios. Bottom panel: PbS NC with Pb atoms in grey and S atoms in yellow constructs from the Wulff ratios. From left to right, the Wulff ratios are: $\frac{1}{2\sqrt{3}}, \frac{\sqrt{3}}{2}, \frac{2}{\sqrt{3}}, \frac{1+\sqrt{2}}{\sqrt{3}}$ and $\sqrt{3}$	16
1.13	Top view arrangement of (100),(110), and (111) PbS surfaces. Reproduced from [15].	17
1.14	(a) Surface energies and equilibrium shape of PbSe NC as a function of surface coverage. Reproduced from [16]. (b) Pb/S ratio with size for model shape PbS NC models compared to XPS data. Reproduced from [17].	19
1.15	Illustration of PbS NC layers prepared based on SSE (top) and PTE (bottom). Reproduced from [18].	19
1.16	(a) Effect of sodium (100) passivation on the colloidal stabilization. Reproduced from [19]. (b) The three main stages that mark PTE development. Reproduced from [20].	21
1.17	Illustration of a synthesis bench.	22
1.18	Image of the NC PbS synthesis. Resulting solution after the lead precursor complexation at t=0 (a) and t = 12 h (b). The final solution that contains the PbS NCs in ODE (c).	23
1.19	Optical measurements of the syntheses following Zhang protocol. (a) Absorption (black line) and PL spectra (purple line) of PbS NCs along with the hexane absorption (red dashed line). (b) Bandgap evolution with the NC size. Blue line: curve given by eq. 1.20 with the Moreels parameters [21]; Purple cross: TEM measurements; Black dot: XRD measurement. (c) Variation of the HWHM with the NC size for our syntheses (black line), and calculated for different size dispersity with eq. 1.21 (dashed lines). (d) Size dispersity (orange line) and size variation (blue line) with the NC size.	24
1.20	Optical absorption spectra with a Pb/S ratio of 1.5 following Hendricks'work [12] (black line); and modified: 2 (brown line) and 2.5 (orange line). The amount of sulfur precursor is increased while the lead amount is kept constant.	25
1.21	XRD diffractograms of Z1, Z2, Z3, and Z4 samples from bottom to top. The vertical lines represent the peak position of bulk PbS taken from [22].	26
1.22	Size distribution histograms and TEM images. Sample Z4 : (a) and (b); sample Z3 : (c) and (d); sample Z2 : (e) and (f); sample Z1 : (g) and (h).	27
1.23	(a) TGA signal of PbS NCs capped by oleate ligands. (b) Model NC used for TGA analysis.	28
1.24	Images of the PTE process.	28

1.25	Absorption (black solid line) and photoluminescence (purple solid line) of oleate-capped PbS NCs and after PTE processes following Gu [23] and Choi [24] protocols. The dashed lines correspond to the solvent absorption: hexane (red) and butylamine (orange).	29
1.26	FTIR spectra of oleate-capped PbS (red line), after Gu [23] (black line), and Choi PTE protocol [24] (purple line).	31
1.27	EDS analysis at the different steps of the PTE process.	31
2.1	Schematic representation of the main approximations underlying ab initio and semi-empirical electronic structure theories. See eq. 2.4 for the definition of Ψ and ϕ ; and eq. 2.5 for the definition of H_{ij} and S_{ij}	35
2.2	Schematic representation of the atomic orbitals s , p , and d forming all possible overlap and two-center integrals which are labeled σ , π , δ depending on the angular momentum position relative to the diatomic bond. Reproduced from [25].	38
2.3	First Brillouin Zone of face-centered cubic lattice. Reproduced from [26].	40
2.4	Electronic structure of a linear chain of s orbitals and its discretization by confinement for a finite chain of 20 atoms (left side). Density of states for the infinite chain (right side). Reproduced from [27].	41
2.5	Electron energy dispersion of bulk PbS calculated by ETBM (black solid line), DFT-HSE (blue solid line), and EPM at 0K (dashed red line).	43
2.6	ETBM band structure of bulk PbS (black line) compared to the one calculated with $E_{pp\sigma} = 2.5 \text{ eV}$, $E_{pc} - E_{pa} = 1.5 \text{ eV}$ and the spin-orbit coupling keeping its bulk value, all other interatomic terms being switched to zero (red dashed line). Parameters taken from [28].	44
2.7	Calculated weights on the cations (left panel) and p orbitals (right panel) of HOMO (blue) and LUMO (orange) states.	45
2.8	Sizing curve. (a) Evolution of the bandgap energy evolution with the diameter of colloidal PbS NCs, showing our own experimental data (exp. of Lhuillier [29]), as well as experimental data from previous works (Cademartiri et al. [10], Maes et al. [30], Moreels et al. [21], Poddubny et al. [31], and Weidman et al. [32]). (b) Schematic representation of the PbCl shell over the sizing curve. Reproduced from [33].	45
2.9	(a) Pb:S ratio of spherical-like, octahedral, cuboctahedral, and truncated octahedral PbS NC models as a function of diameter, compared with experimental data from previous works ([17], [34], [35], and [21]). (b) Bandgap evolution with the NC size calculated by ETBM using the NC models compared to the Moreels fit over experimental data [21]. (c) Same as (b) considering the two limiting size cases for the octahedron, i.e. the diameter of its inscribed sphere (blue dot) and the largest size (down orange triangle).	47
2.10	Electron energy dispersion calculated by ETBM of (a) bulk HgTe with the parameters taken from [36] and (b) bulk CdTe with the parameters taken from [37]. The bands of Γ_6 , Γ_7 , and Γ_8 symmetry are respectively represented by a red, black, and blue solid line.	48

2.11	(a) Evolution of the bandgap with the inverse of NC diameter calculated by ETBM with spherical-like NC model compared to experimental data (Hudson et al. [38] and Zhang et al. [39]). (b) Same as (a) versus the NC diameter.	48
2.12	(a) Calculated weights on the cations (solid line) and s orbitals (dashed line) of HOMO (blue) and LUMO (orange) states. (b) Energy of the HOMO (blue) and LUMO states (orange) with the inverse diameter of spherical-like NCs. Published in [40].	49
3.1	ETBM calculations of the (a) imaginary part, and (b) real part of the complex dielectric function of bulk PbS.	57
3.2	(left panel) imaginary part and (right panel) real part of the complex dielectric function calculated by ETBM in black solid line, by EPM in purple dashed line (Kohn et al. [41]), and measured experimentally in purple dotted line (compiled from different authors and gathered in the optical handbook of Sadao Adachi [42]).	58
3.3	(upper left panel) absorption coefficient, (upper right panel) reflectivity, (bottom left panel) extinction coefficient, and (bottom right panel) refractive index measured experimentally in purple dotted line (compiled from different authors and gathered in the optical handbook of Sadao Adachi [42]), and transformed by the appropriate relations from the complex dielectric function calculated by ETBM in black solid line.	58
3.4	(upper panel) imaginary part and (lower panel) real part of the complex dielectric function calculated by ETBM for bulk PbS (dashed purple line) and for a spherical PbS NC of 4 nm diameter (black solid line).	59
3.5	Imaginary part of the complex dielectric function for a PbS spherical-like NC of 4 nm. The vertical lines under the peaks correspond to the calculated oscillator strength (multiplying by a factor of 5) for each transition between the valence and conduction band. The panel corresponds to the corresponding electronic structure around the bandgap.	60
3.6	Absorption spectra obtained by ETBM calculations (blue solid line), and measured experimentally by Weidman et al. [32] (orange solid line). For each panel the size is given in legend. The first absorption peak is normalized.	61
3.7	Refractive index (n) and extinction (k) calculated by (a,b) ETBM and extracted from (b,e) experimental measurements of Moreels et al. [43]. Comparison of ETBM calculations to the extracted experimental measurements [43] (c) for the extinction coefficient at 2.5 eV, and (f) for the refractive index at 0 eV.	62
3.8	(left panel) imaginary part, and (right panel) real part of the complex dielectric function of bulk HgTe calculated by ETBM in black solid line, by EPM in purple dashed line (Chadi et al. [44]), and measured experimentally in purple dotted line (compiled from different authors and gathered in the optical handbook of Sadao Adachi [42]) and orange dotted line by Szuskiewicz et al. [45].	63

3.9	(a) Imaginary part $\epsilon''(\omega)$ of the complex dielectric function calculated for NCs of different sizes (colored solid lines), and compared to $\epsilon''(\omega)$ calculated for bulk HgTe (black solid line). The values in parenthesis in the legend correspond to the peak position in energy. (b) Same for the real parts $\epsilon'(\omega)$. (c) The optical dielectric constant for different NC sizes. The black vertical line represents the bulk value. (d) $\chi_{12}^0(\omega \rightarrow 0)$ and $\chi_{11}^0(\omega \rightarrow 0)$ susceptibilities (solid lines) and energy gap (dashed lines) versus diameter for CdTe (in blue) and HgTe (in red) NCs.	64
3.10	(a) Imaginary part of the complex dielectric function calculated for a NC of 6.1 nm diameter (red solid lines), compared to bulk HgTe (black solid line), and to a bulk material in which a gap is opened artificially by changing ETBM parameter $E_s(c)$ [36] (dashed lines). The values in parenthesis in the legend correspond to the peak position in energy. (b) Same for the real parts.	65
3.11	(a) Evolution of the oscillator strengths (solid line) and the imaginary part of the complex dielectric function (dashed line) with the NC diameter. (b) Evolution of the first (orange solid line) and second (blue solid line) excitonic peak with the NC size calculated by ETBM and compared to experimental measurements of Zhang et al. [39] and Hudson et al. [38].	66
3.12	(top, green solid line) imaginary part of the complex dielectric function and (bottom, blue vertical lines) corresponding oscillator strengths computed by ETBM. Purple dashed lines correspond to the sum of the analytical formula (3.35) for the first (red dashed line) and second peak (orange dashed line). The diameter of the NCs is indicated above each panel.	67
4.1	(a) uniform layer on a substrate, (b) inhomogeneous layer on a substrate, (c) rough film on a substrate, and (d) multiple layers on a substrate. Reproduced from Ref. [46].	70
4.2	(a) TEM images, and (b) high-resolution TEM of PbS 1550. (c) Absorption measurements for a series of colloidal PbS NCs with the first exciton peak wavelength ranging from 1000 to 1550 nm (see Ref. [29]).	73
4.3	Effect of surface chemistry on the optical properties. Extinction coefficient (k) and refractive index (n) for PbS 1200 passivated with OA, EDT, and NH ₄ I. We used Bruggeman approximation (see eq. 4.8) where the f_{NC} is either fitted (blues solid line) or calculated by the hard-sphere model (orange solid line, see eq. 4.9). We compared these theoretical calculations with the ellipsometry measurements (green crosses). We represent the host refractive index by a dashed grey vertical line at the values: 1.7, 1.9, and 2.1 for OA, EDT, and NH ₄ I, respectively.	74

4.4	Effect of NC size on the optical properties. Extinction coefficient (k) and refractive index (n) spectra for PbS 1000, 1100, 1200, 1370, 1450 and 1550 passivated with OA. The SE measurements (green dots), the Bruggeman (blue line) and the Maxwell-Garnett (red line) approximations are compared. The NC volume fractions (f_{NC}) obtained in the two EMAs are given.	74
4.5	We compare SE measurements (green crosses) with Bruggeman approximation where f_{NC} was either fitted (blue solid line) or calculated with a HSM (orange solid line, see eq. 4.9). (a,c) Effect on the NC size for OA capping. (b,d) Effect on the surface chemistry for PbS 1200. (a-b) The average refractive index over the wavelength range of 750 to 2000 nm. (c) NC volume fraction. (d) Extinction coefficient (k) at the exciton peak.	75
4.6	Scheme of the calculations in the Bruggeman approximation. We compute the volume fraction f_{NC} via the HSM, and the NC complex dielectric function $\epsilon_{\tilde{NC}}$ by ETBM. Assuming the host refractive index n_h to be similar for equivalent surface chemistries (OA, EDT, and NH_4I), we use n_h obtained in Ref. [29].	77
4.7	Absorption spectra within the NC layer for a diode stack composed of glass/ITO(190 nm)/TiO ₂ (120 nm)/PbS (n-type, with PbS 1200 capped by NH_4I), PbS (p-type, with PbS 1200 capped with EDT)/Au (80 nm).	77
4.8	TEM images of HgTe NCs with (a) sphere, (b) planar tripod, and (c) rod shape NCs. (d) NCs model used to compute (e) the bandgap energy of the NCs according to the cube root of the number of semiconductor atoms, and (f) the complex dielectric function (solid line for real part; dashed line for imaginary part) versus photon energy for the three different geometries: sphere (blue), rod (red) and tripod (orange). We used ETBM for the calculations in (e) and (f). The rod and tripod shapes present an aspect ratio of 1.26 in (d). In (e) equivalent sphere diameter = $a_{cell} \sqrt[3]{\frac{3N_{atom}}{4\pi}}$	79
4.9	Extinction coefficient (k), and refractive index (n) of HgTe NC layers presenting (a) spherical, (b) tripod, and (c) rod shape. We compare theoretical calculations (full orange lines) combining ETBM and Bruggeman model with SE measurements (green crosses). The grey dashed line gives the host refractive index n_h	80
4.10	Extinction coefficient (k), and refractive index (n) of HgTe NC layers. We compare the theoretical indices (orange solid lines) obtained by combining ETBM calculation with Bruggeman approximation (see eq. 4.8) to ellipsometry measurements (green crosses). The grey solid line gives the results of the calculations in which $\epsilon_{\tilde{NC}}$ is replaced by the bulk value ϵ_{bulk} while conserving the set of parameters extracted with $\epsilon_{\tilde{NC}}$ (i.e. $\epsilon_h = \sqrt{1.94}$ and $f_{NC} = 53\%$). $\langle n \rangle$ is the average of n over the energy range.	81
5.1	Scheme of the simulation process described in the Chapter.	84

5.2	Presented on two pages. Each panel corresponds to a semiconductor denoted at the upper left. For each one, we give the imaginary part of the complex dielectric function with excitonic correction (green solid line), and corresponding oscillator strengths computed by ETBM (blue vertical lines). The red dashed line corresponds to the analytical formula eq. 5.6, and the purple dashed line to eq. 5.7 for the first absorption peak. The orange vertical line corresponds to ϵ_{im} (see text for details). The diameter of the NCs is indicated above each panel.	88
5.3	Analytical model with parameters from Table 5.1 (solid line) and ETBM calculation (symbols) for (a) $\hbar\omega_1$, (b) \bar{f}_1 , and (c) $\epsilon''_{NC}(\omega_1)$ of the first excitonic peak according to the NC size. The analytical model of $\epsilon''_{NC}(\omega_1)$ for PbS and PbSe is calculated by the eq. 5.7, while we used eq. 5.6 for the other semiconductors. The operation wavelength corresponds to the wavelength of the first excitonic peak ($\hbar\omega = \hbar\omega_1$ in eq. 5.6).	91
5.4	Bruggeman calculations of the (a) refractive index, (b) extinction coefficient, and (c) absorption coefficient of a NC layer. The host parameters are based on EDT-type found in Chapter 4, with a refractive index of 1.9, and a ligand length of 0.5 nm. To compute the NC volume fraction, we used a packing fraction of 64%, and a hard-sphere model (see Chapter 4). In Figures (b) and (c), the NC size maximizing the corresponding optical property are denoted.	92
5.5	Effect of ligands on the (a) refractive index, (b) extinction coefficient, and (c) absorption coefficient of PbS NC layers. The ligand length is decreasing from 2 (red line) to 0.1 nm (blue line) [0.1, 0.34, 0.56, 0.81, 1.05, 1.29, 1.53 1.76, 2.], while the refractive index is set at 1.9. The black dashed line corresponds to the NC size maximizing the absorption coefficient for a given ligand length.	95
5.6	(a) NC size maximizing the absorption coefficient (named optimal NC diameter) for different ligand lengths (see Figure 5.5. The NC volume fractions calculated by the HSM are denoted. Maximal absorption coefficient according to (b) the optimal NC diameter and (c) the operation wavelength.	96
5.7	Illustration of a photodiode stack described in the text.	97
5.8	EQE maps assuming 5% size dispersion and ligand of length of 0.5 nm for (a) PbS, and (b) InAs NC layer.	98
5.9	Performances of photodiodes at the excitonic peak wavelength, with a NC layer thickness of 300 nm for 5% size dispersion and 0.5 nm ligand length (solid red line: PbS, orange: InAs, and blue: HgTe). The solar background is represented in blue.	99

- 6.1 (a) Schematic illustration showing the band bending in ZnO/PbS-TBAI (on the left) and ZnO/PbS-TBAI/PbS-EDT (on the right). Reproduced from [47]. (b) The energy level diagram depicts an arrangement of infrared LEDs using NC layers. Within the active NC layer (MOA-CQDs), there are corresponding energy levels for NCs that emit at 1622nm (illustrated by a solid line) and 1220nm (represented by a broken line). Reproduced from [48]. 101
- 6.2 (a) Variation of the work function of a tungsten crystal with the different surfaces. (b) The lower panel illustrates a dipole layer of length extension L , and an electron at a distance x of the dipole layer. On the upper panel, the potential energy of the electron is shown in relation to the dipole layer. Reproduced from [49]. 102
- 6.3 (a) The valence band spectrum of Au layer on Si(100) obtained by PS with He I α ($h\nu = 21.22$ eV) lines. The spectrum was obtained by applying a -10 V bias (V_b) to the sample. The kinetic energy scale has been appropriately adjusted to account for the applied bias. The intense peak observed at low kinetic energy corresponds to the SEC region of the spectrum. The values for E_k^{max} (Fermi level) and E_k^{min} are displayed. (b) The figure illustrates the energy level diagram for the sample and detector, in the experiment of (a). Reproduced from [50]. 103
- 6.4 (a) The depicted energy diagram illustrates a PS experiment. At the equilibrium, the Fermi level, denoted as E_F , is consistently aligned throughout the system. The diagram includes the vacuum levels of the metal surface, indicated as $E_{vac}(s)$, and the detector, denoted as $E_{vac}(d)$, along with their respective work functions, ϕ_m and ϕ_d . The vacuum level at infinity, symbolized as $E_{vac}(\infty)$, is arbitrarily positioned below $E_{vac}(s)$ and $E_{vac}(d)$. Additionally, the diagram displays a photoelectron emitted from the Fermi level and detected with the kinetic energy E_k^{max} ; and a secondary electron escaping the solid just above $E_{vac}(s)$ with the kinetic energy E_k^{min} . In panel (b), the passivation by ligands of the sample surface creates a dipole layer causing an increase in $E_{vac}(s)$ and E_k^{min} . Reproduced from [51]. 104
- 6.5 Illustration of a layer of NCs. The arrows represent the ligands model as dipoles at the NC surface, and the color (red and blue) represents different chemical identities. We could imagine the blue arrows are iodide ligands while the red arrows illustrate the oxidation of lead atoms by hydroxyl groups. The NCs present different shapes, passivations, and NC-NC distances, and thus present different vacuum energy levels E_{vac}^i at their surfaces. Therefore the vacuum level of the NC layer E_{vac}^{layer} obtained experimentally is likely a non-trivial average of all E_{vac}^i 105

- 6.6 (a) DFT calculation of the conduction band minimum (CBM) shifts of CdSe. The shifts are presented in relation to the z-component of the intrinsic dipole moment density of functionalized ligands on the CdSe surface. Specifically, the shifts are shown for benzylamine on CdSe(100) at 100% coverage (squares), benzylamine on CdSe(100) at 25% coverage (circles), and benzonitrile on CdSe(100) at 25% coverage (triangles). In the case of benzylamine with two or more substitutional F atoms, the data is denoted by open symbols. Reproduced from [52]. (b) DFT calculations of band edges, renormalized by the number of ligands, are depicted for three distinct isolated ligand/NC structural models. These models exhibit varying surface coverage and are plotted as a function of the projected ligand dipole. Reproduced from [53]. 105
- 6.7 (a) Illustration of the repeated-slab approach with alternating vacuum space and PbS Slab. Schematic diagram of modeled (b) PbS (100) slab and (c) PbS (111) slab. For (b) and (c) the yellow dots represent sulfur atoms while the black dots represent lead atoms. Contrary to PbS (100) slab (b) which is apolar and symmetric, PbS (111) slab (c) is asymmetric with Pb and S atoms at each of the extremities, thus pseudo-hydrogen atoms were added to prevent charge transfer at the S-terminated surface. 107
- 6.8 Inplane-averaged potential energy (blue line) for electrons across a PbS (100) slab capped at one extremity by iodide atoms. The PbS (100) slab capped by iodide atoms (purple dots) is represented in the background. The position of the vacuum is roughly given for the sake of clarity. The potential in the slab strongly oscillates due to the alternate semiconductor planes. In the vacuum the potential is constant but a step of potential is present corresponding to the dipole correction required to avoid the divergence (see text for details). The dipole correction is in fact the drop of potential ΔV_{eff} due to the dipole layer μ_{eff} 107
- 6.9 Electrostatic calculations for point dipoles with dipole moment extracted from DFT for TBAI ligands. (a) Illustration of electrostatic calculations of the potential barrier due to dipole layers. The left panel illustrates two dipole layers (blue arrows) of opposite polarization and the z-axis along which the potential has been computed (purple line). The distance between the two planes is 2 nm. As an example, the right panel gives the potential calculated for a slab of 30x30 nm² area. We can observe a divergence of the potential, close to the point dipole position (± 1 angstrom). (b) The upper panel gives the different potential plots calculated for varying slab areas, from left to right: 2x2, 5x5, 10x10, 20x20, and 30x30 nm². The bottom panel gives the convergence of the electrostatic potential calculated in the middle of the two dipole layers for the varying areas described above with respect to DFT calculations. 109

6.10	Electrostatic calculation in a 4 nm cubic PbS NC due to point dipoles corresponding to TBAI ligands. (a) Illustration of a cubic PbS NC passivated by point dipoles. Pb atoms: in grey, S atoms: in purple, and point dipoles: blue arrows. The potential is calculated in the represented (100) plane. (b) Potential due to dipoles calculated in the (100) plane for two NC-dipole distances. The two bottom panels include the dielectric response of the PbS NC. $\Delta\bar{V}$ corresponds to the average potential calculated in the (100) plane.	110
6.11	Same as Figure 6.10 for the potential calculated in the (001) surface plane.	111
6.12	Potential due to point dipoles averaged over all the atoms of the cubic NC (solid line) and the standard deviation of the averaged potential (dashed line) according to (a) the NC-dipole distance, and (b) the NC size. The point dipoles correspond to TBAI ligands with a drop of potential of 1.97 eV calculated by DFT in the slab (grey horizontal line). The black and purple lines correspond to calculations without and with the account of the NC dielectric screening, respectively. . . .	112
6.13	(a) Valence band Maxima (VBM) calculated by ETBM for a 4 nm cubic PbS NC with (left panel) and without (right panel) the NC dielectric response. We compare the perturbation theory (purple line) to the direct Hamiltonian diagonalization (blue line). See text for details. (b) Effect of the ligands on the VBM. For ETBM (orange horizontal lines), the VBM is relative to the VBM of the pristine NC. For experimental work (black cross and red point), the VBM is relative to NC layers capped by 1,3 BDT. The DFT calculations (blue horizontal lines) correspond to a drop of potential in a (100) slab (see Figure 6.8). The red dots are unpublished work performed by the group of Emmanuel Lhuillier. The black cross corresponds to collected measurements from the literature by Ganesan et al. [54]. See text for more details. The different values for equivalent ligands correspond to different binding schemes.	114
6.14	Same as Figure 6.13 for octahedral NCs and (111) slabs for DFT. . . .	115
A.1	Illustration of an atomic layer in the (001) direction.	120

List of Tables

1.1	Summary of the solid-state exchange and phase-transfer exchange process.*PCE means power conversion efficiency and corresponds to the percentage of the solar energy shining on a solar cell device that is converted into usable electricity.	20
1.2	Optical features of PbS NCs following Zhang synthesis [55] (samples named Zi); or Hendricks synthesis [12] (sample named Hi) but increasing the sulfur precursor amount for H2 and H3 to adjust the NC size. Abs1 corresponds to the energy position of the first excitonic peak. *Size is obtained from the Moreels formula eq. 1.20.	24
1.3	Optical features of PbS NCs following the Zhang's synthesis (Z2)[55], and after the PTE process following the Gu [23] and Choi's protocols [24]. Abs1 and pl1 correspond to the energy position of the first absorption and photoluminescence peak, respectively.	30
2.1	Energy integrals corresponding to eq. 2.14 with the notation of Slater and Koster's paper [56]. The factors l and m correspond to the direction cosines of the vector of the diatomic bond.	39
4.1	Primary characteristics from the three studied HgTe NC samples. The excitonic peak is extracted from the SE spectra (k in Figure 4.9). We indicate the number of atoms in the NCs used for ETBM calculations (see Figure 4.8d). We obtained the volume fraction and host refractive index by fitting the film optical indices (see eq. 4.8) in order to reproduce measured data on Figure 4.9.	80
5.1	Fitted parameters obtained from ETBM calculation for each semiconductor. $\hbar\omega_1$ variation with the NC size d : $\hbar\omega_{1,0} + \hbar\omega_{1,1}/d + \hbar\omega_{1,2}/d^2$, and \bar{f}_1 with the NC size d : $\bar{f}_{0,1} + \bar{f}_{1,1}d$. The references of the ETBM parameters are given in the last column. We also give the bulk permittivity ϵ_{bulk} , which replaces ϵ'_{NC} in the Bruggeman equation . *we choose this value according to the work of Chapter 4.	89
A.1	Drop of potential (ΔV) extracted by DFT for (100) PbS slabs passivated by various ligands.	122
A.2	Drop of potential (ΔV) extracted for (111) PbS slabs passivated by various ligands.	122

Abstract

Semiconducting layers made of colloidal nanocrystals (NCs) have shown great potential as active materials in infrared (IR) sensors, with promises to reduce fabrication costs and enhance optoelectronic properties. Although being a relatively new technology, with the first monodisperse synthesis 30 years ago, huge advances including synthesis, surface engineering, deposition methods, device architecture, and fundamental physics have led to commercialization. However, to attain the full potential of NC IR sensors, improvements are still needed with a particular focus on the understanding and control of the material properties and their dependence on the environment.

In this context, we aim to combine experimental and theoretical tools to study the optoelectronic properties of isolated NCs until a layer of NCs integrated into electronic devices. In the first Chapter, we performed different PbS colloidal NC syntheses that allow us to conduct numerous physicochemical investigations from the optical properties to the surface characterization. In the second Chapter, we studied the electronic structure of isolated PbS and HgTe NCs using advanced theoretical tools such as Empirical Tight-Binding Method (ETBM), Density Functional Theory (DFT), and Empirical Pseudopotential Method (EPM). We studied the effect of size and shape on the electronic structure and unveiled a 0D topological phase transition in HgTe NCs. The third Chapter focuses on the optical properties of PbS and HgTe NCs. Using ETBM and EPM, we related electronic structure to the essential features of an experimental absorption spectrum. In the fourth Chapter, we extend the previous results to a solid layer composed of densely packed NCs. However, the properties of a solid layer are different for an isolated NC, due to the interaction with the environment, especially the ligands. Therefore, on top of ETBM calculations we include Effective Medium Approximation (EMA), and in synergy with spectroscopic ellipsometry measurements, we investigated the effect of the surface chemistry, shape, and size of the optical properties of a NC layer. From the knowledge accumulated in the previous Chapters, we developed a model in the fifth Chapter that allowed us a systematic comparison from a single NC to the photodiode stack of various semiconductor materials (PbSe, InAs, InSb, InP, and CdSe). Specifically, we provide abacuses of optical properties according to parameters that can be engineered experimentally, such as the ligand length or NC size. The last Chapter concerns the specific control of the work function with ligands. We started to develop a model that in terms aims to facilitate band-alignment engineering enhancing the device performance.

This work is a collaboration between research institutes (IEMN – Lille and CEA - Grenoble) and the industry (STMicroelectronics – Crolles). Collaborations with the group of Emmanuel Lhuillier at INSP are also acknowledged.

Résumé en français

Les couches semi-conductrices de nanocristaux (NCs) colloïdaux ont montré un grand potentiel en tant que matériau actif dans les capteurs infrarouge (IR), avec des promesses de réduction des coûts de fabrication et d'amélioration des propriétés optoélectroniques. Bien qu'il s'agisse d'une technologie relativement nouvelle, avec la première synthèse de NCs monodisperses réalisée il y a maintenant 30 ans, d'énormes progrès, notamment dans la synthèse, l'ingénierie de surface, les méthodes de dépôt, l'architecture des dispositifs électroniques et la compréhension fondamentale, ont conduit à une commercialisation. Cependant, pour atteindre le plein potentiel des capteurs IR à base de NCs, des améliorations sont encore nécessaires avec un accent particulier sur la compréhension et le contrôle des propriétés des matériaux et de leur dépendance à l'environnement.

Dans ce contexte, nous visons à combiner des outils expérimentaux et théoriques pour étudier les propriétés optoélectriques de NCs isolés jusqu'à une couche de NCs intégrée dans un dispositif électronique. Dans le premier chapitre, nous avons réalisé différentes synthèses de NCs colloïdaux de PbS qui nous a permis d'étudier les propriétés physico-chimiques allant des propriétés optiques à la caractérisation de la surface. Dans le deuxième chapitre, nous avons étudié la structure électronique de NCs de PbS et de HgTe isolés en utilisant des outils théoriques tels que ETBM (pour "Empirical Tight-Binding"), DFT (pour "Density Functional Theory") et EPM (pour "Empirical Pseudopotential Method"). Nous avons étudié l'effet de la taille et de la forme des NCs sur la structure électronique et révélé une transition de phase topologique 0D dans les NCs de HgTe. Le troisième chapitre se concentre sur les propriétés optiques des NCs de PbS et de HgTe. En utilisant l'ETBM et l'EPM, nous avons relié la structure électronique aux caractéristiques essentielles d'un spectre d'absorption expérimental. Dans le quatrième chapitre, nous étendons les résultats précédents à une couche solide composée de NCs densément compactés. Cependant, les propriétés d'une couche solide sont différentes de celles d'un NC isolé, en raison de l'interaction avec l'environnement, en particulier avec les ligands. Par conséquent, en plus des calculs ETBM, nous incluons le modèle EMA (pour "Effective Medium Approximation") et, en synergie avec des mesures d'ellipsométrie spectroscopique, nous avons étudié l'effet de la chimie de surface, de la forme et de la taille sur les propriétés optiques d'une couche de NCs. A partir des connaissances accumulées dans les chapitres précédents, nous avons développé un modèle dans le cinquième chapitre qui nous a permis une comparaison systématique depuis les propriétés intrinsèque d'un NC à ses propriétés quand intégré dans une système électronique (une photodiode). Plus précisément, nous avons établi des abaques de propriétés optiques en fonction de paramètres qui peuvent être modifiés expérimentalement, tels que la longueur du ligand ou la taille du NC, pour divers matériaux semi-conducteurs (PbSe, InAs, InSb, InP et CdSe). Le dernier

chapitre concerne le contrôle spécifique du travail de sortie avec les ligands. Nous avons commencé à développer un modèle qui, à termes, vise à faciliter l'ingénierie de l'alignement des bandes, améliorant ainsi les performances du dispositif.

Ce travail est une collaboration entre les instituts de recherche (IEMN - Lille et CEA - Grenoble) et l'industrie (STMicroelectronics - Crolles). Nous remercions également les nombreuses collaborations avec le groupe d'Emmanuel Lhuillier à l'INSP.

Remerciements

Je tiens ici à consacrer quelques lignes, bien insuffisantes évidemment, pour remercier mes encadrants, ma famille, mes amis et collègues.

Je tiens premièrement à exprimer ma profonde gratitude à Christophe Delerue. Merci de m'avoir guidé, soutenu et inspiré tout au long de ces trois années. Ce fût un grand plaisir de travailler à tes côtés.

Merci à Peter Reiss de m'avoir chaleureusement accueilli lors de mes séjours à Grenoble, de m'avoir fait découvrir la synthèse, et de tous tes conseils.

Je tiens à remercier Arthur Arnaud sans qui cette thèse n'aurait vu le jour. Merci pour ta disponibilité, ton énergie et les nombreuses idées qui parcourent ce manuscrit.

Gabriel Mugny, je te remercie pour ta générosité, ton regard critique et toutes les discussions qui m'ont permis de mieux comprendre mon sujet.

Je n'oublie pas mes collaborateurs qui ont largement contribué à cette thèse. Je pense à Emmanuel Lhuillier que je remercie pour m'avoir donné l'opportunité de visiter le synchrotron, merci pour ton énergie et pour tout le travail accompli. Merci à Jing Li et Benoît Sklénard pour votre aide et expertise.

Maintenant, je remercie tous les doctorants et collègues de l'IEMN qui ont enrichi mon quotidien. Merci pour votre amitié.

Je remercie les collègues et amis du CEA pour leur accueil, aide, et soutien. Merci de m'avoir fait apprécier Grenoble plus que je ne saurais l'avouer.

Pour finir, je tiens à remercier ma famille. Merci pour votre soutien inconditionnel.

List of acronyms and abbreviations

IR Infrared

SWIR Short-wave infrared

LiDAR Light Detection And Ranging

MWIR Mid-wave infrared

LWIR Long-wave infrared

NC Nanocrystal

CMOS Complementary Metal Oxide Semiconductor

ETL Electron transport layer

HTL Hole transport layer

ETBM Empirical Tight-Binding Method

DFT Density Functional Theory

EPM Empirical Pseudopotential Method

PXRD Powder X-Ray Diffraction

TEM Transmission Electron Microscopy

FTIR Fourier Transform Infrared

EDS Energy Dispersive X-Ray

TGA Thermogravimetric Analysis

NG Nucleation and Growth

CNT Classical Nucleation Theory

WC Wulff construction

COBM Charge-Orbital Balance Model

CBC Covalent Bond Classification

SSE Solid-State Exchange

LbL Layer-by-Layer

HWHM	Half Width at Half Maximum
PTE	Phase-Transfer Exchange
HOMO	Highest Occupied Molecular Orbital
LUMO	Lowest Unoccupied Molecular Orbital
IE	Ionization Energy
EA	Electron Affinity
ϕ_m	Work Function
E_F	Fermi Level
E_{vac}	Vacuum Energy Level
VBM	Valence Band Maximum
CBM	Conduction Band Minimum
CP	Critical Point
BZ	Brillouin Zone
FRC	Fresnel Reflection Coefficient
PF	Packing Fraction
HSM	Hard-Sphere Model
EMA	Effective Medium Approximations
SE	Spectroscopic Ellipsometry
EQE	External Quantum Efficiency
UV	Ultraviolet
TMM	Transfer Matrix Method
LED	Light-Emitting Diode
PS	Photoemission Spectroscopy
AA	Ammonium Acetate
NaAc	Sodium Acetate
MPA	Mercaptopropionic Acid
EDT	Ethanedithiol
[(TMS)₂S]]	bis(trimethylsilyl)sulfide
OA	oleic Acid

ODE Octadecene

EGDME Ethylene Glycol Dimethyl Ether

DMF Dimethylformamide

MPA 3-Mercaptopropionic Acid

BDT Benzenedithiol

OLA Oleylamine

Context of the thesis

The study of light and its interaction with matter is a long human history. A good example is the camera obscura which was widely used in the 15th century but already formally analyzed by Ibn al-Haytham in the early 11th century [57] but first studied by Chinese philosopher 500 BC. Then, the 20th century has seen the discovery of quantum physics which not only allowed a profound understanding of light and matter but triggered the development of new technologies that nowadays accompany our daily life. The careful management of light has indeed found applications at all levels of our society from the television to the smartphone including military purposes with night vision or directed-energy weapons. The infrared (IR) light which extends from 0.70 to 30 μm , is especially interesting for its high penetration depth and thermal ability. Indeed, short-wave infrared (SWIR, 1–3 μm) corresponds to the wavelength range where the atmosphere, haze, and dust are less absorbing and enjoy reduced sunlight interference, enabling active imaging such as night vision [58] and LiDAR (Light Detection And Ranging) [59]. The SWIR regime also includes absorption from tissue components such as water (around 1.130, 1.300, and 1.900 μm), lipids (around 1.040, 1.200, 1.400, and 1.700 μm), and collagen (around 1.200 and 1.500 μm), which enables monitoring cancerous tissues, burns, and histological discrimination [60]. The MWIR (mid-wave infrared, 3–5 μm) and LWIR (long-wave infrared, 8–12 μm) are both in atmospheric transparency windows enabling long-distance thermal imaging and are also widely used for molecular detection and hyper-spectral imaging [61].

Since the absorption of Si drastically decreases at wavelengths above 900 nm, most of the commercialized IR photodetectors rely on bulk semiconductor materials with narrow bandgaps such as Ge, InGaAs, InSb, and HgCdTe. They are usually epitaxially grown on lattice-matched substrates by molecular beam epitaxy or chemical vapor deposition under high temperature and vacuum conditions. Therefore, traditional bulk IR semiconductors suffer from strictly controlled fabrication processes, rigorous operation conditions, and high manufacturing costs, and are generally not compatible with flexible devices [62]. To meet the growing demands required for next-generation devices with better portability, wider applicable range, higher scalability, and low-cost fabrication, colloidal NCs show great potential. They can address the above requirements, especially thanks to their solution-processability, flexible substrate compatibility [62], and volume manufacturing [63]. Moreover, their typical strong confinement provides a formidable optical platform such as a tunable bandgap with the NC size [32, 64, 65]. For these reasons, they are already employed in various optoelectronic devices, including light-emitting diodes, solar cells, and photodetectors [66, 67, 68, 69, 2, 70].

The first studies on semiconductor NCs appeared more than 40 years ago. But it is only in 1993 that Murray, Norris, and Bawendi introduced a monodisperse

synthesis of colloidal NCs through the hot precursor injection method [71]. This was a breakthrough in the preparation of monodisperse NCs. In the following decades, the synthesis of NCs operating in the IR has greatly improved, such as lead sulfide (PbS) [9], lead selenide (PbSe) [72], lead telluride (PbTe) [73], mercury telluride (HgTe) [74], indium phosphide (InP) [75], indium arsenide (InAs) [76], and so on [77].

Among them, lead chalcogenide (PbX, X = S, Se) NCs, especially PbS is one of the most studied, presenting the highest optical performances in the SWIR [78]. As a direct semiconductor, PbS NCs have a high molar extinction coefficient [79], with a highly tunable bandgap from 0.8 to 2.2 μm [9], and a good solution stability. Heavily doped PbS NC can also reach the MWIR thanks to intraband transitions [80]. To extend the optical features, HgTe NCs are one of the prominent materials. It is a semimetal in bulk and of semiconductor nature in the NC form presenting a "natural" bandgap in the MWIR and even reaching the terahertz domain ($>15 \mu\text{m}$) when doped [81]. Although the first motivation for the use of HgTe NCs was to extend the optical features, these last years have seen drastic improvements in these materials opening the doors to a new range of applications [69].

Nanocrystal IR sensor

Typically, IR sensors based on NCs relied on Complementary Metal Oxide Semiconductors (CMOS) technology. CMOS image sensor comprises an array of pixels, vertical and horizontal access circuitry, and readout circuitry (Figure 1).

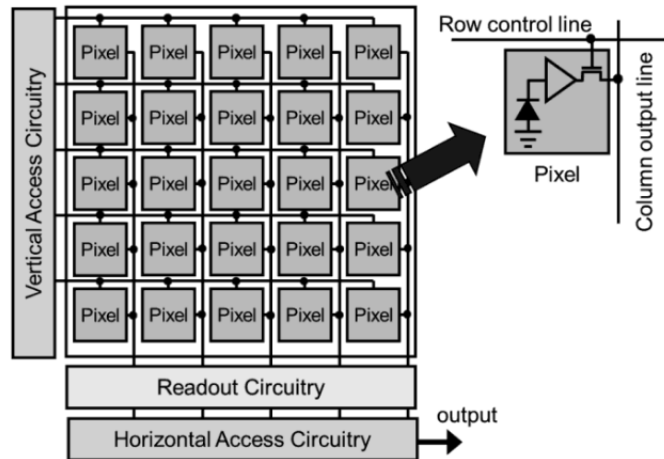


Figure 1: Scheme of CMOS image sensor including an array of pixels, vertical and horizontal circuitry, and readout circuitry. Reproduced from [1].

The pixel is the image sensor's headquarters composed in part of a photosensitive cell element named photodetector. The latter plays a crucial role in converting light into an electrical signal, which is then amplified and analyzed by the readout circuitry. Different configurations exist for the photodetector but the primary is a p-n photodiode, where a built-in field and an applied bias serve to extract the photocarriers. In this architecture, to enhance electron extraction, a metal oxide electron transport layer (ETL) is deposited on a substrate. Then, the NC layers are deposited layer by layer from the colloidal NC solution. Different deposition

techniques exist such as spin-coating, drop casting, dip coating, or spray coating. On top of the stack, a hole transport layer (HTL) is finally deposited, to improve hole extraction (see [2] and Figure 2).

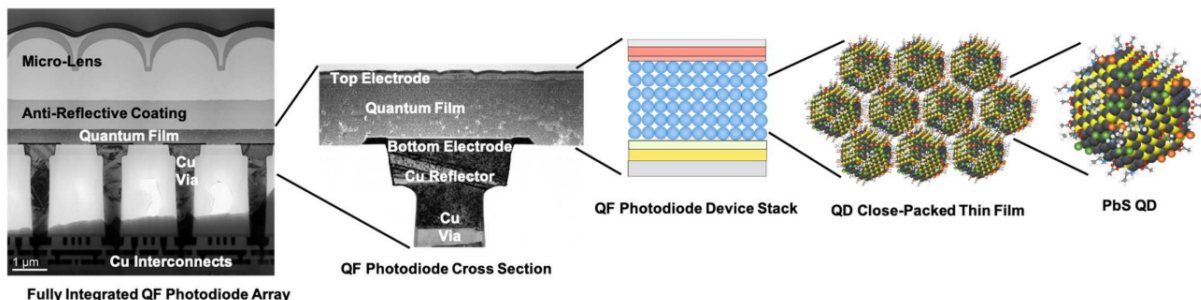


Figure 2: Photodiode array based on NC layers integrated on top of CMOS readout. From left to right are decomposed the different elements. Reproduced from [2].

Evaluation This above technique that integrates NC layers directly on top of the readout circuit enables the reduction of the pixel pitch compared to the hybridization process used for bulk material [82], which leads to an enhanced resolution. Indeed, the current state of the art for InGaAs photodiode is a pixel pitch of $5\mu\text{m}$ [83], while $1.62\mu\text{m}$ pixel pitch based on NC has been achieved [2].

Another key parameter to assess the performance of an IR photodetector is the dark current. The dark current determines the minimum light intensity that can be detected. It usually consists of diffusion current, generation current, defect-assisted tunneling current, direct tunneling current, multiplication current, and ohmic leakage current. Since the defect density in NC materials is higher than in single crystal semiconductors, trap-assisted tunneling leads to higher dark currents for NC devices [70].

The response time, which reflects the speed of transfer of photogenerated charge, is an important criterion for IR sensors. It includes the rise time (τ_r) giving the time between a measured photogenerated signal of 10% to 90% and the fall time (τ_f) between 90% to 10% [84]. One of the best-reported values for PbS NCs is $13\mu\text{s}$ and $41\mu\text{s}$, for τ_r and τ_f , respectively [82]. Again the traps tend to impinge these values which are lower for single crystal materials such as InGaAs ($\tau_r = 0.65\mu\text{s}$, $\tau_f = 2.20\mu\text{s}$) [85].

Other figures of merits exist (external quantum efficiency, responsivity, and more [70]) and have undergone great improvements these last decades in IR photodetector, sometimes by several orders. It allowed the rapid commercialization of this new technology. However, despite all the advances, NC-based IR photodetectors still relied on toxic materials, driven by lead and mercury chalcogenides. Although the risks are limited, due to the low amount used in IR imaging (typically a few mg of active material for one device [86]), the development of nontoxic IR devices with comparable performances will likely be a breakthrough [7].

Moreover, the fundamental knowledge of NCs remains limited compared to single-crystal semiconductors. This is even more the case under a layer form, where the large surface area (a feature of NCs), can drastically modify optical and transport properties. The dependence of the electronic structure on surface chemistry, especially the interaction with passivating molecules, but also the effect of shape or

the NC-NC interaction into the layer are still obscure. In 2018, a road map for NC IR photodetector points out the need to provide a systematic study of the effect of material, size, and surface chemistry on the electronic structure [86]. This would likely allow a step forward in the understanding of these formidable materials but also enable accurate device optimization mandatory in the pursuit of cheaper, less toxic, and more efficient IR sensors.

Objectives and manuscript organization

This thesis aims to assess the optoelectronic properties of materials used in IR sensors. This goes from semimetals to semiconductors under their bulk, NC, and NC layers form. The strategy was first to focus on PbS NCs, which is an ideal model system due to a large amount of available data and then to investigate other materials.

For this, TB_Sim a code developed at CEA by Y.M.Niquet and F.Trioizon and at IEMN by C.Delerue, along with other models implemented during this thesis were used. TB_Sim is a versatile code written in Fortran 90, including modules that allows the construction of atomic structures, and the calculation of numerous physical properties: electronic structure, optical spectrum, electron-phonon coupling, etc. This thesis, although mainly theoretical, carried out experimental works at CEA Grenoble under the supervision of Peter Reiss.

The thesis is divided into 6 Chapters that can be read independently. Each contains an introduction followed by state-of-the-art, then a presentation of the results, and finally a conclusion.

The experimental part of the thesis is presented in Chapter 1 and was focused on the PbS colloidal NC synthesis and its characterization. To introduce the Chapter, the physicochemical characterization methods are presented and followed by a general discussion of the colloidal synthesis methods.

In the second Chapter, numerical methods used in this thesis are presented. Then, they are used to investigate the electronic structure of PbS and HgTe under their bulk and NC form.

In the third Chapter, the optical properties of PbS and HgTe are studied, still under their bulk and NC form. By comparison with the literature, essential features of the absorption spectrum are discussed.

In the fourth Chapter, we extend the results of the previous chapters to layers of NCs, i.e. the final active material incorporated in the devices. Specifically, we investigate the effect of size, shape, and surface chemistry on the properties of the NC layers.

In the fifth Chapter, the models developed on PbS and validated on HgTe are employed to provide a systematic study of various semiconductors materials (PbSe, InAs, InSb, InP, and CdSe), from a single NC to NC layer until the photodiode stack. It provides an abacus of different physical properties according to parameters that can be engineered experimentally, such as the ligand length or NC size.

Finally, in the sixth Chapter, an ongoing model to extract the effect of ligands on the NC electronic structure is presented. The ambition of this study is to accelerate band-alignment engineering at the junctions with electrodes enhancing the device performance. The model already allowed us to unveil some insights and to understand the dependence of the electronic structure on surface chemistry.

Chapter 1

Colloidal PbS nanocrystals: synthesis and characterization

1.1 Introduction

To benefit from the size-dependent physical and chemical properties, colloidal synthesis needs to produce uniform NCs. Broad-size dispersity in a NC ensemble will lead to inhomogeneous properties, impeding their optoelectronic performance. A direct illustration appears on the optical spectra as we will show in sub-section 1.5.2. A colossal research effort has been done in this sense achieving a size dispersity of 5% for a large range of NC sizes [87, 88, 89, 90, 32]. While there is still room for improvement, these successes relied on a growing understanding of the synthesis mechanism [91, 92, 7, 93, 94]. The lead sulfide NCs are mainly synthesized in an organic solution stabilized by long alkyl ligands bound to their surface. Then the solvent is dried to obtain NC films with smaller packing fractions favoring interparticle coupling. However, while the long insulating chain offers solution stability hindering aggregation and reducing surface defect states, they limit the carrier transport under a film form. Therefore, for application purposes, they need to be exchanged with shorter ligands while preserving their initial passivation quality [95, 20].

Because each step of the process, from the precursors to the final NC film, needs an assessment of the physicochemical properties, the main characterization methods are presented in section 1.2. In section 1.3, we will discuss the synthesis mechanism which is fundamental knowledge to control the NCs properties. In section 1.4 some characteristics of the PbS NC surfaces will be presented, and how we can modify them by ligand exchange. The last section (1.5) will be devoted to the results, where we will compare different colloidal syntheses and ligand exchange procedures along with numerous characterizations.

1.2 Characterization methods

Striking a solid with a wave is the basic concept of numerous experimental measurements. According to the wave nature (electron, neutron, or photon) or its energy, different physical properties will be probed, giving birth to different experimental techniques.

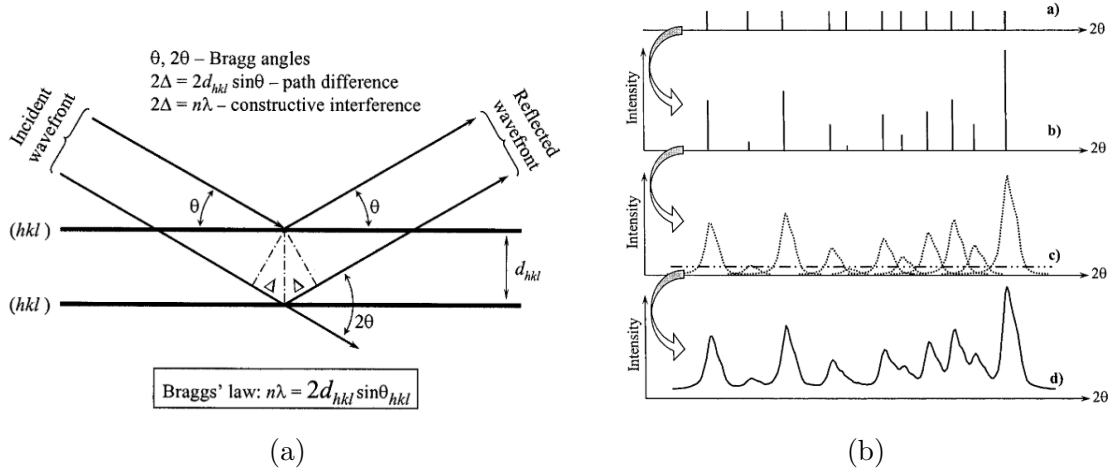


Figure 1.1: (a) Illustration of Bragg's law. (b) Scheme of powder diffraction pattern and the different information that could be obtained: a) the peak positions, b) the peak intensities, c) the peak shapes, d) the resultant. See Figure 1.2 in complementary. (a) and (b) reproduces from [3].

Powder X-Ray diffraction (PXRD) [3, 96] In principle, we expose a powder to X-Ray and obtain a diffraction pattern from the diffracted beams. The diffraction pattern is composed of discrete peaks (Bragg reflections) characterized by their positions, intensities, and shapes. Each of these parameters contains information about the properties of the sample, and the instrumental parameters, as shown in Table 1.2. A standard example is the access of the crystal structure via the peaks position. Indeed, the diffraction will occur if the interference between the incident and diffracted wave is constructive. This is known as the Bragg condition and formulated as following:

$$n\lambda = 2d_{hkl} \sin\theta \quad (1.1)$$

with d_{hkl} the interplanar distances between family of lattice planes labeled (hkl) and 2θ the total deflection angle. The labels (hkl) are known as Miller indices. Considering that the family of planes are in one-to-one correspondence with directions of the reciprocal lattice vectors (to which they are normal), the reciprocal lattice vectors follow:

$$G_{hkl} = hb_1 + kb_2 + lb_3 \quad (1.2)$$

with b_i the primitive lattice vectors of the reciprocal lattice.

The distance between the family of lattice planes (hkl) can be written as:

$$d_{hkl} = \frac{2\pi}{|G_{hkl}|} \quad (1.3)$$

Combining the eqs 1.1 and 1.3 with the known wave incident wavelength (λ) and the measured peak position (2θ), leads to the different reciprocal lattice vectors that allow the deduction of the corresponding Bravais lattice of the sample.

Another example is the extraction of the grain size d with the full width at half maximum (FWHM) by Scherrer's formula [97]:

$$d = \frac{(0.9\lambda)}{(fwhm \cos\theta)} \quad (1.4)$$

Pattern component	Crystal structure	Specimen property	Instrumental parameter
Peak position	Unit cell parameters: $(a, b, c, \alpha, \beta, \gamma)$	<i>Absorption</i>	Radiation (wavelength)
		Porosity	<i>Instrument/sample alignment</i> Axial divergence of the beam
Peak intensity	Atomic parameters $(x, y, z, B, \text{etc.})$	<i>Preferred orientation</i>	Geometry and configuration
		<i>Absorption</i>	Radiation (Lorentz, polarization)
Peak shape	<i>Crystallinity</i>	<i>Porosity</i>	Radiation (spectral purity)
	Disorder	<i>Grain size</i>	Geometry
	Defects	<i>Strain</i>	Beam conditioning
		<i>Stress</i>	

Figure 1.2: Information from a powder diffraction pattern. Reproduced from [3].

However, in practice we used two well-known refinement methods: Rietveld and Le Bail refinement; to relate the pattern components (position, shape and intensity) with the structural information. The two methods used an iterative process based on least square analysis to fit a theoretical line profile until it matches the measured profile, and both need a reasonable initial approximation of the free parameters. Rietveld fitting includes all structural and instrumental parameters, whereas Le Bail includes only the unit-cell parameters, peak width parameters, and peak shape parameters.

Absorption spectroscopy [98, 99, 100] It measures the attenuation of light intensity after crossing a sample. Lambert’s law states that the amount of attenuation is proportional to the intensity and path length; later the Beer’s law advances that it is also proportional to the concentration. Combining the two statements, known as the Beer-Lambert law, allows us to write the attenuation of light after a path length δx as:

$$I(x + \delta x) = I(x) - \alpha(\lambda)\delta x I(x) \quad (1.5)$$

with $\alpha(\lambda)$ the absorption coefficient being uniform for a given wavelength (λ) and a given sample, but depending on the concentration and the ability to attenuate light. Therefore, we usually express its dependence with the concentration as:

$$\alpha = \epsilon C \ln 10 \quad (1.6)$$

with ϵ the molar absorptivity and C the concentration. Integrating eq 1.5, we can express the light intensity at x , by:

$$I(x) = I_0 e^{-\alpha x} \quad (1.7)$$

However, in practice the quantity obtained in an absorption measurement set-up is the absorbance A . It is defined as the base-10 logarithm of the ratio between the incident I_0 and transmitted $I(L)$ light intensity crossing a sample of length L :

$$A = \log \frac{I_0}{I(L)} = \frac{\alpha L}{\ln 10} = \epsilon C L \quad (1.8)$$

The absorption coefficient can also be expressed in terms of extinction coefficient κ :

$$\alpha = \frac{4\pi\kappa}{\lambda} \quad (1.9)$$

The preceding expressions are equivalent from ultraviolet (UV) to infrared (IR) but imply different phenomena. In UV-visible spectra, the absorption is due to electronic transition, while the IR light of lower energy will excite vibrational and rotational states. The first case typically gives a broader absorption peak. Absorption spectroscopy is currently used to characterize a sample (molecular analysis) or for quantitative measurements such as concentration. As vibrational and rotational transitions give more defined spectra, it is typically preferred for molecular analysis. A variety of technical set-ups exist, and the great majority of them used a monochromatic wave as the incident light except for the Fourier Transform Infrared spectroscopy (FTIR). This technique employs a polychromatic wave whose advantage is a better signal-to-noise ratio.

Photoluminescence spectroscopy [101] Owing to the absorption of a photon, electrons undergo a transition from the ground state to the excited state. Then, electrons relax non-radiatively to the lowest excited state and recombine to the ground state by photon emission, called photoluminescence. The lowest photon energy the materials can absorb may (and is often) higher than the emitted photon energy. This difference is called the Stokes shift (shown in Figure 1.4). This property can have a major impact on the device's performance. An important Stokes shift limits the coverage between absorption and emission and thus is desired in solar concentrators to minimize photon reabsorption but should be limited in photovoltaic applications. The origin is still discussed but two phenomenon have emerged. The first one is the Franck-Condon (FC) relaxation where prior to emission the system relaxes to a new configuration with lower energy [102]. The other phenomena are ascribed to the excitonic fine structure. The degenerate valence band edge is split inducing a dark exciton lying at the lowest energy and undetectable in the absorption spectrum but producing strong photoluminescence [103, 104]. It results in a Stokes shift between absorption (bright excitons) and emission (dark excitons) spectra. Recently, it has been shown that the Stokes shifts depend on the size dispersity, the ligands, and defects [105, 106, 33].

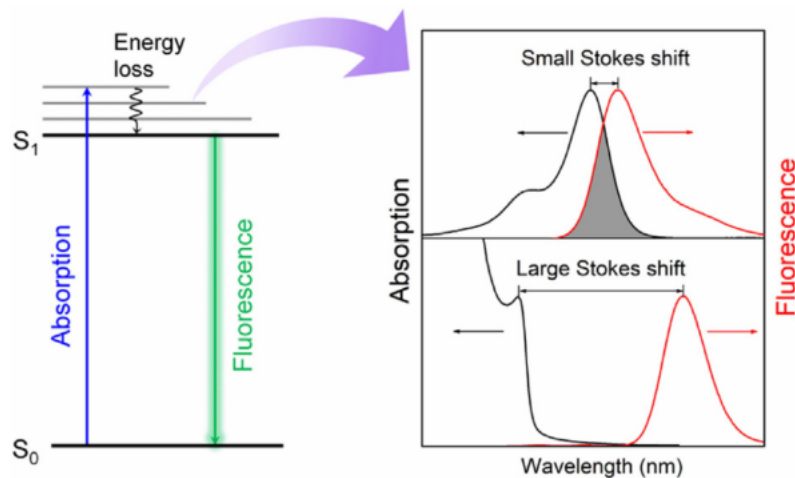


Figure 1.3: Representation of Stokes shift by Jablonski energy diagram. Reproduced from [4].

Transmission Electron Microscopy (TEM) [5] It uses an electron beam to extract various information from a sample. The advantage of using an electron as a probing system comes from the numerous secondary particles created after its interaction with matter (scattered electrons, X-ray, Auger electrons, etc). It gives to the TEM its various operating modes: conventional imaging, diffraction, and spectroscopy. Moreover, electrons usually permit far better resolution than light and e.g. overtook light microscopy resolution only three years after TEM discovery (1931 by Knoll and Ruska). The resolution is proportional to the wavelength, and neglecting the relativistic effect, the electron wavelength can be written as:

$$\lambda = \frac{1.22}{E^{1/2}} \quad (1.10)$$

with E in eV and λ in nm. Therefore, a 100 keV electron energy gives a wavelength of the order of the picometer, far smaller than the characteristic dimension of atoms (see [5] for more details).

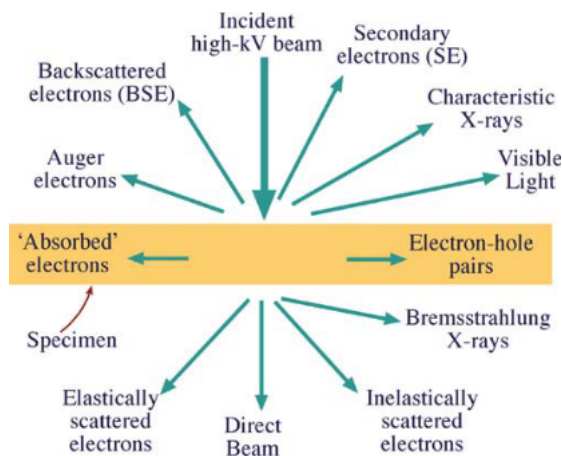


Figure 1.4: Scheme illustrating the different signals that can be detected by TEM. Reproduced from [5].

Energy Dispersive X-Ray (EDS) A beam of high energy, typically electrons or protons, is focused on the sample. This ejects an electron from the inner shell while creating a hole. An electron from a higher-energy shell then recombines with the hole, releasing energy in the form of an X-ray. The number of emitted X-rays versus their energy is measured. Already empirically known by Moseley at the beginning of the 20th century, the X-ray emitted is a unique characteristic of an atom. Therefore the obtained spectrum is a fingerprint allowing element identification. Besides the qualitative analysis, a quantitative one determining the concentration of an element is possible via peak intensity integration. The EDS can be also coupled with several microscopic imaging techniques such as TEM. It allows to visualize but also identify the chemical nature of a sample.

Thermogravimetric analysis (TGA) [6] In this method, the variations in the weight of a sample are measured while increasing the temperature. A highly sensitive scale coupled to a heating ramp allows investigation of the thermal characteristics

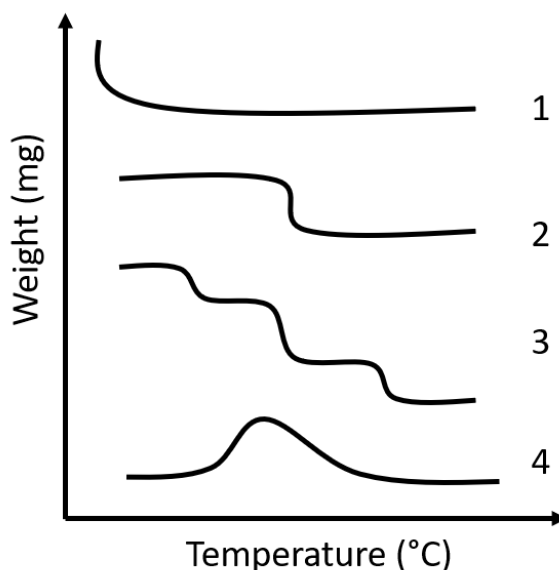


Figure 1.5: Typical signals obtained from TGA. Adapted from [6].

of a sample: thermodegradation, dynamics, and even kinetics. Indeed, the shape of the signals obtained from TGA can lead to different information about the sample (see Figure 1.5):

- signal 1: Fast loss of weight characteristics of an evaporation e.g. a dehydration.
- signal 2: One-step decomposition allowing to determine the kinetic of the reaction.
- signal 3: Several steps of decomposition allowing to determine the stability of the different components. It is particularly useful for stoichiometry analysis as we will see in section 1.5.2.
- signal 4: Gain of weight due to e.g. oxidation of the sample, then decomposition of the oxide.

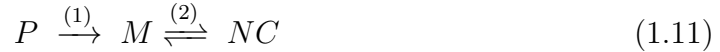
1.3 General considerations about colloidal synthesis

1.3.1 Nucleation and Growth (NG) mechanisms

The build-up of NCs from chemical precursors in solution involves a process of crystallization. A good understanding of this process and parameters helps to control the size and shape of NCs. When addressing the crystallization process, it is convenient to introduce the concept of monomer or solute corresponding to the minimal building block of a crystal. Based on these monomers, new particles (nuclei) will form by nucleation and increase their size by growth.

Until recently, the hot injection model assumed that the injected precursors were the monomers. In 2006, Steckel et al. [107] suggested that the injected precursors

(P), first react to form the monomers M, then combine upon nucleation and growth process producing NCs following the reaction:



The nucleation step has been treated by thermodynamics in the framework of classical nucleation theory (CNT). In the CNT, for a spherical nucleus of radius r , the Gibbs free energy change is expressed as [93]:

$$\Delta G(r) = 4\pi r^2 \gamma + \frac{4}{3}\pi r^3 |\Delta G_v| \quad (1.12)$$

with γ being the surface free energy per unit area and $|\Delta G_v|$ the free energy per unit volume of a crystal written as:

$$|\Delta G_v| = \frac{-k_B T \ln(C^*)}{v} \quad (1.13)$$

where v is defined as the monomer molar volume and C^* the supersaturation of the solution in monomer:

$$C^* = \frac{[M]}{[M_0]} \quad (1.14)$$

Therefore, the formation of a nucleus is limited by an unfavorable surface term proportional to the surface energy (γ) but driven by a favorable bulk term depending on the monomer concentration in solution ($[M]$). Thus, a maximum is reached for a critical radius r_c (see Figure 1.6a):

$$r_c = \frac{2\gamma v}{k_b T \ln(C^*)} \quad (1.15)$$

Any nuclei formed with a size inferior to r_c will redissolve while the others with $r > r_c$ will grow. In 1950, LaMer and Dinegar proposed a qualitative model to understand how a bath of precursors could lead to monodisperse NCs [108]. They postulated that once the supersaturation reached a critical value, the nucleation occurs infinitely fast named a burst nucleation. Then, the nucleation stops by monomer depletion, and growth continues with monomers addition giving homogeneous NCs (see Figure 1.6b). Therefore, the evolution of monomers concentration depends on the monomer generation rate Q , the nucleation rate J , and the growth rate G :

$$\frac{d[M]}{dt} = Q - m_n J_N - G n_p \quad (1.16)$$

with m_n the amount of monomer in a nucleus and n_p the number of particles. Different authors [109, 110] attempted to give a quantitative aspect to the model by solving this mass balance equation (eq. 1.16). They showed that the final number of NCs in the solution is proportional to the monomers generation and inversely proportional to the growth rate during the nucleation stage:

$$n_p = \frac{Q}{G} \quad (1.17)$$

Since the NC size depends on the number of NC generated upon nucleation, we could control the NC size by adjusting the kinetic of the growth or monomer generation (see Figure 1.6b). Even if this model allows us to conceptualize and predict some outcomes, it remains not fully accurate as the recent disproving of the nucleation burst and a growth limited diffusion [111, 112]; but other models exist [94] and a lot of research are still on-going.

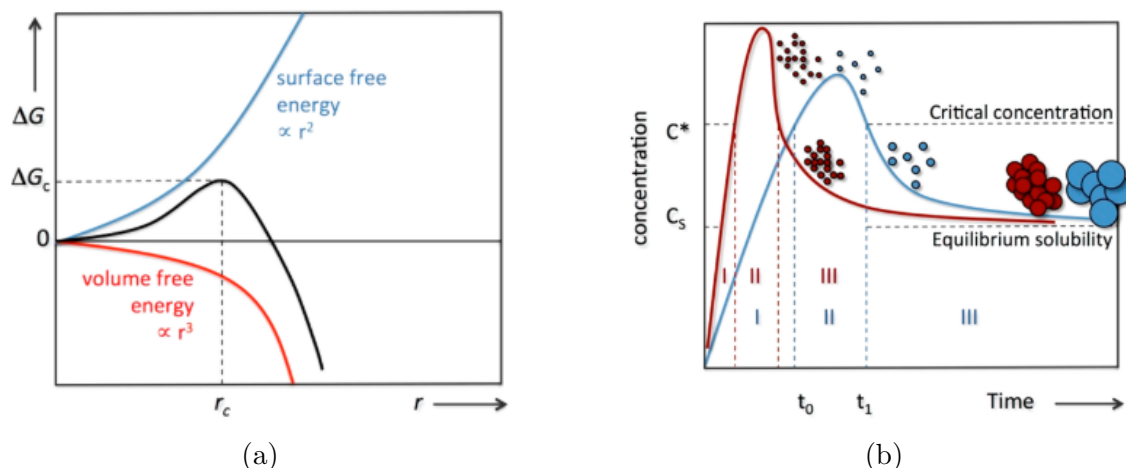


Figure 1.6: (a) The bulk energy term (red) and surface energy term (blue) contribute to the Gibbs free energy change (black) as a function of nucleus size. A critical radius (r_c) exists at which newly formed nuclei enter the nucleation-growth stage if $r > r_c$, otherwise redissolved. Reproduced from [7]. (b) The diagram of the LaMer features the monomer generation (I), burst nucleation (II), and growth (III). A faster monomer generation rate induces a larger number of nuclei that grow toward a smaller NC size (red curve). Reproduced from Ref [7].

1.3.2 State of art about PbS colloidal syntheses

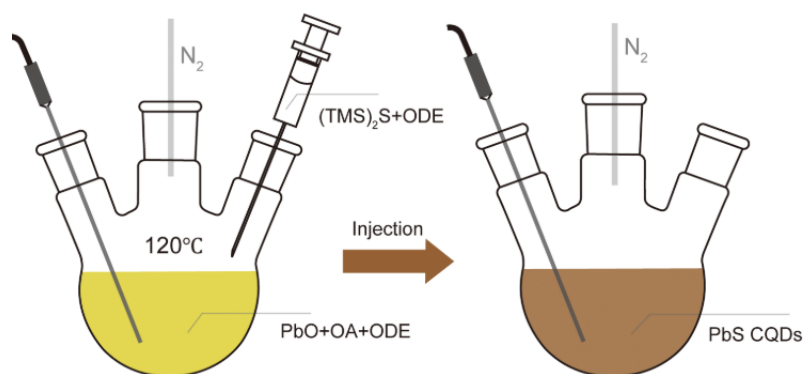


Figure 1.7: Illustration of the hot injection for PbS NC synthesis. Reproduced from [8].

A typical colloidal synthesis of lead sulfide NC relies on hot injection methods where the sulfur precursor is quickly injected in a hot solution of lead precursor.

Hines synthesis The first synthetic route has been developed by Hines in 2003 [90]. The lead precursor is obtained by dissolving lead oxide (PbO) into a liquid mixture of octadecene (ODE) and oleic acid (OA). ODE serves as an organic solvent, while OA is used as a ligand. The sulfur precursor is the bis-(trimethylsilyl)-sulfide ((TMS)₂S), which is used for its high reactivity. An illustration is given in Figure 1.7. The OA ligands bind to the surface of growing NCs improving their stability in the organic solvent and playing a key role in the final size control. This synthesis has been widely adopted in device applications [113, 114, 115, 116]. It has also

been adapted to better control the NC size and polydispersity e.g. with Zhang et al. [9] acting on the OA concentration, Cademartiri et al. [10] using PbCl_2 as the lead precursor, or Hendricks et al. [12] modifying the monomer generation rate by changing the sulfur precursor.

Zhang synthesis Based on Hines synthesis [90], they described a method linking the oleic acid concentration and the resulting NC size for different injection temperatures by the following formula :

$$\lambda_{1S} = 935 + s(T_{inj})g_{OAH} \quad (1.18)$$

with λ_{1S} corresponds to the wavelength of the first absorption peak, $s(T_{inj}) = 5.9 + 0.0026T_{inj}^2$, which is the temperature-dependent slope, and g_{OAH} the quantity of OA in gram. Increasing the temperature and the OA concentration leads to bigger NCs. Via eq. 1.17, the former statement could be rationalized by an increase of the growth rate with the temperature and OA concentration leading to a smaller number of particles and thus bigger NC size.

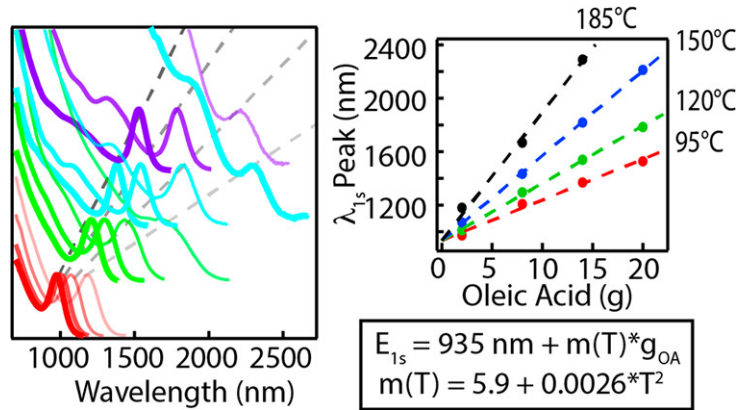


Figure 1.8: Zhang synthesis. Absorption spectra of PbS NC (left panel), and variation of the first absorption peak with the grams of OA (right panel). Reproduced from [9].

Cademartiri's synthesis This alternative to the Hines synthesis uses PbCl_2 in oleylamine as a lead precursor. It has been first proposed by Cademartiri [10] and then modified by Moreels [21], Weidman [32], and even adapt to a non-injection heating-up method by Zhang et al. [11] (see Figure 1.9). These methods all use a high Pb:S ratio that leads to the formation of PbCl_x shells, as shown by Winslow et al. [117]. Although this method allows high monodispersity, the isolating PbCl_x shells limits the charge transport and constrain the application to luminescence.

Owen's synthesis [12] Contrary to traditional synthetic methods where the final NC size is controlled by the growth rate (e.g., reaction temperature, and surfactant concentration as discussed above), Owen and his group propose a control by the monomers supply and thus the NC size (see again eq 1.17). They propose a library of sulfur precursors that allows control of the final size of the precursor reaction rate (see Figure 1.10). They claimed that this method improves the batch-to-batch

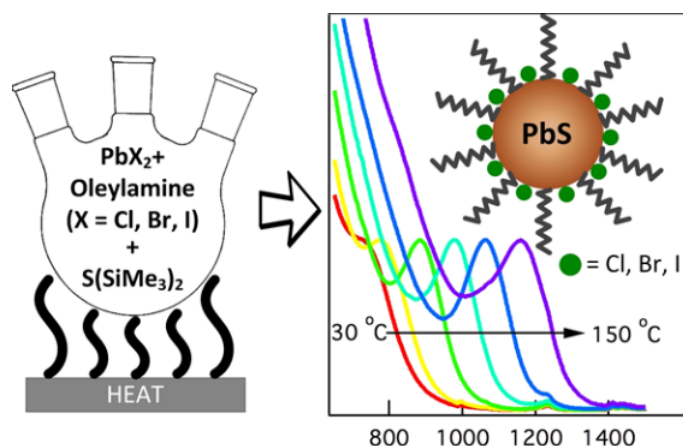


Figure 1.9: Illustration of the non-hot-injection synthetic route adapted from Cademartiri [10] by Zhang et al. [11]. Reproduced from [11].

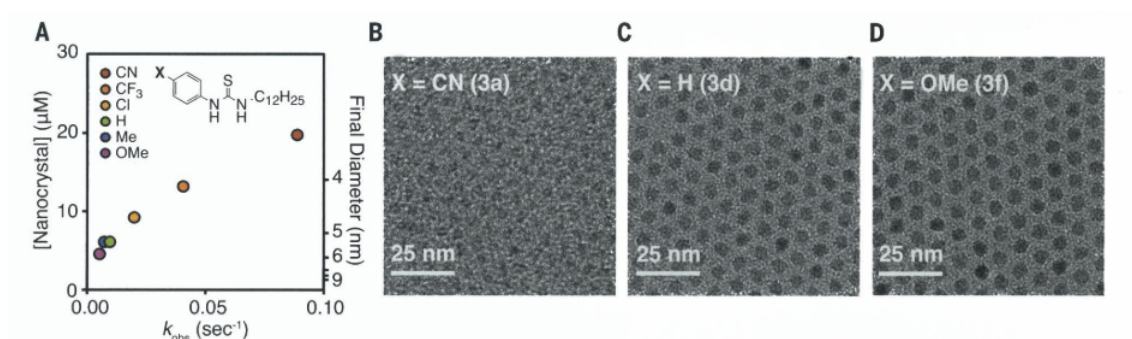


Figure 1.10: **A** NC concentration and final NC size according to the rate constant of PbS NC formation (k_{obs}) for different sulfur precursors. **B**, **C**, and **D** give the TEM images of three NC syntheses. Reproduced from [12].

consistency regarding the final size. They showed for two thiourea precursors that scale, concentration, and stoichiometry imply little change over the resulting size.

This description is not exhaustive but presents the primary PbS colloidal synthetic methods. They are largely used in NC-based devices and have been adapted to upscaling for industrial transfer [63]. However, this transition needs a profound understanding of the NC surface, which serves as the interface with the surrounding environment, and rules out many physical properties.

1.4 What we know about surfaces

Owing to their small dimensions, the NCs present a high surface-to-volume ratio that increases with decreasing size. As a matter of fact, the atoms on the surface are uncoordinated compared to their bulk counterparts which can lead to dangling bonds. It is known that dangling bonds create trap states in the bandgap hindering the device performance [118]. Thus, passivating the undercoordinated sites by ligands is of fundamental importance [119]. Moreover, the size and nature of ligands will modify the NC optoelectronic properties, e.g. altering their energy levels and carrier mobility [13] (see Figure 1.11). Surface engineering is consequently a formidable platform for improvements. However, contrary to the bulk structure that

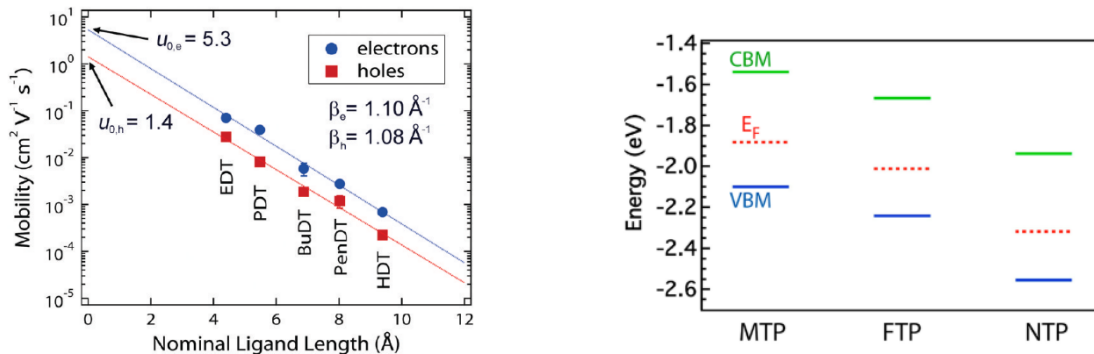


Figure 1.11: (a) Carrier mobility as a function of ligand length for PbSe NC layers. Reproduced from [13]. (b) Positions of the valence band maximum (VBM), conduction band minimum (CBM), and Fermi energy E_F of PbS NCs passivated with different thiophenol ligand molecules. Reproduced from [14].

can be accurately determined by crystallography, the surface structure complexity (composed of edges and vertices with interacting ligands) is difficult to probe by direct analysis. However, different qualitative models coupled with analysis methods have proven to be great tools to rationalize NC-ligand interactions. This section will detail different chemistry models that allow the description of the NC surface. It will follow a status about the PbS NC surfaces, and how we can modify them by ligand exchange.

1.4.1 Model tools for surfaces analysis

Covalent bond classification (CBC) [120, 121, 122, 123] The CBC model inherited from organometallic chemistry is widely employed to describe the ligands binding the NC surface. As a covalent model, every bond is made of two atoms - the ligand atom and the surface atom of the NC - sharing two electrons. The ligands are classified from their neutral form as L-, X-, or Z-type, depending on the number of electrons they donate to the NC-ligand bond (2, 1, or 0 respectively). As a two-electron donor with a lone electron pair such as amines (RNH₂) or phosphines (R₃P), the L-type ligands bind to surface metal atoms, while Z-type ligands are electron acceptors coordinating to surface nonmetal atoms. Finally, the X-type ligands require one electron from the NC surface site to form a two-electron covalent bond, thus they can bind either to metal or nonmetal atoms; typical examples of this class are oleate molecule or halide atoms.

Charge-orbital balance model (COBM) [124] The NCs are in apolar solvent (at least for the syntheses discussed here) requiring that the total system (NC and ligands) be uncharged. Therefore, we can use the charge orbital balance model that writes the number of excess electrons in the system as :

$$N_{exc} = \sum_i N_i q_i \quad (1.19)$$

considering $N_{exc} = 0$. N_i is the number of species of type i composing the neutral colloidal system and q_i is their oxidation state. Contrary to the CBC, the choice

of oxidation state originates from the most stable configuration. For example, the halides (X-type) are in 1 oxidation state while L-type is in 0 oxidation state. As we will see in the following sub-section, a proper combination of these two models (CBC and COBM) with analytical measurements allows us to get insights into the number, nature, and position of the ligands on the surfaces [125].

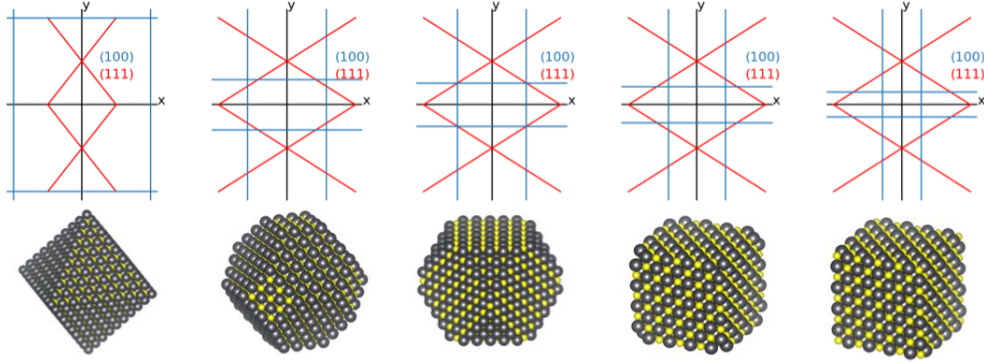


Figure 1.12: Wulff construction for PbS rocksalt NC. Top panel: 2D scheme of the planes (100) and (111) drawn according to the Wulff ratios. Bottom panel: PbS NC with Pb atoms in grey and S atoms in yellow constructs from the Wulff ratios. From left to right, the Wulff ratios are: $\frac{1}{2\sqrt{3}}$, $\frac{\sqrt{3}}{2}$, $\frac{2}{\sqrt{3}}$, $\frac{1+\sqrt{2}}{\sqrt{3}}$ and $\sqrt{3}$.

Wulff construction According to the Gibbs' thermodynamic, the shape of a crystal will be a polyhedron obtained by minimizing the total surface energy $\sum_{hkl} A_{hkl} \gamma_{hkl}$ where A_{hkl} is the area of the hkl plane with the surface energy of γ_{hkl} [34]. Considering that the surface energy of each plane is proportional to the length of a vector l_{hkl} normal to the corresponding plane (hkl), Georg Wulff suggested a method to construct the equilibrium shape of a crystal. For all the sets of Miller indices defining the crystal's Bravais lattice, one draws the planes (hkl) at a distance $c\gamma_{hkl}$ of the center; c being a constant. Thus, the smaller distances (equivalently lowest surface energies) will define the planes that shape the crystal surfaces. In other words, the surface with higher energies γ_{hkl} will be pushed out by the vectors with relative lengths l_{hkl} .

We give an example of Wulff constructions in Figure 1.12, for lead sulfide NCs with ratios l_{111}/l_{100} ranging from $\frac{1}{2\sqrt{3}}$ to $\sqrt{3}$ and considering the other (hkl) planes having higher energies. We took the ratios from Bealing et al. work [16] which are $\frac{1}{2\sqrt{3}}$, $\frac{\sqrt{3}}{2}$, $\frac{2}{\sqrt{3}}$, $\frac{1+\sqrt{2}}{\sqrt{3}}$ and $\sqrt{3}$ corresponding to octahedra, truncated octahedra, cubooctahedra, truncated cube, and cube, respectively. In this example, we started with known surface energies (which can be extracted from DFT calculations [126]) to deduce the NC shape but the TEM images of NCs allow us to measure the distances from the NC center to the surfaces and then deduce the ratio of the surface energies.

1.4.2 PbS: a story of surface

The possible facets present at the surface of PbS NCs correspond to a family of lattice planes: (100), (110), and (111) (see Figure 1.13). The (100) atomic plane presents a checkerboard arrangement alternating Pb and S atoms. In this configuration, each

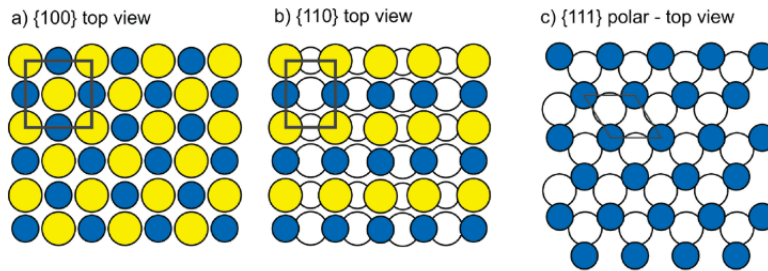


Figure 1.13: Top view arrangement of (100), (110), and (111) PbS surfaces. Reproduced from [15].

atom misses one nearest neighbor. The (110) surface contains also an equal number of Pb and S atoms but misses two nearest neighbors. Finally, the (111) planes are polar presenting one type of atom, either S or Pb, and missing three nearest neighbors. It is known since 1994 [127], from backscattering spectroscopy performed on epitaxially grown PbSe (111), that (111) planes present preferentially Pb atoms. Therefore, the latter contains a net charge, i.e. Pb^+ , that requires passivation by X-type ligands to fulfill the charge orbital balance model. It is consistent with the findings of Moreels et al. in 2008 [128] that unveiled nonstoichiometric PbS and PbSe NCs with lead-rich surfaces whose number of OA ligands matches the number of excess Pb atoms. Indeed, Fang et al. [15] (2010) showed that the bare Pb-rich (111) plans are unstable and they need surface passivation to decrease their energy surface e.g. upon ligand annealing the (111) surfaces spontaneously reconstruct to (100) surfaces. In line with these results, Bealing et al. [16] combined the WC and DFT calculations to show that ligand concentration modifies the PbSe morphology. At low concentrations, only the (111) surfaces exhibiting Pb atoms are passivated, leading to a low ratio l_{111}/l_{100} , thus forming NCs with octahedron shape (see Figure 1.14a). While at higher concentrations, the (100) surfaces having less affinity with OA ligands start to be passivated and decrease their surface energy, resulting in a cubic equilibrium shape. In line with these results, Choi et al. [17] show a variation of morphology with size for the same synthetic condition of PbS NCs. Combining WC with the measured Pb/S ratio, they suggested a shape evolution from octahedron to cuboctahedron with the NC size, as represented in Figure 1.14b. They impute this shape variation to increase steric hindrance between OA ligands with increasing NC size [129]. They also unveil that the (100) surfaces are self-passivated without any dangling bond implying a weak affinity with ligands. Therefore, these surfaces were prone to oxidation forming PbO , PbSO_3 , or PbSO and the large NCs with a high portion of (100) surfaces were unstable upon air exposure. The steric hindrance of OA ligands on (111) flat surfaces (slab) has been approved by DFT calculations in 2014 [130]. They showed that each Pb surface atom (111) is an alternate binding of OA and hydroxide ligands (a by-product of precursor decomposition) with a ratio OA/OH of 1:1, while the (111) is passivated by L-type oleic acid ligand forming bidentate bridges between Pb and S atoms. In this fully passivated configuration, the resulting projected density of states (PDOS) presents no trap states. From the DFT calculation, they determine a Wulff ratio of 0.82 corresponding to a truncated octahedron. In addition, Beygi et al. [34] computes the Wulff ratio for 1.5 to 7 nm NC size confirming the shape dependence of PbS with size. However, combining their proposed PbS morphology with the weight percentage of ligands on the surface of

NCs they disclaim the OA/OH 1:1 ratio and propose a 5:1 in compliance with other works [35, 125]. Kessler and Dempsey used an original technique tool developed by Owen's group [131] to probe the surface composition. They used an L-type ligand to induce Z-type ligand (PbOA_2) displacement of the NC surface as a probe surface composition. They showed on a 2.8 nm NC two distinct sites of displacement that were ascribed to an octahedron shape, with one site coming from the vertices (111)/(111) with Pb bound to a single S atom, and another from the edges with Pb coordinated to two S atoms. They also found an OA/OH ratio of 5:1. They perform the same analysis on a 3.9 nm and end up with a truncated octahedron with an OA/OH ratio of 3:1.

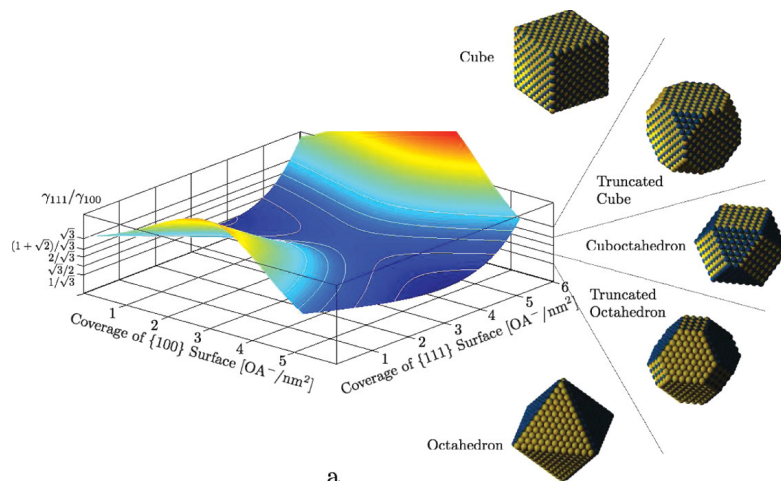
To conclude this sub-section, the shape of the surfaces of PbS NC vary in size from octahedron to cubooactehdron presenting respectively only (111) lead-rich surfaces and an alternate of (111) and (100) surfaces (see Figure 1.12). The (111) has a strong affinity with OA ligands but hydroxide groups seem also present on this surface. On the opposite, the (100) surface is stable without passivation and thus presents a weak affinity to the ligands. Therefore, they are prone to irreversible oxidation implying blue shifts of the absorption edge, and p-type doping. The OA ligands discussed here offer good solution stability but have to be exchanged for shorter ligands for carrier transport improvement. The insulating nature of long organic ligands limits the close packing of NCs and results in weak interparticle coupling.

1.4.3 Ligand exchange

The surface of a NC can be modified by exchanging the capping ligands. Two main procedures exist for a ligand exchange procedure (see Figure 1.15): (i) a post-treatment of NC solid films named solid-state exchange (SSE) and (ii) prior to the deposition of NCs (i.e. in solution) a phase-transfer exchange (PTE) (a recap of the methods is given Table 1.1). In both cases, the resulting film thickness ranges from tens to hundreds of nanometers and can be achieved by deposition techniques such as spin-coating.

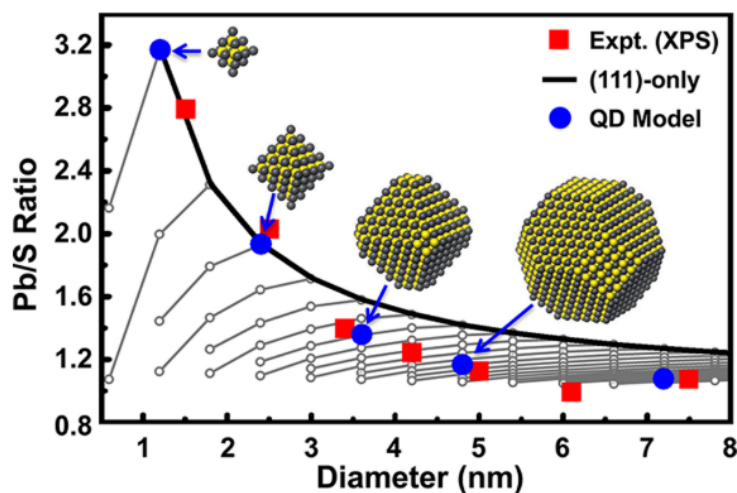
An SSE process replaces the long insulating organic ligands by dropping on the NC layer a polar solution containing a high concentration of ligands with a stronger affinity to the NCs than the initial ones. The newly capped NCs rendered insoluble in the initial nonpolar solvents allow a subsequent deposition. Thus, the repetition of the process enables a layer-by-layer (LbL) film assembly until the desired total thickness is reached. Although in a solid state, the replacement of long by shorter ligands reduces the overall inter-particle distance, a volume contraction leads to the formation of cracks and inhomogeneous NC-to-NC spacing. These drawbacks tend to lower the electronic transport, degrading the open-circuit voltage and limiting the device performance.

The PTE tackles the limitations encountered in the post-treatment by producing highly concentrated colloidal NC (ink) through solution-phase ligand exchange. The apolar solution containing the NCs capped by long organic ligands is mixed and stirred with the corresponding polar solution in which the target ligands are added. Then, a one-step deposition results in an homogeneous layer whose thickness depends on the ink concentration. Contrary to the SSE, the PTE approach is difficult to adapt to LbL deposition, which can limit thickness control.



a

(a)



(b)

Figure 1.14: (a) Surface energies and equilibrium shape of PbSe NC as a function of surface coverage. Reproduced from [16]. (b) Pb/S ratio with size for model shape PbS NC models compared to XPS data. Reproduced from [17].

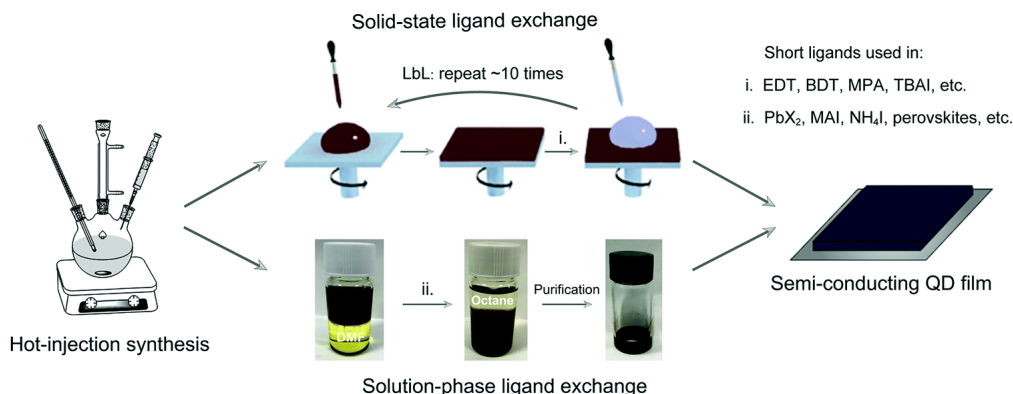


Figure 1.15: Illustration of PbS NC layers prepared based on SSE (top) and PTE (bottom). Reproduced from [18].

SSE

PTE

	SSE	PTE
process	material consuming	thickness-dependent concentration
film morphology	cracks due to volume contraction	homogeneous film
NCs quality	fusion	better passivation control
best PCE*	12.5% [132]	14% [133]

Table 1.1: Summary of the solid-state exchange and phase-transfer exchange process.*PCE means power conversion efficiency and corresponds to the percentage of the solar energy shining on a solar cell device that is converted into usable electricity.

Latest PTE development for PbS NCs [20]

At the early stage of the PTE process, the NCs were only stable at low concentrations ($50 \text{ mg}\cdot\text{mL}^{-1}$) because of non-sufficient electrostatic repulsion leading to NCs aggregation. Because the thickness of the deposited layer is concentration-dependent, the range of applications was limited. Ning et al. [134] used butylamine to re-disperse the NCs, improving their stability at higher concentrations ($200 \text{ mg}\cdot\text{mL}^{-1}$). In 2017 Liu et al. [115] unveiled a new PTE process with a mixture of lead halides (bromide and iodide) in which ammonium acetate (AA) was added. They proposed that the ammonium ions support the exchange of oleate ligands by the $[\text{PbX}_3]^-$ anions in the polar solvent. A washing step removes the AA and the excess lead halide salts, leaving $[\text{PbX}_3]^-/[\text{PbX}]^+$ passivating the NC surface without any organic residue. Wang et al. [135] support the accelerating removal of OA ligands by AA and give an optimized concentration to improve the device performance. The above exchange process was performed on 3 nm NC size with mainly (111) facets. However, as discussed in the preceding sub-section, ligands have a weak affinity to (001) surfaces (electrically neutral and self-passivated). In 2019, Fan [136], and Kim [19] were interested in the passivation of larger PbS NCs for IR applications. Kim suggested the replacement of ammonium acetate [115] with sodium acetate (NaAc), which would passivate (100) facets. By DFT calculations, they show that Na preferentially binds to the sulfur atoms on (001) facet (see Figure 1.16). Fan, in addition to sodium acetate, proposed a mixed passivation solution (bromide, iodide, and chloride), suggesting that large lead iodide ligands would passivate (111) facets while smaller lead halides would passivate (100) facets. During the same year, Gu [23], on top of a first PTE step (with lead iodide and AA), performed a second passivation step with mercaptopropionic acid (MPA). Adding MPA would replace -OH groups, providing additional surface passivation and improving colloidal ink stability in butylamine via its thiols and carboxyl moieties. One year later, Choi et al. [24] developed a cascade surface modification procedure where the initial oleic acid ligands are first replaced by halogens (bromide and iodide), forming the n-type NC ink. A successive step of passivation by the thiol group (cysteamine) modifies the doping character transforming the n-type ink to p-type. This CSM procedure produces miscible p-type and n-type ink, presenting distinct potential differences, good coverage, and unveiling NC bulk homojunction solids in solar cells with a record power conversion efficiency (PCE) of 13.3%. The same group [137], by replacing NaAc with potassium iodide (KI) on top of standard iodide-bromide passivation [115] demonstrates an im-

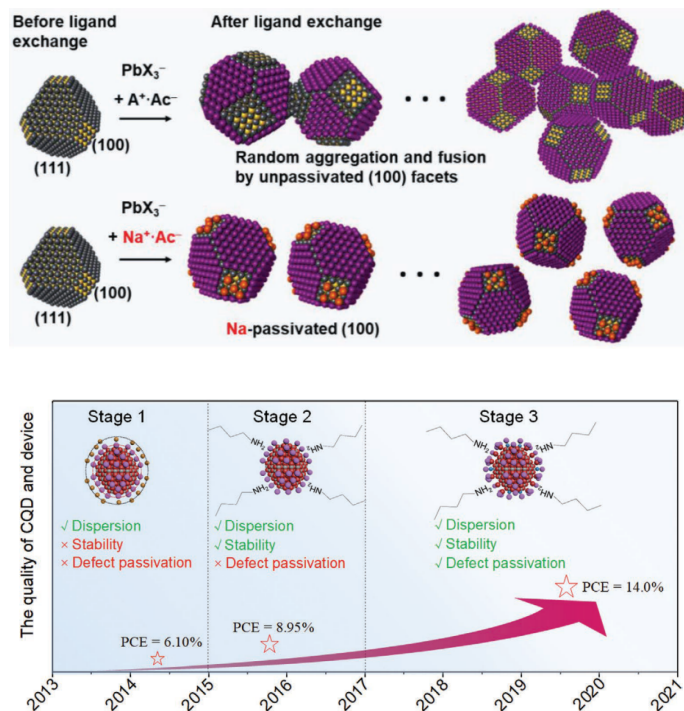


Figure 1.16: (a) Effect of sodium (100) passivation on the colloidal stabilization. Reproduced from [19]. (b) The three main stages that mark PTE development. Reproduced from [20].

proved NC photovoltaic devices stability under continuous operation in an ambient condition. Compared to a control device structure ITO/ZnO/PbS–PbI₂/ PbS–1,2-ethanedithiol (EDT)/Au, the KI shielded sample (ITO/ZnO/KPbS/PbS-EDT/Au) showed increased charge carriers mobility, and PCE, resulting from the prevention of surface passivation from oxidation (PbO, PbSO₃, and PbSO₄).

1.5 Results on NC colloidal formation

1.5.1 Syntheses

We followed two standard syntheses where the control of NC size is either by monomer generation (Owen synthesis [12]) or by growth control (Zhang synthesis [9]). We illustrate in Figure 1.17 the typical bench synthesis.

Zhang synthesis [9] Following Zhang protocol, we performed four NC syntheses. Instead of using PbO as the lead precursor, Pb₃O₄ has been used and implies a slight modification of the method suggested by Zhang et al. First, 0.7 g of lead oxide (Pb₃O₄ -2 eq.), 5 g oleic acid (OA), and 8 g octadecene (ODE) has been added into a two-neck flask, and the resulting red suspension was heated at 150°C under Ar atmosphere for 12 hours until a clear yellow solution was obtained. Then 15 ml ODE was added into the flask. The temperature of the flask was lowered to 100°C followed by the fast injection of a solution of 1.5 mmol (268 mg⁻¹ 1 eq.) bis(trimethylsilyl)sulfide [(TMS)₂S] in 10 mL ODE, prepared inside the glove box.

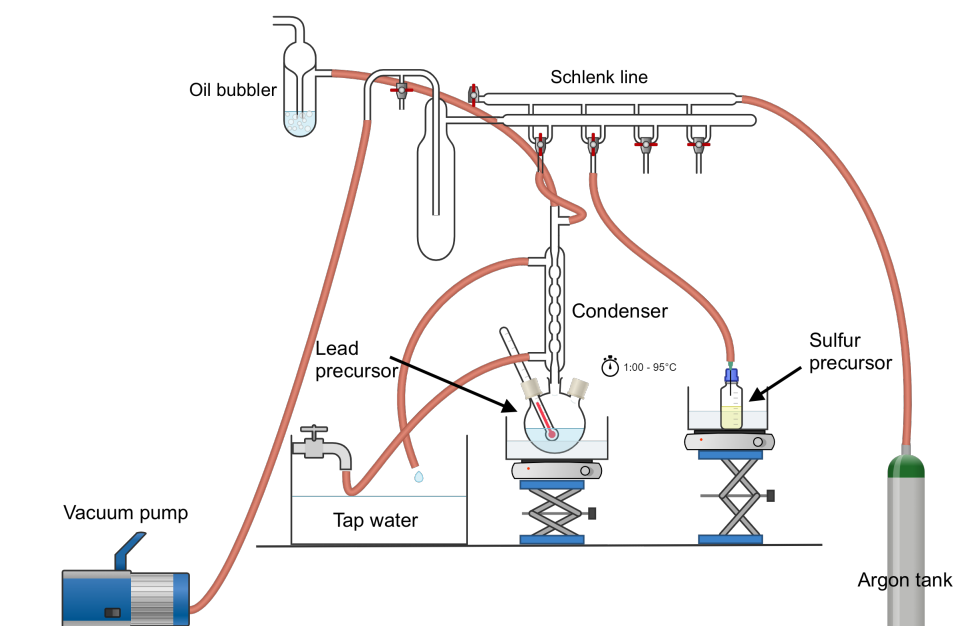


Figure 1.17: Illustration of a synthesis bench.

Before the injection, the heater was removed, and efficient stirring was assured. A few seconds after the injection, the color of the solution in the flask changed to black, and the reaction mixture was left to cool naturally. This synthesis results in NCs of 2.8 nm, that will label the Z1 sample. For bigger sizes, we increased the injection temperature to 120 °C and changed the amount of OA to 10, 20, and 50 g, which gave NC sizes of 3.6, 4.0 and 4.5 nm, respectively.

Owen synthesis [12] We performed three NC syntheses following Owen protocol. Lead oleate (0.259 mmol– 1.5 eq.) and 1-octene (3.34 mL) are added to a 3-neck round bottom flask. In a 10 mL vial, N,N'-diphenylthiourea (0.173 mmol – 1 eq.), and ethylene glycol dimethyl ether (EGDME: 113 μ L) are mixed. Both solutions are brought to 95 °C, then the solution of thiourea is injected into the PbOA solution. The reaction is allowed to run for 60 seconds before the flask is removed from the hot oil bath. This synthesis leads to NC size of 3.70 nm. We modify the initial protocol by decreasing the sulfur precursor amount while keeping the lead precursor constant. We observed a decrease in the NC size with decreasing sulfur amount. A Pb:S ratio of 2 and 2.5 gave respectively NC sizes of 3.3 and 2.9 nm.

1.5.2 Characterization

Optical characterization

Figure 1.19 gives the absorption and photoluminescence spectra of the syntheses following Zhang protocol named Z1, Z2, Z3 and Z4. The main characteristics are given in Table 1.2. For photoluminescence measurements, to avoid the screen of the peak at a high energy range due to reabsorption, we diluted the samples. However, this dilute system suffers from enhanced solvent absorption impeding a part of the peak represented by red dashed line. The size of a NC can be estimated via the first

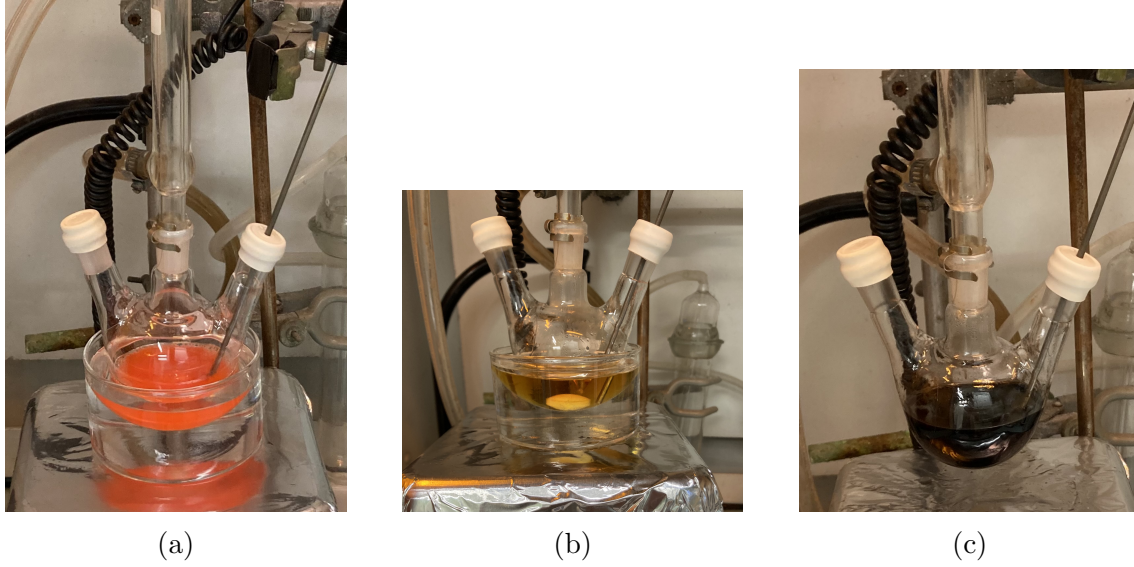


Figure 1.18: Image of the NC PbS synthesis. Resulting solution after the lead precursor complexation at $t=0$ (a) and $t = 12$ h (b). The final solution that contains the PbS NCs in ODE (c).

absorption peak position (E_0) using a benchmark fitting equation:

$$E_0 = 0.41 + \frac{1}{ad^2 + bd} \quad (1.20)$$

with d the diameter in nm. We used the Moreels parameter corresponding to $a = 0.0252$ and $b = 0.238$ [21]. We obtained NC sizes ranging from 2.8 nm to 4.5 nm resumed in Table 1.2 and represented in Figure 1.19 by the black empty dots. Weidmann et al. [32] linked the half width at half maximum (HWHM) of the first absorption peak to the size dispersity σ of the sample:

$$HWHM = 0.005 \frac{ad^2 + (b - 2a)d - b}{(ad^2 + bd)(ad + b)} \sigma \quad (1.21)$$

with HWHM in meV and the dispersity σ in % and defined as:

$$\sigma = \frac{\delta d}{d} 100 \quad (1.22)$$

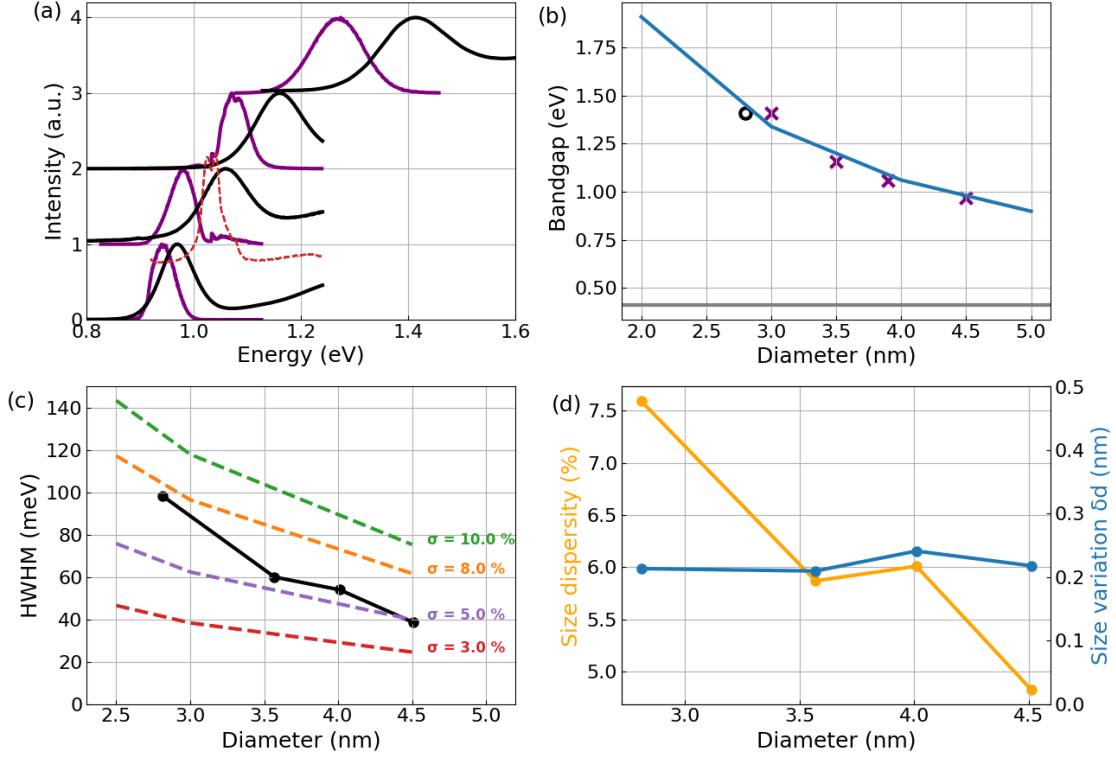


Figure 1.19: Optical measurements of the syntheses following Zhang protocol. (a) Absorption (black line) and PL spectra (purple line) of PbS NCs along with the hexane absorption (red dashed line). (b) Bandgap evolution with the NC size. Blue line: curve given by eq. 1.20 with the Moreels parameters [21]; Purple cross: TEM measurements; Black dot: XRD measurement. (c) Variation of the HWHM with the NC size for our syntheses (black line), and calculated for different size dispersity with eq. 1.21 (dashed lines). (d) Size dispersity (orange line) and size variation (blue line) with the NC size.

name	abs1 (eV)	size* (nm)	Stokes shift (meV)	HWHM (meV)	dispersity (%)
Z1	1.41	2.81	140	99	8
Z2	1.16	3.57	90	60	6
Z3	1.06	4.01	79	54	6
Z4	0.97	4.51	39	39	5
H1	1.12	3.71	N/A	60	6
H2	1.24	3.28	N/A	82	7
H3	1.374	2.91	N/A	N/A	N/A

Table 1.2: Optical features of PbS NCs following Zhang synthesis [55] (samples named Zi); or Hendricks synthesis [12] (sample named Hi) but increasing the sulfur precursor amount for H2 and H3 to adjust the NC size. Abs1 corresponds to the energy position of the first excitonic peak. *Size is obtained from the Moreels formula eq. 1.20.

The eq. 1.21 is a clear example of an inhomogeneous broadening of a physical property (here the linewidth of optical spectra) due to the size distribution of an ensemble of NCs. Because the bandgap energy has a strong dependence on the NC

size, the broadening is known to mainly originate from the size dispersion but the shape distribution and electron-phonon interactions can also play a role. Indeed, as the bandgap energy variation is exacerbated at small NC size, thus the HWHM is enhanced for decreasing size and makes the HWHM not a relevant comparator of size dispersity. Indeed, we can see in Figure 1.19c that for the same size dispersity the broadening (HWHM) of the absorption peak increases with decreasing size. Moreover, it is obvious from eq. 1.22 that dispersity depends also on the size, small variations δd will be amplified for smaller NCs. It is apparent for our syntheses where the dispersity decreases but the size variation is constant. The Stokes shift (Table 1.2) also increases with smaller sizes. It has been shown [106, 105] that the Stokes shift originates mainly from the polydispersity, due to energy transfer among NCs, from small to larger. This phenomenon is also observed in dilute systems due to aggregation and is enhanced in closed-packed systems such as films. In line with the previous arguments, we advance that the Stokes shift is exacerbated in small range size.

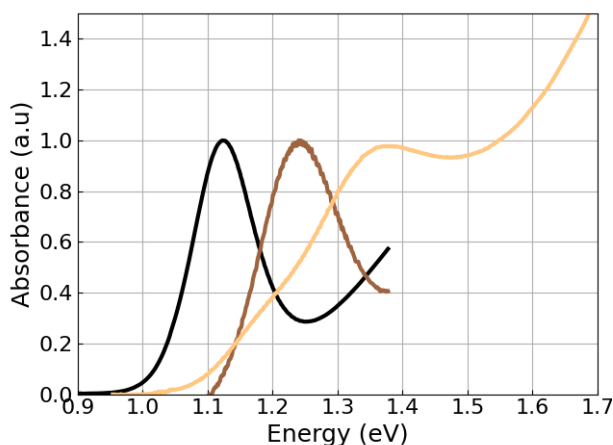


Figure 1.20: Optical absorption spectra with a Pb/S ratio of 1.5 following Hendricks' work [12] (black line); and modified: 2 (brown line) and 2.5 (orange line). The amount of sulfur precursor is increased while the lead amount is kept constant.

We also performed three syntheses following Hendricks protocol [12]. To assess the effect of stoichiometry on the synthesis, we modified the initial protocol by decreasing the sulfur precursor amount while keeping the lead precursor constant (see Figure 1.20). Even though, we observed an increase in the reaction time with decreasing sulfur amount, the NC size decreased. These results are in contradiction with the NG model presented in section 1.3.1 and with what has been observed for CdSe NCs [110]. Indeed, they showed that the monomer generation rate is in first-order on cadmium and selenium amount. Therefore, the monomer generation rate decreases with decreasing precursor amount as the number of particles (see eq. 1.17) which should lead to larger NCs. Further investigations are needed to understand this behavior.

PXRD characterization

The structural analysis of powder PbS NCs was carried out with a beam of 15.4 nm for a 2θ angle from 15 to 150 °C. Figure 1.21 shows the diffraction pattern obtained

for the four PbS NCs: Z1, Z2, Z3, and Z4. We can see sharper peaks from Z1 to Z4, characteristic of bigger NC (see eq. 1.4).

We performed a refinement method on Z1 diffraction patterns which gives a cubic phase of PbS with a rocksalt structure of the space group Fm3m and a lattice parameter of 5.954 angströms, in compliance with other works [34]. The rocksalt structure corresponds to two interlocked face-centered cubic (fcc) lattices for each of the ions. Each atom of the crystal has 6 nearest neighbors and thus is in 1:1 stoichiometry. The Z1 sample presents a crystallite size of 2.81 nm in total agreement with the optical measurements.

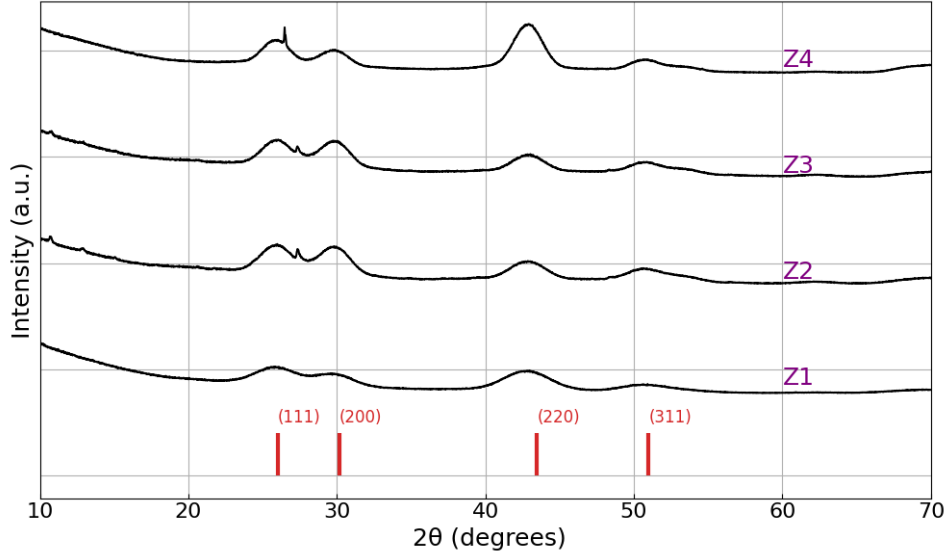


Figure 1.21: XRD diffractograms of Z1, Z2, Z3, and Z4 samples from bottom to top. The vertical lines represent the peak position of bulk PbS taken from [22].

TEM analysis

In Figure 1.22h, we give the TEM images with the size distribution histograms for the samples Z1, Z2, Z3, and Z4. The obtained sizes are in good accordance with the optical measurements (see Table 1.2). The overall size dispersity is 10 %, which is higher than the one predicted by eq. 1.22 (see Table 1.2). However, the number of sampled NCs is not enough to obtain an accurate measurement. As expected, the NCs present spherical-like shapes.

TGA analysis

In Figure 1.23a, we show a TGA spectrum measured on the H2 sample corresponding to PbS NCs of 3.3 nm capped by oleate ligands. As discussed above, this NC size corresponds to a truncated octahedron. We constructed this NC, shown in Figure 1.23b, using a Wulff ratio of $\frac{\sqrt{3}}{2}$, which gives a NC made of 1045 atoms, 459 of which are S atoms and 586 are Pb atoms. The Pb:S ratio is 1.26 in compliance with Figure 1.14b [17] and Hendricks et. al. [12] and corresponding to an excess of 127 Pb^{2+} ions, which needs 254 charge compensation from X-type ligands. The TGA shows 32% of weight loss which corresponds to the thermal decomposition of oleate

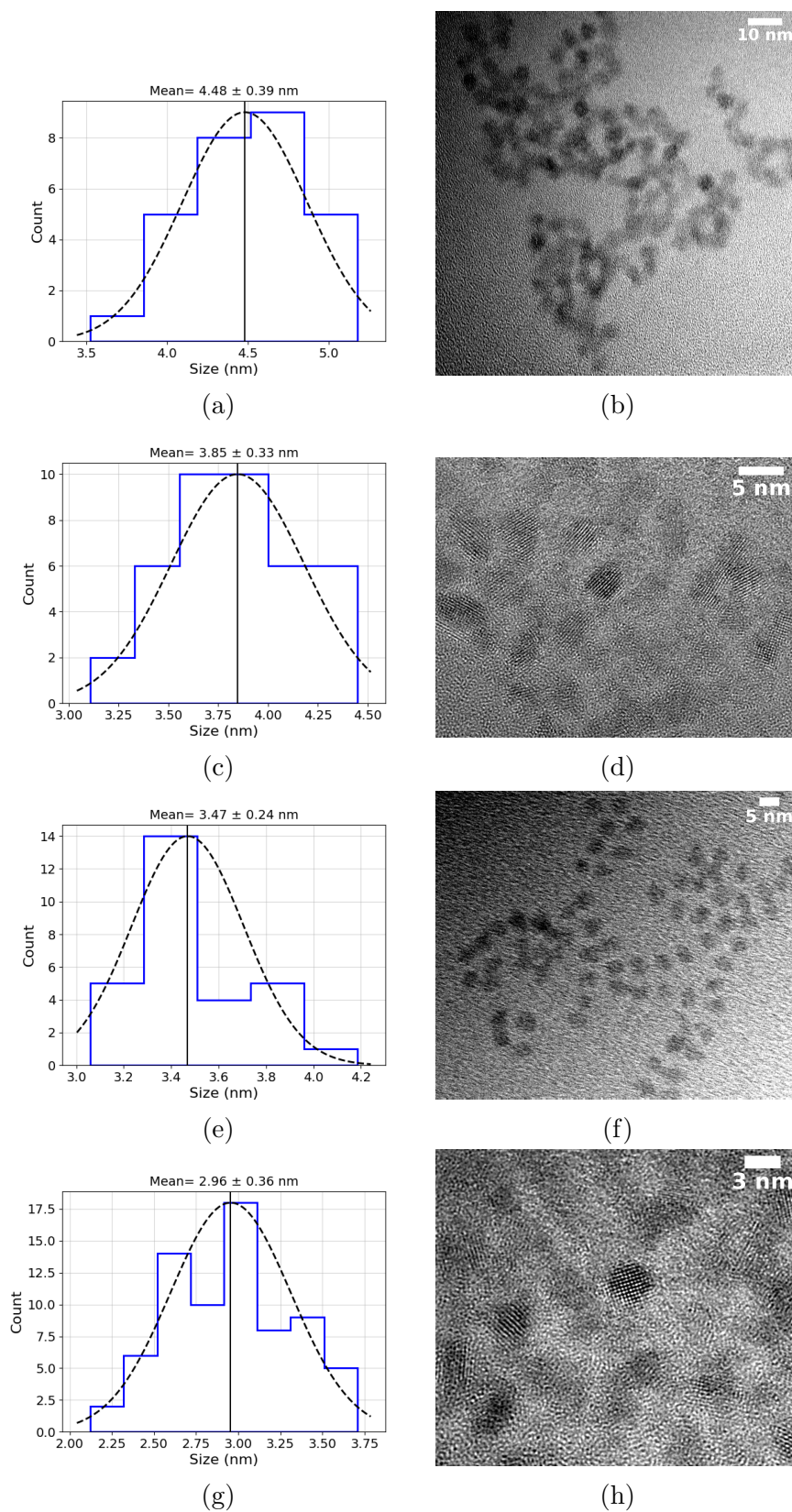


Figure 1.22: Size distribution histograms and TEM images. Sample Z4 : (a) and (b); sample Z3 : (c) and (d); sample Z2 : (e) and (f); sample Z1 : (g) and (h).

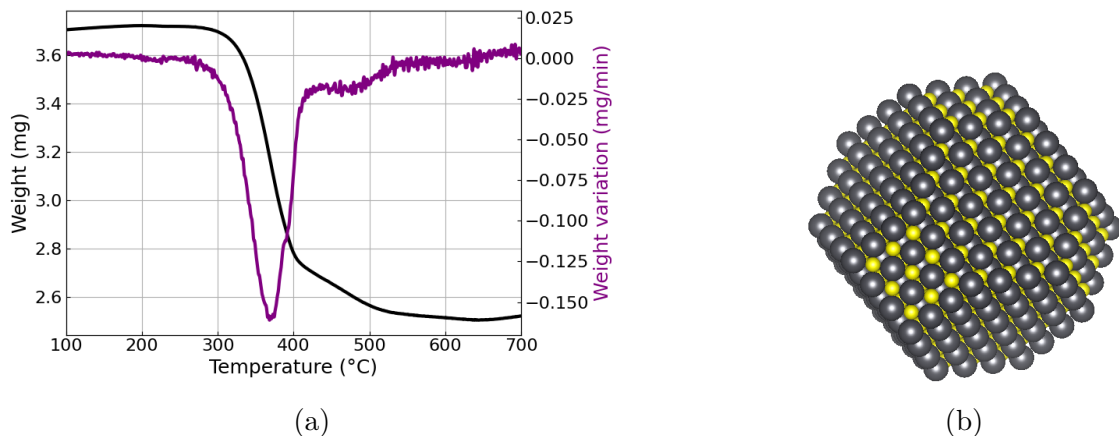


Figure 1.23: (a) TGA signal of PbS NCs capped by oleate ligands. (b) Model NC used for TGA analysis.

ligands in total accordance with Beygi et. al. [34]. Combining the TGA result with our model NC, we obtain 227 oleate ligands by NC, which implies a lack of 27 X-type ligands. Assuming these ligands correspond to hydroxide groups, we found an OA/OH ratio of 8:1, higher than other works [34, 125, 126]. However, the 227 oleate ligands spread on the truncated octahedron surfaces give 5.9 OA per nm^2 in good accordance with Hendricks work (5.7 OA/ nm^2 [12]).

1.5.3 Ligand exchange

We performed two different PTE processes to assess the surfaces of PbS NCs. As initial NCs, we used the sample Z2 whose optical properties have been analyzed in section 1.5.2. To recall, they present an excitonic peak at 1.16 eV, corresponding to a size of 3.6 nm (from Moreels fit), HWHM of 90 meV, giving a polydispersity of 6%, and a Stock shift of 90 meV.

PTE processes

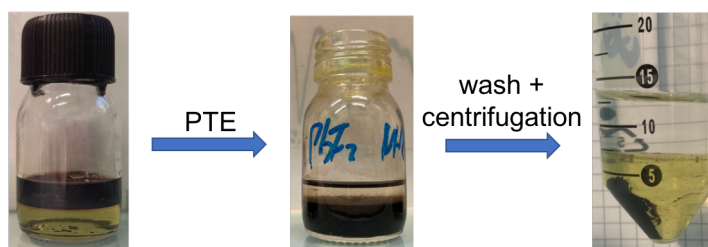


Figure 1.24: Images of the PTE process.

We followed the protocol of Gu et al. [23], where lead iodide (230 mg) and NH_4Ac (20 mg) are dissolved in dimethylformamide (DMF) (5 mL). To obtain a mass concentration of Pb-OA of $8 \text{ mg}\cdot\text{mL}^{-1}$, we dissolved 40 mg of Z2 sample in 5 mL of hexane. The latter solution was added in the former, then mixed vigorously for 2–3 min until the NCs completely transferred to the DMF phase. After ligand exchange, the DMF solution was first washed one time with toluene. Finally, the

NCs were precipitated through centrifugation via the addition of toluene (see Figure 1.24).

In parallel, we followed Choi's PTE procedure [24], where lead iodide (230 mg), lead bromide (37 mg) and NH_4Ac (20 mg) are dissolved in DMF (5 mL). Then, we dissolved 35 mg of Z2 sample in 5 mL of hexane, that we added in the former solution. Then the solution was mixed vigorously for 1–2 min until NCs were transferred to DMF phase. The same washing procedure as described above was applied.

Optical characterization

The absorption and photoluminescence spectra are given in Figure 1.25, and the optical features recapped in Table 1.3.

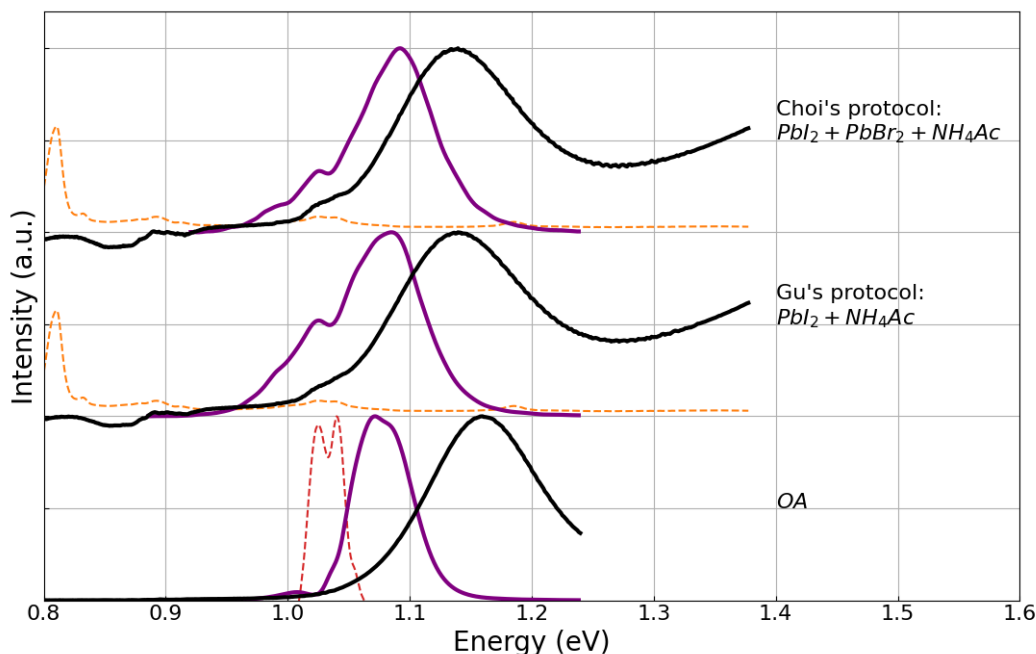


Figure 1.25: Absorption (black solid line) and photoluminescence (purple solid line) of oleate-capped PbS NCs and after PTE processes following Gu [23] and Choi [24] protocols. The dashed lines correspond to the solvent absorption: hexane (red) and butylamine (orange).

For the two PTE processes, we obtained well-defined absorption spectra witnessing of the good stability of the colloidal solution (shown in Figure 1.25). The excitonic peak is at 1.14 eV, and the HWHM value of 73 meV gives a polydispersity at 7%. Compared to oleate-capped PbS NCs (see Table 1.3), the excitonic peak is 0.02 eV (equivalently 19 nm) red-shifted, which is expected from the literature [138, 134, 139, 140, 141, 142] but still not well understood. Different hypotheses have been proposed:

- Ning [134] suggested that the highest occupied molecular orbital (HOMO) is shallower for the iodide element than for the initial oleate ligand decreasing the exciton confinement.
- The new ligands (assimilated to a dipole) would help delocalize the electron wave function shrinking the optical bandgap [14].

- Sklénard et al. show that changing the dielectric environment of the NCs can modify the bandgap [143].
- Inhomogeneous passivation could create an electric field inside the NC separating the hole and electron wavefunctions and therefore decreasing the first exciton energy [144].

In addition to the red-shift of the absorption peak, the PL position is blue-shifted giving a Stokes shift divided by almost a factor of 2. This is an indication of a better surface passivation limiting the energetic disorder.

We also followed the work of Choi et. al. [24] adding lead bromide to the ligand solution. It gives equivalent optical features even though it has been shown that bromide atoms have higher binding energies on the Pb (100) facets compared to iodide and thus would improve the colloidal stability [136].

name	abs1 (eV)	pl1 (eV)	size (nm)	Stokes shift (meV)	HWHM (meV)	dispersity (%)
Z2	1.16	1.07	3.57	90	60	6
Gu	1.14	1.09	3.65	47	73	7
Choi	1.14	1.09	3.65	47	67	7

Table 1.3: Optical features of PbS NCs following the Zhang’s synthesis (Z2)[55], and after the PTE process following the Gu [23] and Choi’s protocols [24]. Abs1 and pl1 correspond to the energy position of the first absorption and photoluminescence peak, respectively.

FTIR

To check the completeness of the PTE process, we performed three FTIR spectra, represented in Figure 1.26. The peaks around 2900 and 1400-to-1600 cm^{-1} are features of the oleate ligands [145, 146]. These peaks disappear after the two PTE processes, which suggests the replacement of all OA ligands by the halides. The peak at 2300 cm^{-1} before ligand exchange corresponds to CO_2 molecules from the environment, and the peak at 1700 cm^{-1} after ligand exchange corresponds to DMF molecules.

EDS

By EDS (Figure 1.27), we assessed the effect of post-process steps (washing and centrifugation). For both samples, we notice a large excess of iodide is still present after the washing step in toluene. This step using an organic solvent is mainly performed for removing the oleate ligand still present in the exchange solution. However, we observed a decrease in the excess of iodide elements after the centrifugation and particularly for Gu protocol with an I/Pb ratio going from 1.37 to 0.40. It is less than what Gu et al. [23] obtained (0.67), which we ascribe to their smaller NCs with more polar (111) surfaces. For Choi protocol [24], as the centrifugation did not properly remove the excess of precursors, we cannot assume any efficient bromination of the surface.

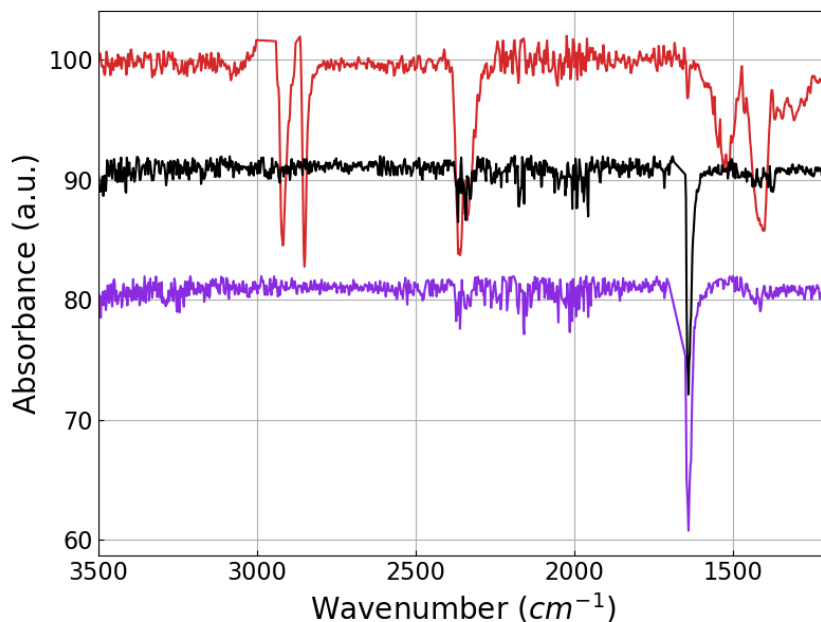


Figure 1.26: FTIR spectra of oleate-capped PbS (red line), after Gu [23] (black line), and Choi PTE protocol [24] (purple line).

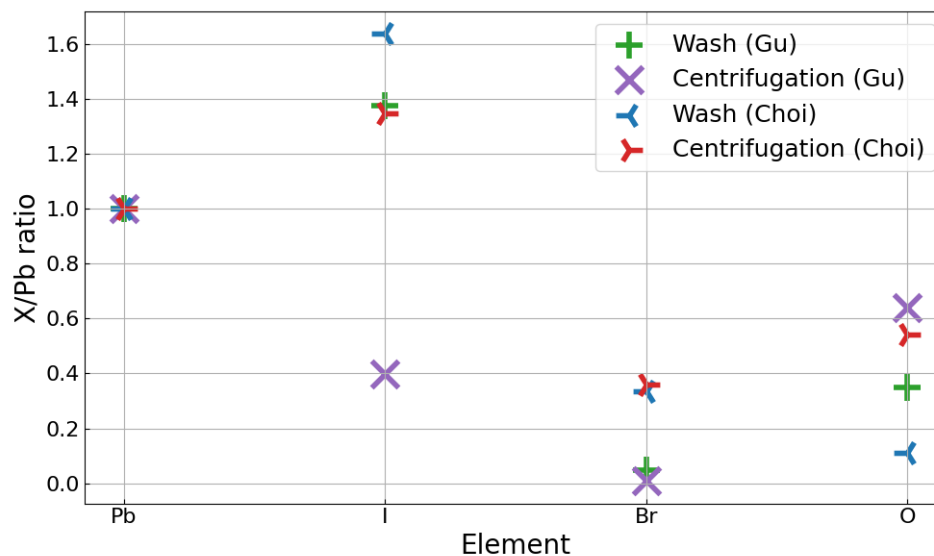


Figure 1.27: EDS analysis at the different steps of the PTE process.

1.6 Conclusion

These last decades have seen numerous developments in the synthesis and characterization of NCs. They enable better control but also better understanding of these nano-objects, which have been the recipe for their recent success at the industrial level. The first section 1.2 of this Chapter is devoted to a presentation of experimental characterization methods currently used to probe different aspects of NCs, e.g. the size and crystalline structure with PXRD, or the surface by TGA or EDS. The second section 1.3 presents the mechanisms of formation of NCs in solutions, along with the primary synthesis protocol of PbS NCs. The former unveils insights

that allow the development of reproducible synthetic routes with well-defined NC size and shape. As an object goes smaller, its surface-to-volume ratio increases. It is why we dedicated the section 1.4 to the PbS NC surfaces, discussing recent results such as different properties of (111) and (100) surfaces, and how they can be modified by ligand exchange. This knowledge serves us to carry out different experiments presented in section 1.5. In sub-section 1.5.1, we followed two synthesis protocols, namely Zhang [9] and Owen synthesis [12], that allows us in sub-section 1.5.2 to highlight the effect of size dispersity on optical properties, and we studied the NC surfaces by TGA. Finally, we performed two PTE processes, one with PbI_2 [23], and the other combining PbI_2 and PbBr_2 ligands [24]. The efficiency of the exchange was analyzed by FTIR and EDS, while the effects on the optical properties were probed by absorption and photoluminescence spectroscopy.

Chapter 2

Bulk to nanocrystals: electronic structure

2.1 Introduction

The electronic structure is a key material property from which numerous physical quantities are extracted: ionization potential, work function, optical gap, absorption spectra, etc. This Chapter reviews the theoretical approaches used during this thesis for the determination of the bulk and NC electronic structure. We detail two semi-empirical methods known as Empirical Tight-Binding Method (ETBM) and Empirical Pseudopotential Method (EPM), and one *ab initio* method named Density Functional Theory (DFT). We describe the theoretical aspect of these methods and emphasize the connections between them.

We apply these formalisms to the calculation of bulk and 0D confined structures named NC. More precisely, using the three methods mentioned above, we compute the band structure of bulk PbS which allows us to understand its peculiar behavior and also to check the validity of the ETBM compared to advanced DFT calculations. Then, we apply ETBM calculations to NCs that are out of reach of *ab initio* simulations. The variation of the bandgap energy with size along with different fundamental properties are studied. In line with this methodology, the bulk and NC structures of mercury telluride (HgTe) are also investigated by ETBM. An important result is the prediction of a topological transition, when going from an NC to a bulk structure, for a diameter of ~ 26 nm.

Therefore, this Chapter introduces the numerical methods used in the rest of the thesis. It gives an overview of the fundamental physics underlying HgTe and PbS materials, and of equal importance it allows us to check the accuracy of the numerical methods by comparing their results to experimental data.

2.2 Numerical methods

In quantum mechanics [147], we describe the state by vectors that spanned in the Hilbert space, and thus any states can be expressed as a linear combination in a complete basis set. For numerical purposes, we often represent the states on a truncated basis set. To obtain the physical value of an observable (energy, position, spin, etc), we construct linear operators usually represented by a matrix in a basis

of the Hilbert space. In the majority of cases, the action of an operator over a state will give one of the values of the observable with a certain probability. However, in the case of an eigenstate of the operator, we will obtain every time the same value named the eigenvalue. Thus, a matrix expressed in the basis of its eigenstates is diagonal with the diagonal elements being the eigenvalues. Therefore, one of the main goals of the numerical tools is to solve eigenvalue equations. In the electronic structure field, a key observable is the ground state energy. Indeed, it allows us to study a variety of properties: equilibrium structure, cohesive energy, molecule adhesion, and many others. The operator corresponding to the system energy is the Hamiltonian and, in the case where it is independent of time, its eigenstates are solutions of the time-independent Schrödinger equation (eigenvalue equation):

$$\hat{H}\Phi = E\Phi \quad (2.1)$$

with E the energy of the system, ϕ the many-body wavefunction and \hat{H} the Hamiltonian operators. For a system composed of electrons and nuclei, the Hamiltonian writes:

$$\hat{H} = \hat{T}_e + \hat{V}_{ee} + \hat{T}_N + \hat{V}_{NN} + \hat{V}_{eN} \quad (2.2)$$

with \hat{T} the kinetic energy and \hat{V} the potential energy. In principle, we should solve this many-body eigenvalue equation (eq. 2.1) incorporating electron-electron, electron-nuclei, and nuclei-nuclei interactions. However, although these many-body terms are essential to describe complex structures and their properties, these terms make eq. 2.1 unsolvable. Therefore, the core idea of the electronic structure theory is to find approximations to make the time-independent Schrödinger equation solvable while incorporating sufficient descriptions of the many-body effects.

Figure 2.1 depicts the main approximations included in the numerical methods used during this thesis. First, the nuclei present a mass much larger than the electrons, thus the motions of electrons and nuclei can be separated. This is the so-called Born-Oppenheimer (BO) or adiabatic approximation that leads to an electronic Hamiltonian H_{BO} describing electrons moving in the field of fixed nuclei with the wavefunction depending explicitly on the electron coordinates but parametrically on the nuclear coordinates. Although simplified, the eigenvalue equation is still unsolvable due to the inter-electronic repulsion. By consequence, the second approximation is to transform the impossible problem of interacting electrons into an easier one of non-interacting electrons. Thus we consider a system of an almost independent particle, in which each electron moves in an effective potential V_{eff} including all the other electrons and the nuclei. At this stage, we need to consider separately the semi-empirical methods with a non-explicit form of V_{eff} to the ab initio ones. But first, we will discuss the Ritz theorem which gives a general method (a generalization of the variational method) to solve the eigenvalue equation.

Ritz theorem [148, 147] The Ritz theorem states that the mean value of the Hamiltonian that is written:

$$\langle E \rangle [\Psi] = \frac{\langle \Psi | H | \Psi \rangle}{\langle \Psi | \Psi \rangle} \quad (2.3)$$

is stationary in the neighborhood of the eigenstates. Therefore, the integro-differential equation, being the time-independent Schrödinger equation, can be solved by find-

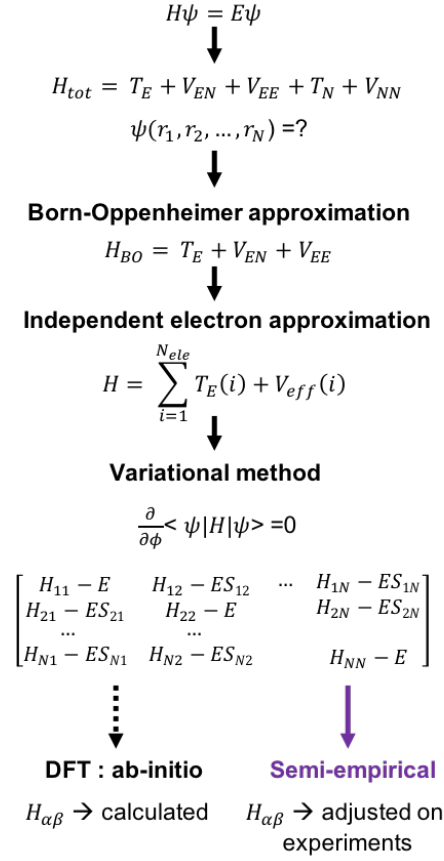


Figure 2.1: Schematic representation of the main approximations underlying ab initio and semi-empirical electronic structure theories. See eq. 2.4 for the definition of Ψ and ϕ ; and eq. 2.5 for the definition of H_{ij} and S_{ij} .

ing the wavefunction Ψ that makes extremum the functional $\langle E \rangle [\Psi]$. A common strategy is to express the wavefunction on the basis of known functions:

$$\Psi = \sum_i c_i \Phi_i \quad (2.4)$$

and then re-write the eq. 2.3 as:

$$\langle E \rangle [\Psi] = \sum_i \sum_j \frac{c_i c_j \langle \Phi_j | H | \Phi_i \rangle}{c_i c_j \langle \Phi_j | \Phi_i \rangle} = \sum_i \sum_j \frac{c_i c_j H_{ij}}{c_i c_j S_{ij}} \quad (2.5)$$

where H_{ij} is a matrix element and S_{ij} an overlap matrix. This allows us to search the coefficients that minimize the energy in the form of:

$$\frac{\partial \langle E \rangle (c_1 \dots c_n)}{\partial c_l} = 0 \quad \forall c_l \in \{c_1, c_2, \dots, c_n\} \quad (2.6)$$

Doing the derivation for each coefficient gives N equations with N unknowns. The solution of this linear system is non-trivial if the determinant of the coefficients is non-zero:

$$\begin{vmatrix} H_{11} - E & H_{12} - ES_{12} & \dots & H_{1N} - ES_{1N} \\ H_{21} - ES_{21} & H_{22} - E & \dots & H_{2N} - ES_{2N} \\ \vdots & \vdots & \vdots & \vdots \\ H_{N1} - ES_{N1} & H_{N2} - ES_{N2} & \dots & H_{NN} - E \end{vmatrix} = 0 \quad (2.7)$$

The secular equation leads to N eigenvalues which are approximations of the ground state energy and the $(N-1)$ excited states. The approximation comes from the truncation of the base which restrains the explored Hilbert space. In the case of the empirical method, matrix elements are adjusted to experimental values while *ab initio* ones use first principle calculations.

Ab initio methods through the Density Functional Theory (DFT) [25]

The DFT relies on the Hohenberg-Kohn theorems [149] that state that the ground state energy (actually any ground state observable) of a system is a unique functional of the density. However, the form of the functional and the density are unknown. The idea of Kohn and Sham [150] is to construct an auxiliary system of non-interacting particles sharing the same density as the interacting one. Using a variational principle (special case of the Ritz theorem for the ground state), they unveil a set of equations for the auxiliary system (named the Kohn-Sham equations) in which each independent electron feels an effective potential V_{eff} written as a sum of three terms: the potential due to nuclei V_{eN} , the mean potential due to the other electrons V_{ee} and the exchange-correlation potential V_{xc} . This set of coupled equations:

$$[T_e + V_{eff}(\mathbf{r}, [n])] \Psi(\mathbf{r})_i = \epsilon_i \Psi(\mathbf{r})_i \quad ; \quad i = 1, 2, \dots, N \quad (2.8)$$

gives in principle the exact ground state density of the interacting system. However, the exchange-correlation potential is unknown. Tremendous work has been done to approximate V_{xc} giving birth to a variety of functionals and it is still an active field of research. Moreover, the Hamiltonian depends on the density which depends itself on the wavefunction, the solution of the equation. Therefore eq. 2.8 needs to be solved iteratively (so-called a self-consistent field approach) by starting with an initial guess of wavefunctions. The latter can be developed in a variety of basis: plane waves, atomic orbitals, Gaussian, etc; and the Ritz theorem is employed to construct the Hamiltonian and diagonalize it. The DFT is an *ab initio* method in a sense that the matrix elements (integrals) are calculated self-consistently from first-principles, without relying on fitting parameters. The eigenstates obtained can be used to get the density which is exact in principle and can be used as input of any observable. However, while the eigenvalues obtained from the matrix diagonalisation (see eq. 2.7) have the dimension of energy, they do not correspond to the real energy of electrons of the interacting system but can at least be used as an approximation of them whose quality depends on the exchange-correlation approximation. Moreover, corrections can be applied using many-body approaches, e.g., GW approximation or hybrid functionals [151, 152]. It also exists extensions of the DFT to go beyond the ground state and access the excited states with the time-dependent density-functional theory (TDDFT) [153]. Despite their quantitative accuracy, *ab initio* methods are restrained by the size of the system. Indeed, the numerical cost quickly escalates with the number of atoms. It is why semi-empirical methods are often preferred or used in parallel to study NCs composed of thousands of atoms.

Empirical Pseudopotential Method (EPM) [154, 155, 156] To reduce the many-body problem, EPM considers only the valence electrons assuming that the inner electrons are tightly bound to the nuclei. This approximation is known as the frozen core. However, the wavefunction of the valence electrons needs to follow the Pauli principle and needs to be orthogonalized to the core states. This last statement makes the outer electrons wave functions rapidly oscillating near the atomic core but has a smooth plane-wave-like nature between neighboring cores [157, 158]. The idea of the pseudo-potential is to incorporate the strongly oscillating behavior while the pseudo-wavefunction describes the plane-wave nature [159]. In other words, the pseudopotential approach offers a justification for describing an outer electron by a linear combination of plane waves, the so-called pseudo-wavefunction:

$$\Psi_{n,\mathbf{k}}(\mathbf{r}) = \frac{1}{\sqrt{\Omega}} \sum_{\mathbf{G}} c_{n,\mathbf{k}}(\mathbf{G}) e^{i(\mathbf{G}+\mathbf{k})\cdot\mathbf{r}} \quad (2.9)$$

where \mathbf{G} are reciprocal lattice vectors (see below for Bloch theorem). Then, the effective pseudopotential can be written as a linear superposition of atomic potentials situated at every atom:

$$V_{eff} = \sum_{\mathbf{R}_I} v_I(\mathbf{r} - \mathbf{R}_I) \quad (2.10)$$

encompassing the electron-electron interaction, the electrons-nuclei interaction, and the effects of core electrons. At this stage, we have the wave function described by a linear combination of plane waves and a one-particle Hamiltonian. To resolve the time-independent Schrödinger equation with these ingredients we can use the Ritz theorem. The matrix elements of the determinant eq. 2.7 corresponds of integrals over all space of the form:

$$\begin{aligned} H_{\mathbf{G}',\mathbf{G}} = & \frac{1}{\Omega} \int e^{-i(\mathbf{k}+\mathbf{G}')\cdot\mathbf{r}} \left(-\frac{\hbar^2}{2m_0} \nabla^2 \right) e^{i(\mathbf{k}+\mathbf{G})\cdot\mathbf{r}} d\mathbf{r} \\ & + \frac{1}{\Omega} \int e^{-i(\mathbf{k}+\mathbf{G}')\cdot\mathbf{r}} V_{eff} e^{i(\mathbf{k}+\mathbf{G})\cdot\mathbf{r}} d\mathbf{r} \end{aligned} \quad (2.11)$$

which leads to:

$$H_{\mathbf{G}',\mathbf{G}} = \frac{\hbar^2}{2m_0} |\mathbf{G} + \mathbf{k}|^2 \delta_{\mathbf{G}',\mathbf{G}} + V(\mathbf{G}' - \mathbf{G}) \quad (2.12)$$

The energy potential $V(\mathbf{G}' - \mathbf{G})$ can be expressed as the multiplication of the structure factor $S_f(\mathbf{G}' - \mathbf{G})$ and the form factor $V_f(\mathbf{G}' - \mathbf{G})$. The former depends on the structure system and is easily obtained while the latter corresponds to the Fourier transform of the effective potential of eq. 2.10 and is known as the pseudo-potential form factor. The empirical nature is embodied by adjusting V_f to reach the best agreement of the calculated energy levels with those measured by experimental methods or calculated by ab initio methods.

Empirical Tight-Binding Method (ETBM) [25, 56, 160, 27] As represented in Figure 2.1, the ETBM relies on the same approximations that the EPM (BO, independent electron, and frozen core approximations). Contrary to the EPM method

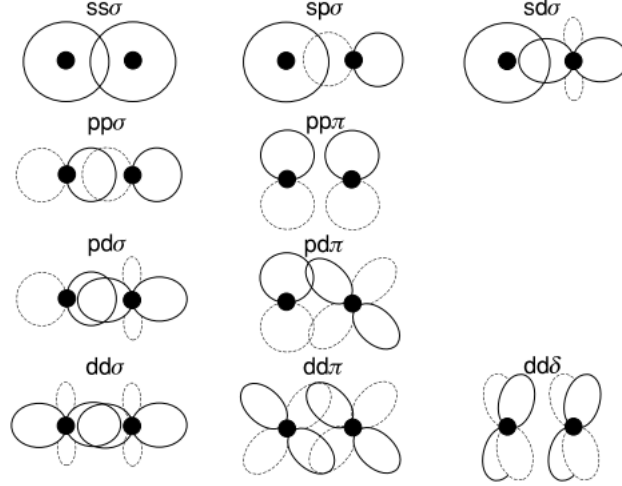


Figure 2.2: Schematic representation of the atomic orbitals s , p , and d forming all possible overlap and two-center integrals which are labeled σ , π , δ depending on the angular momentum position relative to the diatomic bond. Reproduced from [25].

where the pseudo-wavefunction is explicitly defined (see eq. 2.11), only the symmetry of the wavefunction is required for constructing the ETBM matrix elements H_{ij} and S_{ij} .

The ETBM's wavefunctions are expressed as linear combinations of atomic orbitals (depicted in Figure 2.2). The atomic orbitals (s, p_x, p_y, p_z , etc) are localized on the atom site and their radial part decreases exponentially. Moreover, since they are eigenstates of the Hamiltonian, they form in principle a complete basis set for expanding the electron wavefunction:

$$\Psi(\mathbf{r}) = \frac{1}{\sqrt{\Omega}} \sum_{\mathbf{R}_I} \sum_{\alpha} c_{\alpha I} \chi_{\alpha}(\mathbf{r} - \mathbf{R}_I) \quad (2.13)$$

with Ω a normalization volume, and $\chi_{\alpha}(\mathbf{r} - \mathbf{R}_I)$ an orbital of type α localized at the atomic site \mathbf{R}_I . As described for EPM, the potential in the Hamiltonian is also developed into a sum of terms centered on each atomic site (see eq. 2.10), and thus the integrals E_{ij} write as:

$$E_{\mathbf{R}_I \mathbf{R}'_I \alpha \alpha'} = \frac{1}{\Omega} \int \chi_{\alpha}(\mathbf{r} - \mathbf{R}_I) \hat{H} \chi_{\alpha'}(\mathbf{r} - \mathbf{R}'_I) d\tau \quad (2.14)$$

and are either one-, two- or three-center terms depending on the position of the two orbitals $\chi_{\alpha}(\mathbf{r} - \mathbf{R}_I)$ and the potential $v_I(\mathbf{r} - \mathbf{R}'_I)$ on the atomic sites. For instance, the three-center integrals consider the two orbitals and the potential on different atomic sites ($\mathbf{R}_I \neq \mathbf{R}'_I \neq \mathbf{R}''_I$). Slater and Koster [56] in a goal to reduce the integrals into a set of scalar parameters to fit (named the Slater-Koster parameters), they suggest neglecting the three-center integrals; which is known as the two-center approximation. This approximation is justified due to the localized form of the atomic orbitals. Therefore, one only considers the integrals with the potential located on one of the two atoms holding an orbital ($\mathbf{R}_I'' = \mathbf{R}'_I$ or \mathbf{R}_I); reducing the problem to a set of diatomic molecules. Moreover, the ETBM also neglects the interatomic overlap S_{ij} , and the matrix S becomes the identity matrix I [160, 161].

As discussed above, the form of the orbitals is not explicitly written, however, due to symmetry considerations, only a reduced number of integrals are non-zero. Indeed, they are non-zero if the orbitals share an equivalent azimuthal angular momentum (noted m) quantized on the diatomic bond. These orbitals are labeled σ, π, δ for $m = 0, \pm 1, \pm 2$ and correspond respectively to an orientation parallel, perpendicular, and parallel to the diatomic bond (see Figure 2.2). Slater and Koster [56] have introduced a notation e.g. ($sp\sigma$) for an integral between s and p orbital along the bond direction or ($pp\pi$) for an integral between two p orbitals perpendicular the bond direction (see Figure 2.2). This constitutes a basis set for which any integral between two orbitals is expressed as a linear combination of the Slater-Koster parameters ponderated by the direction cosines of the vector of the diatomic bond, noted l, m, n (given in table 2.1). It is good to notice that these integrals depend on the distance between atoms, therefore we must distinguish the nearest neighbor integrals from the second nearest neighbor integrals and so on. From the same arguments of the two-center approximation, it is often sufficient to consider only the first nearest neighbors. Thus, the Hamiltonian matrix is constructed with a set of independent terms (e.g. $E_{s,s}$) that can be used as disposable constants to be fitted on ab initio or experimental data.

To conclude, the ETBM takes advantage of the atomic orbitals to justify the approximations (two-center, and nearest neighbors approximation), and to construct by symmetry the matrix; but the only parts of the wavefunction that are output are the coefficients and the eigenvalues.

	Expression
$E_{s,s}(\mathbf{R}_I - \mathbf{R}'_I)$	$(ss\sigma)$
$E_{s,x}(\mathbf{R}_I - \mathbf{R}'_I)$	$l(sp\sigma)$
$E_{x,x}(\mathbf{R}_I - \mathbf{R}'_I)$	$l^2(pp\sigma) + (1 - l^2)(pp\pi)$
$E_{x,y}(\mathbf{R}_I - \mathbf{R}'_I)$	$lm(pp\sigma) - lm(pp\pi)$
:	:

Table 2.1: Energy integrals corresponding to eq. 2.14 with the notation of Slater and Koster's paper [56]. The factors l and m correspond to the direction cosines of the vector of the diatomic bond.

Bloch theorem [162] To describe the wavefunction of a bulk crystal as a linear combination such as previously described would imply a summation over a considerable number of atoms which is impracticable. However, the Bloch theorem states that an electron in a periodic potential has eigenstates of the form:

$$\Psi_{\gamma\mathbf{k}}(\mathbf{r}) = e^{i\mathbf{k}\mathbf{r}} u_{\gamma\mathbf{k}}(\mathbf{r}) \quad (2.15)$$

where $u_{\gamma\mathbf{k}}(\mathbf{r})$ is periodic in the unit cell and \mathbf{k} the crystal momentum defined in the first Brillouin zone (BZ). The first BZ for face-centered cubic lattice is a truncated octahedron (shown in Figure 2.3 with high symmetry points).

As an example, we can extend the ETBM to electrons wavefunction in a periodic potential by defining a basis state named Bloch sum as:

$$\chi_{\alpha\mathbf{k}}(\mathbf{r}) = \frac{1}{\sqrt{N}} \sum_{\mathbf{R}_I} e^{i\mathbf{k}\mathbf{R}_I} \chi_{\alpha}(\mathbf{r} - \mathbf{R}_I) \quad (2.16)$$

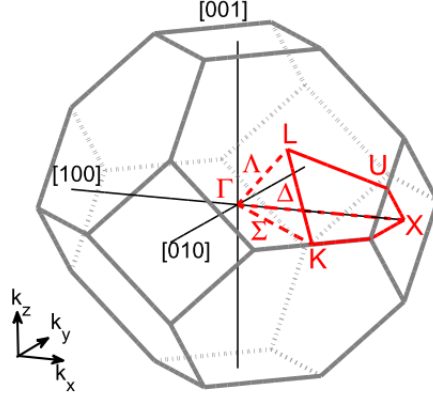


Figure 2.3: First Brillouin Zone of face-centered cubic lattice. Reproduced from [26].

where the sum is over the atoms in equivalent positions in the N unit cells of the crystal. Here, χ_α is an atomic orbital of an atom of the unit cell. Typically, for a zinc-blende structure composed of two different atoms in the unit cell, if we choose a sp^3 basis set, the number of χ_α orbitals to consider is eight. Then the eigenstates of the Schrödinger equation in a periodic potential can be written as:

$$\Psi_{\mathbf{k}}(\mathbf{r}) = \sum_{\alpha} c_{\alpha}(\mathbf{k})\chi_{\alpha\mathbf{k}}(\mathbf{r}) \quad (2.17)$$

Therefore, the size of the basis set is reduced to the number of orbitals multiplied by the number of atoms in the unit cell. As before, we can use the Ritz theorem to derive the determinant of eq. 2.7 and the matrix elements of the form:

$$E_{II'\alpha\alpha'} = e^{i\mathbf{k}(\mathbf{R}_I - \mathbf{R}_{I'})} \int \chi_{\alpha}(\mathbf{r} - \mathbf{R}_I) \hat{H} \chi_{\alpha'}(\mathbf{r} - \mathbf{R}_{I'}) d\tau \quad (2.18)$$

We can appreciate that the above equation differs from eq. 2.14 by a plane wave of wavevector \mathbf{k} . Therefore, the diagonalization has to be performed at different \mathbf{k} values spanned in the Brillouin zone and, for each \mathbf{k} , there will be a number of eigenvalues of the size of the basis set. Then the function of \mathbf{k} having the lowest energy will form the first energy band and so on to build up the well-known band structure.

ETBM for confined structures [27, 161] The lack of translational symmetry going from bulk to NCs deeply modifies the optoelectronic properties. The delocalized electronic states of bulk material are constrained physically by the boundaries where the wave function needs to be canceled. In NCs, the confinement affects the three space directions and thus are named 0D materials. This confinement folds the bulk 3D BZ into the center leading to a discretization of the dispersion energy as represented in Figure 2.4.

The ETBM parameters are transferred without change from the bulk to confined structures with appropriate boundary conditions. In the framework of ETBM calculations, the confinement is taken into account explicitly, by constructing the NC and thus the boundaries in real space. The NCs are constructed by a starting atom at the center and neighbors atoms are added within a region of space defined by the

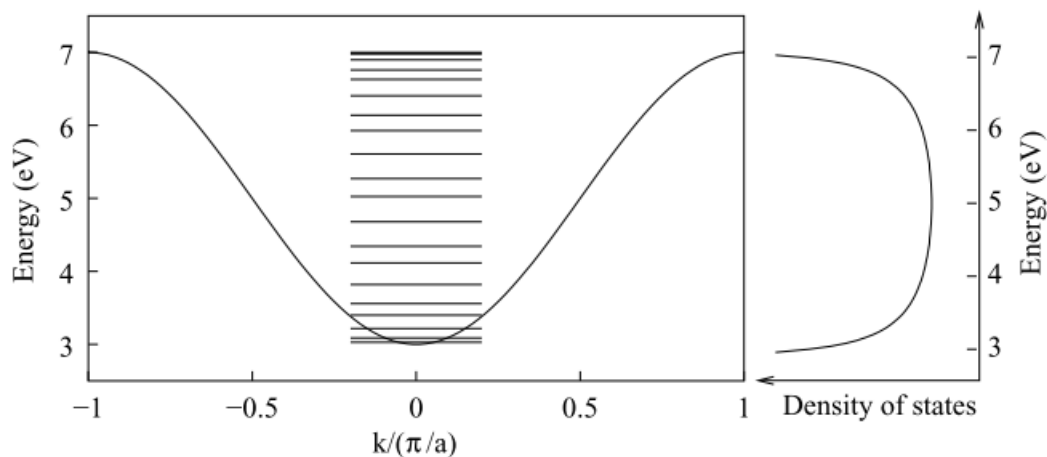


Figure 2.4: Electronic structure of a linear chain of s orbitals and its discretization by confinement for a finite chain of 20 atoms (left side). Density of states for the infinite chain (right side). Reproduced from [27].

distance from the center. As discussed in Chapter 1, the surface atoms are under-coordinated may lead to trap states in the bandgap. Therefore, pseudo-hydrogen atoms are usually employed to passivate the dangling bonds and clean the bandgap of surface states [163, 164, 165].

2.3 Lead sulfide

2.3.1 Bulk: a peculiar semiconductor

The lead chalcogenides semiconductors PbX ($X=\text{S}$, Se , and Te) crystallizing in a rock-salt structure (see Chapter 1) belong to the IV-VI family. Richard Dalven published in 1974 [166] an exhaustive review of the bulk electronic structure of lead chalcogenides PbX ($X=\text{S}$, Se , and Te). He presented the last theoretical and experimental results (at the time), but above all, he highlighted the next challenges to tackle. Indeed, he unveiled the peculiar properties of this IV-VI family compared to III-V and II-VI counterparts, which were at the time not understood:

- a direct bandgap of energy E_g at L point.
- a bandgap order that does not follow the usual decrease with increasing anion atomic number.
- a positive dE_g/dT slope.

Twenty years later, Wei and Zunger [167] proposed a common origin of these anomalies in the peculiar location of the Pb 6s band. Indeed, the latter lies in the valence band (VB) while the cation s band of II-VI and III-V semiconductors is usually located in the conduction band (CB). Due to symmetry, the presence of an occupied-cation s band leads to repulsion between the valence states and therefore deeply modifies the band structure.

Band structure The band structures presented in Figure 2.5 have been computed by ETBM, EPM, and DFT with the Heyd-Scuseria-Ernzerhof hybrid functional (HSE) [151]. The latter has proven successful in describing the electronic properties of the lead chalcogenides [168]. The ETBM parameters (can be found in [29]) were adjusted by Guy Allan and Christophe Delerue on reference band structures. The Hamiltonian matrix is written in a $sp3d5s^*$ basis (s^* is a second s orbital [169]), the overlaps are neglected, and a first nearest-neighbor approximation is considered. Because Pb is a heavy element with 82 electrons in the configuration $[Xe]4f^{14}5d^{10}6s^26p^2$, one must include the spin-orbit coupling. Other parameters exist that give a slightly better description at high energies but have been fitted on low temperature experiments (4K) [170]. The EPM parameters are taken from [41] (fitted on experiments at 5K) and also include the spin-orbit coupling. It is worth to notice that the EPM parameters date from 1973, and give pretty good results. We discretized the k values on a mesh following high-symmetry directions (see Figure 2.3).

The band structures obtained from the different theories are in good agreement and give bandgap energy of 0.41 eV (300K) for DFT and ETBM; and 0.28 eV (4K) for EPM. These values are in good agreement with the experimental bandgaps at 300K and 4K, given respectively at 0.41 and 0.287 eV [166]. The PbX family presents a direct bandgap between the valence band maximum (VBM) and the conduction band minimum (CBM) located both at the eight equivalent L points of the first BZ. The eight surfaces of constant energy have the shape of an hemi-ellipsoid but correspond in fact to four ellipsoids [171]. These four isoenergy-surfaces so called

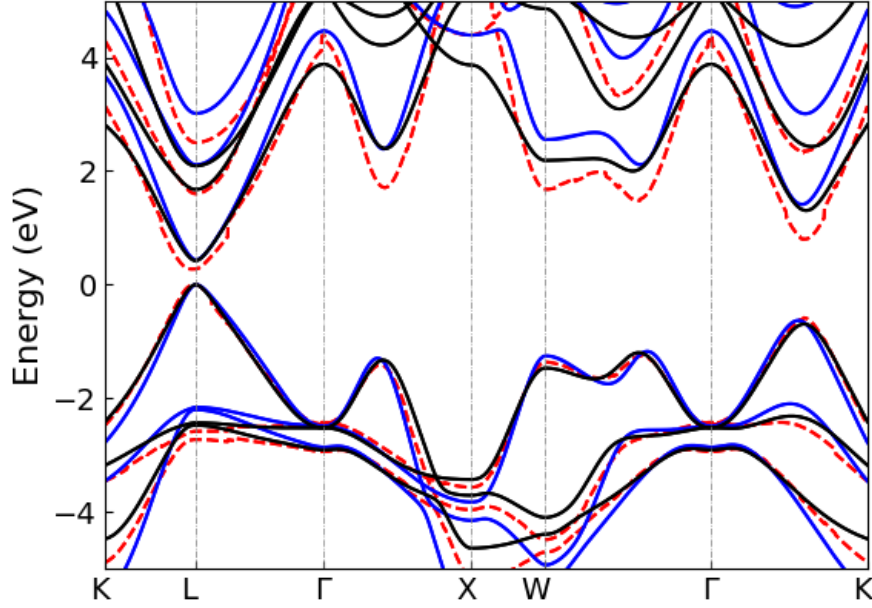


Figure 2.5: Electron energy dispersion of bulk PbS calculated by ETBM (black solid line), DFT-HSE (blue solid line), and EPM at 0K (dashed red line).

”valleys” are a good approximation of the Fermi surface at low carrier concentration, and can be written in the effective mass approximation framework as [166]:

$$E = \frac{\hbar^2}{2} \left(\frac{k_1^2}{m_l} + \frac{k_2^2 + k_3^2}{m_t} \right) \quad (2.19)$$

with k_1 the component of the wave vector in a [111] direction, k_2 , and k_3 , being mutually orthogonal and in a plane perpendicular to k_1 . m_l and m_t correspond to the longitudinal and transverse effective masses, respectively. It is important to point out that eq. 2.19 is only valid very close to the band edges, the band dispersion becoming rapidly linear away from extrema.

In 2004, Guy Allan and Christophe Delerue [28] showed by ETBM calculations that the PbSe electronic states are mainly p -like near the bandgap. Using an ab initio approach, the so-called quasiparticle self-consistent GW method, the p -like band structure of PbSe was confirmed by Svane et al. [172]. They also revealed that the p bands around the bandgap while hybridized are predominantly anionic below and cationic above the Fermi level. Following the work of Guy Allan et al. [28], we plotted in Figure 2.6 (red dashed line) the band structure of PbS with all the tight-binding parameters set to zero, except the spin-orbit coupling and the hopping integral $E_{pp\sigma}$. In line with their results, the band structure composed mainly of p orbitals reproduces remarkably the true one (see Figure 2.6). These results, which confirm those obtained for PbSe [28] have important implications for NCs as we will see in the following paragraph.

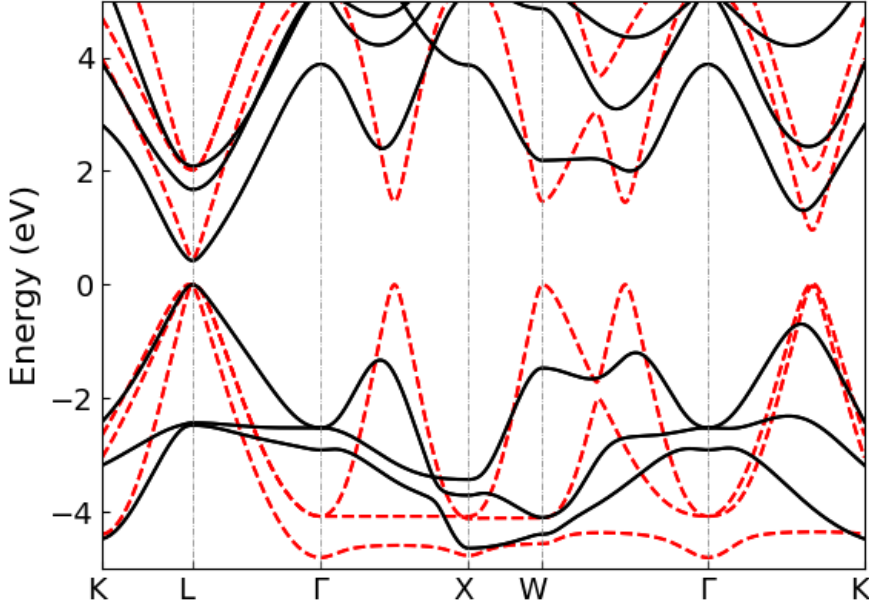


Figure 2.6: ETBM band structure of bulk PbS (black line) compared to the one calculated with $E_{pp\sigma} = 2.5 \text{ eV}$, $E_{pc} - E_{pa} = 1.5 \text{ eV}$ and the spin-orbit coupling keeping its bulk value, all other interatomic terms being switched to zero (red dashed line). Parameters taken from [28].

2.3.2 Nanocrystal: size and shape

The quantum confinement lifts the fourfold degenerate (eightfold with spin) VBM and CBM by the effect of intervalley coupling and the anisotropy of the effective masses [28, 173, 31, 174, 170]. The lift of the degeneracy also depends on the NC size, surface, and geometry [170]. The p-like character of the bulk band structure discussed in the preceding section persists in NCs. This can be seen in Figure 2.7 in which we present the calculated weights on the cations and p orbitals of the HOMO and LUMO wavefunctions. Independently of the NC size, the HOMO state is mainly composed of the anionic p orbitals while the LUMO state is composed of the cationic p orbitals. It is also a good representation of the strong ionicity of PbS. Allan and Delerue [28] showed that this peculiar electronic structure, in addition to the cubic rocksalt lattice, allows the surface atoms to remain coupled with the ones at the interior. As a consequence, no surface state emerge in the bandgap of unpassivated PbS NCs, which has been confirmed in different ETBM studies [170, 175] and ab initio calculations [143]. Therefore the PbS NCs studied theoretically in this manuscript will not be passivated or the passivation will be explicitly mentioned.

Size and confinement Figure 2.8a gives the evolution of the energy gap with the diameter. Owing to the small effective mass of the charge carriers at VBM and CBM ($m_e \approx m_h \approx 0.1$ [176]), and therefore the large bulk exciton Bohr radius of 18 nm, the PbS energy is tunable from 0.6 eV ($\sim 2000 \text{ nm}$) to 1.6 eV ($\sim 700 \text{ nm}$). The

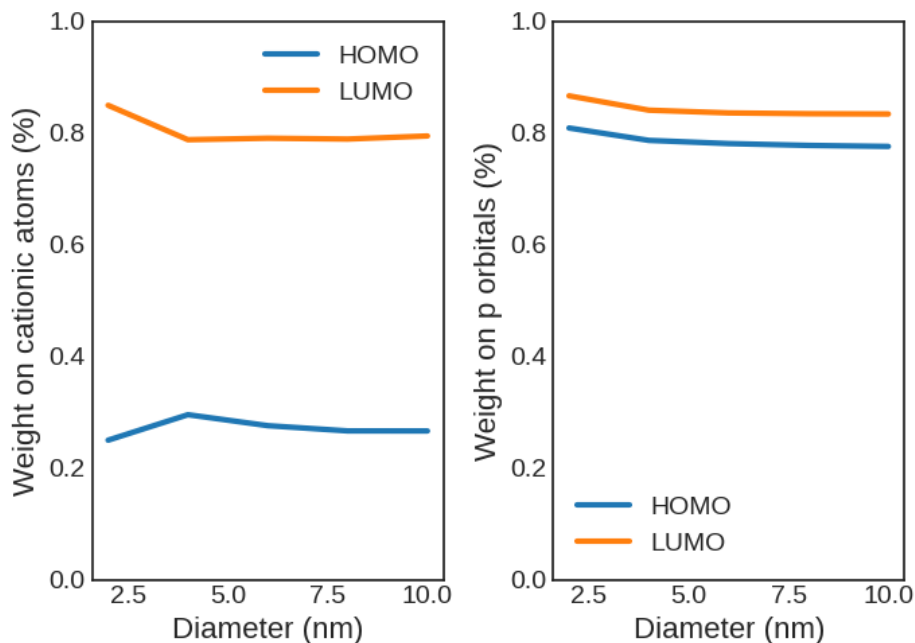


Figure 2.7: Calculated weights on the cations (left panel) and p orbitals (right panel) of HOMO (blue) and LUMO (orange) states.

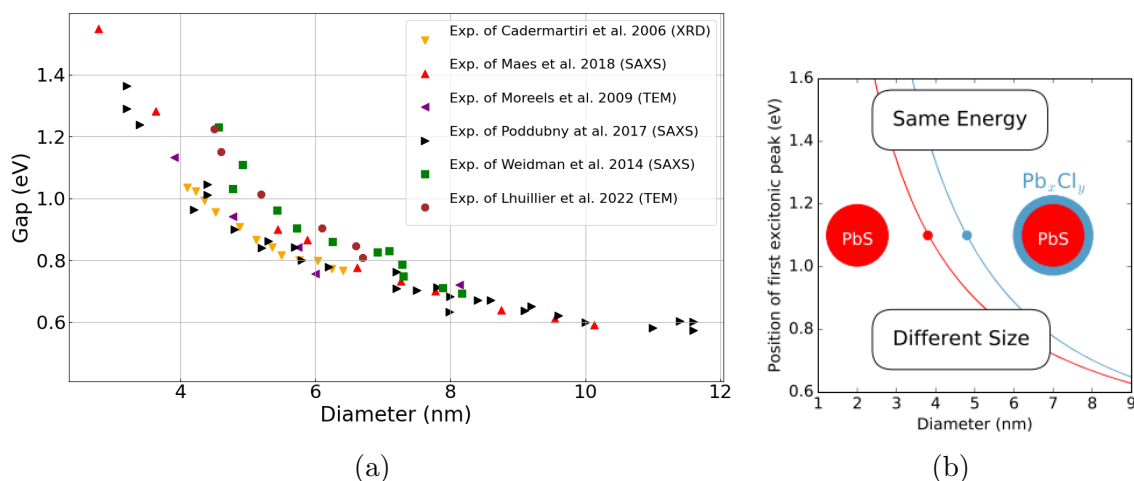


Figure 2.8: Sizing curve. (a) Evolution of the bandgap energy evolution with the diameter of colloidal PbS NCs, showing our own experimental data (exp. of Lhuillier [29]), as well as experimental data from previous works (Cademartiri et al. [10], Maes et al. [30], Moreels et al. [21], Poddubny et al. [31], and Weidman et al. [32]). (b) Schematic representation of the PbCl shell over the sizing curve. Reproduced from [33].

important discrepancy among the experimental data could potentially be explained by the formation of a lead chloride shell [177, 117, 33]. This shell results from the use of lead chloride precursors (PbCl_2) with important stoichiometric excesses (24:1) relative to the elemental sulfur precursors [32]. As represented in Figure 2.8b, it implies that the measured diameter is larger compared to synthesis using PbOA precursors [31, 30] or with weaker PbCl_2 excess [21]. Therefore, we will use the Moreels sizing curve as a reference for future comparison and studies [21]. Indeed,

Green et al. [33] showed that the Moreels fit accurately describes the size-to-gap dependence of synthesis using PbOA precursors.

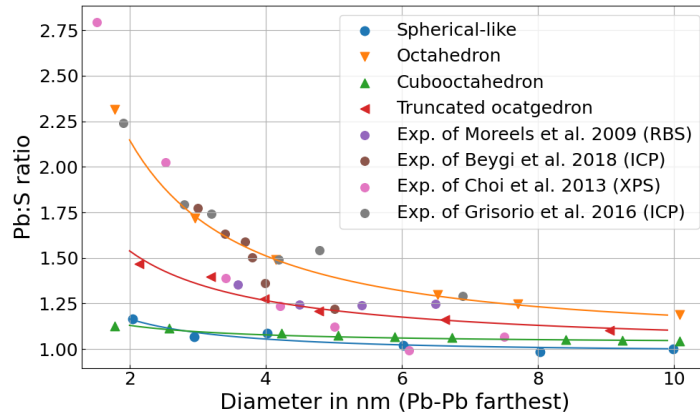
Shape and confinement PbS NCs are known to form octahedra for diameters below ~ 3 nm, truncated octahedra for diameters between ~ 3 nm and ~ 4 nm, and cubooctahedra for diameters above [17, 34] (see Chapter 1). This trend is confirmed by Figure 2.9a which delineates the Pb:S ratio evolution with the NC size (defined as the farthest Pb-Pb distance). Indeed, we can see that the modeled NCs (solid line) follow the experimental results in their corresponding range of size; e.g. for NCs size < 3 nm the Pb:S ratio of the constructed Pb-rich octahedron (orange line) is in good accordance with the experimental results [35, 17, 34]. However, using the same theoretical NCs with ETBM calculation, the bandgap energy evolution with the size (see Figure 2.9b) shows that the octahedral NCs separate from the Moreels experimental curve for a size smaller than 3 nm (~ 2 nm). This can be explained by an artefact of the TEM images that give a 2D representation of 3D NCs. Thus, the average size given by TEM measurements would be framed by the inscribed sphere of an octahedron as the bottom limit and the farthest Pb-Pb distance as the top limit. This result is shown in Figure 2.9c. Moreover, we can see that a spherical-like structure would be a good estimation of the overall geometry of an NCs assembly over the confinement. Indeed, this geometry presents a similar confinement evolution with the cubooctahedron, the truncated octahedron, and is in-between the two limited cases of the octahedron NCs (see Figure 2.9b and 2.9c).

Although the ETBM bandgap corresponds to the difference between the LUMO and HOMO energy states, the comparison of the single particle gap energy (ETBM) with optical measurements is in good accordance. This is in part due to the high dielectric constant of PbS ($\epsilon_0 = 169$ and $\epsilon_\infty = 17$) which induces a strong screening of carrier-carrier interactions.

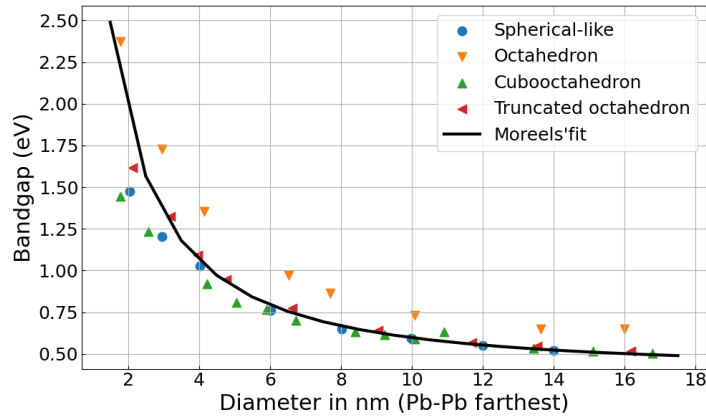
2.4 Mercury telluride

HgTe belongs to the II-VI family and crystallizes in a zinc-blende structure. An exhaustive review can be found in [69]. In standard II-VI semiconductors such as CdTe, the VBM presents a Γ_8 symmetry mainly composed of the anionic p orbitals, while the CBM is Γ_6 composed of s cationic orbitals. Groves et al. showed in 1967 [178] that bulk HgTe presents an inverted band ordering compared to standard II-VI semiconductors. Indeed, as represented in Figure 2.10, the HgTe band structure exhibits the bands with Γ_8 symmetry above the Γ_6 bands. In addition, ETBM [36] and ab initio [179] calculations show a strong band mixing in HgTe with the Γ_6 band (Γ_8 resp.) having a pure s (p resp.) character that drops to zero (acquires s character resp.) when k moves away from Γ . In line with lead chalcogenides, the presence of a cationic s-type band in the VB could explain the unusual positive dE_g/dT slope. The band structures given in Figure 2.10 have been calculated by ETBM. Concerning HgTe, we took the ETBM parameters from [36] where the authors showed a good agreement with a k·p band structure [180], and with a quasiparticle self-consistent GW approximation calculation [181].

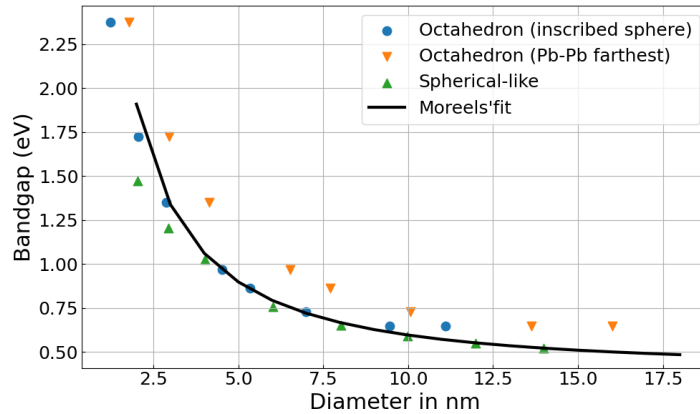
In the literature, the inverted band ordering of HgTe is expressed by considering a negative bandgap value between Γ_6 and Γ_8 bands. This gap energy is sensitive to



(a)



(b)



(c)

Figure 2.9: (a) Pb:S ratio of spherical-like, octahedral, cubooctahedral, and truncated octahedral PbS NC models as a function of diameter, compared with experimental data from previous works ([17], [34], [35], and [21]). (b) Bandgap evolution with the NC size calculated by ETBM using the NC models compared to the Moreels fit over experimental data [21]. (c) Same as (b) considering the two limiting size cases for the octahedron, i.e. the diameter of its inscribed sphere (blue dot) and the largest size (down orange triangle).

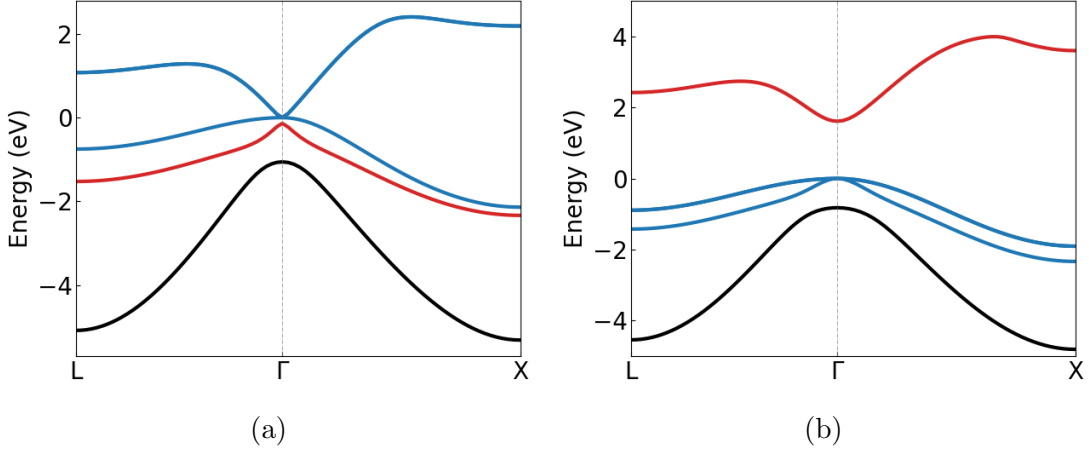


Figure 2.10: Electron energy dispersion calculated by ETBM of (a) bulk HgTe with the parameters taken from [36] and (b) bulk CdTe with the parameters taken from [37]. The bands of Γ_6 , Γ_7 , and Γ_8 symmetry are respectively represented by a red, black, and blue solid line.

the temperature with experimental values of -0.30 and -0.12 eV at 0 and 300K, respectively [182]. The ETBM bandgap energy is given at -0.14 eV for a fit at 300K, in good agreement with the experimental data. But in fact, HgTe exhibits a semimetal behavior with zero bandgap energy. Indeed, the Γ_8 is fourfold degenerate with two positive dispersion bands forming the CB while the two remaining form the VB [179]. The strong dispersion of the Γ_8 CB (features of a weak electron effective mass $\sim 0.01m_0$ [180, 183]) leads to important carrier mobility. As a consequence, even though bulk HgTe exhibits a zero bandgap energy, the gap (induced by confinement) can be tuned over a broad spectral range (see Figure 2.11).

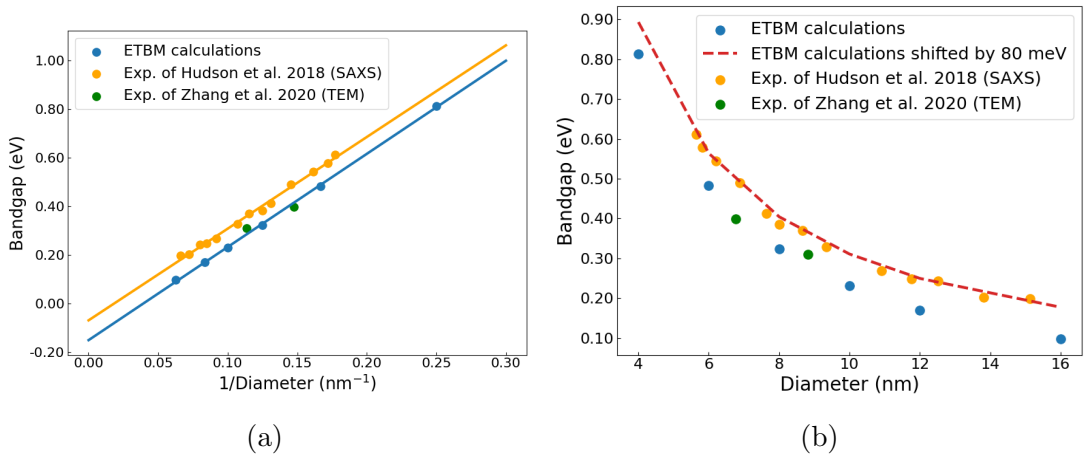


Figure 2.11: (a) Evolution of the bandgap with the inverse of NC diameter calculated by ETBM with spherical-like NC model compared to experimental data (Hudson et al. [38] and Zhang et al. [39]). (b) Same as (a) versus the NC diameter.

Confined structures The bulk parameters are transferred without change to the confined structures. Contrary to lead chalcogenide NCs, pseudo-hydrogen atoms are used to passivate HgTe surfaces [36, 165, 184]. The impact of the excitonic effect is

weak in HgTe NCs [36] due to its large Bohr radius ($\sim 40nm$ [185]). Figure 2.11 shows that the calculated ETBM bandgap energy for spherical-like HgTe NCs varies linearly with $1/d$ (d being the NC diameter):

$$E_g = -0.15 + \frac{3.83}{d} \quad (2.20)$$

This can be explained using the particle in a sphere picture. In this model, the k value is related to the sphere diameter as $2\pi/d$ [186], and the linear dispersion energy ($E \propto k$) for the CB around Γ (see [180, 183] and Figure 2.10a) leads to the observed energy dependence of eq. 2.20. In addition, the ETBM calculations are in good accordance with experimental measurements (of Zhang et al. [39]), but a rigid shift difference is present with the data of Hudson et al. [38]. This shift does not seem to originate from a size effect as observed for PbS but an effect of confinement. Indeed, a size effect would decrease as $1/d$, but a rigid shift of 80 meV for all NCs gives almost perfect accordance with Hudson data (see Figure 2.11b). Moreover, both experimental data come from optical measurements on rather spherical NCs, thus a shape effect seems to be excluded. A passivation effect could explain this discrepancy, e.g. with the presence of more electron-donor ligands at the surfaces of Hudson's NCs which would increase the confinement effect.

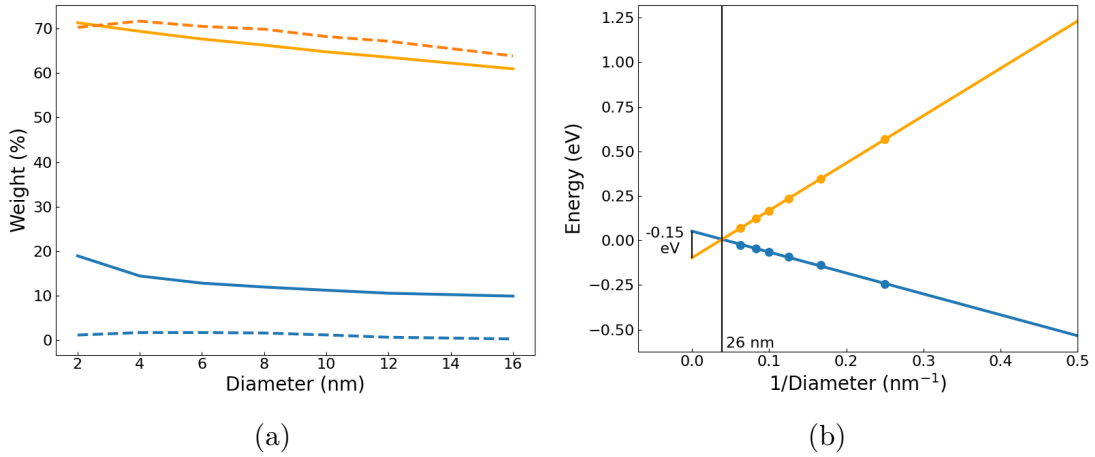


Figure 2.12: (a) Calculated weights on the cations (solid line) and s orbitals (dashed line) of HOMO (blue) and LUMO (orange) states. (b) Energy of the HOMO (blue) and LUMO states (orange) with the inverse diameter of spherical-like NCs. Published in [40].

It has been shown in HgTe/(Hg,Cd)Te quantum wells that the 1D confinement can restore a normal band ordering (CdTe-like) [187, 188]. It is shown that for a thick HgTe layer, the quantum well is in the inverted regime with the Γ_8 bands above the Γ_6 ones, but for a thinner layer, a normal band order appears. The gap-closing transition occurs for thickness d_c ($\sim 6.3 nm$), and this transition is a topological phase transition between a conventional insulating phase ($< d_c$) and a phase presenting the quantum spin hall effect ($> d_c$) [187, 188]. We unveil a similar topological phase transition in HgTe NCs with a 3D confinement. We show in Figure 2.12a that the LUMO (resp. HOMO) state recovers a CdTe-like band ordering with mainly cationic s (resp. anionic p) orbitals. In line with the work of Bernevig et al. [187], we assume that it exists an NC size d_0 at which a topological

phase transition occurs. Drawing in Figure 2.12b, the evolution of the LUMO and HOMO eigenvalues with the inverse of the diameter, we extrapolate this crossing point for a size of 26 nm. In good compliance with the ETBM bandgap (-0.14 eV), an extrapolation for diameters tending to infinity (bulk regime) gives a negative gap of -0.15 eV. As we will see in the next Chapter, this topological phase transition [189] has a fundamental impact on the optical properties.

2.5 Conclusion

Through different examples, we emphasized that the electronic structure is at the core of fundamental physical properties. We showed that the bulk PbS electronic structure is mainly p-like around the bandgap. This behavior is also observed in NCs and allows the great stability of PbS against trap states in the bandgap. We also unveiled the effect of size and shape on the electronic structure and particularly the effect over the bandgap energy. We also studied the bulk and NC electronic structure of HgTe. It is a semi-metal in bulk, and a bandgap opens in NCs under the effect of quantum confinement. HgTe is known to exhibit a non-trivial topological phase under moderate confinement in quantum wells. In this thesis, we showed this effect for NCs. Indeed, when going from a semi-metal in the bulk form to a standard semiconductor under NC form, HgTe undergoes a transition of topological nature that we predict for a NC diameter of about 26 nm. Future works should be undertaken to study this quantum phase transition in detail.

Chapter 3

Bulk to nanocrystals: optical and dielectric properties

3.1 Introduction

The interaction between light and matter is a crucial phenomenon in electromagnetic devices, with significant implications for areas like material science, electronics, and photonics. To accurately describe this interaction, the complex dielectric function $\tilde{\epsilon}$ plays a key role. Therefore, understanding and measuring this function is essential. This Chapter establishes the primary equations related to $\tilde{\epsilon}$. In the first part of section 3.2, we discuss how classical approaches can derive it and its relationship with other optical properties, such as the complex refractive index. However, due to the dependency of the macroscopic dielectric function on the microscopic and quantum nature of the electronic structure, classical approaches are insufficient. Therefore, we present in the second part of section 3.2 the derivation of $\tilde{\epsilon}$ using quantum formalism, specifically the density matrix formalism [27], and apply it in the framework of ETBM to calculate $\tilde{\epsilon}$ of bulk and NC structures.

We use this formalism to relate electronic structure to optical calculations and understand the essential features of an experimental absorption spectrum. For example, in section 3.3 we compare experimental measurements of $\tilde{\epsilon}$ to ETBM calculations for bulk PbS and PbS NCs, highlighting sources of errors from both sides but demonstrating good quantitative agreement. Furthermore, in section 3.4 we apply this formalism to HgTe to reveal the modification of $\tilde{\epsilon}$ due to the quantum effects in NCs. Finally, an analytical equation for the absorption coefficient is derived, which provides quick access to the absorption spectrum in the low-energy range.

3.2 Optical indices

We consider the light propagating in the material to be uniform since its wavelength contains many interatomic distances [160]. A uniform electric field applied to a dielectric media will induce charge displacement leading to a total dipolar momentum \mathbf{p} . Thus we can define the polarisation \mathbf{P} as the dipole moment \mathbf{p} per unit volume, averaged over the volume of a cell Ω . At the microscopic scale, we can define the polarisability α of an atom in terms of the local electric field at the atom [190]:

$$\mathbf{p} = \alpha \mathbf{E}_{local} \quad (3.1)$$

Thus, for a crystal, the polarisation can be approximated as the sum of the dipole moments of the atoms [190]:

$$\mathbf{P} = \sum_i N_i \mathbf{p}_i = \sum_i N_i \alpha_i \mathbf{E}_{local}(i) \quad (3.2)$$

where N_i is the concentration and \mathbf{p}_i the dipole moment of the atoms i .

At the macroscopic scale, in the case of a small enough macroscopic electric field \mathbf{E} inside the dielectric, the polarisation is linear with \mathbf{E} :

$$\mathbf{P} = \epsilon_0 \chi \mathbf{E} \quad (3.3)$$

with the proportionality constant named the electric susceptibility χ . The latter depends on the intrinsic characteristic of the material but also the external conditions such as temperature.

Classical theory [191] In a first approach, the electric susceptibility can be obtained via the second Newton's law. Indeed, the electrons of a dielectric are tightly bound to the nuclei, and the binding interaction around the equilibrium can be approximated by a harmonic potential $((1/2)k_0x^2)$. Therefore, the force binding the electrons to the core nuclei writes:

$$F_{binding} = -k_0x = -m\omega_0^2x \quad (3.4)$$

with x the electron displacement from the equilibrium, m the electron's mass, and ω_0 the natural oscillation frequency. A uniform electric field inside the media, of the form $E = E_0 \cos(\omega t)$ with ω the frequency of the light, applies on the electron of charge q a force:

$$F_E = qE_0 \cos(\omega t) \quad (3.5)$$

For now, we can assume a damping force on the electron:

$$F_{damping} = -m\gamma \frac{dx}{dt} \quad (3.6)$$

whose the origin will become clear latter. Gathering all the terms in the Newton's second law allows us to write:

$$\frac{d^2x}{dt^2} + \gamma \frac{dx}{dt} + \omega_0^2x = \frac{q}{m} E_0 \cos(\omega t) \quad (3.7)$$

which can be re-written for simplified calculations as the real part of a complex equation:

$$\frac{d^2\tilde{x}}{dt^2} + \gamma \frac{d\tilde{x}}{dt} + \omega_0^2\tilde{x} = \frac{q}{m} E_0 e^{-i\omega t} \quad (3.8)$$

In the steady state, the solution writes:

$$\tilde{x}(t) = \tilde{x}_0 e^{-i\omega t} \quad (3.9)$$

with the complex amplitude being:

$$\tilde{x}_0 = \frac{q}{\omega_0^2 - \omega^2 - i\gamma\omega} \frac{E_0}{m} \quad (3.10)$$

Thus, the dipole moment corresponds to the real part of the following equation:

$$\tilde{p}(t) = q\tilde{x}(t) = \frac{1}{m} \frac{q^2}{\omega_0^2 - \omega^2 - i\gamma\omega} E_0 e^{-i\omega t} \quad (3.11)$$

Then inserting eq. 3.11 in eq. 3.2, and assuming the local electric field equal to the macroscopic electric field gives:

$$\tilde{\mathbf{P}} = \frac{q^2}{m} \sum_i \frac{N_i}{\omega_i^2 - \omega^2 - i\gamma_i\omega} \tilde{\mathbf{E}} \quad (3.12)$$

with the complex electric susceptibility being the proportionality constant between the macroscopic electric field and the polarisation. Moreover, from the Maxwell's equation of a dielectric media the wave equation writes:

$$\nabla^2 \tilde{\mathbf{E}} = \tilde{\epsilon}\epsilon_0\mu_0 \frac{\partial^2 \tilde{\mathbf{E}}}{\partial t^2} \quad (3.13)$$

with $\tilde{\epsilon} = 1 + \tilde{\chi}$ being the complex permittivity. The solution of the eq. 3.13 is the plane wave $\tilde{\mathbf{E}}_0 e^{i(\tilde{k}x - \omega t)}$ where the complex wave number \tilde{k} is related to $\tilde{\epsilon}$ by:

$$\tilde{k} = \frac{\omega}{c} \sqrt{\tilde{\epsilon}} \quad (3.14)$$

The complex index of refraction $\tilde{n} = n + ik$, the complex dielectric function $\tilde{\epsilon} = \epsilon' + i\epsilon''$, the reflectivity R , and the absorption coefficient α are the most common optical indices, and are related to each other by:

$$\begin{aligned} \epsilon' &= n^2 - k^2 \\ \epsilon'' &= 2nk \\ R &= \frac{(n-1)^2 + k^2}{(n+1)^2 + k^2} \\ \alpha &= \frac{4\pi k}{\lambda} \end{aligned} \quad (3.15)$$

with n the refractive index, k the extinction coefficient, and λ the wavelength. Thus, the propagating wave becomes [27]:

$$\tilde{\mathbf{E}}_0 = \tilde{\mathbf{E}}_0 e^{-\frac{\omega}{c} kx} e^{i(\frac{n\omega}{c}x - \omega t)} \quad (3.16)$$

We can now acknowledge that the propagating wave is damped (see eq. 3.6) by an absorption phenomena measured via the extinction coefficient term k , and refracted through the term n .

Although, this demonstration in the classical framework gives a crude approximation of the electric susceptibility, it allows us to define the key optical parameters (\tilde{n} and $\tilde{\epsilon}$), their relation (see eq. 3.15), and provide a taste of the underlying physics.

Density matrix formulation [27, 192] The density matrix ρ is an alternate form (compared to the wavefunction) to represent a quantum state, and is particularly useful for describing statistical ensemble. Moreover, it allows us to obtain the expectation value of an observable \mathbf{O} by the trace of the matrix $\rho\mathbf{O}$:

$$\langle \mathbf{O} \rangle = Tr(\rho\mathbf{O}) \quad (3.17)$$

From the quantum point of view, the polarisation eq. 3.2 is due to the transitions of electrons between different energy levels which are induced by the interaction with the propagating wave. In the case of a two states system, $|g\rangle$ the ground state of energy ϵ_g , and $|e\rangle$ the excited state of energy ϵ_e , the polarisation is given by the statistical average of the operator $-\mathbf{qr}$:

$$\langle \mathbf{P} \rangle = (1/\Omega) \text{Tr}[\rho(-\mathbf{qr})] \quad (3.18)$$

To obtain the matrix elements of ρ , we can use the Liouville-Von Neumann equation:

$$\frac{\partial \rho}{\partial t} = \frac{-i}{\hbar} [H, \rho] \quad (3.19)$$

with the Hamiltonian for the electron-light system written as:

$$H = \epsilon_g |g\rangle \langle g| + \epsilon_e |e\rangle \langle e| + \mathbf{qr} \cdot \mathbf{E} \quad (3.20)$$

The last term corresponds to the perturbation by the electric field under the dipolar form, with \mathbf{r} being the electron position. This leads to the polarisation:

$$\langle \mathbf{P} \rangle = -\frac{q^2 |\langle g | \mathbf{r} \cdot \mathbf{e} | e \rangle|^2 [f_g - f_e]}{\Omega} \left\{ \frac{1}{\hbar\omega - (\epsilon_e - \epsilon_g) + i\sigma} - \frac{1}{\hbar\omega + (\epsilon_e - \epsilon_g) + i\sigma} \right\} \mathbf{E} \quad (3.21)$$

with the equilibrium population given by f_e and f_g , σ is a parameter accounting the experimental broadening, and \mathbf{e} corresponds to the polarization vector of light. From eq. 3.21, we can finally write the complex dielectric function $\tilde{\epsilon} = 1 + \mathbf{P}/(\epsilon_0 \mathbf{E})$ for a NC in which the transitions occur between the valence u_v and the conduction bands u_c :

$$\tilde{\epsilon}(\omega) = 1 - \sum_{v,c} \frac{q^2 |\langle u_v | \mathbf{r} \cdot \mathbf{e} | u_c \rangle|^2 [f_v - f_c]}{\Omega \epsilon_0} \left\{ \frac{1}{\hbar\omega - (\epsilon_c - \epsilon_v) + i\sigma} - \frac{1}{\hbar\omega + (\epsilon_c - \epsilon_v) + i\sigma} \right\} \quad (3.22)$$

which can be re-written according to the dimensionless oscillator strength [27]:

$$f_{ij} = \frac{2m_0}{\hbar^2} (\epsilon_i - \epsilon_j) |\langle i | \mathbf{r} \cdot \mathbf{e} | j \rangle|^2 \quad (3.23)$$

as:

$$\tilde{\epsilon}(\omega) = 1 - \frac{\hbar^2 q^2}{2m_0 \Omega \epsilon_0} \sum_{v,c} \frac{f_{vc} [f_v - f_c]}{\epsilon_c - \epsilon_v} \left\{ \frac{1}{\hbar\omega - (\epsilon_c - \epsilon_v) + i\sigma} - \frac{1}{\hbar\omega + (\epsilon_c - \epsilon_v) + i\sigma} \right\} \quad (3.24)$$

The imaginary part of eq. 3.22 can be concisely written under the form of the Fermi's golden rule [160]:

$$\epsilon''(\omega) = \frac{\pi q^2}{\epsilon_0 \Omega} \sum_{v,c} |\langle u_v | \mathbf{r} \cdot \mathbf{e} | u_c \rangle|^2 \delta(\epsilon_c - \epsilon_v - \hbar\omega) \quad (3.25)$$

with the energy conserving delta function δ (obtained in the limit $\sigma \rightarrow 0^+$). On the other hand, the real part of the complex dielectric function can be obtained from the Kramers-Kronig relation:

$$\epsilon'(w) = 1 + \frac{2}{\pi} P \int_0^\infty \frac{\omega' \epsilon''(\omega')}{\omega'^2 - \omega^2} d\omega' \quad (3.26)$$

where the integral requires the knowledge of $\epsilon''(\omega')$ over a range of frequencies ω' as wide as possible. A more practical form of $\epsilon'(\omega)$ is the frequency-independent optical dielectric constant ϵ_∞ (where ∞ simply means that ω is large compared to phonon frequency) which can be evaluated from [160]:

$$\epsilon_\infty = 1 + \frac{2q^2}{\epsilon_0\Omega} \sum_{ij} \frac{|\langle i|\mathbf{r}\cdot\mathbf{e}|j\rangle|^2}{\epsilon_j - \epsilon_i} \quad (3.27)$$

ϵ_∞ is often referred as the optical dielectric constant, and is a fundamental quantity for describing dielectric materials.

Although the optical matrix of \mathbf{r} is well suited for transitions between localized states such as in NCs, it is not suited for transitions between delocalized states such as in bulk materials. Hence, the matrix of \mathbf{p} is preferred and the imaginary part for a bulk material can be written as [41]:

$$\epsilon''(\omega) = \frac{\hbar^2 q^2}{3\pi m^2 \omega^2} \int |\langle u_{\mathbf{k},v}|\mathbf{p}\cdot\mathbf{e}|u_{\mathbf{k},c}\rangle|^2 \delta(\epsilon_c(\mathbf{k}) - \epsilon_v(\mathbf{k}) - \hbar\omega) d\mathbf{k} \quad (3.28)$$

where $u_{\mathbf{k},v}$ and $u_{\mathbf{k},c}$ are the periodic part of the valence and conduction-band of the Bloch wave function at \mathbf{k} and with energies $\epsilon_v(\mathbf{k})$, and $\epsilon_c(\mathbf{k})$ respectively. We can note that transitions are vertical in the BZ ($\mathbf{k}_v = \mathbf{k}_c$) fulfilling the momentum conservation law. The preceding equation is often re-written in terms of a surface integral [193]:

$$\epsilon''(\omega) = \frac{\hbar^2 q^2}{3\pi m^2 \omega^2} \int_S |\langle u_{\mathbf{k},v}|\mathbf{p}\cdot\mathbf{e}|u_{\mathbf{k},c}\rangle|^2 \frac{dS}{|\nabla_{\mathbf{k}}(\epsilon_c - \epsilon_v)|_{\epsilon_c - \epsilon_v = \hbar\omega}} \quad (3.29)$$

where the integration runs over the equal-energy-difference surface ($\epsilon_c - \epsilon_v = \hbar\omega$) in \mathbf{k} space (ϵ_c stands for $\epsilon_c(\mathbf{k})$). In the usual case where the optical matrix elements slowly vary with \mathbf{k} , this equation shows that $\epsilon''(\omega)$ peaks when $\nabla_{\mathbf{k}}(\epsilon_c - \epsilon_v) = 0$ (known as Von Hove singularities) at critical points (CPs) in the BZ that will induce characteristic features on the absorption spectrum [101]. Thus, the peaks observed in an absorption spectrum usually allow us to determine interband CPs from the energy band structure, and vice-versa.

To conclude, the absorption of an electromagnetic wave in a dielectric medium will depend on:

- the strength of the optical coupling between valence and conduction states, which can be described by the dimensionless oscillator strength (see eq. 3.24).
- the joint density of states, which is a measure of the number of allowed optical transitions.

Moreover, only knowledge of $\epsilon''(\omega)$ (or $\epsilon'(\omega)$) is needed to completely specify the optical indices (see eqs. 3.15 and 3.26). But, contrary to the evaluation of $\epsilon''(\omega)$ at a frequency ω that requires electronic states of energy difference peaked around $\hbar\omega$ (see eqs. 3.25, and 3.28), the states needed to evaluate $\epsilon'(\omega)$ at any frequency ω spread over an extensive spectral range (see eqs. 3.26 and 3.27).

Optical matrix in ETBM [194, 27] The optical matrix of \mathbf{r} is expressed in the basis of atomic orbitals $|\alpha\mathbf{R}\rangle$ with α the atomic orbital located on the atom \mathbf{R} . Thus we can write the optical matrix as:

$$\langle \beta\mathbf{R}'|\mathbf{r}|\alpha\mathbf{R}\rangle \quad (3.30)$$

If we discard the overlapping between orbitals belonging to different atoms, only remains the intra-atomic matrix element $d_{\alpha\beta}$:

$$\langle \beta\mathbf{R}'|\mathbf{r}|\alpha\mathbf{R}\rangle = (\mathbf{R}\delta_{\alpha\beta} + d_{\alpha\beta})\delta_{\mathbf{R}\mathbf{R}'} \quad (3.31)$$

Some authors [31] neglect the intra-atomic matrix element leading to a matrix with no other fitting parameters. During this thesis we calculate the intra-tomic terms from free atom orbitals [195, 196]. However, the influence of these terms is usually weak on $\tilde{\epsilon}$.

Concerning the matrix of \mathbf{p} , the following relation is used [194]:

$$\mathbf{p} = \frac{m}{\hbar}\nabla_{\mathbf{k}}H(\mathbf{k}) \quad (3.32)$$

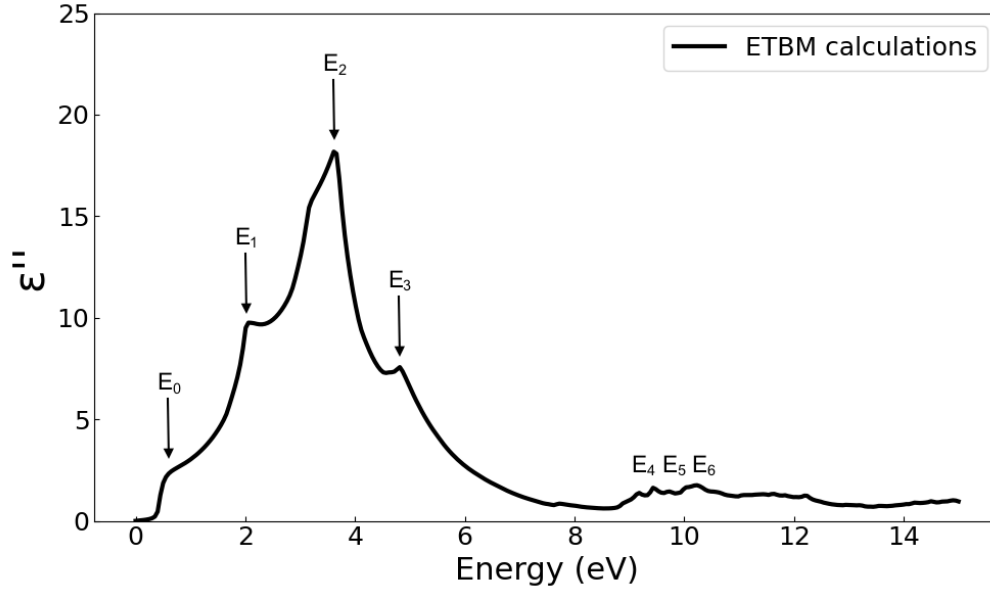
where $H(\mathbf{k})$ is the Hamiltonian in the momentum representation.

3.3 Lead sulfide

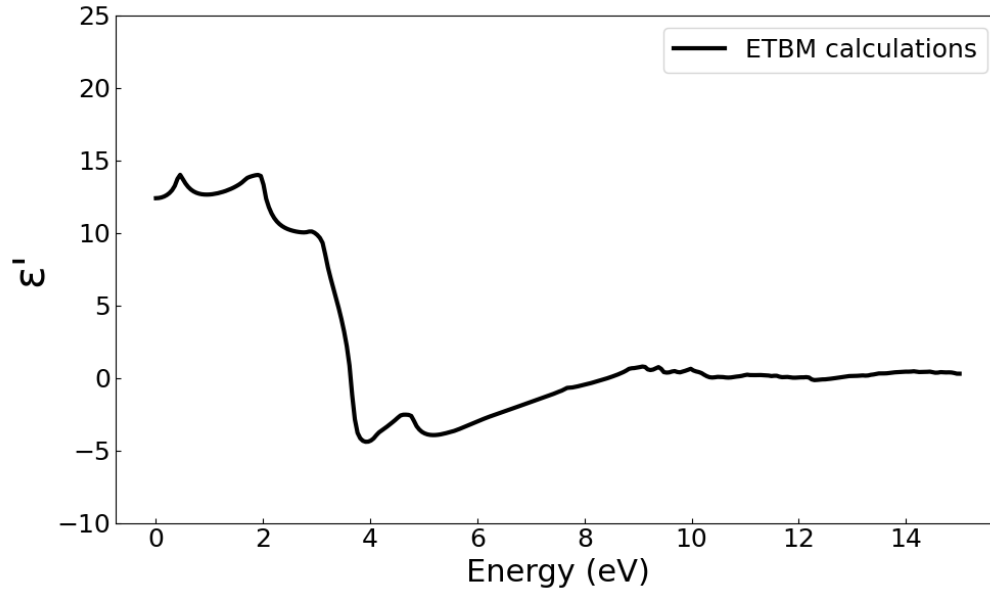
Bulk We have shown that the energy-band structure of semiconductors plays a fundamental role in determining their optical constants. Specifically, the dielectric function $\tilde{\epsilon}(\omega)$ of a semiconductor can be obtained from its band structure, as shown in equation 3.29. The BZ and band structure of bulk PbS are given in Chapter 2.

In Figure 3.1a, we have plotted $\epsilon''(\omega)$ calculated using ETBM between 0 and 15 eV, highlighting seven significant features. According to an EPM band-structure calculation [41], these peaks correspond to different CPs. For example, the E_0 peak is associated with a CP at L points of the BZ, while the E_1 transition involves two CPs at Σ and L . The E_2 peak is characterized by a mixture of CPs at Σ and Δ points, represented by the E_3 peak. Finally, transitions near Γ and X points were attributed to the E_4 , E_5 , and E_6 peaks. Figure 3.2 presents a comparison of $\epsilon(\omega)'$ and $\epsilon(\omega)''$ obtained from ETPM, EPM [41], and experimental measurements [42]. The results indicate that ETBM, and to a lesser extent EPM calculations, underestimate $\epsilon(\omega)''$ at the E1 and E2 transitions when compared to the experimental data. It is worth noting that the real part of $\epsilon(\tilde{\omega})$ is related to the imaginary part through the Kramers-Kronig relation (eq. 3.26). Thus, any error in $\epsilon''(\omega')$ impacts $\epsilon'(\omega)$, especially when ω' is close to ω , and explain the underestimation of ϵ' at low energy.

The discrepancy between the ETBM calculations and the experimental results could be attributed to several factors. While the ETBM electronic-band structure accurately describes the CPs, the higher energy bands-position, and anisotropy may not match reality. Additionally, ETBM does not describe the excitonic effects except indirectly through its parametrization, which are particularly significant for transitions involving a high joint density of states. However, an overestimation of the experimental data cannot be ruled out, as doping is common in narrow bandgap semiconductors [197]. Moreover, taking a look at the related fundamental optical indices (absorption coefficient α , the reflectivity R , the refractive index n , and the



(a)



(b)

Figure 3.1: ETBM calculations of the (a) imaginary part, and (b) real part of the complex dielectric function of bulk PbS.

extinction coefficient k) in Figure 3.3, we can acknowledge that the underestimation is not as important as we would first think. Indeed, the deviation from the experimental measurements at the transition E_2 (point with the most discrepancy) for α , R , n , and k is respectively of 10%, 11%, 20%, and 16% which is not far from the experimental accuracy ($\sim 10\%$ [42]). Besides, the spectrometric ellipsometry method used by Adachi et al. [198] is an indirect method to obtain $\epsilon(\tilde{\omega})$, thus propagation of uncertainty could lead to errors on $\epsilon(\tilde{\omega})$ which might echos on the other optical constants. As an example, we can relate the standard deviation of ϵ'' to the

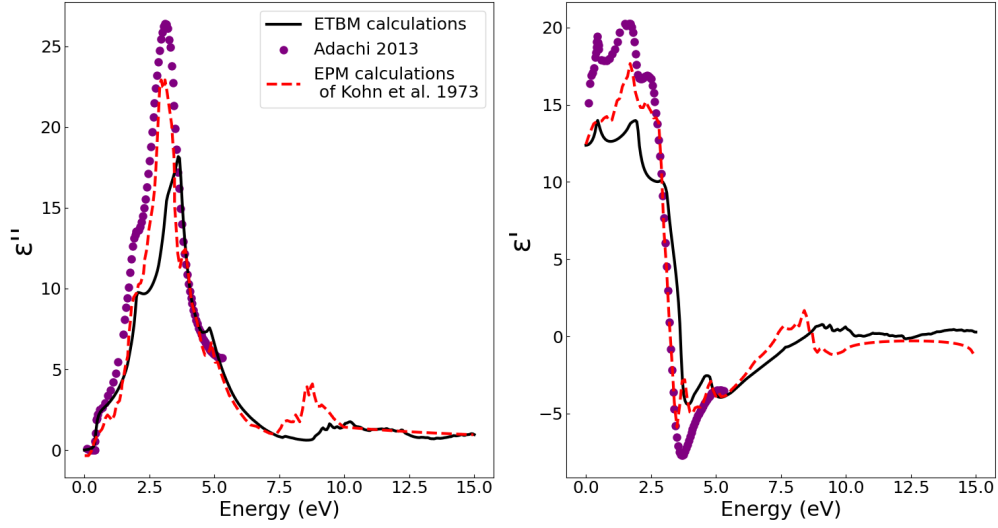


Figure 3.2: (left panel) imaginary part and (right panel) real part of the complex dielectric function calculated by ETBM in black solid line, by EPM in purple dashed line (Kohn et al. [41]), and measured experimentally in purple dotted line (compiled from different authors and gathered in the optical handbook of Sadao Adachi [42]).

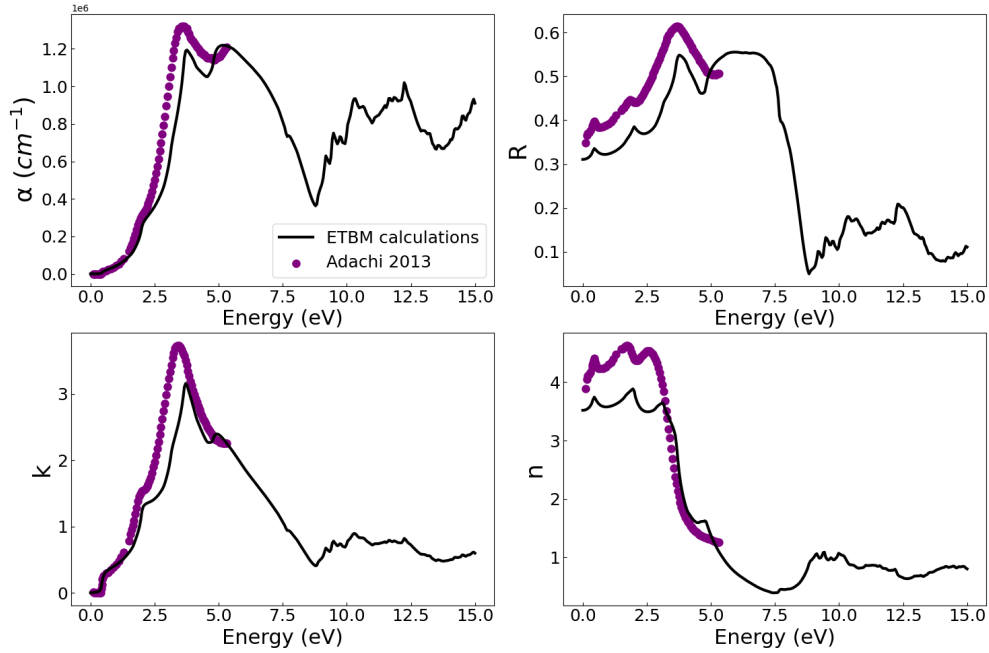


Figure 3.3: (upper left panel) absorption coefficient, (upper right panel) reflectivity, (bottom left panel) extinction coefficient, and (bottom right panel) refractive index measured experimentally in purple dotted line (compiled from different authors and gathered in the optical handbook of Sadao Adachi [42]), and transformed by the appropriate relations from the complex dielectric function calculated by ETBM in black solid line.

standard deviation of n and k by:

$$\frac{\delta \epsilon''}{\epsilon''} = \frac{\delta n}{n} + \frac{\delta k}{k} \quad (3.33)$$

Thus the experimental error on ϵ'' is the sum of the error on k and n which is consistent with the deviation between theory and experiment being 31%, 16% and 20% for ϵ'' , k and n , respectively.

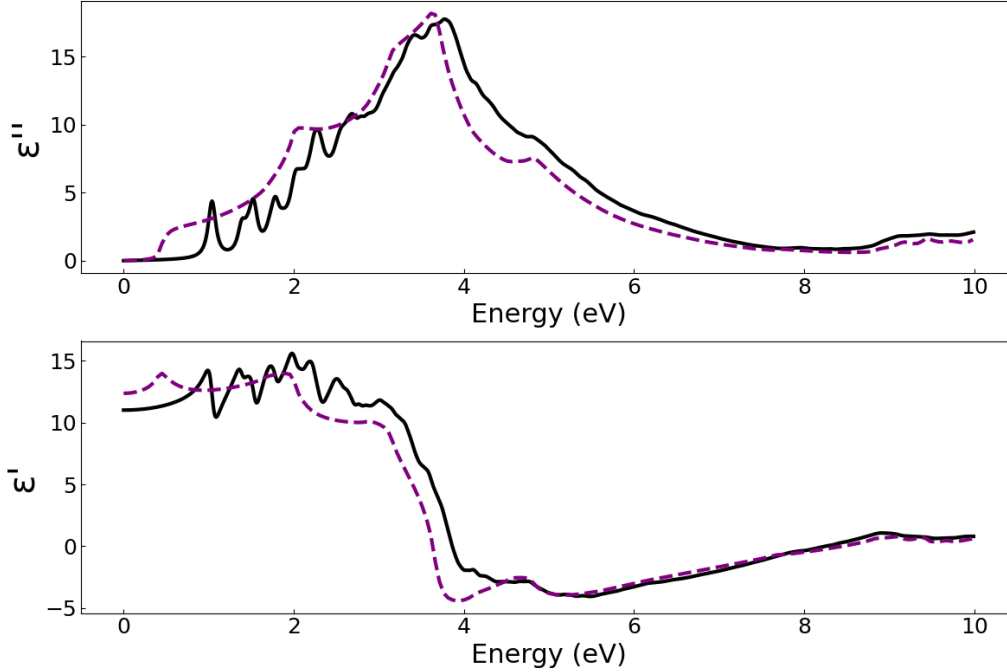


Figure 3.4: (upper panel) imaginary part and (lower panel) real part of the complex dielectric function calculated by ETBM for bulk PbS (dashed purple line) and for a spherical PbS NC of 4 nm diameter (black solid line).

Nanocrystals Figure 3.4 gives $\epsilon''(\omega)$ and $\epsilon'(\omega)$ calculated by ETBM for a spherical NC of 4 nm in size compared to the bulk counterpart. The calculation for the NC employs eq. 3.22 with a broadening σ of 50 meV. The discretization of the electronic structure by the confinement translates into the optical absorption spectrum. Indeed, the first absorption peak is blue-shifted by the gap opening, and in the low energy spectrum (< 2 eV) we can resolve several absorption peaks for the NC when only one is visible for the bulk. Thus, the confinement concentrates the bulk oscillator strength into discrete lines [27]. Figure 3.5 highlights the low absorption spectrum of $\epsilon''(\omega)$, and gives the oscillator strength (vertical lines under the peaks) corresponding to different transitions. We calculated each oscillator strength with eq. 3.36 multiplying by 5 to be apparent on the spectrum. This reveals that each peak includes several transitions with different oscillator strengths. In the envelope function approximation, the optical matrix elements of the interband transitions reduce to [27, 199]:

$$\langle \phi_v | \phi_b \rangle \langle u_v | \mathbf{r} | u_b \rangle \quad (3.34)$$

where ϕ_v and ϕ_b are the envelope functions. Thus, the transitions will only occur for non-orthogonal envelope functions i.e. $n'S - nS$, $n'P - nP$, $n'D - nD$ etc. This has been confirmed in different works, and recently by Poddubny et al. [31] on PbS NCs. In line with their results, we give in Figure 3.5 the electronic states of the NC around the bandgap, and we use the same notations to label the electronic states according

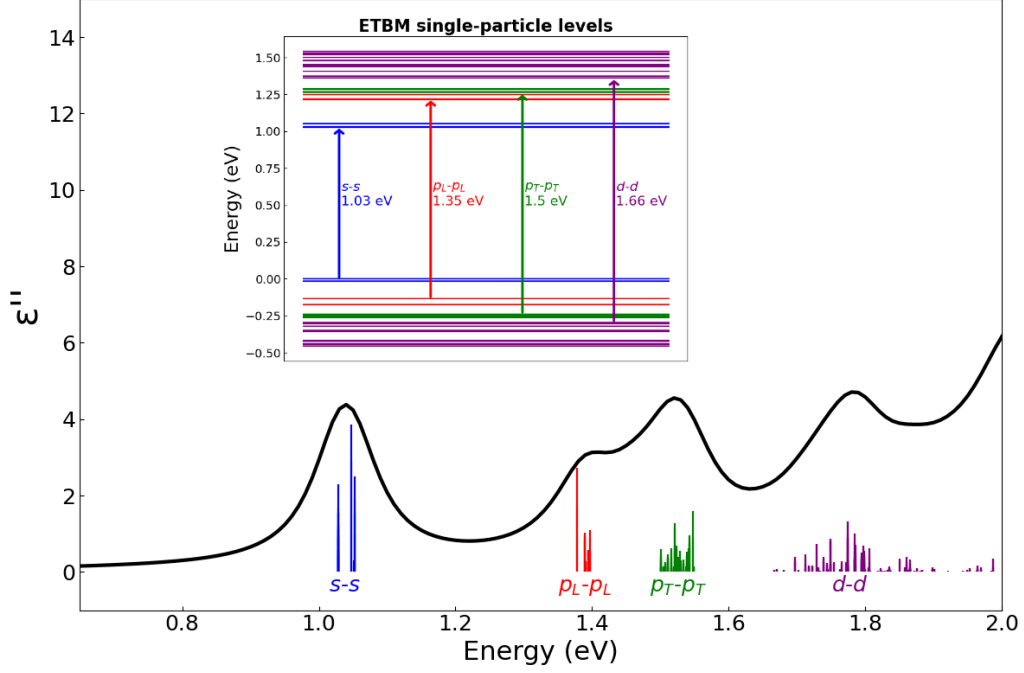


Figure 3.5: Imaginary part of the complex dielectric function for a PbS spherical-like NC of 4 nm. The vertical lines under the peaks correspond to the calculated oscillator strength (multiplying by a factor of 5) for each transition between the valence and conduction band. The panel corresponds to the corresponding electronic structure around the bandgap.

to the angular momentum of the corresponding envelope function. The bulk PbS bandgap is fourfold degenerated at the L points of the BZ and eightfold including spin. As seen in the previous Chapter, four valleys are formed at the L points associated with transverse and longitudinal effective masses. By confinement, this degeneracy might be lifted by intervalley coupling and due to the anisotropy of the valleys. In the electronic structure panel, the blue, red, green, and purple horizontal lines correspond to eight S , eight P_L (longitudinal P states), sixteen P_T (transversal P states) and forty D states in the valence and the conduction band. Thus, the anisotropy of effective masses lifts the 24 degenerated P states into 8 longitudinal and 16 transverse states. On the other hand, the lift of the degeneracy due to intervalley coupling can not be resolved at the scale of the figure. We can see that only the transitions between states with the same orbital momentum (e.g. $S - S$) present strong oscillator strength and appear as peaks in the optical absorption spectrum.

Figure 3.6 compares the absorption spectra calculated by ETBM and measured experimentally in dilute systems (colloidal solution) by Weidman et al. [32]. The latter shows high-monodisperse NCs with a size dispersion of 3.3 %. Therefore, we used the same dispersity to calculate the absorption spectra. We adjusted the ETBM NC size to coincide with the first experimental excitonic peak. The accordance between ETBM and the experimental data is remarkable. It is worth noticing that the second peak is well given by ETBM calculations, which was not observed for PbSe [28]. This is a witness of the quality of the ETBM parameters, and the validity of transferability from bulk to NCs. As discussed earlier, the second peak originates

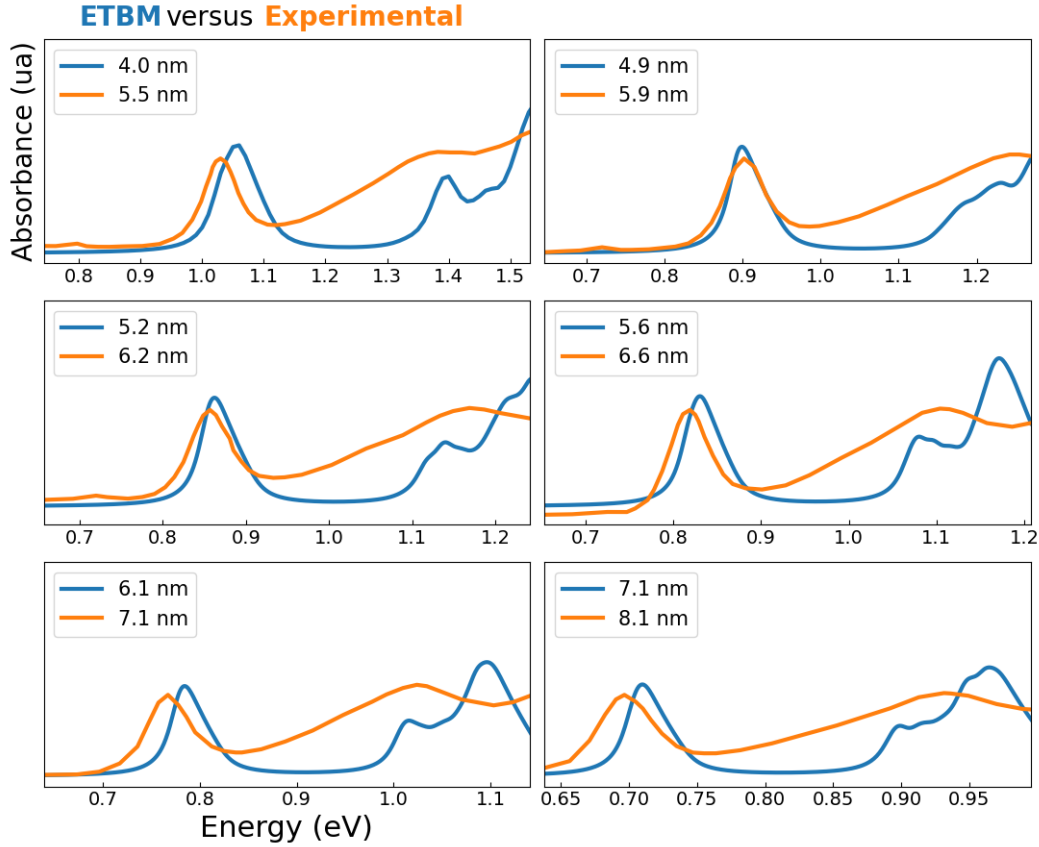


Figure 3.6: Absorption spectra obtained by ETBM calculations (blue solid line), and measured experimentally by Weidman et al. [32] (orange solid line). For each panel the size is given in legend. The first absorption peak is normalized.

from the P-states whose degeneracy is lifted by the anisotropy of effective masses. Regarding, the NCs size, we observe an overall difference of 1 nm between ETBM and experimental measurements. These theoretical results support the likely formation of a PbCl_2 shell deduced experimentally by the use of a high Pb:S precursor ratio [33, 117, 200] (see Chapter 2).

We also calculated the complex refractive index ($\tilde{n} = n + ik$, see eq. 3.15) for different NC sizes, as shown in Figures 3.7a, and 3.7d. It shows that, when the NC size decreases, the first absorption peak is blue-shifted, while for the real part, the optical dielectric constant (ϵ_∞) is reduced. It is good to note that at 0 eV, $\epsilon_\infty = n_\infty^2$. At first thought, we could be tempted to attribute the reduction of ϵ_∞ to the quantum confinement [201, 202] which increases the denominator energy difference of eq. 3.27, and therefore lowers ϵ_∞ for decreasing size. However, this is an error unveiled by previous works on Si and InAs NCs [203]. It is in fact a surface effect that we will discuss in the following section 3.4. We also plot in Figures 3.7b, and 3.7e the complex refractive index for different NC sizes deduced for experiments following the procedure in [43]. Briefly, they combined Maxwell-Garnett model with colloidal absorption measurements to extract the complex optical index. As expected from the previous discussion, the theoretical calculation gives lower values (for the same NC size) at the absorption peak of around 2.5 eV (see Figure 3.7c) and at low energy for the refractive index (see Figure 3.7f). However, in line with the bulk discussion, the experimental results use an indirect method that is not without

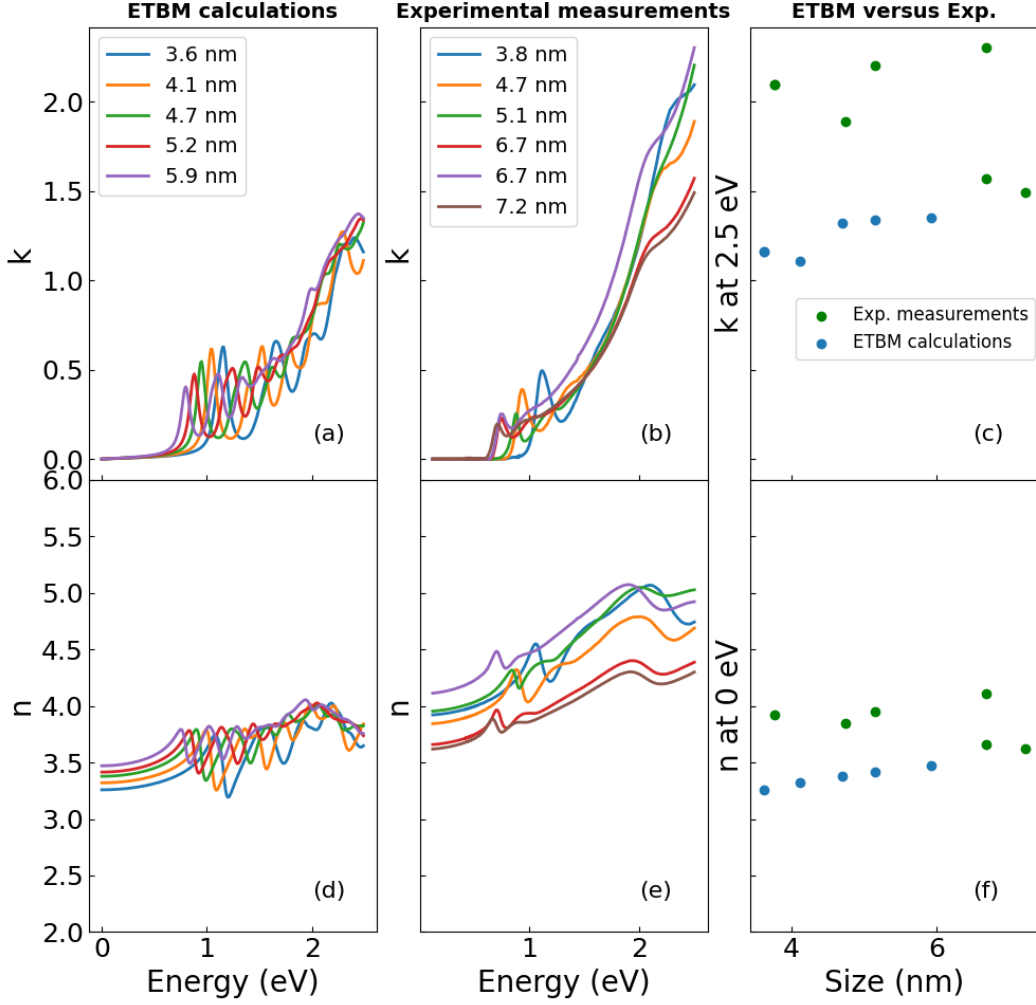


Figure 3.7: Refractive index (n) and extinction (k) calculated by (a,b) ETBM and extracted from (b,e) experimental measurements of Moreels et al. [43]. Comparison of ETBM calculations to the extracted experimental measurements [43] (c) for the extinction coefficient at 2.5 eV, and (f) for the refractive index at 0 eV.

uncertainty, and even if variation can be observed for NCs of equivalent sizes, the compliance with the theoretical work is satisfying considering the different levels of approximations used.

3.4 Mercury telluride

The main results of this section have been published in [40].

From bulk to nanocrystals The semi-metallic behavior of bulk HgTe is apparent in its interaction with light. A visible consequence of the zero value for the bulk bandgap energy is the divergence of the calculated optical dielectric constant ϵ_∞ (see Figure 3.8). Therefore, the optical dielectric constant is usually evaluated at 0.1 eV, giving a value around 14 [204, 45, 205, 206]. The bulk ETBM complex dielectric is in good accordance with the experimental measurements over all the available energy ranges. The peaks attribution on $\epsilon''(\omega)$ spectra has been done by Chadi et

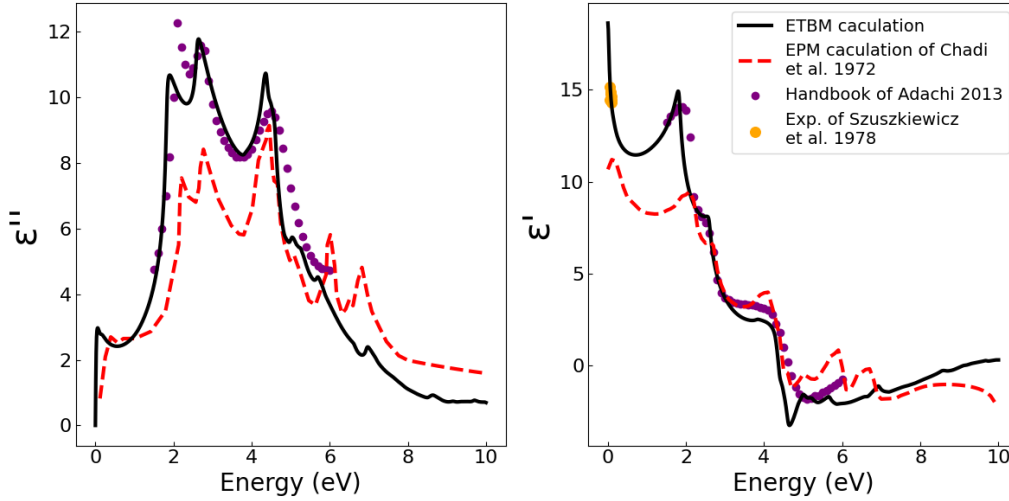


Figure 3.8: (left panel) imaginary part, and (right panel) real part of the complex dielectric function of bulk HgTe calculated by ETBM in black solid line, by EPM in purple dashed line (Chadi et al. [44]), and measured experimentally in purple dotted line (compiled from different authors and gathered in the optical handbook of Sadao Adachi [42]) and orange dotted line by Szuszkiewicz et al. [45].

al. [44] thanks to EPM calculations. The first peak appears at 0 eV, feature of zero bandgaps inverted band structure, and originates from the Γ_8 - Γ_8 transitions between the heavy-hole valence band and the light-electron conduction band. However, the quantum confinement induces the emergence of a bandgap, which, in the case of NCs, allows to cover an extensive range of energy [69], from the visible [183], to terahertz [207, 81].

In Figure 3.9a, we present $\epsilon''(\omega)$ calculated by ETBM for a series of NCs. Their size ranges from 2 to 6 nm, and the first excitonic peak spreads from 0.45 (=2750 nm) to 1.84 eV (=670 nm). We note an important variation of $\epsilon'(\omega)$ (see Figure 3.9b), especially for ϵ_∞ that almost increases linearly with the diameter (see Figure 3.9c). Moreover, a particularly striking result is the strong reduction of ϵ_∞ from bulk to NC, and even for the largest NC $\sim 6nm$, we still predict a 35% decrease in comparison to bulk HgTe. As briefly discussed in the previous section ??, the reduction of ϵ_∞ with decreasing size is not due to the opening of the gap due to quantum confinement. One effective approach to illustrate this is to calculate the bare polarizability, $\chi_{ij}^0(\omega)$ (also named susceptibility), between two neighboring atoms i and j , located at the NC core. We define the bare polarizability $\chi_{ij}^0(\omega)$ as the variation in electronic charge on atom i in response to a potential variation on atom j [27, 208]. In Figure 3.9d, $\chi_{12}^0(\omega \rightarrow 0)$ and $\chi_{11}^0(\omega \rightarrow 0)$, give the bare polarizability values between two neighboring atoms, labeled as 1 and 2, respectively, and located at the center of a CdTe or HgTe NC. Remarkably, the two polarizabilities remain constant, regardless of the NC size, for both CdTe, which is a large gap material, and HgTe, which is semi-metallic in bulk, despite HgTe NCs exhibiting a gap variation of almost four times. This result confirms that ϵ_∞ is not affected by quantum confinement. It is actually true not only for ϵ_∞ , but also for $\epsilon'(\omega)$ with $\omega \ll E_g/\hbar$. The reason is that, similar to Si or InAs NCs [203], the quantum confinement preserves the barycenter of the valence and conduction bands, which renders $\chi_{ij}^0(\omega)$ independent of the NC size (as shown in Figure 3.9d). In fact, the size variation of ϵ_∞ results purely from

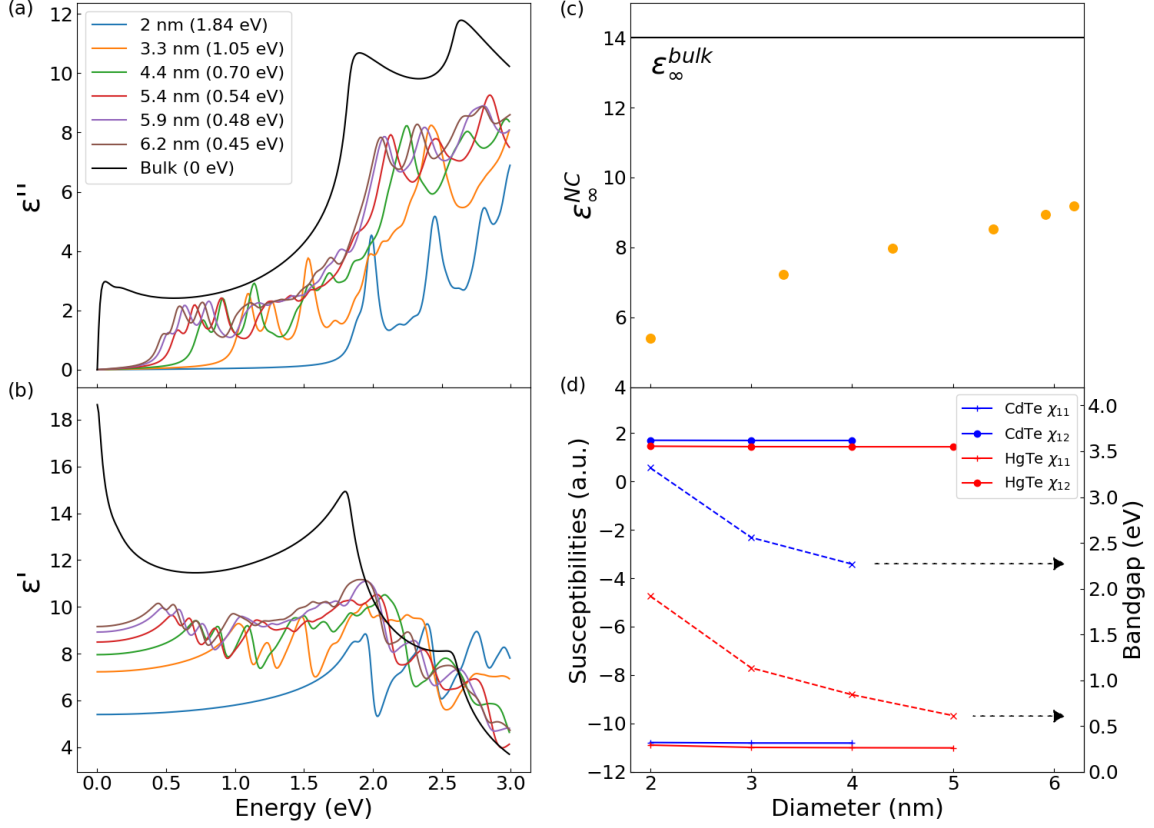


Figure 3.9: (a) Imaginary part $\epsilon''(\omega)$ of the complex dielectric function calculated for NCs of different sizes (colored solid lines), and compared to $\epsilon''(\omega)$ calculated for bulk HgTe (black solid line). The values in parenthesis in the legend correspond to the peak position in energy. (b) Same for the real parts $\epsilon'(\omega)$. (c) The optical dielectric constant for different NC sizes. The black vertical line represents the bulk value. (d) $\chi_{12}^0(\omega \rightarrow 0)$ and $\chi_{11}^0(\omega \rightarrow 0)$ susceptibilities (solid lines) and energy gap (dashed lines) versus diameter for CdTe (in blue) and HgTe (in red) NCs.

surface effects which are not described by $\chi_{ij}^0(\omega)$ inside the NC. Indeed, the broken bonds at the surface lead to rapid spatial variations in charge, which diminish the screening ability in the vicinity of the surface [203].

Although surface effects can contribute to differences in optical dielectric constant between bulk HgTe and NCs, they cannot fully explain the significant variation of $\sim 35\%$ with the largest NCs. In particular, when the energy of the light approaches the bandgap energy, $\epsilon'(\omega)$ exhibits a peak that gradually shifts to zero as the size of the NCs increases, and in the bulk limit, this peak diverges. We unveiled in Chapter 2, that this transition occurs for an NC of 26 nm and this transition is of topological nature. Because of the limitations in the size of NCs that can be studied through numerical simulations, we investigated in Figure 3.10 this physic with artificial bulk material. To create the artificial material, the band order of bulk HgTe was restored to a normal configuration by artificially shifting the on-site energy on the s orbital of the Hg orbital. This results in the opening of a gap as in NCs, and allows us to study the effect of the electronic structure on the complex dielectric constant without considering surface effects. It appears in Figure 3.10 that a tiny gap opening of 0.039 eV removes the divergence of $\epsilon'(\omega)$ at 0 eV, which is a characteristic

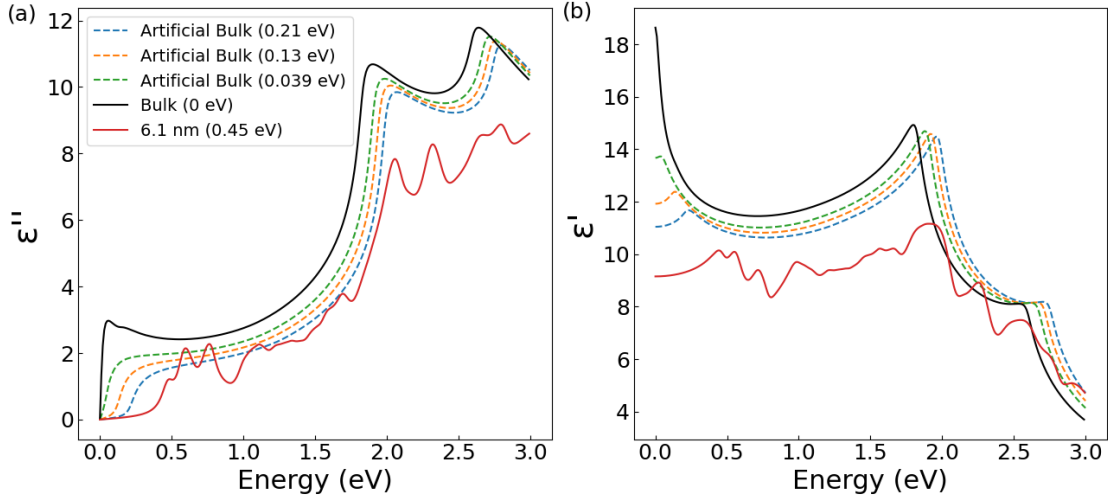


Figure 3.10: (a) Imaginary part of the complex dielectric function calculated for a NC of 6.1 nm diameter (red solid lines), compared to bulk HgTe (black solid line), and to a bulk material in which a gap is opened artificially by changing ETBM parameter $E_s(c)$ [36] (dashed lines). The values in parenthesis in the legend correspond to the peak position in energy. (b) Same for the real parts.

of a metallic behavior, and reduces it at higher energy. In addition, increasing the gap to 0.13 and 0.2 eV brings us closer to the situation of NCs, although important differences remain. The artificial increase of the bulk bandgap results in a strong variation of $\epsilon'(\omega)$ at low energy values where the Γ_8 and Γ_6 band states are the main contributors. Since bulk HgTe and HgTe NCs smaller than 26 nm in diameter are on opposite sides of a boundary in terms of the electronic structure, we conclude that the topological transition affects $\epsilon'(\omega)$ when going from bulk to NCs, even though we cannot precisely determine its contribution near the crossing point.

It is worth noting that the $\epsilon'(\omega)$ of NCs has a limited spectral dependence over a broad energy range, which is of special interest for device simulations. Therefore, it is reasonable to approximate $\epsilon'(\omega)$ by a constant value determined away from resonance when simulating the electromagnetic behavior of NC layers. However, the imaginary part, $\epsilon''(\omega)$, exhibits fine structure features that are crucial, especially at low photon energy. Hence, in the subsequent paragraph, we will derive an analytical equation for $\epsilon''(\omega)$ at low photon energy.

Analytical form of $\epsilon''(\omega)$ at low photon energies To derive an analytical equation for $\epsilon''(\omega)$ for each absorption peak (i) at low energy, we simply assume an inhomogeneous broadening by transforming the delta distribution of eq. 3.25 by a Gaussian function:

$$\epsilon''(\omega) = \frac{\pi q^2 \hbar \bar{f}_i(d)}{2m_0 \epsilon_0 \Omega(d) \omega_i(d)} \frac{1}{\sqrt{2\pi\sigma(d)}} e^{-\frac{(\hbar\omega - \hbar\omega_i(d))^2}{2\sigma^2(d)}} \quad (3.35)$$

where $\bar{f}_i(d)$ corresponds to the total oscillator strength of all transitions contributing to a peak at energy $\hbar\omega_i(d)$:

$$\bar{f}_i(d) = \frac{2m_0 \omega_i(d)}{\hbar} \sum_{i,j} |\langle i | \mathbf{r} \cdot \mathbf{e} | j \rangle|^2 \quad (3.36)$$

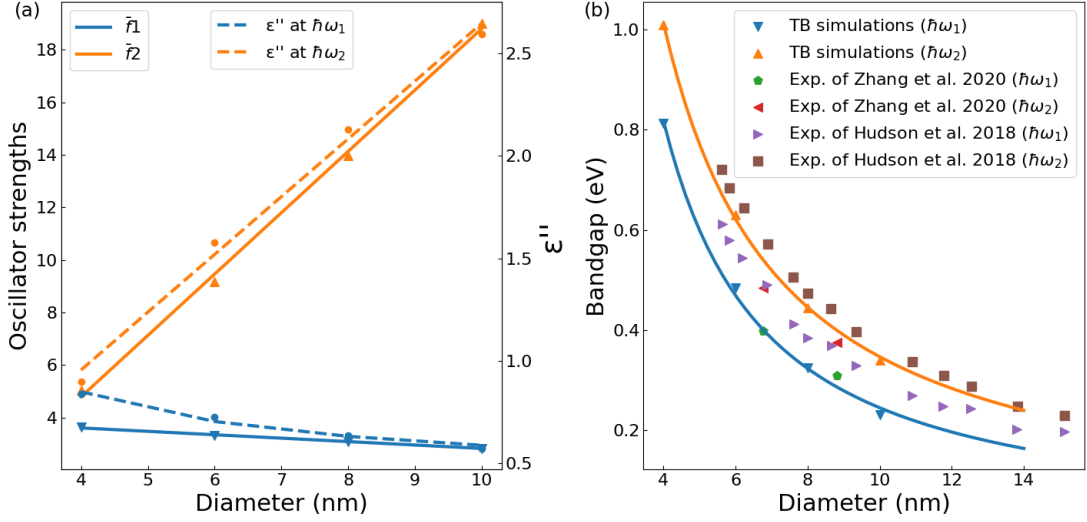


Figure 3.11: (a) Evolution of the oscillator strengths (solid line) and the imaginary part of the complex dielectric function (dashed line) with the NC diameter. (b) Evolution of the first (orange solid line) and second (blue solid line) excitonic peak with the NC size calculated by ETBM and compared to experimental measurements of Zhang et al. [39] and Hudson et al. [38].

Finally, we can express $\sigma(d)$ and $\hbar\omega_i(d)$ in eV, and d the NC diameter in nm to give:

$$\epsilon''(\omega) = \frac{1.65\bar{f}_i(d)}{d^3\hbar\omega_i(d)\sigma(d)} e^{-\frac{(\hbar\omega - \hbar\omega_i(d))^2}{2\sigma^2(d)}} \quad (3.37)$$

To exploit this equation, we computed in Figure 3.11 the total oscillator strength $\bar{f}_i(d)$ and the bandgap energy $\hbar\omega_i(d)$ for the two first absorption peaks (of $\epsilon''(\omega)$) for NC sizes ranging from 4 to 10 nm. The results are represented in Figure 3.12. The oscillator strength of the second peak is linear in d :

$$\bar{f}_2(d) = 2.34d - 4.55 \quad (3.38)$$

which is currently found for the lowest excitonic peak in zinc-blende CdSe [209] or PbS [79] NCs. This is attributed to a roughly constant matrix element of the electron momentum with size. But, the first peak slightly decreases with the size as:

$$\bar{f}_1(d) = -0.13d + 4.13 \quad (3.39)$$

We impinge this unusual behavior to the peculiar nature of LUMO in HgTe and HgS NCs [189], whose weight increases towards the surface with increasing NC size (see Figure 1 and 2 in Supporting Information [210]). Concerning, the bandgap-size relation for the two first absorption peaks, we found from Figure 3.11b:

$$\hbar\omega_1(d) = \frac{1.91}{d} + \frac{5.46}{d^2} \quad (3.40)$$

and:

$$\hbar\omega_2(d) = \frac{3.08}{d} + \frac{3.86}{d^2} \quad (3.41)$$

Thus, the only size-dependent function that is unknown in eq. 3.37 is the energy

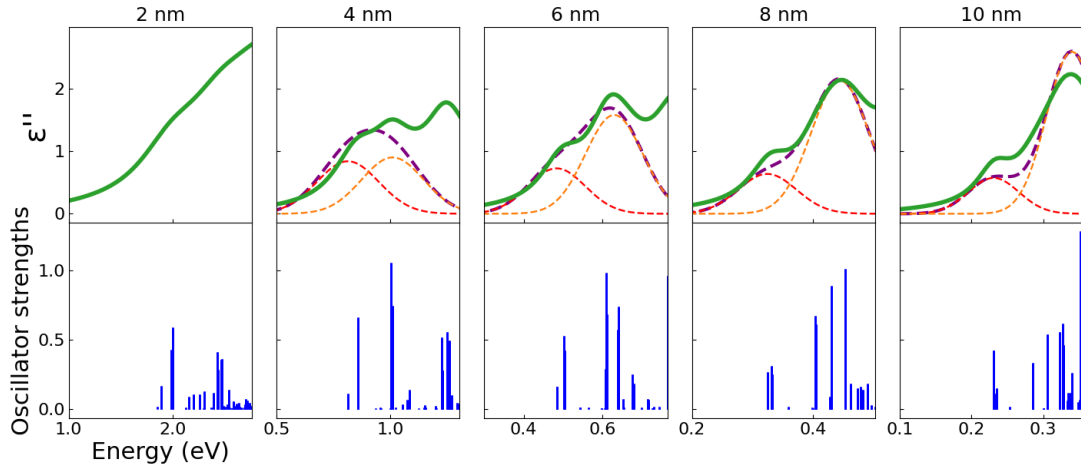


Figure 3.12: (top, green solid line) imaginary part of the complex dielectric function and (bottom, blue vertical lines) corresponding oscillator strengths computed by ETBM. Purple dashed lines correspond to the sum of the analytical formula (3.35) for the first (red dashed line) and second peak (orange dashed line). The diameter of the NCs is indicated above each panel.

broadening $\sigma(d)$. It is straightforward to obtain it by deriving the size-bandgap relation of the first absorption peak (eq. 3.40), which gives:

$$\sigma(d) = \delta\hbar\omega = \left| \left(-\frac{1.91}{d} + \frac{2 * 5.46}{d^2} \right) \frac{\delta d}{d} \right| \quad (3.42)$$

where $\frac{\delta d}{d}$ is the size dispersity that we fixed at 10%, value usually given for HgTe colloidal NCs [38]. We assume an equivalent broadening energy for the second absorption peak. Thus, we can input the eqs. 3.39, 3.38, 3.40, 3.41, and 3.42 into the eq. 3.37 to describe the low energy range of $\tilde{\epsilon}''(\omega)$. Figure 3.12 compares the analytical results of $\epsilon''(\omega)$ to the ETBM calculations. Besides the excellent accordance, we can note that, as the NC size increases, the first peak becomes comparatively smaller in intensity than the second peak [39]. This is due to the evolution of the oscillator strength with size which is constant for the first peak while increasing linearly for the second.

3.5 Conclusion

Although the complex dielectric function is a crucial parameter, its experimental determination is difficult and mostly indirect. Thus, for two small band-gap semiconductors (PbS and HgTe), we used ETBM to calculate $\tilde{\epsilon}(\omega)$ of the bulk and NC structures. For bulk PbS, we show an overall good agreement compared to experimental measurements, especially for the refractive index (n) and the extinction coefficient (k). The origins of discrepancies are discussed. We put in perspective the experimental errors unveiling how an error can propagate through the different related optical functions. We emphasize the effect of confinement over the complex dielectric function by the apparition of discrete peaks. We attribute these peaks to different electronic transitions following the selection rules. Furthermore, a detailed study of the effect of confinement on HgTe allows us to uncover the effect of the topological transition over the optical properties, with an important reduction

of the refractive index. In addition to the impact on $\tilde{\epsilon}$, a topological insulator is known to present a conductivity at the surface protected by symmetry, where charge carriers would be transported without dissipation [188]. This could have important applications in electronic and spintronic technologies. Finally, we obtain an accurate analytical formula that characterizes the absorption coefficient, enabling swift access to the low-energy region of the absorption spectrum and illuminating how it varies with size. These works improve the knowledge of the properties of isolated NCs and will be exploited in the following Chapter to simulate the complex optical index of NC films.

Chapter 4

Layer of nanocrystals: optical properties

4.1 Introduction

In the previous Chapters, we focused on the electronic and optical properties of a single NC. For industrial applications, these synthesized NCs are usually deposited on a substrate, and a solid layer composed of densely packed NCs is created, forming the light-absorbing medium. The properties of this solid layer can be significantly different from a single NC, owing to the interaction of NCs with the organic surrounding media, formed by ligands. We will focus in this Chapter on the study of the properties of these dense solid layers. In this context, we couple theoretical calculations with experimental measurements to assess the different parameters of the NC layers affecting the optical properties.

In section 4.2, we first present spectroscopic ellipsometry, which is a primary technique to access the optical properties of layers. However, it is an indirect method that relies on analytical models to fit experimental parameters. We discuss some of these, especially the Effective Medium Approximations (EMA) that were developed for heterogeneous layers.

Specifically, we investigate in section 4.3 the effect of the surface chemistry and NC size on PbS NC layers in the SWIR region [29]. This region of great interest for active imaging presents a strong water absorption band that enhances the contrast regarding the visible region [2]. We develop a joint model combining ETBM calculations to effective medium approximations that not only ease access to the optical indices of NC layers but unveils fundamental properties such as the density of NCs in the layer. Then we show that quick access to optical indices is applicable for device optimization.

In section 4.4, we extend the wavelength region. Following the joint model that is successful for PbS NCs, we focus on HgTe NCs with a bandgap ranging from 1700 nm to 2220 nm [211]. Herein, we study the effect on the NC shape. We consider three geometries with sphere, rod, and planar tripod, and reveal that their shape is of central importance to improving the NC layer optical properties.

4.2 Determination of the complex dielectric function in a NC layer

The main experimental technique to determine the complex dielectric function in a NC layer is spectroscopic ellipsometry (SE). For further details about SE, the reader can refer to Refs. [212, 46, 213, 214]. In fact, many other properties can be extracted from this technique such as layer morphology, layer thickness, and surface roughness. SE is a fast, non-destructive, sensitive but indirect method that measures the change of the polarization of light upon its reflection. By measuring two angles ($\Psi; \Delta$) associated with this change, SE can provide the complex refractive ratio of Fresnel reflection coefficients (FRCs):

$$\rho = \frac{r_p}{r_s} = \tan\Psi e^{i\Delta} \quad (4.1)$$

where $r_p(r_s)$ is the complex FRC for light polarized parallel (perpendicular) to the plane of incidence. In the case of a single thin layer over a substrate as represented in Figure 4.1a, two reflecting surfaces are present, and the FRCs for polarizations p and s are respectively referred to as r_j , with $j = p, s$, and are given by:

$$r_j = \frac{r_{01j} + r_{12j}e^{-i2\beta}}{1 + r_{01j}r_{12j}e^{-i2\beta}} \quad (4.2)$$

where r_{mnj} are the FRC with mn corresponding to the interface and j denotes either p the parallel or s perpendicular component of the polarized light ($0 \equiv$ vacuum, $1 \equiv$ layer, and $2 \equiv$ substrate or air). These coefficients as well as the β coefficient (see Refs. [46, 212] for details) are functions of the sample characteristics such as the film thickness and the complex refractive index of each layer. To obtain the latter

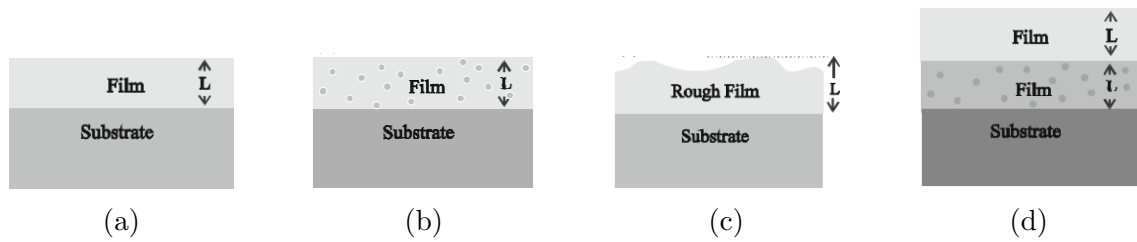


Figure 4.1: (a) uniform layer on a substrate, (b) inhomogeneous layer on a substrate, (c) rough film on a substrate, and (d) multiple layers on a substrate. Reproduced from Ref. [46].

physical properties from the ellipsometric measurements of Δ and Ψ , an optical stack model must be used to approximate the sample system (including the substrate, film, and ambient). Figure 4.1 provides some examples of these models. Once the optical model is established, the complex refractive ratio (ρ) can be calculated based on the Fresnel reflection coefficients (FRCs) of the various interfaces:

$$\rho = \tan\Psi e^{i\Delta} = \rho(\tilde{n}_0, \tilde{n}_1, \dots, \tilde{n}_i, L_0, L_1, \dots, L_i, \phi_0, \lambda) \quad (4.3)$$

where \tilde{n}_i and L_i are the complex refractive index and the thickness of the layer i . λ is the wavelength of the probing light, while ϕ is the angle of incidence at which the

light is measured. Therefore, from the eq. 4.3, the measurement of Δ and ϕ gives access to only two properties. The other unknowns can be obtained from different strategies which are often complementary :

- from independent measurements,
- by systematically varying additional experimental variables, one can increase the number of independent equations,
- dispersion models of the complex refractive index depending on parameters that are fitted on the measured data (detail below).

The dispersion models [46] are widely used to access the refractive index of unknown layers. These models must be physically relevant to the optical layer being studied and consistent with Kramers-Kronig relations. For example, for a non-absorbing layer in the range of wavelength considered, the Cauchy equation is often a good option and writes:

$$n(\lambda) = A + \frac{B}{\lambda^2} + \frac{C}{\lambda^4} \quad (4.4)$$

where A , B , and C are the Cauchy parameters. For more complex layers, oscillator models are more suitable since they can describe optical constants in both transparent and absorbing regions simultaneously, maintain Kramers-Kronig consistency and require fewer fitting parameters. For instance, the Tauc-Lorentz model is mainly employed for description near the bandgap while the Gaussian model is ideal for system with different oscillators, such as NCs.

Other models named effective medium approximations (EMAs) [215, 216, 217, 218, 219] serve to describe layers composed of small particles embedded in a matrix of a host material, typically NC layers. They allow the description of the effective properties of the layer such as the effective complex dielectric function in terms of its constituent. In other words, EMAs enable the replacement of an inhomogeneous property, e.g. variations of refractive indices, with a homogeneous one that has a single effective refractive index. For this, it requires that the incident light presents a wavelength larger than the particle size to make the heterogeneous layer appears as a homogeneous macroscopic medium. The two most commonly used EMAs are the Maxwell-Garnett [220] and Bruggeman [221] models. A variety of derivations exist in the literature, see Ref. [216, 215, 222, 223]. A simple derivation [46] is to start with the Clausius-Mossotti relation which relates the complex dielectric function $\tilde{\epsilon}$ (macroscopic property) to the electronic polarisability α (microscopic property) by:

$$\frac{\tilde{\epsilon} - 1}{\tilde{\epsilon} + 2} = \frac{1}{3\epsilon_0} N\alpha \quad (4.5)$$

This equation describes a system containing one type of atomic specie with a concentration N and polarisability α . If we extend this relation to a system of different species with polarisabilities α_j in a host medium of dielectric constant $\tilde{\epsilon}_h$, then we find:

$$\frac{\tilde{\epsilon} - \tilde{\epsilon}_h}{\tilde{\epsilon} + 2\tilde{\epsilon}_h} = \sum_j f_j \frac{\tilde{\epsilon}_j - \tilde{\epsilon}_h}{\tilde{\epsilon}_j + 2\tilde{\epsilon}_h} \quad (4.6)$$

where f_j are the volume fraction of the specie j , also called inclusions. This equation is named the Maxwell-Garnett equation. It is worth noticing that the parameters

of the inclusions ($\tilde{\epsilon}_j$ and f_j) enter eq. 4.6 symmetrically, contrary to the host one ($\tilde{\epsilon}_h$ and $f_h = 1 - \sum_j f_j$) [216]. Unless we have specific information about the medium components and if the volume fraction of the host is significantly greater than that of the inclusions, there is no justification for applying different rules to them. Therefore, we can let the host dielectric constant $\tilde{\epsilon}_h$ equals the effective one $\tilde{\epsilon}$ which leads to the Bruggeman equation:

$$0 = \sum_j f_j \frac{\tilde{\epsilon}_j - \tilde{\epsilon}}{\tilde{\epsilon}_j + 2\tilde{\epsilon}} \quad (4.7)$$

This equation is symmetric with respect to all inclusions and presents the physical property that if $f_j = 1$, then $\tilde{\epsilon} = \tilde{\epsilon}_j$ and if $f_j = 0$, then $\tilde{\epsilon}$ does not depend on $\tilde{\epsilon}_j$. Hence, the Bruggeman equation can be used, in principle, for composites with any volume fraction, without leading to apparent inconsistencies.

4.3 Lead sulfide: size and ligand effects

The results of this section have been published in our following work Ref. [29]. The experimental part, as well as the device simulation, have been performed by our collaborators, the group of E.Lhuillier at the Institut des NanoSciences de Paris (INSP). By SE measurements, we provide a methodical exploration of how the size and surface chemistry of NCs influence the intricate optical index of layers of PbS NCs. We then combine in sub-section 4.3.2 these experimental outcomes with simulations based on EMAs incorporating ETBM calculations. EMAs are mainly used for dilute systems [79, 43, 224, 98, 225, 226, 227, 228] but they have recently shown great promise for NC thin films [229, 230, 231, 232]. However, to the best of our knowledge, the integration of electronic structure calculations with EMA models has not been previously reported. This approach allowed us to obtain valuable parameters of the NC film, such as the NC volume fraction and the optical index of the surrounding medium (host) which includes the ligand shell. In sub-section 4.3.3, we incorporated the obtained complex optical indices into electromagnetic simulations of PbS NC-based diode stacks to investigate their absorption properties.

4.3.1 Synthesis and characterization

Synthesis For this study, following the procedure of Moreels et al [21, 233], a series of PbS NC was grown with exciton peak from 1000 to 1550 nm corresponding to NC size ranging from 4.5 to 6.7 nm, see Figure 4.2c. Subsequently, we will denote each population of PbS NCs according to their respective peak wavelength. For instance, the population displaying an exciton feature at 1200 nm will be referred to as PbS 1200. The synthesis uses PbCl_2 and atomic sulfur as precursors, and the final NCs are obtained with oleic acid (OA) as ligands stabilizing the colloidal solution. The NC size is tuned via the time and temperature reaction. Although the shape of the PbS NCs is known to change with their size (see Chapter 1), we assume a spherical-like shape for all NCs as shown by the images obtained from transmission electron microscopy (TEM) in Figures 4.2a and 4.2b. The colloidal NCs have been deposited under a solid thin layer onto a transparent glass substrate by spin coating. The latter is a deposition technique that uses centrifugal force to obtain homogeneous layers.

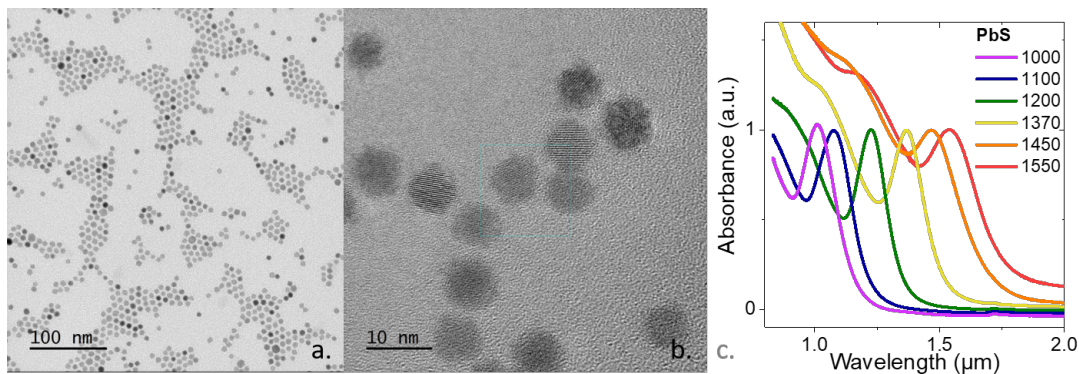


Figure 4.2: (a) TEM images, and (b) high-resolution TEM of PbS 1550. (c) Absorption measurements for a series of colloidal PbS NCs with the first exciton peak wavelength ranging from 1000 to 1550 nm (see Ref. [29]).

In addition, ligand exchange experiments were conducted for three particle sizes to investigate the impact of surface chemistry on the optical properties, specifically on PbS 1200, PbS 1370, and PbS 1550. PbS 1200 and PbS 1370 were selected due to their proximity to the water absorption edge and spectrally located on each side of the absorption. Regarding PbS 1550, it matches the wavelength using in telecommunication applications (telecom C-band). Concerning surface chemistry, each of the three chosen NCs has been passivated by ethanedithiol (EDT) or iodide ion (NH_4I) due to their ability to form respectively p- and n-type layers in the case of small PbS NCs [234, 235].

SE SE was employed to characterize the PbS NC layers within the 450 to 2000 nm wavelength range. As previously described, the Ψ and Δ measurements were fitted to multilayer modeling to determine the dielectric function of the NC layer. The imaginary part of the dielectric function of the NCs was modeled using a linear combination of one Tauc-Lorentz oscillator and four Gaussian oscillators. The real part was calculated using Kramers-Kronig relations. The parameters of the fit were optimized using a least-square fitting procedure to minimize the difference between the measured and estimated (Ψ , Δ) values. The unbiased mean-squared error (MSE) was used for this purpose. We obtained the refractive index (n) and extinction coefficient (k) for 6 NC samples of different sizes passivated by OA, 3 passivated by EDT, and 3 by NH_4I . However, we present in Figure 4.3 the optical indices (n, k) for PbS 1200 capped with the three ligands. To give a better understanding of the various effects on optical properties, we present theoretical calculations in the following subsection.

4.3.2 ETBM-EMA model

The effect of surface chemistry on the complex refractive index is shown in Figure 4.3. In order to have a deeper insight into these evolutions, we used the two EMA models, namely Bruggeman and Maxwell-Garnett approximation, coupled with ETBM calculations to obtain the complex refractive index of the NC layer and compared it to SE measurements. Both models (Figure 4.4) give the shape, position, and magnitude of the peaks in good agreement with SE data. The volume fractions

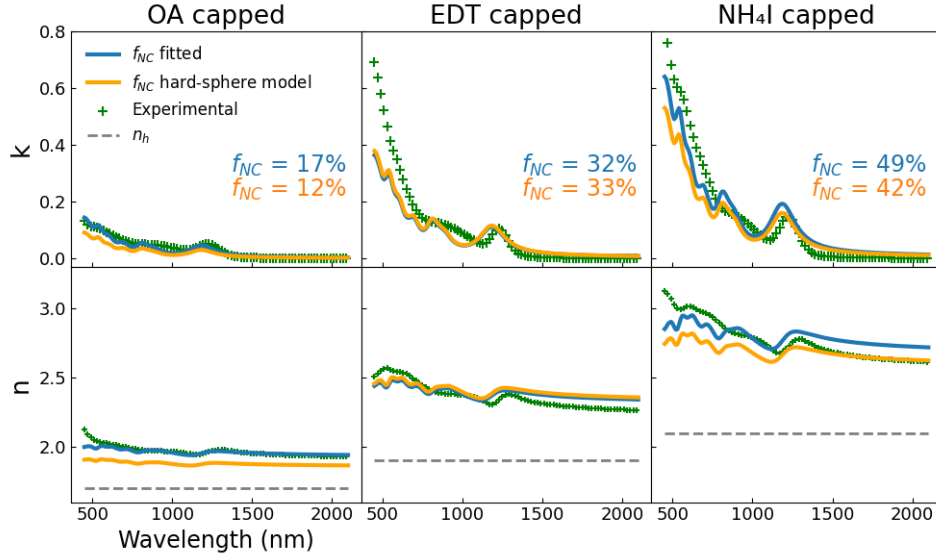


Figure 4.3: Effect of surface chemistry on the optical properties. Extinction coefficient (k) and refractive index (n) for PbS 1200 passivated with OA, EDT, and NH₄I. We used Bruggeman approximation (see eq. 4.8) where the f_{NC} is either fitted (blues solid line) or calculated by the hard-sphere model (orange solid line, see eq. 4.9). We compared these theoretical calculations with the ellipsometry measurements (green crosses). We represent the host refractive index by a dashed grey vertical line at the values: 1.7, 1.9, and 2.1 for OA, EDT, and NH₄I, respectively.

extracted (details below) from Maxwell-Garnett are higher than those from Bruggeman. Although the theory is consistent with experimental data, it becomes invalid (as explained in the previous section) when the concentration of the host material is comparable to that of the inclusion, such as in the case of NH₄I capping.

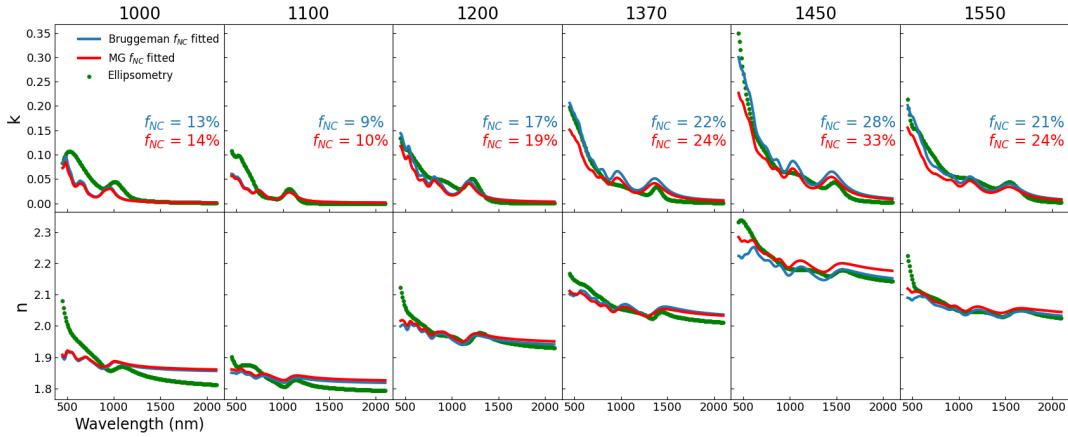


Figure 4.4: Effect of NC size on the optical properties. Extinction coefficient (k) and refractive index (n) spectra for PbS 1000, 1100, 1200, 1370, 1450 and 1550 passivated with OA. The SE measurements (green dots), the Bruggeman (blue line) and the Maxwell-Garnett (red line) approximations are compared. The NC volume fractions (f_{NC}) obtained in the two EMAs are given.

The Bruggeman formula (see eq. 5.8) relates the effective complex dielectric function $\tilde{\epsilon}$ of a layer with its constituent. In this study, we consider only two in-

clusions, the NCs ($\tilde{\epsilon}_{NC}$, f_{NC}), and the ligands with the void surrounding the NCs, which we named host ($\tilde{\epsilon}_h$, $1 - f_{NC}$). The Bruggeman formula eq. 5.8 becomes:

$$0 = f_{NC} \frac{\tilde{\epsilon}_{NC} - \tilde{\epsilon}}{\tilde{\epsilon}_{NC} + 2\tilde{\epsilon}} + (1 - f_{NC}) \frac{\tilde{\epsilon}_h - \tilde{\epsilon}}{\tilde{\epsilon}_h + 2\tilde{\epsilon}} \quad (4.8)$$

where $\tilde{\epsilon}_{NC}$ is obtained from ETBM calculations (see Chapter 3), while $\tilde{\epsilon}_h$, and f_{NC} are used as fitting parameters to reproduce SE measurements. We assume that the imaginary part of ϵ'_h equals zero because the ligands are non or weakly absorbing at the wavelength studied. Furthermore, we consider the real part ($\epsilon'_h = n_h^2$) constant over the spectral range since its frequency dependence is assumed to be weak. Moreover, ϵ'_h depends only on the ligands, void, and any residual organics in a solid-state form. Thus, for each passivation type (OA, EDT, and NH_4I), we evaluated ϵ'_h as the overall best value to fit the Bruggeman optical indices to PbS 1200, 1370, and 1550 SE measurements. We obtained n_h of 1.7, 1.9, and 2.1 for OA, EDT, and NH_4I passivation type, respectively. The evolution is expected but seems overestimated in regard to their molecule's refractive index, e.g. 1.4 for the OA molecule. However, at the interface between the NC and the ligands, it is known that electrostatic dipoles form [236, 14] and probably increase the host refractive index. Moreover, we showed in Chapter 3 that the ETBM calculations tend to underestimate the refractive index. But, the trends of the results are unaffected as well as the following conclusions. The remaining unknown parameter in eq. 4.8 is

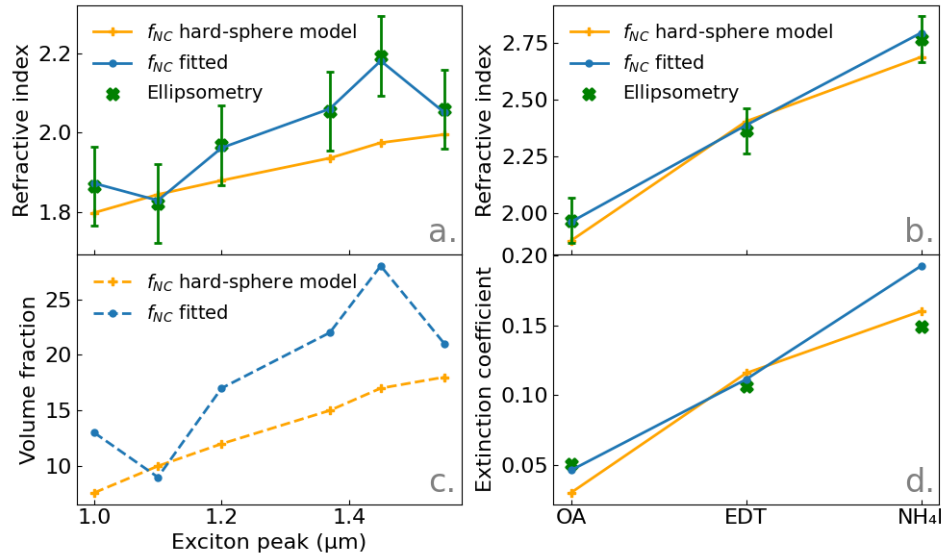


Figure 4.5: We compare SE measurements (green crosses) with Bruggeman approximation where f_{NC} was either fitted (blue solid line) or calculated with a HSM (orange solid line, see eq. 4.9). (a,c) Effect on the NC size for OA capping. (b,d) Effect on the surface chemistry for PbS 1200. (a-b) The average refractive index over the wavelength range of 750 to 2000 nm. (c) NC volume fraction. (d) Extinction coefficient (k) at the exciton peak.

the NC volume fraction f_{NC} , which is fitted to experimental data by a least-squares minimization procedure using the root mean square error as the figure of merit.

As illustrated in Figure 4.3, for equivalent NC size, the NC volume fraction varies for different passivation types. The values are 17%, 32%, and 42% for OA,

EDT, and NH_4I respectively. This rise is explained by the decreasing ligand length which increases the packing fraction of the layer. Indeed, Weidman et al. [237] gave values around 2.6 nm, 1.2 nm, and 0.7 nm for the interparticle spacing between NCs surrounding by OA, EDT, and NH_4I ligands, respectively. It is worth noticing that these values may vary with the deposition technique.

Furthermore, we show in Figures 4.5c and 4.4 that, at identical surface chemistry, f_{NC} also increases with increasing NC size. Assuming a hard-sphere model (HSM) where ligands form a rigid shell surrounding the NCs, we can express the volume fraction according to the NC radius (r_{NC}) as follows:

$$f_{NC} = PF \frac{r_{NC}^3}{(r_{NC} + l)^3} \quad (4.9)$$

where PF is the packing fraction, and l is the ligand length. Thus, from the eq. 4.9, we can see that f_{NC} is proportional the NC radius r_{NC} . It is worth noticing that eq. 4.9 also unveils that the decrease of the ligand length increases the VF.

Since the optical indices (n, k) of the NC layer increase with the NC volume (see Figures 4.3 and 4.5b,d), we just demonstrate two possible tuning strategies of optical device performances, specifically the ligand length and the NC size. As we will see in the following Chapter, optimal values of these parameters can be found maximizing the device performance.

In addition to the fitting procedure, we calculated f_{NC} using eq. 4.9. For this, we consider the NCs in the layer organized in a random close-packed distribution corresponding to a PF of 64% [238]. It was a good estimation of the packing for glassy films of CdSe NCs [239]. As discussed above, the length of the ligands in the films is taken close to the literature [237], and the NC radius are those calibrated by ETBM. In accordance with Dement et al., [231], the volume fractions obtained with the HSM match those fitted from experiments using the Bruggeman model (Figures 4.5 and 4.3). However, we observe a slight underestimation for the HSM, both with varying surface chemistry (Figure 4.3) and size (Figure 4.5). This observation is in line with the work of Diroll et al. [240], a picture of hard cores with rigid organic shells tends to overestimate the denominator term of eq. 4.9, leading to an underestimation of f_{NC} .

Although the calculated f_{NC} slightly underestimates the fitted one, we use it to solve the Bruggeman formula. Thus, as illustrated in Figure 4.6, the eq. 4.8 becomes exempt from any variables, i.e. ϵ'_h is known from the previous fit and applied as long as the surface chemistry is unchanged, $\tilde{\epsilon}_{NC}$ and f_{NC} are calculated by ETBM, and HSM, respectively. Figure 4.3 reveals that the optical indices using the Bruggeman equation exempt from free parameters are in good accordance with experimental measurements over the spectral range. This method offers spectral features, especially the first excitonic peak but also higher-energy peaks, in reasonable agreement with experiments. The agreement is also confirmed in Figure 4.5b with the average refractive index, and Figure 4.5d corresponding to the value of the extinction coefficient at the first excitonic peak.

In summary of this subsection, we have provided proof that by combining EMA models and electronic structure calculations, film parameters such as the NC volume fraction can be estimated. Furthermore, incorporating the analytical HSM and utilizing known ligand optical indices and length, a parameters-free model (see Figure 4.6) enables direct calculation of the film optical index. Thereafter, we aim to

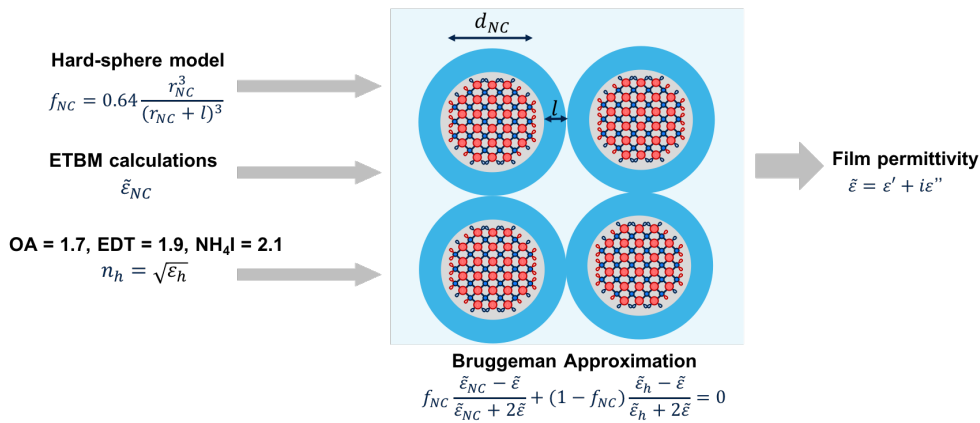


Figure 4.6: Scheme of the calculations in the Bruggeman approximation. We compute the volume fraction f_{NC} via the HSM, and the NC complex dielectric function $\epsilon_{\tilde{NC}}$ by ETBM. Assuming the host refractive index n_h to be similar for equivalent surface chemistries (OA, EDT, and NH₄I), we use n_h obtained in Ref. [29].

use this model to reveal the absorption properties of a diode stack used for SWIR sensing.

4.3.3 Device simulations

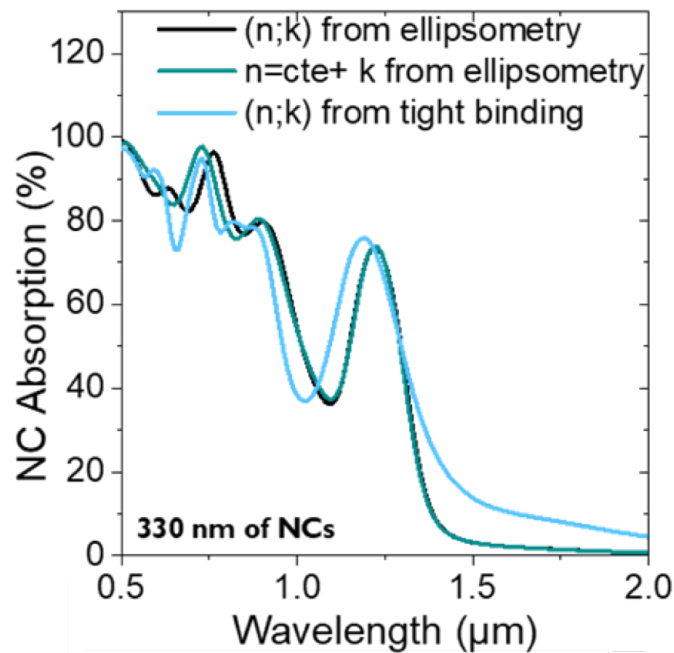


Figure 4.7: Absorption spectra within the NC layer for a diode stack composed of glass/ITO(190 nm)/TiO₂(120 nm)/PbS (n-type, with PbS 1200 capped by NH₄I), PbS (p-type, with PbS 1200 capped with EDT)/Au (80 nm).

In Figure 4.7, absorption spectra were simulated by our collaborators for a typical diode stack [241, 242] made of glass/ITO (190 nm)/TiO₂(120 nm)/PbS (n-type, with PbS 1200 capped by NH₄I), PbS (p-type, with PbS 1200 capped with EDT)/Au (80 nm). The electromagnetic simulations were performed using a frequency-domain

modal method known as the Rigorous Coupled Wave Analysis (RCWA), implemented into RETICOLO [243], a code written in MATLAB language. 100 Fourier orders were chosen for the calculation. Furthermore, we input the complex refractive index of each layer. For the ITO [236], the TiO_2 [241], and the gold [244], we used the previously reported refractive index. Concerning the NC layer, we first used the SE data. We have observed that the spectral dependence of the refractive index is less significant compared to that of the extinction coefficient. This was confirmed in Figure 4.7, where the absorption spectra remain mostly unaltered when accounting for the entire spectral dependence or using the average spectral value of n . This observation has the potential to simplify future measurements, as spectrally resolved measurements of the refractive index may not be required unless precise simulations are necessary.

In addition, we have simulated the absorption spectrum of the diode stack using the (n, k) values obtained directly from the parameter-free Bruggeman equation. It indicates that coupling ETBM calculations, Bruggeman, and hard-sphere models can be used for the scaling rule of design.

4.4 Mercury telluride: shape effect

We have shown in the previous section how the size and surface chemistry influence the optical properties of a NC layer. Hereinafter, we will study the impact of the shape with HgTe NC layers. The main results of this section have been published in [40]. The NC synthesis and SE characterization below were performed by the E.Lhuillier group. HgTe NCs with spherical, rod, and planar tripod shapes present a bandgap ranging from 1700 nm to 2220 nm. Theoretically, following a methodology already validated in the case of PbS NCs [29], we calculate the complex optical index of the NCs from their electronic structure using ETBM, then we inject it into the Bruggeman formula eq. 4.8 to deduce the complex optical index of a NC layer.

4.4.1 Synthesis and characterization

Synthesis We study HgTe NCs of three different shapes, that is sphere-, rod- and planar tripod-shaped NCs. Their synthesis follow the same backbone i.e. mercury halide (HgX_2) reacts with the Te complex and trioctylphosphine (TOP:Te) in a mixture of a coordinating solvent (OLA). The rod- and tripod-shaped NCs use HgCl_2 with a reaction time of 3 min. Their difference lies in the reaction temperature of 58° , and 82° for the latter and for the former, respectively. Concerning the spherical NCs, HgBr_2 is used with a temperature of 110°C and a reaction time of 30 s. The three types of NCs are capped by dodecanethiol (DDT) molecules. To produce a photoconductive thin film, an ink is made in which the NCs are passivated by a combination of short thiol (mercaptoethanol) and HgCl_2 [245, 246]. Finally, homogeneous layers between 100 nm and 200 nm thick are obtained by spin-coating the ink on a glass substrate at 4000 rpm for 30 s.

SE The complex optical index of the films was acquired by SE using a model of multiple oscillators. As described for PbS NC layers, the model parameters are fitted to minimize the error between the calculated and measured angles (Δ, Φ) at three incidence angles: 50° , 60° , and 70° .

4.4.2 ETBM-EMA model

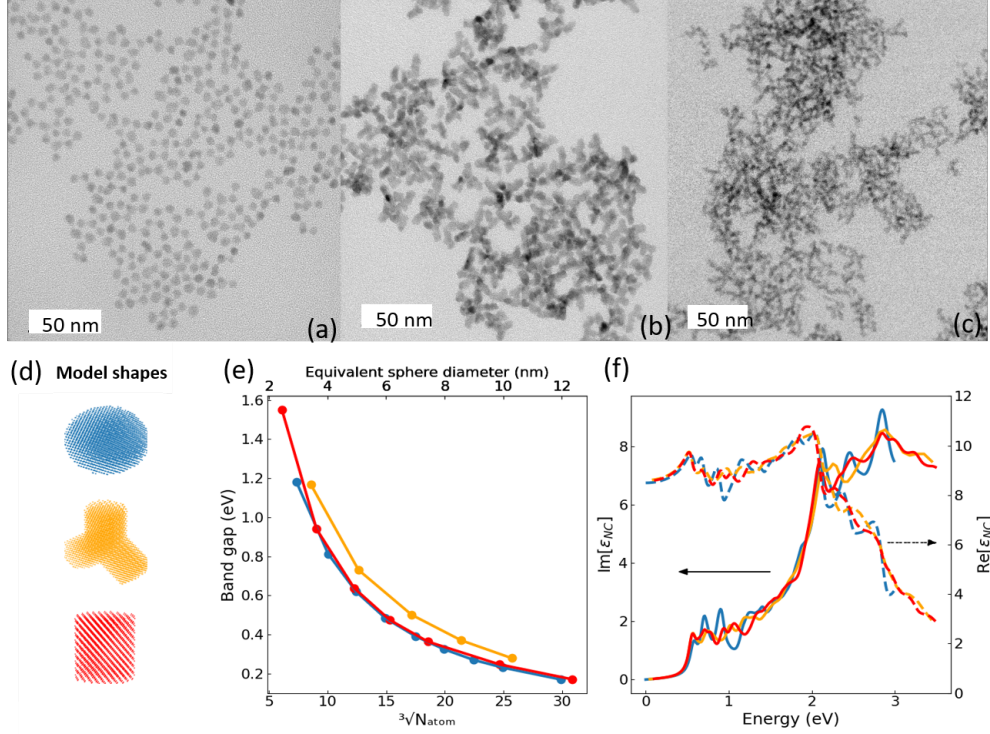


Figure 4.8: TEM images of HgTe NCs with (a) sphere, (b) planar tripod, and (c) rod shape NCs. (d) NCs model used to compute (e) the bandgap energy of the NCs according to the cube root of the number of semiconductor atoms, and (f) the complex dielectric function (solid line for real part; dashed line for imaginary part) versus photon energy for the three different geometries: sphere (blue), rod (red) and tripod (orange). We used ETBM for the calculations in (e) and (f). The rod and tripod shapes present an aspect ratio of 1.26 in (d). In (e) equivalent sphere diameter = $a_{cell} \sqrt[3]{\frac{3N_{atom}}{4\pi}}$.

ETBM To theoretically investigate the shape effect on the optical properties of HgTe NC layers, we construct the model NC (used for ETBM calculations) via the information extracted from TEM images (Figure 4.8a-c) which reveal that the three samples are made-off sphere-, rod-, and planar tripod-shaped NCs, respectively.

Concerning the rods, the aspect ratio is small (i.e. < 3). Moreover, the ETBM calculations predict optical indices $\epsilon_{\tilde{N}C}$ very close to those of spheres (Figure 4.8f). This similitude would be likely enhanced within the layer with the random orientation of the rods.

For the tripods [247], we constructed three connected rods lying in the same plane and making an angle of 120° between them (Figure 4.8d). From the TEM analysis (Figure 4.8b), we fix the aspect ratio of each cylinder to 1.26. We performed these measurements on a tripod clearly visible in the TEM observation plane. Although this ratio is approximately met for other tripods, it is difficult to guarantee that it is the precise average value for all NCs of the layer. However, as illustrated in Figure 4.8f, the shape has a weak influence on $\epsilon_{\tilde{N}C}$, especially at high energy (> 1.5 eV).

	Sphere	Tripod	Rod
Exp. first excitonic peak (nm)	2000	2200	1700
Number of atoms (in ETBM)	3742	3869	1433
Volume fraction f_{NC}	53%(41%*)	39%	46%
Host refractive index ($\sqrt{\epsilon_h}$)	1.94(1.92)	1.74	1.84

Table 4.1: Primary characteristics from the three studied HgTe NC samples. The excitonic peak is extracted from the SE spectra (k in Figure 4.9). We indicate the number of atoms in the NCs used for ETBM calculations (see Figure 4.8d). We obtained the volume fraction and host refractive index by fitting the film optical indices (see eq. 4.8) in order to reproduce measured data on Figure 4.9.

To compute $\epsilon_{\tilde{NC}}$, for the three samples, we fixed the broadening energy at 50 meV, which corresponds to 8.5% of size dispersity for the spherical NCs. Even if size and shape distributions are not known, it is a typical dispersity value for HgTe NC synthesis [39].

Concerning the NC size, we use the sizing curve of Figure 4.8d in order to have the theoretical bandgap in agreement with the experimental value (Table 4.1). However, as shown in the previous Chapter, when the NC size increase the second peak becomes dominant over the first peak, and depending on the broadening the two peaks can finally merge. This effect appears with the SE data of the spherical NCs. Therefore, for this sample, we calibrated the size of the NCs in order to have the second ETBM transition energy in agreement with the experimental value.

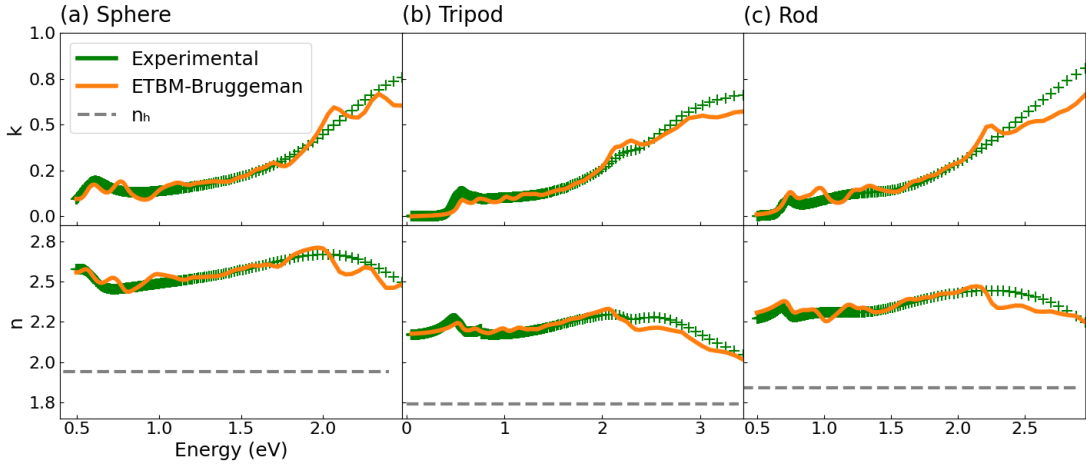


Figure 4.9: Extinction coefficient (k), and refractive index (n) of HgTe NC layers presenting (a) spherical, (b) tripod, and (c) rod shape. We compare theoretical calculations (full orange lines) combining ETBM and Bruggeman model with SE measurements (green crosses). The grey dashed line gives the host refractive index n_h .

EMA In line with our work on PbS NC layers (see previous section), we solved the effective permittivity $\tilde{\epsilon}$ of HgTe NC layers from the Bruggeman formula eq. 4.8 by fitting f_{NC} and ϵ_h on the experimental data. In this case, the fitting procedure has been applied to the high energy range, after the first excitonic peaks. In this

domain of energy, $\epsilon_{\tilde{N}C}$ is weakly dependent on the shape (Figure 4.8f) and the size dispersion [21]. Both the real and imaginary parts of the spectra show excellent agreement between theory and experiment. However, the measured spectra appear to be less structured than the calculated spectra, which may be due to the presence of an inhomogeneous distribution in size and shape of the NCs, as suggested by Rastogi et al. [248].

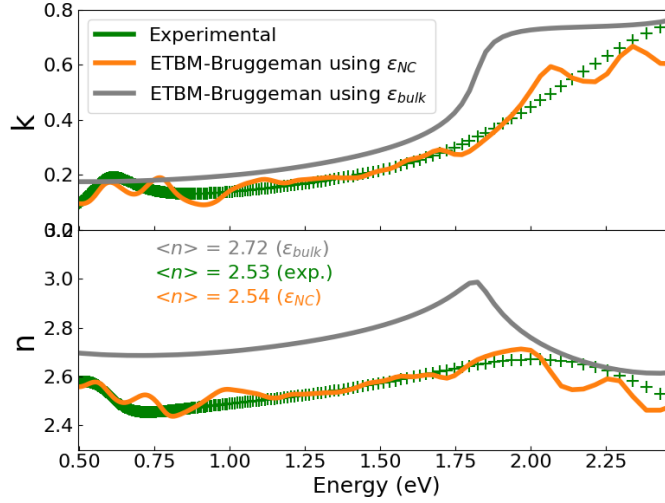


Figure 4.10: Extinction coefficient (k), and refractive index (n) of HgTe NC layers. We compare the theoretical indices (orange solid lines) obtained by combining ETBM calculation with Bruggeman approximation (see eq. 4.8) to ellipsometry measurements (green crosses). The grey solid line gives the results of the calculations in which $\epsilon_{\tilde{N}C}$ is replaced by the bulk value ϵ_{bulk} while conserving the set of parameters extracted with $\epsilon_{\tilde{N}C}$ (i.e. $\epsilon_h = \sqrt{1.94}$ and $f_{NC} = 53\%$). $\langle n \rangle$ is the average of n over the energy range.

The values obtained from the fit are recalled in Table 4.1. The spherical NCs present the highest volume fraction f_{NC} , corresponding to a value of 53%. This result, in regard to the hard-sphere model (see eq. 4.9), was expected. Hudson et al. [38] showed that monodisperse HgTe spheres formed well-ordered superlattices maximizing their packing density. Thus, combining a large volume of semiconductor (r_{NC}^3) and a high PF, the spherical NCs lead to layers with important NC volume fraction, hence strong optical activity. Considering a ligand length of 0.5 nm and a PF of 64%, we can use the HSM to compute f_{NC} . We obtain a value of 41% underestimating the fitted one. This result is in accordance with what we found for PbS NC layers. Furthermore, it is interesting to see that the fitted refractive index of 1.94 for the host medium (ligands, void, and impurities) is close to the one found for PbS NC layer with the EDT passivation. It is worth noticing because $\tilde{\epsilon}$ calculated by ETBM for HgTe was in close agreement with the experimental data (see previous Chapter). Thus, this high refractive index would more likely originate from the polarizability of dipoles at the NC-ligand interface.

Regarding the rods, we extract a NC volume fraction 7% smaller than for the spheres. Two explanations could be evoked. The first and simpler is that the rods are smaller compared to the spheres counterpart. Another explanation could be due to a smaller PF. But, even if spherical particles tend to pack more efficiently [249], since the rods present a low aspect ratio, we expect a weak difference in PF. Still,

we can observe a smaller host refractive index that could indicate a smaller PF and a less efficient passivation.

Among the three samples, the tripods present the lower volume fraction. This likely results from a greater difficulty to form dense layers in the case of complex shapes. It also corroborates with the drop of n_h .

For comparison, we incorporated the bulk permittivity ϵ_{bulk}^{\sim} into the Bruggeman formula using the parameters obtained for the spherical NC sample ($\epsilon_h = \sqrt{1.94}$ and $f_{NC} = 53\%$). However, as shown in Figure 4.10, this led to an overestimation of the complex optical index, particularly the real part, compared to the experimental data. This outcome was not surprising given that we had previously observed a significant reduction in ϵ_{NC}^{\sim} relative to ϵ_{bulk}^{\sim} . In addition, when we attempt to fit f_{NC} and ϵ_h to obtain the best agreement with experimental data while using ϵ_{bulk}^{\sim} , we end up with a much smaller NC volume fraction ($f_{NC} = 41\%$).

The results presented here reinforced the interest in combining electronic structure calculations (like ETBM) with effective medium theories of the Bruggeman-type [29]. They also confirm the ability of ETBM-EMA calculations to predict the optical properties of semiconductor NCs over a wide energy range. These types of combined studies give access to the NC volume fraction, an important quantity to characterize not only because it impacts the quality of the film and the efficiency of its optical response, but also because its electrical properties are strongly correlated to the compactness of the film. We have shown that the volume fraction could be largely tuned by the NC size, ligand length, and NC shape. This can be used to enhance the carrier mobility by allowing a higher packing density in the layer [250].

4.5 Conclusion

To design efficient devices working in the IR requires an optimized harvesting of the incident photon. In this context, we conducted a comprehensive study of the effect of the surface chemistry, shape, and size of the NC layer. For this, we developed a joint model combining ETBM calculation with Bruggeman approximation, namely the ETBM-EMA model. To cover the broader wavelength as possible, we have chosen among the two most compelling NC materials in the SWIR, namely lead and mercury chalcogenides.

Concerning lead sulfide NCs, we use the ETBM-EMA model with SE measurements to extract essential parameters of NC layers, such as the NC volume fraction and the refractive index of the host. We show how the size and surface chemistry impact the NC layer optical properties. Adding another layer of theory with the hard-sphere model, we are able to calculate the effective complex dielectric function of a NC layer $\tilde{\epsilon}$ without fitting parameters. We use this procedure to inject $\tilde{\epsilon}$ into the electromagnetism simulations of the diode stack and predict photonic device performance. This theoretical procedure could guide new experimental works and industrial development.

We applied the same methodology to mercury telluride to study the influence of the shape on the layer optical properties. Our findings suggest that layers composed of spherical NCs exhibit the highest density. We estimated the NC volume fraction at more than 50%, in good accordance with a random assembly of hard spheres capped with 0.3 nm-long ligands. In contrast, samples containing tripod-shaped NCs are comparatively less dense and exhibit lower values of both the real part

(refractive index) and the imaginary part (extinction coefficient) of the refractive index.

This validated joint model (ETBM-EMA) will be applied to various semiconductors in the following Chapter. We believe that these insights are of great importance on the road to designing more efficient optical devices.

Chapter 5

Optical performances: material comparison

5.1 Introduction

As discussed in Chapter 2, the advantage of the ETBM over ab initio methods is the ability to study large systems in a reduced amount of time. Furthermore, we showed in the previous Chapters that ETBM quite accurately describes electronic structures, and also optical properties such as the complex dielectric function of PbS and HgTe NCs. In this Chapter, we extend this study to various semiconductor materials (PbSe, InAs, InSb, InP, and CdSe) to provide a bottom-up comparison of the optical properties from a single NC to NC layer until the photodiode stack. The comparison is performed for the first absorption peak. The method is represented in Figure 5.1.

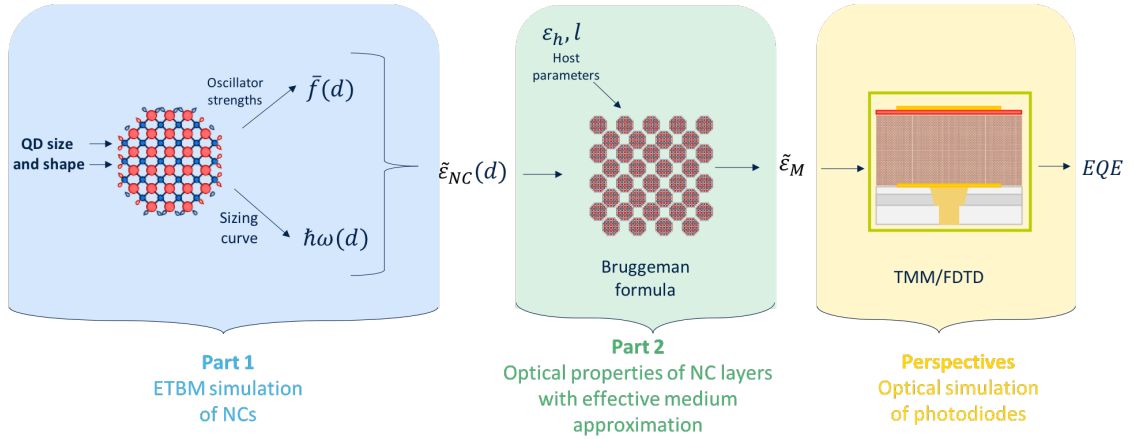


Figure 5.1: Scheme of the simulation process described in the Chapter.

In section 5.2, we provide an analytic compact model which is physically-driven and accurately predicts the optical performances of NCs, as functions of materials, and NC size. It allows us to construct an abacus of intrinsic parameters, extracted from ETBM simulation, and describes the variation of the total oscillator strength (\bar{f}_1), peak maximum position ($\hbar\omega_1$), and NC absorption (ϵ''_{NC}) versus NC size for the first excitonic peak.

In section 5.3, we extend the model to solid NC layers, by injecting ϵ''_{NC} into

Bruggeman approximation. We study the influence of the different layer parameters (such as ligand length l and host refractive index ϵ_h) and unveil optimum values maximizing the optical performances of the layers.

Finally, in section 5.4, we employ the Transfer Matrix Method (TMM) to compute the performance of photodiode stacks by examining the external quantum efficiency (EQE).

5.2 Single nanocrystal performances

This Chapter focuses on the optical properties at low energy. Therefore, we used the Jacobi-Davidson algorithm, which enables partial diagonalization of the Hamiltonian [251] to accurately compute electronic states close to the gap and allows the simulation of large NCs at low simulation cost. Thus, for numerous semiconductors, we obtain a polynomial equation of $\hbar\omega_1$ and \bar{f}_1 according to the NC size. The results are recapped in Table 5.1, and are used as inputs into two analytical equations of ϵ''_{NC} (which will be described later).

Methods To theoretically obtain $\hbar\omega_1$ with the NC size, it is usual to extract it from the electronic structure by $\hbar\omega_1 = LUMO - HOMO$. However, the experimental value is mainly obtained by taking the photon energy at the maximum of the first peak. Thus, the theoretical $\hbar\omega_1$ might deviate from the experimental due to two main reasons: (i) the difference between optical and electronic bandgap, due to excitonic effects (which are, as discussed in the previous Chapters, very small in PbS and HgTe, but can be important in large bandgap materials such as CdSe) and (ii) the extraction procedure.

Hence, to tackle (i), we took into account the excitonic effect for each of them using the following formula [27]:

$$E_{xc} = -E_{eh} + 2E_{se} \quad (5.1)$$

where E_{eh} is the electron-hole interaction, and E_{se} is the self-energy. As a NC usually presents a dielectric mismatch at its interface with the medium ($\epsilon_{NC} - \epsilon_h$), the charges (electron or hole) will form polarization charges at the interface. It is what the self-interaction accounts for, and writes [27]:

$$E_{se} = \frac{q^2}{4\pi\epsilon_0 d_{NC}} \frac{\epsilon_{NC} - \epsilon_h}{\epsilon_{NC}[\epsilon_{NC} + \epsilon_h]} \left(\frac{\epsilon_{NC} + \epsilon_h}{\epsilon_h} + 0.933 - 0.376 \frac{\epsilon_h}{\epsilon_{NC} + \epsilon_h} \right) \quad (5.2)$$

where d_{NC} corresponds to the NC diameter. We fixed ϵ_{NC} to the real part of the bulk value (see Table 5.1), and ϵ_h to the permittivity of the hexane ($=2$), often used for dispersed PbS NCs in colloidal solution. The electron-hole interaction E_{eh} includes a Coulombic term due to direct interaction between the charges and an interaction term between one of the charges and the polarized charges of the others [27]:

$$E_{eh} = 1.79 \frac{q^2}{2\pi\epsilon_0\epsilon_{NC}d_{NC}} + \frac{q^2(\epsilon_{NC} - \epsilon_h)}{2\pi\epsilon_0\epsilon_{NC}\epsilon_h d_{NC}} \quad (5.3)$$

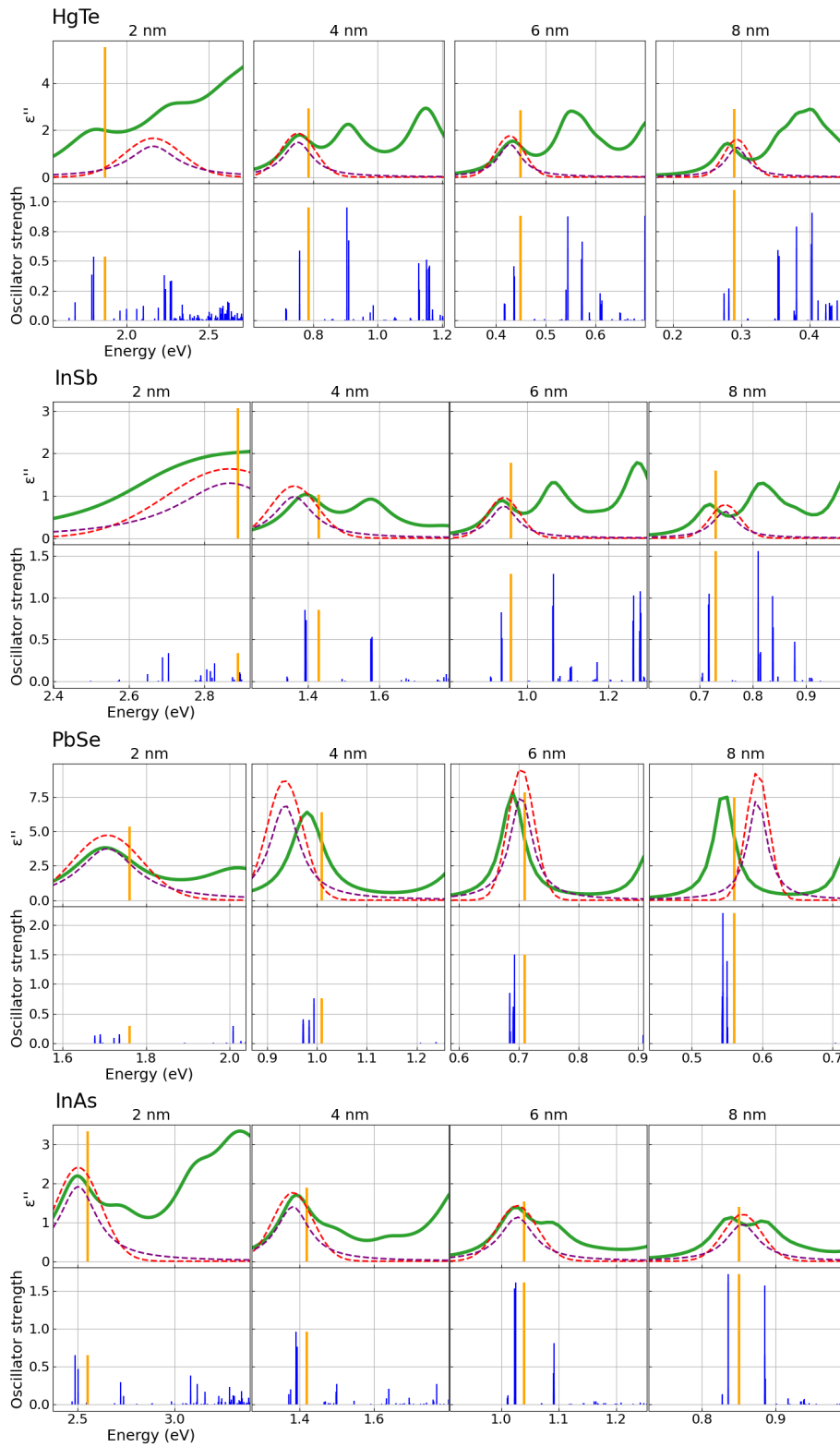
This formula shows to be in remarkable accordance with ab initio calculations for PbS [143]. Then we corrected the single particle electronic structure computed by

ETBM by adding E_{xc} to the conduction band energy, and calculated the absorption spectra for NC size of 2, 4, 6, and 8 nm (see Figure 5.2, green solid line).

Thus, from these spectra, we extracted the maximum absorption peak position to tackle (ii), and used it to fit the following model:

$$\hbar\omega_1(d) = \hbar\omega_{1,0} + \frac{\hbar\omega_{1,1}}{d} + \frac{\hbar\omega_{1,2}}{d^2}. \quad (5.4)$$

The obtained parameters $\hbar\omega_{1,0}$, $\hbar\omega_{1,1}$, and $\hbar\omega_{1,2}$ for each of the semiconductor are given in Table 5.1. Those have been finally used to plot $\hbar\omega_1$ according to the NC size (d) in Figure 5.3a.



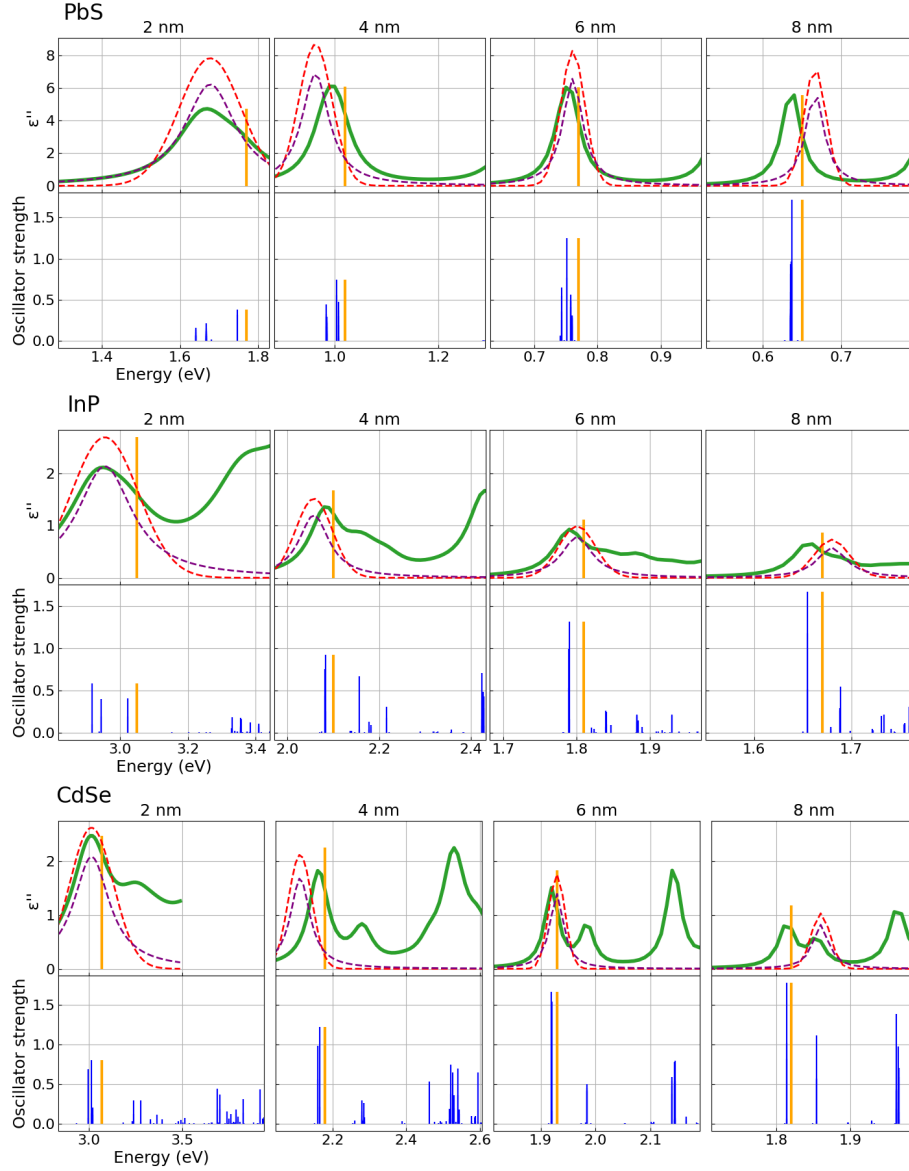


Figure 5.2: Presented on two pages. Each panel corresponds to a semiconductor denoted at the upper left. For each one, we give the imaginary part of the complex dielectric function with excitonic correction (green solid line), and corresponding oscillator strengths computed by ETBM (blue vertical lines). The red dashed line corresponds to the analytical formula eq. 5.6, and the purple dashed line to eq. 5.7 for the first absorption peak. The orange vertical line corresponds to ϵ_{lim} (see text for details). The diameter of the NCs is indicated above each panel.

Concerning \bar{f}_1 , we also used the computed absorption spectra (see Figure 5.2). The latter depends on the size dispersity through the broadening energy σ (see Chapter 3). Since we want to evaluate the theoretical best optical performances, we fixed the size dispersity at 5%, which is a state-of-the-art value. We know that an absorption peak is made of different transition energies ϵ_i and corresponds to different oscillator strength f_i (see blue vertical lines in Figure 5.2). Thus to obtain the total oscillator strength \bar{f}_1 at the first excitonic peak, we need to select the transitions of energy ϵ_i which enter into the sum $\bar{f}_1 = \sum_i f_i$. Since we are interested in the first peak, the energies will spread from 0 eV to a limit value ϵ_{lim} . We define ϵ_{lim} as the second inflection point, represented by the orange vertical line in Figure 5.2. This choice enables us to have a consistent approach for extracting \bar{f}_1 with the four NC sizes and for all semiconductors. We used the calculated \bar{f}_1 to fit the following model:

$$\bar{f}_1(d) = \bar{f}_{1,0} + \bar{f}_{1,1}d \quad (5.5)$$

Again, the obtained parameters $\bar{f}_{1,0}$, and $\bar{f}_{1,1}$ for each of the semiconductors are given in Table 5.1, and used to plot \bar{f}_1 according to the NC size in Figure 5.3b.

	ϵ_{bulk}	$\hbar\omega_1$			\bar{f}_1		ETBM parameters
		$\hbar\omega_{1,0}$	$\hbar\omega_{1,1}$	$\hbar\omega_{1,2}$	$\bar{f}_{1,0}$	$\bar{f}_{1,1}$	
HgTe	9*	0	1.69	5.27	3.10	-0.04	[36]
InSb	15.7	0.23	3.77	3.01	3.40	0.22	[252]
PbSe	23	0.28	2.39	0.93	-4.9	4.07	[170]
InAs	12.3	0.35	3.95	0.71	1.80	0.82	[169]
PbS	17	0.41	1.89	1.29	-0.2	2.65	[29]
InP	9.6	1.35	2.45	1.52	2.8	0.51	[169]
CdSe	6.2	1.74	0.43	4.24	3.4	0.54	[253]

Table 5.1: Fitted parameters obtained from ETBM calculation for each semiconductor. $\hbar\omega_1$ variation with the NC size d : $\hbar\omega_{1,0} + \hbar\omega_{1,1}/d + \hbar\omega_{1,2}/d^2$, and \bar{f}_1 with the NC size d : $\bar{f}_{1,0} + \bar{f}_{1,1}d$. The references of the ETBM parameters are given in the last column. We also give the bulk permittivity ϵ_{bulk} , which replaces ϵ'_{NC} in the Bruggeman equation. *we choose this value according to the work of Chapter 4.

Finally, we can inject \bar{f}_1 and $\hbar\omega_1$ relations with the NC size into the analytical equation of ϵ''_{NC} (see Chapter 3):

$$\epsilon''_{NC}(\omega, d) = \frac{1.65\bar{f}_1(d)}{d^3\hbar\omega_1(d)\sigma(d)} e^{-\frac{(\hbar\omega - \hbar\omega_1(d))^2}{2\sigma^2(d)}} \quad (5.6)$$

However, we noticed that ϵ''_{NC} of PbS and PbSe are better described by a Lorentzian distribution:

$$\epsilon''_{NC}(\omega, d) = \frac{1.31\bar{f}_1(d)}{d^3\hbar\omega_1(d)} \left[\frac{1}{1 + \left(\frac{\hbar\omega - \hbar\omega_1(d)}{\sigma}\right)^2} \right] \quad (5.7)$$

We believe that is a consequence of the high degeneracy of L valley and of intervalley splittings induced by the confinement in NCs (see Chapter 2). The results of the eqs. 5.6, and 5.7 are represented in Figure 5.2 by the dashed red and purple lines, respectively. We can appreciate the good accordance between the first peak computed analytically and by ETBM. This enables the interpolation of the low

energy range spectrum for any NC size ranging from 2 to 8 nm. The maximum of $\epsilon''_{NC}(\omega)$ is obtained when $\hbar\omega = \hbar\omega_1$ and is plotted as a function of NC size (or equivalently, the operation wavelength $\hbar\omega_1$) in Figure 5.3c.

Discussion For this study, we choose to study mainly narrow gap semiconductors for applications at infrared wavelengths such as PbS, PbSe, HgTe, InSb, and InAs. The two latter are part of the III-V family and are seen as alternatives for Pb and Hg replacements due to their known toxicity [7, 254]. InAs (InSb) exhibits a broad-range photo response from visible to SWIR (see Figure 5.3a). However, In-based NCs show lower optical performance (see Figures 5.3c) and still suffer from their high-polydispersity and poor surface passivation [255, 256].

We also choose two semiconductors mainly used in the visible range (Figure 5.3a), namely CdSe and InP. Cd-based NCs enjoy to be one of the most investigated NCs and are therefore highly optimized in terms of synthesis and passivation [71]. They present high photoluminescence efficiency, and narrow emission linewidths [257] but Cd is highly toxic [258]. InP of the III-V family is one the prominent candidate to replace Cd-based NCs [256]. Although the properties of InP are still insufficient, the development of new synthetic routes has led to enhance optical properties, which paves the way for their potential use in various applications [75]. At any rate, we can see in Figure 5.3c that InP NCs present similar optical properties to CdSe but they can reach the NIR (see Figure 5.3a). Figure 5.3c also shows the formidable optical properties of lead chalcogenide NCs, which among high stability and earth-abundance, explained why they are widely used in device applications and are difficult to replace.

5.3 Nanocrystal layer performances

Methods In line with the work in Chapter 4, we use the Bruggeman model to extend the results from isolated NCs to layers of NCs. We remind below the Bruggeman formula for convenience:

$$0 = f_{NC} \frac{\tilde{\epsilon}_{NC} - \tilde{\epsilon}}{\tilde{\epsilon}_{NC} + 2\tilde{\epsilon}} + (1 - f_{NC}) \frac{\tilde{\epsilon}_h - \tilde{\epsilon}}{\tilde{\epsilon}_h + 2\tilde{\epsilon}} \quad (5.8)$$

We assume a HSM where the NCs are capped by a rigid shell representing the ligands, which allows us to compute the NC volume fraction as :

$$f_{NC} = PF \frac{r_{NC}^3}{(r_{NC} + l)^3} \quad (5.9)$$

where we assumed the NCs organized in a random close-packed distribution, which gives a packing fraction (PF) of 64% (for more details see Chapter 4). The assumption has shown good results [29] and is all the more valid as the ligand length is short. The imaginary part of ϵ_{NC} is extracted from the previous section while the real part is taken equal to the bulk one, except for HgTe for reasons detailed in Chapter 4 (see Table 5.1). Finally, since the ligands do not absorb at the wavelength studied, only $n_h = \sqrt{\epsilon'_h}$ is considered and fixed at 1.9, which corresponds to a mean value for EDT passivation according to the results of Chapter 4.

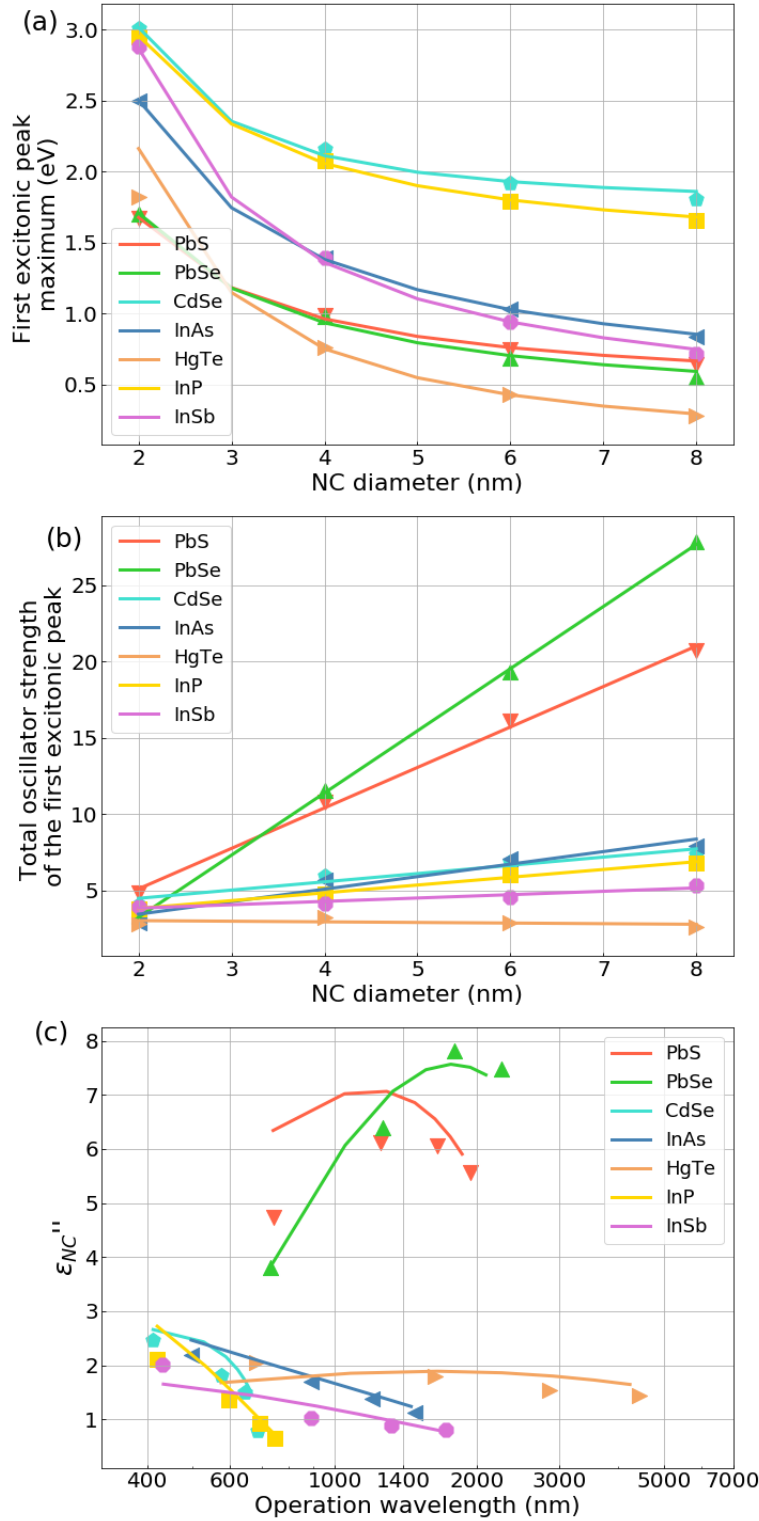


Figure 5.3: Analytical model with parameters from Table 5.1 (solid line) and ETBM calculation (symbols) for (a) $\hbar\omega_1$, (b) f_1 , and (c) $\epsilon''_{NC}(\omega_1)$ of the first excitonic peak according to the NC size. The analytical model of $\epsilon''_{NC}(\omega_1)$ for PbS and PbSe is calculated by the eq. 5.7, while we used eq. 5.6 for the other semiconductors. The operation wavelength corresponds to the wavelength of the first excitonic peak ($\hbar\omega = \hbar\omega_1$ in eq. 5.6).

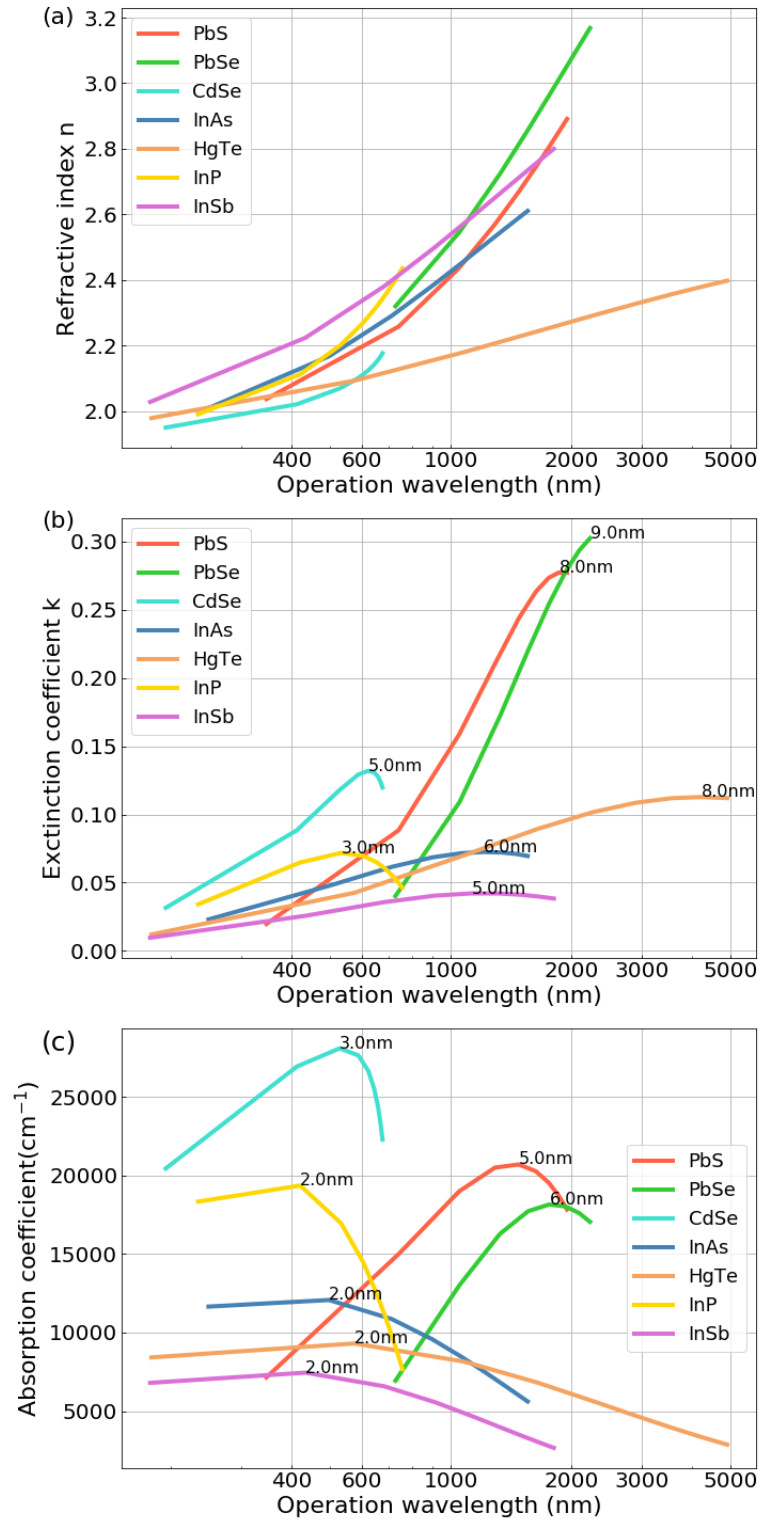


Figure 5.4: Bruggeman calculations of the (a) refractive index, (b) extinction coefficient, and (c) absorption coefficient of a NC layer. The host parameters are based on EDT-type found in Chapter 4, with a refractive index of 1.9, and a ligand length of 0.5 nm. To compute the NC volume fraction, we used a packing fraction of 64%, and a hard-sphere model (see Chapter 4). In Figures (b) and (c), the NC size maximizing the corresponding optical property are denoted.

Discussion Figures 5.4a,b, and c give the optical properties for a NC layer with 0.5 nm ligand length and a host refractive index of 1.9 (EDT-like). Although the intrinsic optical properties of InP and CdSe are close (see Figure 5.3), the latter seems to dominate the former in a NC layer (Figures 5.4b, and c). This is explained by the lower dielectric constant of bulk CdSe (6.2) compared to InP (9.6) which induces a stronger electric field into the NCs (see Table 5.1). Indeed, we can define the local field factor F such as the ratio between the external field \mathbf{E}_{out} and the resulting local field \mathbf{E}_{in} [27, 98]. If we assume a single NC in the host medium, the local field factor reads:

$$F = \frac{3\tilde{\epsilon}_h}{\epsilon_{\tilde{N}C}(\omega) + 2\tilde{\epsilon}_h} \quad (5.10)$$

As a result, the dielectric screening will reduce the local field inside a NC affecting the optical properties. In fact, in a very dilute system ($f_{NC} \ll 1$), ϵ'' of the composite system can be approximated from the Maxwell-Garnett formula as:

$$\epsilon'' = f_{NC}|F|^2\epsilon''_{NC} \quad (5.11)$$

Eq. 5.11 reveals that ϵ'' is not only proportional to the NC optical properties ϵ''_{NC} but also to the NC volume fraction f_{NC} and to the local field factor F . In the case where $\epsilon'_{NC} > \epsilon'_h$ (which is safe to assume), then the local field factor ($F < 1$, see eq. 5.10) will attenuate the absorption of the composite system. Moreover, F decreases with increasing ϵ'_{NC} , which explains that even if ϵ''_{NC} is similar for InP and CdSe, since $\epsilon'_{InP,bulk} > \epsilon'_{CdSe,bulk}$, then NC layer presents better optical performances for CdSe than InP (see eq. 5.11). On the other hand, eq. 5.10 shows that F increases with the permittivity of the host (ligand), thus it could be used as a tuning parameter to boost the optical performance.

Remarkably, the absorption coefficient α of CdSe reaches and even outperforms those of lead chalcogenides, which is not observed for the extinction coefficient k (see Figures 5.4b, and c). This can be understood from two related facts:

- α is inversely proportional to the wavelength λ .
- CdSe operates in UV-Visible while PbS(e) in IR.

Another striking feature in Figure 5.4c is the presence of a maximum reached for a given NC size. In fact, the latter impacts the NC volume fraction as $f_{NC} \propto d_{NC}$, and the intrinsic optical performances as $\epsilon''_{NC} \propto 1/d_{NC}$. Thus, an optimum NC size exists boosting the film absorption. The maxima are reached for different NC sizes according to the semiconductors. This is related to their ϵ''_{NC} -NC size relationship (see Figure 5.3c). As an example, $\epsilon''_{NC,CdSe}$ decreases faster with d_{NC} than for lead chalcogenides (see Figure 5.2), which for the latter, shifts the optimum at greater sizes.

Furthermore, this analytical model allows us to study the influence of the ligand length l on the optical properties (shown in Figure 5.5 for PbS NCs). The ligand length impacts the NC volume fraction. Indeed, shorter ligands lead to denser layers with improved absorption properties. For each ligand length, we extracted the optimal NC size corresponding to the size maximizing the absorption coefficient (dashed black line in Figure 5.11c). Thus, we can draw for the different semiconductors the optimal NC size according to the ligand length, shown in Figure 5.6a. This result indicates that if we are constrained by the ligand chemistry, specifically the ligand

length, which NC size will optimize the absorption performances. We also denote the NC volume fraction, which increases with the NC size and with decreasing ligand length.

For each set of parameters from Figure 5.6a (ligand length, NC size), we extracted the value of the absorption coefficient at the maximum of the first excitonic peak. This actually corresponds to the maximum theoretical absorption coefficient, which we draw according to the NC size or the operation wavelength in Figures 5.6b, and c. We found that for equivalent NC diameter, CdSe NC layer presents equivalent optical performances that lead chalcogenides, and outperformed the other semiconductors. This report while being not good environmental news where the best absorbing semiconductors are also the most toxic, gives understanding and directions for future development. It will be also valuable to evaluate them integrating in electronic device.

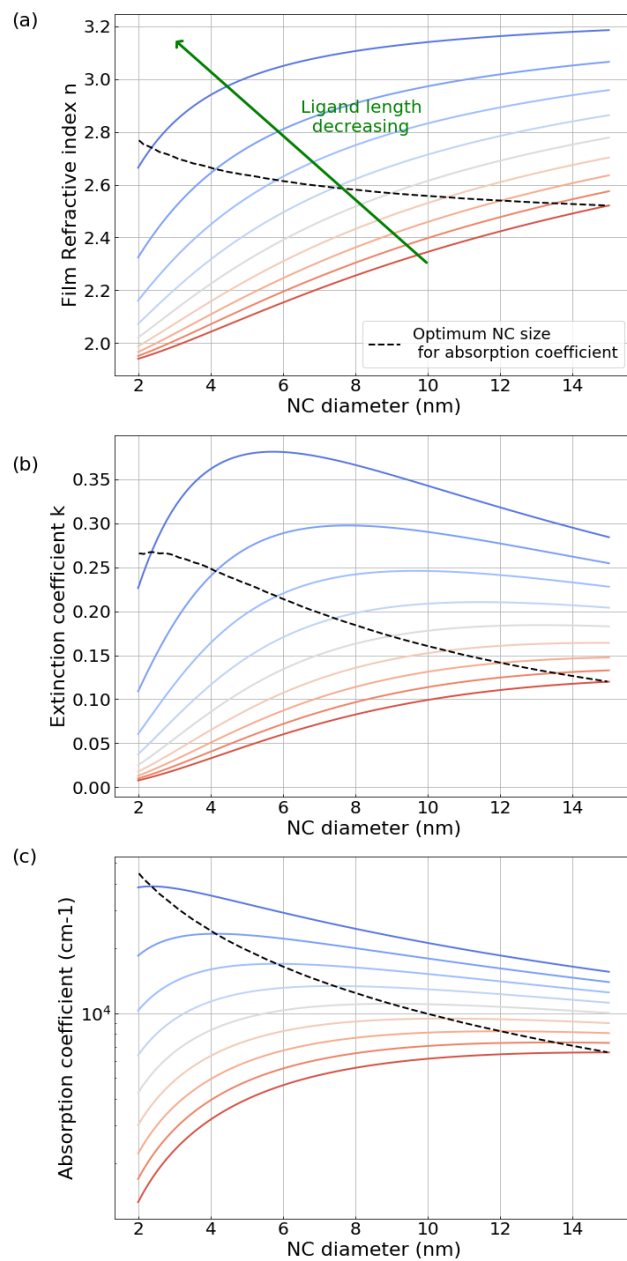


Figure 5.5: Effect of ligands on the (a) refractive index, (b) extinction coefficient, and (c) absorption coefficient of PbS NC layers. The ligand length is decreasing from 2 (red line) to 0.1 nm (blue line) [0.1, 0.34, 0.56, 0.81, 1.05, 1.29, 1.53, 1.76, 2.], while the refractive index is set at 1.9. The black dashed line corresponds to the NC size maximizing the absorption coefficient for a given ligand length.

5.3. NANOCRYSTAL LAYER PERFORMANCES

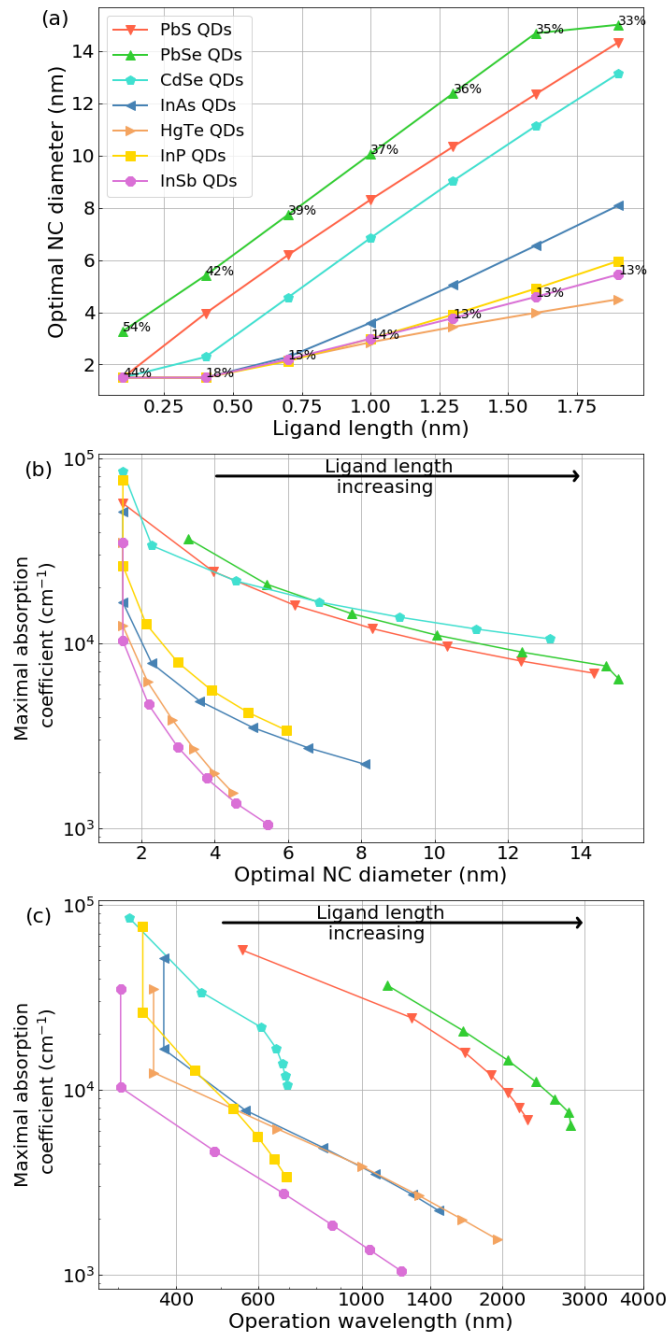


Figure 5.6: (a) NC size maximizing the absorption coefficient (named optimal NC diameter) for different ligand lengths (see Figure 5.5). The NC volume fractions calculated by the HSM are denoted. Maximal absorption coefficient according to (b) the optimal NC diameter and (c) the operation wavelength.

5.4 Photodiode performances

In the preceding section, we compared the theoretical optical performances of different semiconductors in the form of a NC layer. Concerning the small gap semiconductors, the lead chalcogenides outperformed the In-based NC layer in terms of optical absorption. Herein, we assess the theoretical performances of InAs and PbS when integrated into a simple stack of vertical photodiodes. As a figure of merit, we calculated the external quantum efficiency (EQE) via the transfer matrix method (TMM). The TMM is a well-known method to compute electromagnetic fields within a 1D stack, through the resolution of a matrix system describing the fields at the stack interfaces [259].

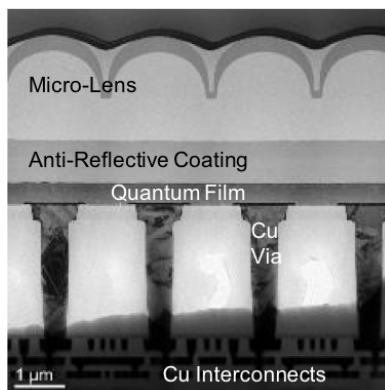


Figure 5.7: Illustration of a photodiode stack described in the text.

Methods The EQE is defined as the ratio of the number of charge carriers collected to the total number of incident photons, within the active layer of the device, in our case the NC layer. The simulated diode stack is made of SiON/Microlens/Anti-reflective coating / NC layer / Cu (see Figure 5.7 for illustration). We use TMM to extract the optical properties of the photodiode such as the light absorption. As inputs, it requires the complex optical indices of each layer. For SiON, microlens, anti-reflective coating, and Cu, we used reported indices. Regarding the NC layer, we took those obtained in the previous section. The structure of the diode was unchanged regardless of the type of semiconductor. This is a practical choice that allows direct comparison but can differ from realistic constraints (e.g. chemical compatibility or non-optimum band alignment). Figures 5.8a, and 5.8b depict the EQE maps of PbS and InAs NCs, respectively. The thickness of the NC layer was varied at different wavelengths, and the size of the NCs was adjusted to obtain their excitonic peak position at the incident light wavelengths.

Discussion The Figures 5.8a, and b reveal that the EQE increases with the thickness of the NC layer, which is expected because of the increasing absorbing materials.

The device optical system can also be optimized. Indeed, when the thickness of the NC layer is equal to an integer multiple of half of the wavelength of the incident light, a Fabry-Perot resonance effect occurs enhancing the absorption. This phenomenon is observed in Figure 5.8 with a series of resonances.

Finally, we present in Figure 5.9 the optical performances related to the excitonic peak. We simulated photodiodes without anti-reflective coating on top, with a 300

5.4. PHOTODIODE PERFORMANCES

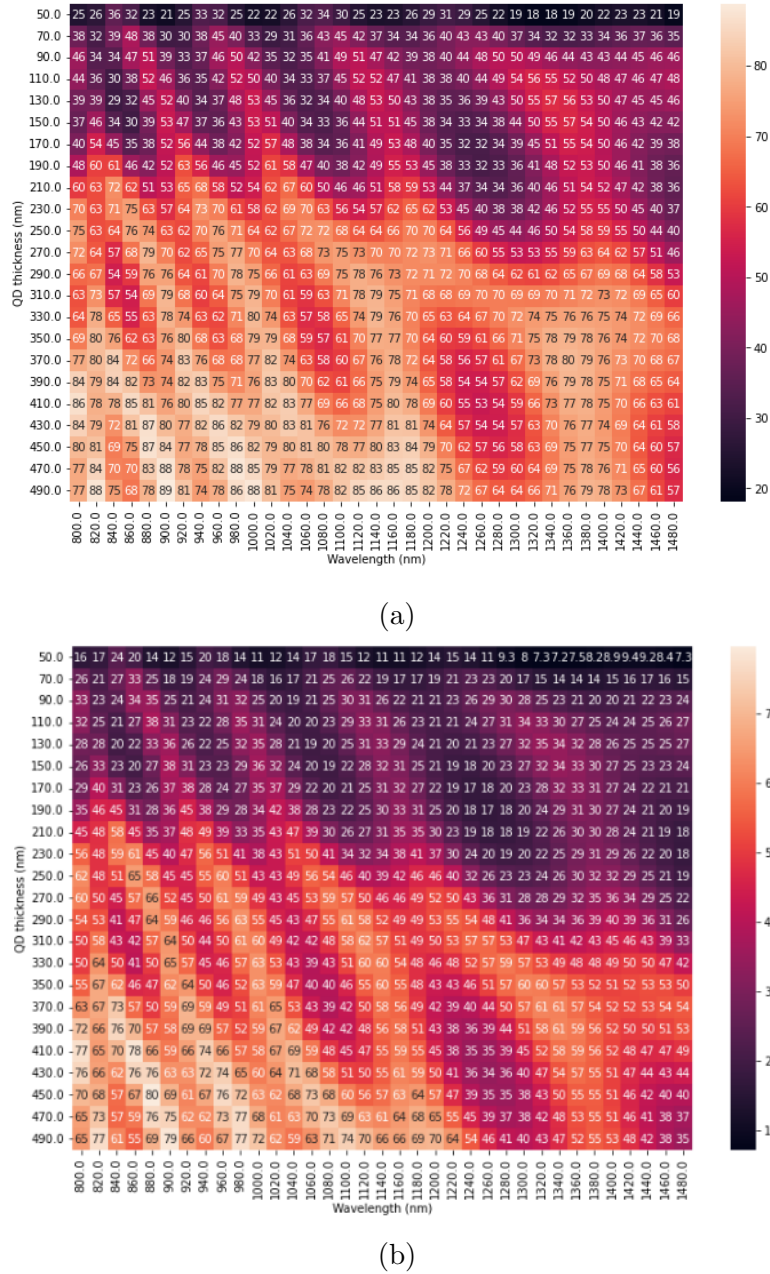


Figure 5.8: EQE maps assuming 5% size dispersion and ligand of length of 0.5 nm for (a) PbS, and (b) InAs NC layer.

nm NC layer thickness, NC polydispersity of 5%, and a ligand length of 0.5 nm. We adjusted the NC size to have the excitonic peaks at 940, 1130, and 1380 nm, corresponding to a spectral region with reduced solar background. This allows the development of electronic devices for active imaging. Specifically, we can see in Figure 5.9 that the EQE reaches values above 60% with a sharp transition, which enables a good rejection ratio of solar background. These results highlight the benefits of using photodiodes made of NC layers for active light systems in infrared applications.

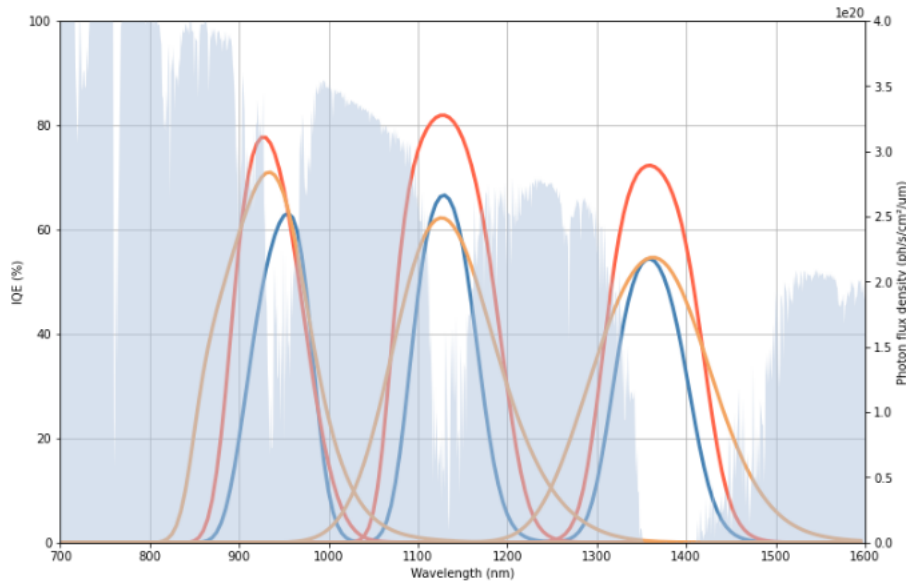


Figure 5.9: Performances of photodiodes at the excitonic peak wavelength, with a NC layer thickness of 300 nm for 5% size dispersion and 0.5 nm ligand length (solid red line: PbS, orange: InAs, and blue: HgTe). The solar background is represented in blue.

5.5 Conclusion

In this Chapter, we presented a methodology to predict the optical performances of NC-based photodiodes. We apply it for various semiconductors presenting applications from UV to IR: CdSe, InP, PbS, InAs, PbSe, InSb, and HgTe.

First, we studied the optical performance of isolated NCs. We have shown that lead chalcogenides dominate their In-based counterparts in terms of optical properties. Concerning visible applications, the benchmark CdSe NCs present a similar absorption coefficient to their potential substitute, namely InP. However, under a NC layer, CdSe NCs show stronger optical properties than InP. We reveal that this is a result of the lower refractive index of CdSe. We also investigate the role of different material parameters such as NC size, and ligand length over the performance of NC layer. Finally, we evaluate the NCs-based photodiode performances in terms of EQE, highlighting the interest in NCs for active imaging applications.

This model offers a valuable tool to predict technological advancements, which can be used in standard imaging applications such as hyperspectral imaging devices, among other applications. It is worth noticing, that this model has already been used for performance prediction on devices produced at STMicroelectronics and matches the expected values.

Chapter 6

Work function for device application

6.1 Introduction

Changing the identity of the chemical binding group and dipole moment of the ligand surrounding the NCs modifies the band edge energies in a NC layer [260, 144, 261, 236, 241, 262, 14, 53]. Thus, it opened the possibility of manipulation of bands in a NC layer but also band-alignment engineering at junctions or at the interface with electrodes. During the last decade, this enabled to strongly increase NC-based device performances, whether for LEDs [263, 264, 265], solar cells [266, 244, 24], or photodetectors [267, 268], by optimizing the charge transport into the NC layer and charge extraction by the contacts. Despite the tremendous work performed by researchers, numerous controversies and questions remain. Ligand effects are often decomposed into two contributions [52]: the intrinsic dipole of the ligand, and the induced dipole at the ligand/NC interface. Some authors attributed the induced dipole as the determining entity for the band-edge shift while they found no correlation with the intrinsic dipole [260, 144, 261]. However, more recent studies unveil a major contribution from the intrinsic dipole [269, 236, 14, 53]. The effect of the ligands on the bandgap is also controversial. Some authors found no effect [236, 260] whereas others show variation due to electronic delocalization [14], mixing orbitals between ligands and NCs [270], solvatochromicity [143], NC-NC interactions [271], or Stark effect [144]. Other effects on the work function are debated, such as the binding schemes of bidentate ligands, the effect of hybrid passivation, the self-ligand interaction, etc [53].

These questions are arduous to address due to the difficulty of modeling the NC with the surrounding ligands by *ab initio* methods in reason of the numerical cost. In this context, we will discuss the ongoing project to develop a model using ETBM and DFT calculations to evaluate the effect of ligands on the electronic structure. In terms, this model would allow us to study NCs of realistic size surrounded by dipoles. We would be able to study the effect of facets, shape, and size. We also ambition to conduct studies of mixed passivation e.g. one type of ligand for one type of facet or different ligands for one facet. These studies could allow us to bring answers to the preceding unknown questions.

6.2 State of art

Previous works showed that ligands at the surface of NCs can be assimilated as a dipole layer. Thus, surface chemistry became a tool to modify the NC electronic structure. For example, Chuang et al. [47] engineered the band alignment in PbS NC layers by the use of different capping ligands. They achieve a band offset of 0.19 eV between two PbS layers that allows optimization of the charge transport and charge extraction (see Figure 6.1a). These bi-layers of NCs have also been employed in photodetectors leading to faster light response, broader linear dynamic range, larger detectivity, and higher signal-to-noise ratio [267]. Yang et al. [48] used the tuning ability of the NC size and surface chemistry to construct an infrared LED with NC layers not only as active layers but also as charge transport layers (see Figure 6.1b). These recent achievements have been performed thanks to the capability of accurately measuring the NC electronic structure, and also via the fundamental understanding brought by theoretical calculations, specifically by DFT. In the following paragraphs, some experimental measurements and theoretical calculations of the effect of ligands on the electronic structure will be described.

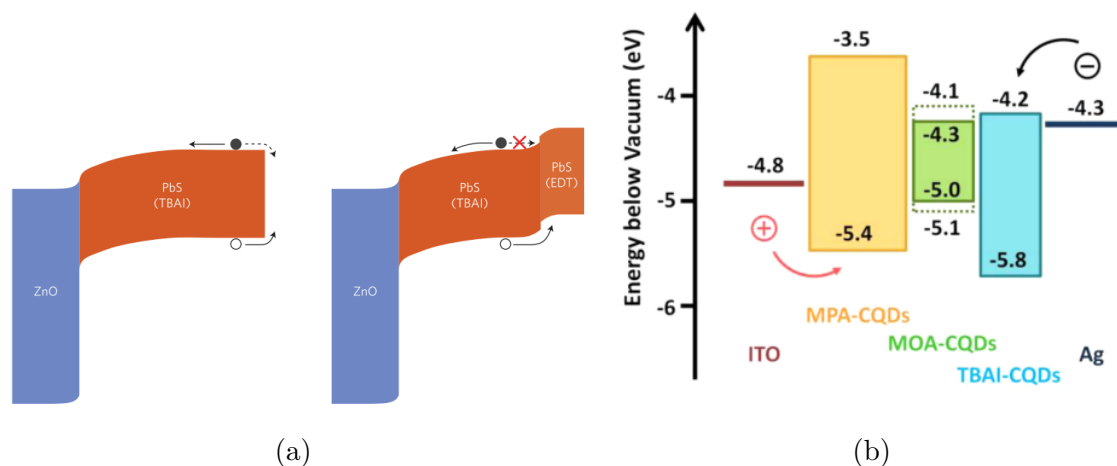


Figure 6.1: (a) Schematic illustration showing the band bending in ZnO/PbS-TBAI (on the left) and ZnO/PbS-TBAI/PbS-EDT (on the right). Reproduced from [47]. (b) The energy level diagram depicts an arrangement of infrared LEDs using NC layers. Within the active NC layer (MOA-CQDs), there are corresponding energy levels for NCs that emit at 1622nm (illustrated by a solid line) and 1220nm (represented by a broken line). Reproduced from [48].

6.2.1 Experimental measurements

The experimental determination of the electronic structure is often relative to the vacuum energy level ($E_{vac}(s)$). The latter is usually defined as the energy of an electron just above the surface of the sample. Thus, we can define the ionization energy (IE), the electron affinity (EA), and the work function (ϕ_m) as the energy separation of the HOMO, LUMO, and Fermi level (E_F) from $E_{vac}(s)$, respectively. The vacuum energy level as defined above is dependent on the solid surface. A good illustration has been given by Ishii et al. [49] with tungsten and the dependence of its work function on the crystalline surface (see Figure 6.2a). The different work

functions found at the different surfaces are in fact due to the modification of $E_{vac}(s)$, since the Fermi level is constant throughout the solid. The electronic surface dipole modifies the $E_{vac}(s)$, and thus the ϕ_m , IE, and AE. Indeed, a dipole layer will create a potential barrier that either drops or rises the vacuum energy level $E_{vac}(s)$ according to the dipole direction, as represented in Figure 6.2b.

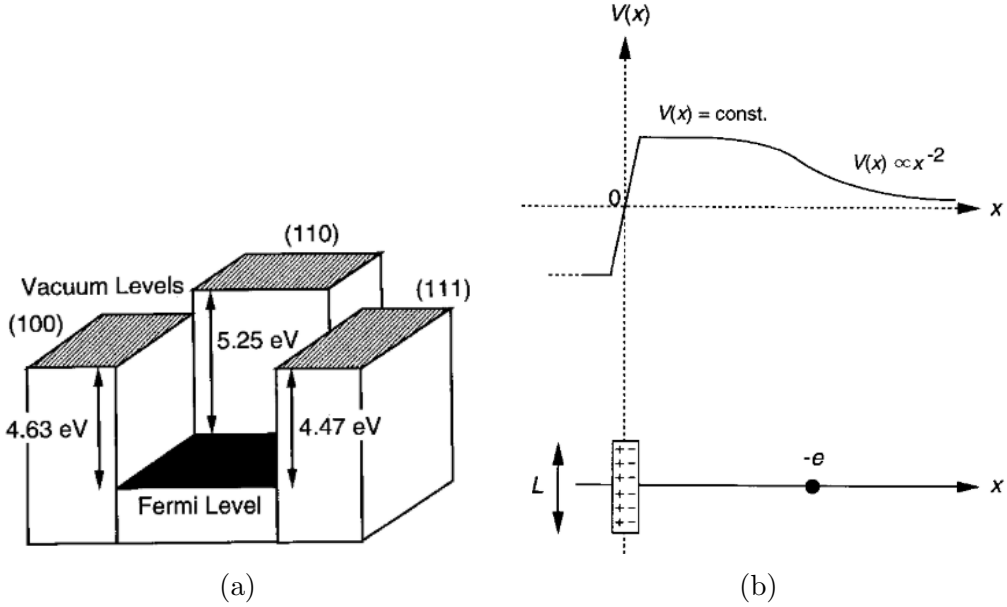


Figure 6.2: (a) Variation of the work function of a tungsten crystal with the different surfaces. (b) The lower panel illustrates a dipole layer of length extension L , and an electron at a distance x of the dipole layer. On the upper panel, the potential energy of the electron is shown in relation to the dipole layer. Reproduced from [49].

In Figure 6.2b, Ishii et al. explain that for an electron at a distance x from a dipole layer of finite extension (represented by a length L in the bottom panel), two cases appear: (i) for $x \ll L$, the dipole layer is seen as infinitely extended, and can be assimilated to a capacitor with potential energy as a step function across the dipole layer, and a potential constant at each side. (ii) For $x \gg L$, the dipole layer is seen as a point dipole, and the potential decrease as x^{-2} with the energy of free electron converging to vacuum level at infinity $E_{vac}(\infty)$. Thus, as the dipole layer extension L becomes smaller, the electron position has to be located at a closer distance from the surface, to be in case (i) of a capacitor. Since, the physical properties of interest (ϕ_m , IE, and EA) are defined according to vacuum level, we need to know which one between $E_{vac}(s)$ and $E_{vac}(\infty)$ is measured experimentally. This question is all the more important when we consider NCs presenting surfaces at the nanometer scale. However, Cahen and Kahn explain [51], that the measured quantity is always $E_{vac}(s)$, the vacuum level "right outside the solid", and is independent of $E_{vac}(\infty)$. They illustrate their statement by the description of a photoelectron emission experiment (see below), which is one of the main techniques to access AE, IE, and ϕ_m . This technique can be performed with X-ray and UV incident photons and can probe the entire valence electronic structures.

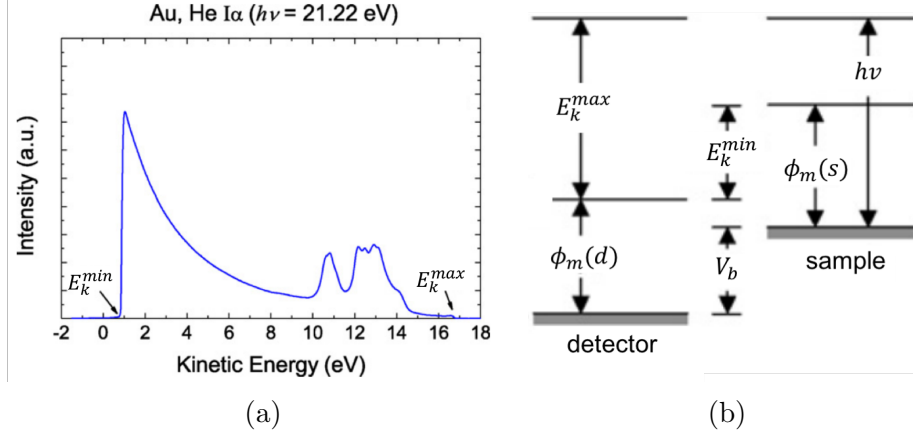


Figure 6.3: (a) The valence band spectrum of Au layer on Si(100) obtained by PS with He I α ($h\nu = 21.22$ eV) lines. The spectrum was obtained by applying a -10 V bias (V_b) to the sample. The kinetic energy scale has been appropriately adjusted to account for the applied bias. The intense peak observed at low kinetic energy corresponds to the SEC region of the spectrum. The values for E_k^{max} (Fermi level) and E_k^{min} are displayed. (b) The figure illustrates the energy level diagram for the sample and detector, in the experiment of (a). Reproduced from [50].

Photoemission spectroscopy In the PS experiment, the sample is irradiated by a high-energy monochromatic light (photon energy = $h\nu$), and the measured quantity is the kinetic energy E_k of the ejected electron from the sample (see Figure 6.3a). The maximum kinetic energy E_k^{max} that can be measured corresponds to electrons ejected from E_F . On the other side of the energy distribution spectrum, there is the secondary electron cut-off (SEC) [50]. This region presents a point of interest namely the cut-off energy. This corresponds to the transition between electrons leaving the sample with energy less than $E_{vac}(s)$, and those with nearly zero kinetic energy escaping from the solid just above $E_{vac}(s)$ at the cut-off. If we consider that the vacuum level of the detector $E_{vac}(d)$ being below $E_{vac}(s)$, electrons acquire kinetic energy during their journey from the sample surface to the detector entrance. This energy increase corresponds to the difference in potential energy between these two locations. According to this statement, the minimum kinetic energy (E_k^{min}) is thus not dependent on $E_{vac}(\infty)$, but rather determined by the difference: $E_{vac}(s) - E_{vac}(d)$ (an illustration is given in Figure 6.4).

Therefore, the work function of the sample is given by (see Figure 6.3b):

$$\phi_m(s) = h\nu - E_k^{max} + E_k^{min} \quad (6.1)$$

Furthermore, as illustrated in Figure 6.4, E_k^{max} does not depend on the surface contrary to E_k^{min} . Thus, a dipole layer induces a modification of E_k^{min} which echoes on the work function (see eq. 6.1). Again, this is totally independent of $E_{vac}(\infty)$.

It is worth noticing that, in the case where $E_{vac}(s) = E_{vac}(d)$, the work function simply writes:

$$\phi_m(s) = h\nu - E_k^{max} \quad (6.2)$$

The latter equation is consistent with the Einstein relation (where E_b corresponds to the binding energy of the electron):

$$E_k = h\nu - E_b \quad (6.3)$$

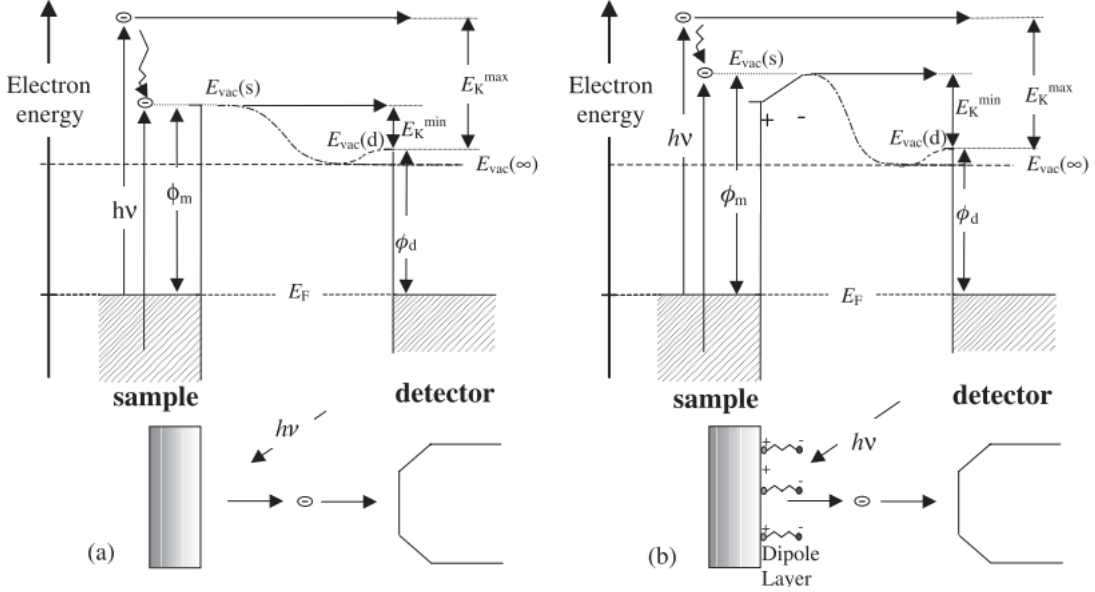


Figure 6.4: (a) The depicted energy diagram illustrates a PS experiment. At the equilibrium, the Fermi level, denoted as E_F , is consistently aligned throughout the system. The diagram includes the vacuum levels of the metal surface, indicated as $E_{vac}(s)$, and the detector, denoted as $E_{vac}(d)$, along with their respective work functions, ϕ_m and ϕ_d . The vacuum level at infinity, symbolized as $E_{vac}(\infty)$, is arbitrarily positioned below $E_{vac}(s)$ and $E_{vac}(d)$. Additionally, the diagram displays a photoelectron emitted from the Fermi level and detected with the kinetic energy E_k^{max} ; and a secondary electron escaping the solid just above $E_{vac}(s)$ with the kinetic energy E_k^{min} . In panel (b), the passivation by ligands of the sample surface creates a dipole layer causing an increase in $E_{vac}(s)$ and E_k^{min} . Reproduced from [51].

and the definition of the work function where the maximum kinetic energy E_k^{max} comes from the excitation from the Fermi level. Since electrons with nearly zero kinetic energy could not reach the detector, a negative bias V_b is typically applied to the sample accelerating the electrons (see Figure 6.3b). This bias offsets all of the energy levels in the sample, therefore eq. 6.1 is still valid.

While this discussion suggests that the measured vacuum energy level corresponds to $E_{vac}(s)$, an interrogation remains about its meaning in the case of a layer of NCs. Indeed, it is known that a NC presents different surfaces, with different surface coverages, stoichiometry, etc., and thus distinct $E_{vac}(s)$. Since a layer of NCs is composed of a variety of NCs with different orientations and presenting different surfaces (see Figure 6.5), the measured quantities (ϕ_m , IE, and EA) will be a nontrivial average of the $E_{vac}(s)$ of the NCs. It will likely depend on the deposition method, the NC-NC distance, the synthesis, and the arrangement of NCs in superlattices.

6.2.2 Theoretical calculations

Due to the numerical cost of ab initio calculation, the effect of ligands is mainly studied on quasi-two-dimensional slabs [236, 52] or on very small clusters [14, 53]. Although they do not provide quantitative values of band energy shifts in realistic

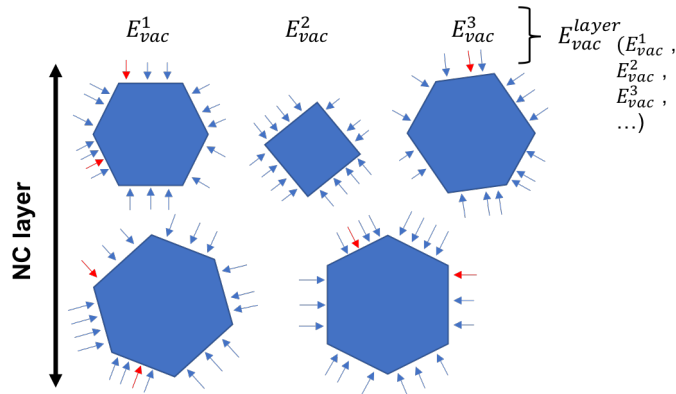


Figure 6.5: Illustration of a layer of NCs. The arrows represent the ligands model as dipoles at the NC surface, and the color (red and blue) represents different chemical identities. We could imagine the blue arrows are iodide ligands while the red arrows illustrate the oxidation of lead atoms by hydroxyl groups. The NCs present different shapes, passivations, and NC-NC distances, and thus present different vacuum energy levels E_{vac}^i at their surfaces. Therefore the vacuum level of the NC layer E_{vac}^{layer} obtained experimentally is likely a non-trivial average of all E_{vac}^i .

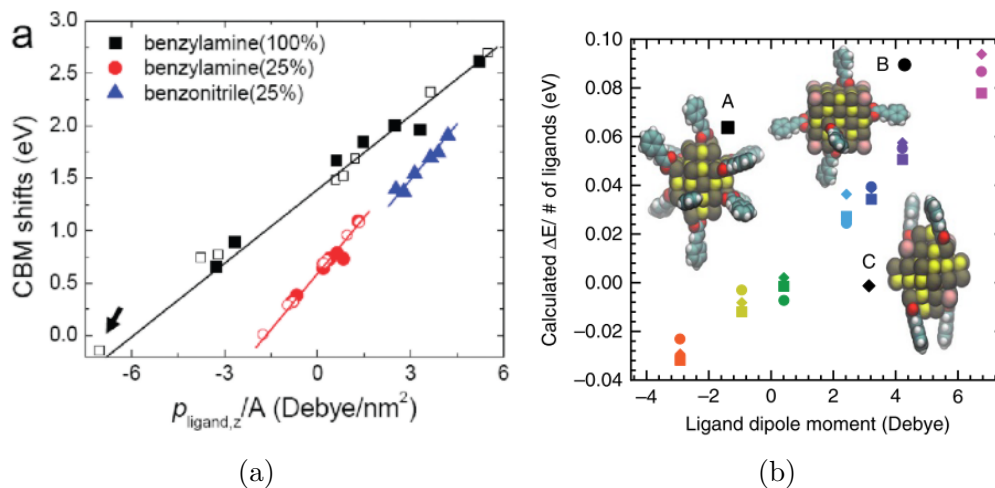


Figure 6.6: (a) DFT calculation of the conduction band minimum (CBM) shifts of CdSe. The shifts are presented in relation to the z-component of the intrinsic dipole moment density of functionalized ligands on the CdSe surface. Specifically, the shifts are shown for benzylamine on CdSe(100) at 100% coverage (squares), benzylamine on CdSe(100) at 25% coverage (circles), and benzonitrile on CdSe(100) at 25% coverage (triangles). In the case of benzylamine with two or more substitutional F atoms, the data is denoted by open symbols. Reproduced from [52]. (b) DFT calculations of band edges, renormalized by the number of ligands, are depicted for three distinct isolated ligand/NC structural models. These models exhibit varying surface coverage and are plotted as a function of the projected ligand dipole. Reproduced from [53].

NCs, insights and understanding can be obtained. The DFT calculations on a slab of PbS NCs performed by Yang et al. [52] showed that ligands bound to the NC surface can be assimilated to an effective dipole moment (μ_{eff}) decomposed into two contributions: surface dipole due to electronic rearrangement at the NC/ligand

interface (μ_{surf}), and the intrinsic dipole (μ_{intr}) of the ligand. As already discussed, a dipole layer creates a potential barrier, which can be obtained from the Helmholtz equation:

$$\begin{aligned}\Delta V &= \frac{-\mu_{eff}}{\epsilon_0 A} \\ &= \frac{-\mu_{surf}}{\epsilon_0 A} + \frac{-\mu_{intr}}{\epsilon_0 A}\end{aligned}\tag{6.4}$$

where A is the surface area of the ligand. This decomposition has also been suggested by Heimel et al. [269] in the field of self-assembled monolayers on metals. Yang et al. [52] calculated μ_{intr} by DFT which allows them to plot its variation with the band edge shifts for different ligand density (A), see Figure 6.6a. Therefore, they could extrapolate the surface dipole by the intercept. They found comparable values of μ_{intr} and μ_{surf} . With the same binding group, Kroupa et al. show linear band edge shift with the ligand dipole moment [53]. They did not observe an effect of the shape on the band edge shift but proposed an impact of the interaction between ligands located on the same NC, and on different NCs (see Figure 6.6b). Although insightful, these studies were carried out on very small clusters, which is why we propose to combine DFT calculations with ETBM to model realistic NCs size and obtain quantitative band edge shifts.

6.3 Simulation methodology and results

Due to the complexity of the system, the modeling of the NC-ligand interaction and its effect on the electronic structure is challenging. It requires the description of charge redistribution and self-consistent resolution of the potential, such as what is done in ab initio calculations, but is limited by the computational cost, therefore we propose to combine DFT calculations with ETBM. In this ongoing project, different preliminary questions have been raised, which will be discussed in the following:

1. How can we obtain the effective dipole moment of the ligands bound to the NC? Can we model ligands as point dipoles?
2. Is the effective dipole extracted from a slab transferable to the NC surface?
3. How can we compute the effect of the dipole potential on the electronic structure in the ETBM framework?

1. Ligands as dipoles Jing Li and Benoît Sklénard at CEA Leti have performed DFT calculations employing periodic boundary conditions and the repeated-slab approach [236], utilizing VASP package with PBE functional [272] and verified results using HSE functional [151]. The study has been carried out on (111) and (100) surfaces, which are dominant for PbS NCs. (100) slab is stoichiometric and apolar presenting alternate Pb and S atoms at its two surfaces. On the contrary, the (111) surface is polar with Pb atoms at one extremity and S atoms at the other to preserve the slab stoichiometry. This asymmetry creates a dipole that is compensated by adding pseudo-hydrogens at the S-terminated surface (see Figure 6.7). The slabs are then passivated by ligands on one side (Pb-terminated surface for (111)). Atomic structures of the PbS-ligand interface are constructed and then relaxed. As

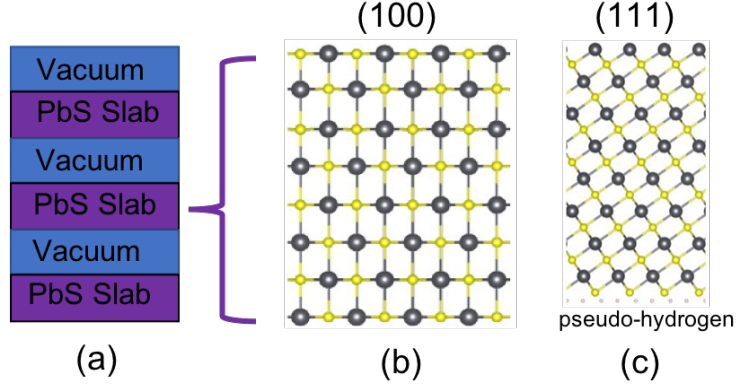


Figure 6.7: (a) Illustration of the repeated-slab approach with alternating vacuum space and PbS Slab. Schematic diagram of modeled (b) PbS (100) slab and (c) PbS (111) slab. For (b) and (c) the yellow dots represent sulfur atoms while the black dots represent lead atoms. Contrary to PbS (100) slab (b) which is apolar and symmetric, PbS (111) slab (c) is asymmetric with Pb and S atoms at each of the extremities, thus pseudo-hydrogen atoms were added to prevent charge transfer at the S-terminated surface.

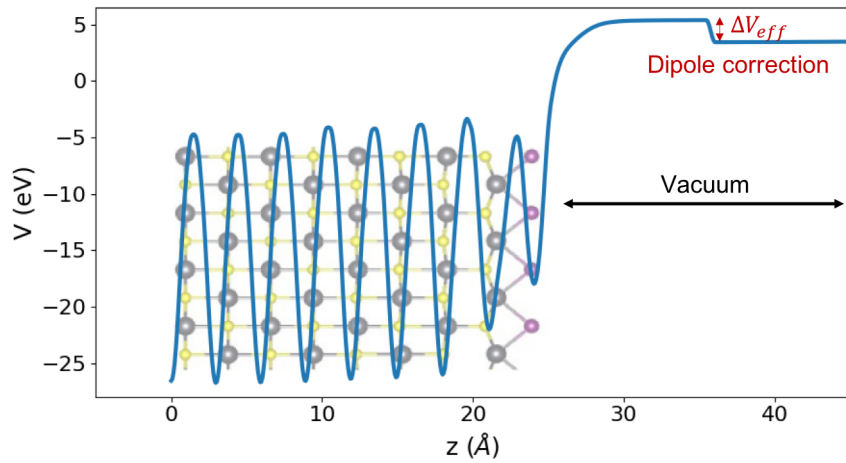
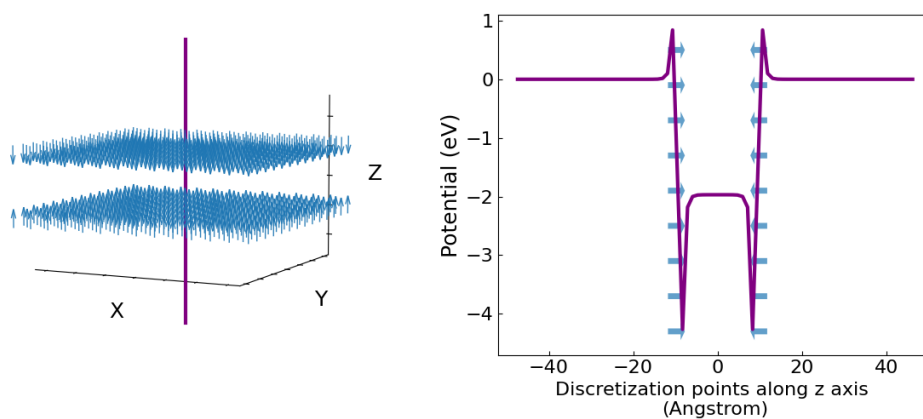


Figure 6.8: Inplane-averaged potential energy (blue line) for electrons across a PbS (100) slab capped at one extremity by iodide atoms. The PbS (100) slab capped by iodide atoms (purple dots) is represented in the background. The position of the vacuum is roughly given for the sake of clarity. The potential in the slab strongly oscillates due to the alternate semiconductor planes. In the vacuum the potential is constant but a step of potential is present corresponding to the dipole correction required to avoid the divergence (see text for details). The dipole correction is in fact the drop of potential ΔV_{eff} due to the dipole layer μ_{eff} .

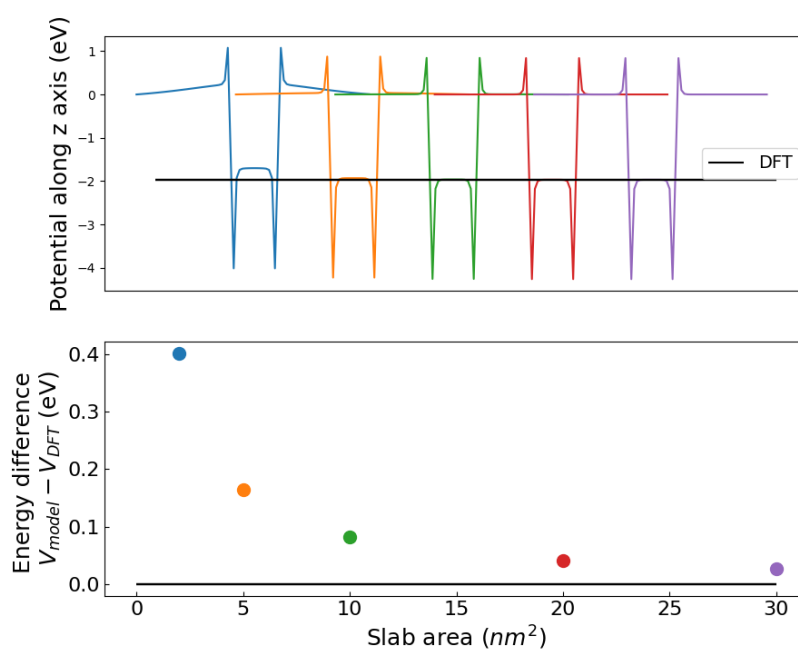
seen in the previous Section 6.2, the ligands form a dipole layer creating a potential difference ΔV_{eff} . Due to the asymmetry of the slab, ΔV_{eff} is not compensated at the other extremity, and a correction to cancel ΔV_{eff} is mandatory to avoid a divergence due to periodic boundary conditions. Therefore, the correction corresponds to the drop of potential ΔV_{eff} due to the dipole layer. In order to obtain ΔV_{eff} , the in-plane electrostatic potential along the passivated slab is calculated. As il-

lustrated in Figure 6.8 for a PbS (100) slab capped by iodide atoms, the inplane electrostatic potential gives the atomic planes represented by the strong oscillation, whereas the correction is observed in the vacuum layer by a potential step. ΔV_{eff} is then injected into the Helmholtz formula eq. 6.4 to obtain the effective dipole moment μ_{eff} . The latter includes the two contributions, to know the intrinsic and interface dipole. This procedure has been applied to several X-type ligands like benzenedithiol (BDT), ethanedithiol (EDT), 3-mercaptopropionic acid (MPA), and halides (I, F, Cl, Br). For ligands presenting one binding group, the ligand coverage has been set to one ligand per surface Pb atom. For ligands presenting two binding groups, the ligand coverage is fixed at one ligand per two surfaces Pb atoms. In the latter case, two configurations type have been considered, either only one group is linked to the Pb atom (named monodentate), or the two groups are linked (named bidentate). The barriers of potential for the different ligands and PbS surfaces are given in the Appendices. As halides, such as iodide, are single atoms, with no intrinsic dipole, they induce only surface dipoles due to their interaction with the lead atoms. Therefore, they tend to increase the barrier of potential or equivalently give a larger work function compared to pristine (uncapped) surfaces. On the contrary, for organic ligands such as BT, the surface dipoles μ_{surf} are more than compensated by intrinsic dipoles μ_{intr} in the opposite direction. Thus BT tends to reduce the barrier of potential compared to the pristine case, smaller shallower work functions.

To assess the possibility of modeling ligands as point dipoles, we construct a non-periodic slab, see Figure 6.9a. This slab is in fact two upside-down planes of point dipoles separated by a fixed distance of 2 nm, while the area of the two planes is varied uniformly from 2x2 to 30x30 nm². The effective dipole moment μ_{eff} of the point dipole was deduced from DFT calculations (described above). In this study, we choose iodide ligands with $\Delta V_{eff} = 1.97$ eV and using classical electrostatics, we computed the potential along the z-axis. We give an example in the right panel of Figure 6.9a, with a slab of 2 nm thickness, and 30x30 nm² area. We can see that the potential at the exterior of the two planes is constant and equal, while it is constant inside, it differs from the exterior forming a drop of potential features of two capacitors facing each other. In Figure 6.9b, we performed this calculation by increasing the slab area from 2x2 to 30x30 nm². The drop of potential ΔV_{eff} at the center of the slab converges to the DFT value for an area of 30x30 nm². However, as expected from electrostatic considerations, at a close distance from the point dipole the potential diverges. Therefore, assimilating a ligand by a point dipole seems reasonable as long as the potential is calculated far enough, i.e. of the order of a few angstroms.



(a)



(b)

Figure 6.9: Electrostatic calculations for point dipoles with dipole moment extracted from DFT for TBAI ligands. (a) Illustration of electrostatic calculations of the potential barrier due to dipole layers. The left panel illustrates two dipole layers (blue arrows) of opposite polarization and the z-axis along which the potential has been computed (purple line). The distance between the two planes is 2 nm. As an example, the right panel gives the potential calculated for a slab of $30 \times 30 \text{ nm}^2$ area. We can observe a divergence of the potential, close to the point dipole position (± 1 angstrom). (b) The upper panel gives the different potential plots calculated for varying slab areas, from left to right: 2×2 , 5×5 , 10×10 , 20×20 , and $30 \times 30 \text{ nm}^2$. The bottom panel gives the convergence of the electrostatic potential calculated in the middle of the two dipole layers for the varying areas described above with respect to DFT calculations.

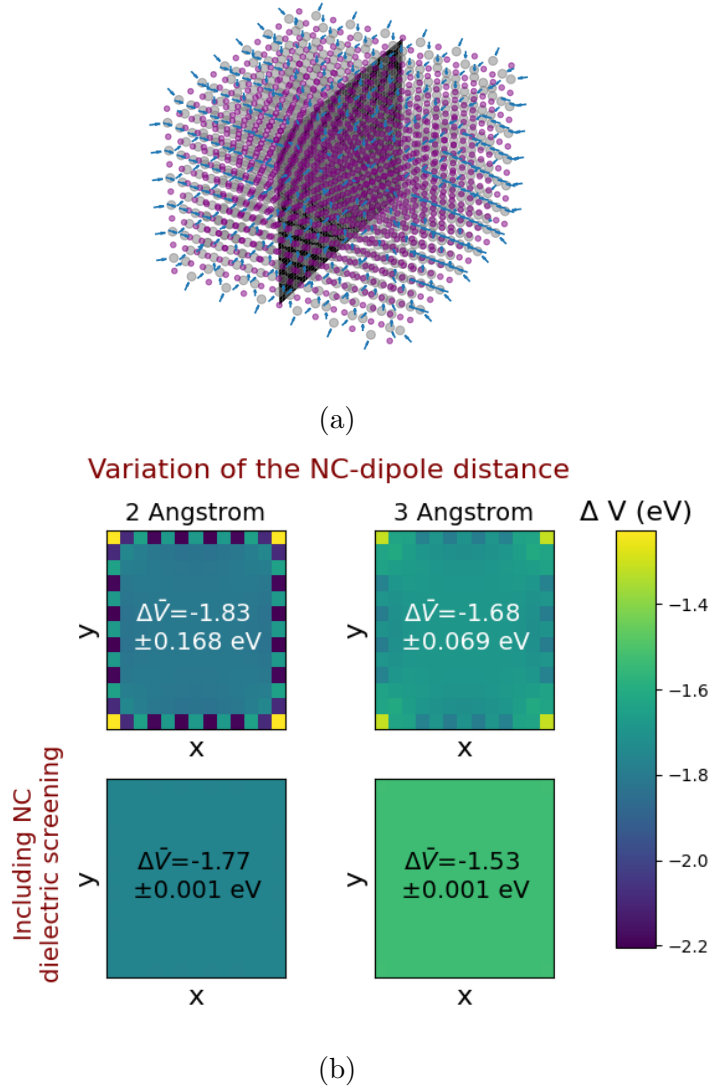


Figure 6.10: Electrostatic calculation in a 4 nm cubic PbS NC due to point dipoles corresponding to TBAI ligands. (a) Illustration of a cubic PbS NC passivated by point dipoles. Pb atoms: in grey, S atoms: in purple, and point dipoles: blue arrows. The potential is calculated in the represented (100) plane. (b) Potential due to dipoles calculated in the (100) plane for two NC-dipole distances. The two bottom panels include the dielectric response of the PbS NC. $\Delta \bar{V}$ corresponds to the average potential calculated in the (100) plane.

2. Ligands on nanocrystals Figure 6.10a shows a cubic PbS NC of 4 nm size where each Pb surface atom is passivated by one ligand, modeled as a point dipole. As above, we choose iodide ligands as point dipoles. We computed in Figure 6.10b the potential in the (100) plane intersecting the NC, for two NC-dipole distances. In the upper panel of Figure 6.10b, we can see that the potential varies close to the NC/dipole interface, especially when the NC-dipole distance is small (from 3 to 2 angstroms), and the potential becomes constant below the first atomic layer in the NC. Moreover, the potential and its average $\Delta \bar{V}$ depends on the NC-distance. At the surface, the potential alternates in magnitude between Pb passivated by dipoles, and unpassivated S. This alternating potential is even more visible in the (001)

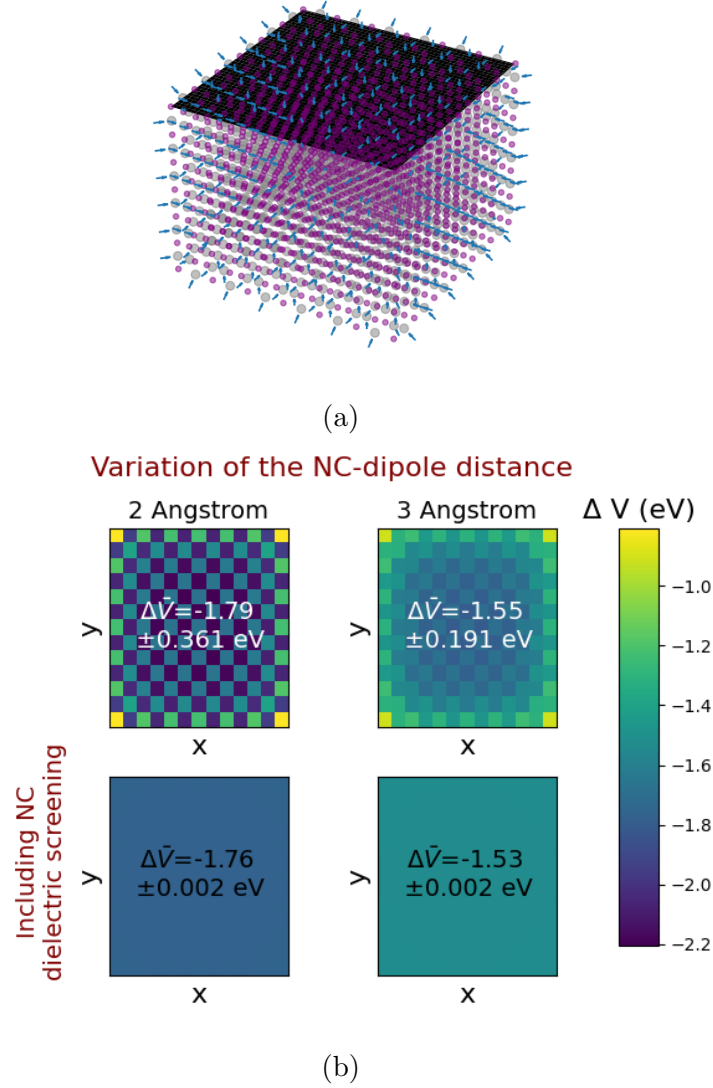


Figure 6.11: Same as Figure 6.10 for the potential calculated in the (001) surface plane.

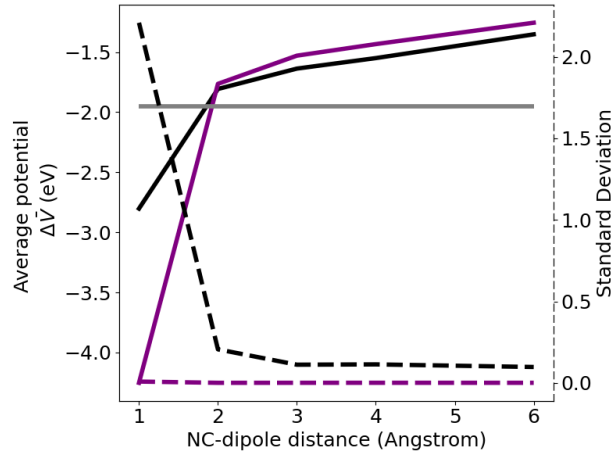
surface plane (Figure 6.11b), where the surface appears as a chessboard. Moreover, in Figure 6.11b, we can observe stronger potential inside the plane than on the edges and corners. This phenomenon is known as the edge effect and is due to the finite size of the NC that let the edge atoms be less surrounded by ligands. In principle, this effect could also influence the magnitude of the dipole moment. Indeed, the magnitude of the dipoles at the center of the plane is reduced due to the interaction with their neighbors, an effect that would logically be lessened for dipoles on the edges and corners. It would be possible to include this dipole variation using the following equation [273]:

$$\mu_i = \mu_0 + \alpha_i E_i \left(\sum_{j \neq i} \mu_j \right) \quad (6.5)$$

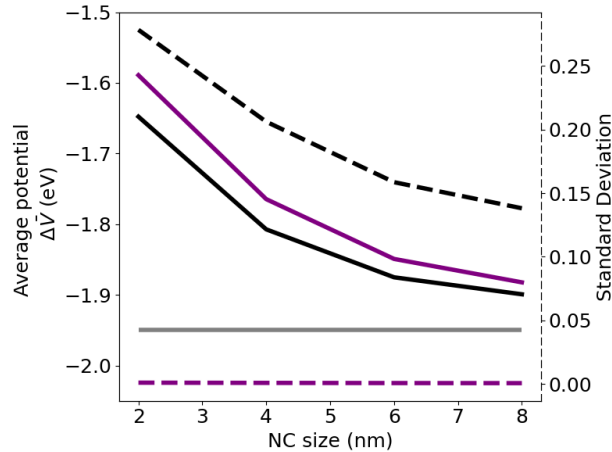
where μ_i , the final dipole moment at i , is obtained self-consistently with the initial dipole moment μ_0 , the polarizability of the dipole α_i , and the electric field E at i due to the other dipoles j . This effect could be considered in future works.

The potential variation observed in the upper panels of Figures 6.10b and 6.11b

implies the presence of an electric field inside the NC. Therefore we expect a polarization of the ions of the NC which tends to screen the electric field induced by the dipoles. We took into account this dielectric screening by the method described in [203] (see Appendices). Since the dipoles are static, the electronic and ionic contributions need to be included, thus we choose the static permittivity of bulk PbS: $\epsilon = 170$ [166]. The results are given in the bottom panels of Figures 6.10b and 6.11b. We can see that the dielectric screening in the NC leads to the homogenization of the potential inside the NC, and thus cancels the electric field due to the surface dipoles. However, the potential inside the NC varies with the NC-dipole distance. It is worth noticing that the dielectric screening is already included in the DFT calculation so in the μ_{eff} . However, we expect no electric field inside the NC when considering a slab (see Figure 6.9a), whereas in 0D structure such as cubic NC, edge effects induce an electric field, as seen above.



(a)



(b)

Figure 6.12: Potential due to point dipoles averaged over all the atoms of the cubic NC (solid line) and the standard deviation of the averaged potential (dashed line) according to (a) the NC-dipole distance, and (b) the NC size. The point dipoles correspond to TBAI ligands with a drop of potential of 1.97 eV calculated by DFT in the slab (grey horizontal line). The black and purple lines correspond to calculations without and with the account of the NC dielectric screening, respectively.

Figure 6.12a gives the mean potential (solid lines) and the standard deviation (dashed lines) over the whole NC volume with increasing NC-dipole distance for a PbS cube of 4 nm passivated by iodide ligands with (purple lines) and without (black lines) the NC dielectric screening. The standard deviation of the potential inside the NC is always lower when accounting for the screening, and is almost vanishing (~ 0 eV) regardless of the NC-dipole distances. The grey horizontal line corresponds to the barrier of potential obtained in DFT. At a NC-dipole distance of 2 angstroms, the potential is around 0.1 eV lower than in a slab. This is likely due to the edge effects discussed above. This is apparent in Figure 6.12b where the potential into the NC converges to the DFT with increasing NC size. Indeed, it is well known that the edge effects decrease with increasing NC size. On the other hand, when the distance between the NC and the dipoles is increased, convergence is not observed. This is attributed to the fact that the dipole layers on the six faces of the cube are positioned far apart from each other. This situation is obviously unrealistic.

3. Empirical Tight-Binding Method We used two approaches for calculating the effect of the dipole potential on the NC electronic structure by ETBM. In both cases, we start by constructing the potential on the atomic orbital basis. Since we consider in ETBM atomic orbitals which are orthogonal and localized on their corresponding atoms, the matrix of the potential is diagonal. We can use the stationary perturbation theory which decomposes the Hamiltonian of the system as:

$$H = H_0 + V \quad (6.6)$$

where H_0 is the unperturbed (initial) Hamiltonian, and where V is the time-independent perturbation, which corresponds in our case to the dipole potential. Once the eigenstates and eigenvalues of H_0 are known, the perturbation theory allows quick access to the perturbed eigenvalues ϵ . The first-order correction to eigenvalues ϵ^0 , is simply equal to the expectation value of V in the unperturbed state Φ^0 :

$$\epsilon = \epsilon^0 + \langle \Phi^0 | V | \Phi^0 \rangle \quad (6.7)$$

However, this method requires that the coupling between the zero-order states due to the perturbation is much weaker than the difference between their eigenvalues (i.e. $|\epsilon_m^0 - \epsilon_n^0| \gg |\langle \Phi_m^0 | V | \Phi_n^0 \rangle|$). This is always the case when the potential inside the NC is constant (as seen above when accounting for NC dielectric screening), which gives a coupling equal to zero. But, for more complicated and perhaps more realistic systems where the passivation is inhomogeneous, the coupling is no longer zero. Moreover, special treatment needs to be considered for degenerate eigenstates, where the perturbation matrix in the subspace of the degenerate states must be diagonalized. A more accurate approach that allows the discarding of the preceding requirements is to directly inject the dipole potential into the ETBM Hamiltonian matrix. Then, the direct diagonalization of H gives the perturbed eigenstates and eigenvalues. We compare the two methods in Figure 6.13a for a cube of 4 nm size with iodide ligands as a capping ligand at a distance of 2 angstroms. The latter distance while reasonable has been fixed arbitrarily. This is for the moment one of the shortcomings of the model. Moreover, the NC-dipole distance is likely to vary across the different ligands, which is why this point should be taken into consideration in future work. We considered the case with and without dielectric

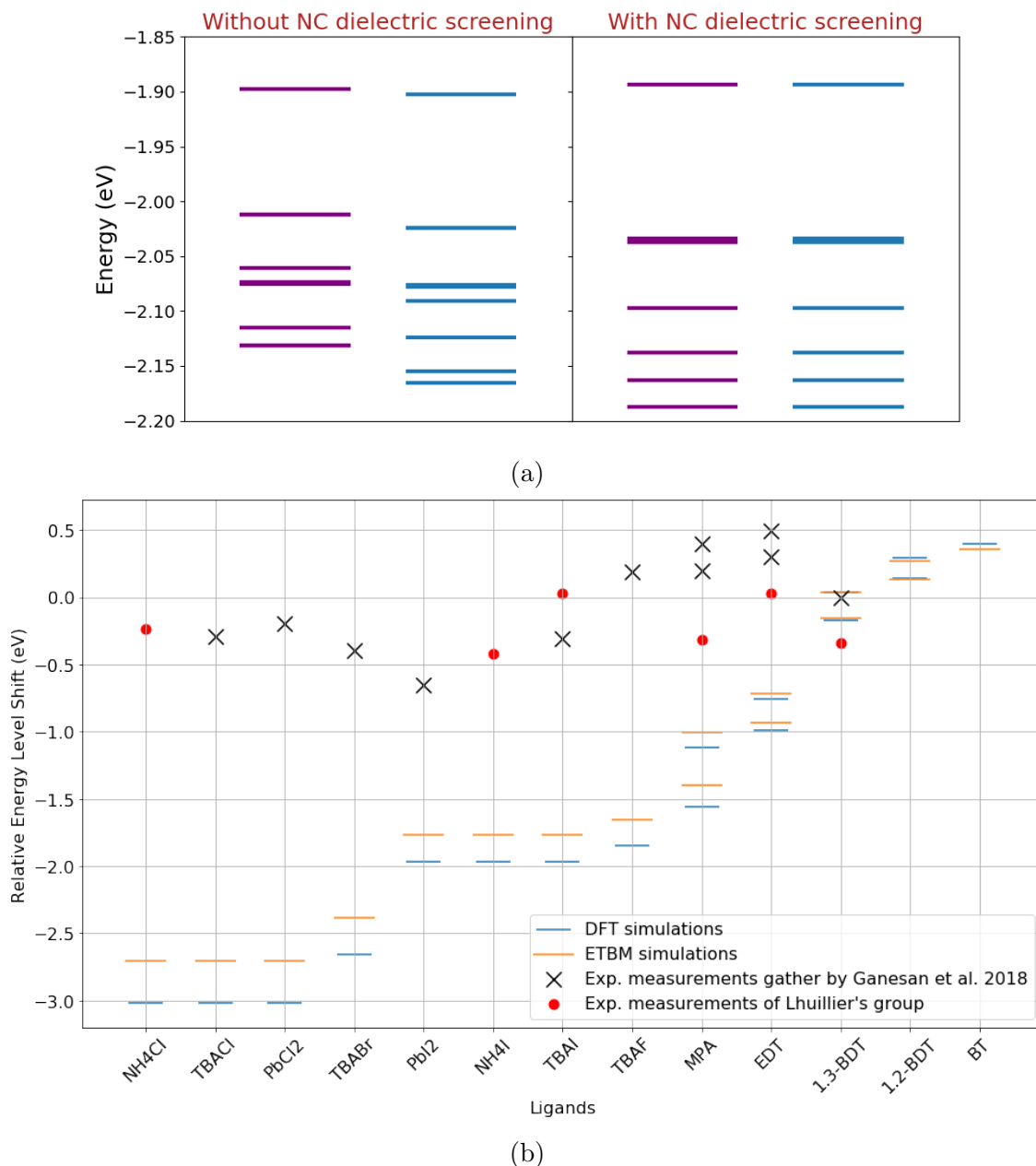


Figure 6.13: (a) Valence band Maxima (VBM) calculated by ETBM for a 4 nm cubic PbS NC with (left panel) and without (right panel) the NC dielectric response. We compare the perturbation theory (purple line) to the direct Hamiltonian diagonalization (blue line). See text for details. (b) Effect of the ligands on the VBM. For ETBM (orange horizontal lines), the VBM is relative to the VBM of the pristine NC. For experimental work (black cross and red point), the VBM is relative to NC layers capped by 1,3 BDT. The DFT calculations (blue horizontal lines) correspond to a drop of potential in a (100) slab (see Figure 6.8). The red dots are unpublished work performed by the group of Emmanuel Lhuillier. The black cross corresponds to collected measurements from the literature by Ganesan et al. [54]. See text for more details. The different values for equivalent ligands correspond to different binding schemes.

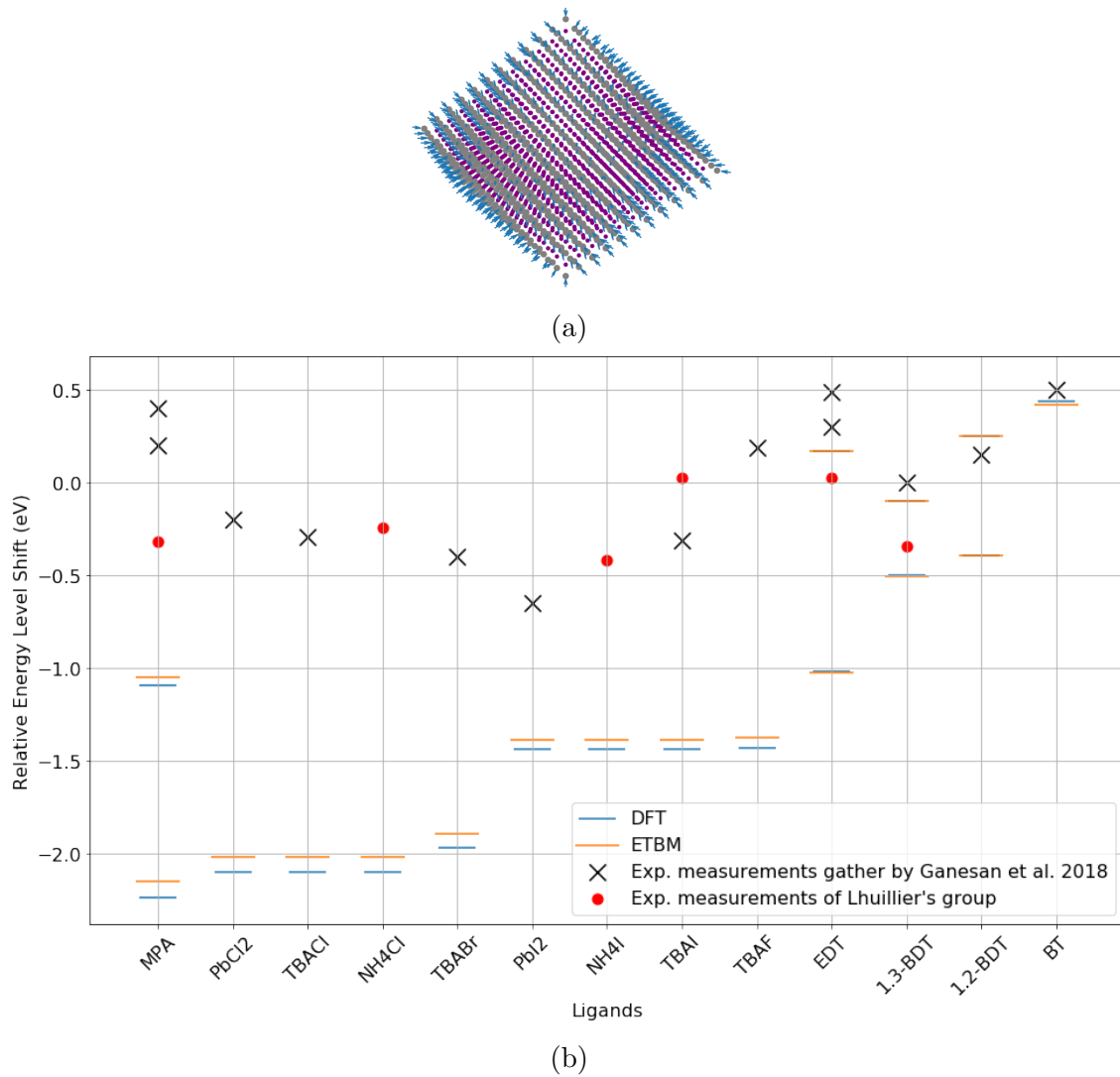


Figure 6.14: Same as Figure 6.13 for octahedral NCs and (111) slabs for DFT.

screening. The latter case implies a varying potential in the NC which makes the perturbation approach inaccurate. On the contrary, the two methods give similar results when the potential is constant due to the screening.

In Figure 6.13b, we apply the "diagonalization method" to cubic NCs capped with all the ligands under study and compared them to DFT calculations on slabs and to experimental measurements. Since DFT calculations give only the drop of potential due to ligands, we consider for the ETBM calculations and experimental measurements the shift of the VBM relative to the VBM computed on a bared NC, and to NC layers capped by 1,3 BDT, respectively. Since 1,3 BDT ligand presents almost no dipole [236], NC capped with 1,3 BDT could be considered as a bared NC, making a fairer comparison with theoretical calculations.

The experimental shifts are much smaller which could be explained in part by a lower ligand coverage. We can also note that due to the edge effect observed in the 0D structure (discussed above), ETBM gives smaller shifts than DFT calculations.

Since the experimental measurements have been performed on a 3 nm PbS NCs size which is known to form octahedral, we performed the same calculation that the cubic NC to octahedral NC presenting (111)-Pb-rich surfaces (see Figure 6.14b).

While still overestimating experimental shifts, it reduces compared to cubic NC.

These results are the first steps to construct a more comprehensive model. It remains a lot of work to do, to allow an insightful comparison with experimental measurements. For example, the distance of 2 angstroms between the NC surface and dipoles has been fixed arbitrarily. To tackle this issue, we are currently working to describe the NC/ligand interface in the framework of a bond polarizability model, which avoids this issue. Moreover, we certainly need to take into account the ligand-ligand interaction in a self-consistent picture (eq. 6.5), which would be more important as the NC size decreases. In the present, the dipole is assumed to be the same as in an infinitely extended 2D layer.

6.4 Conclusion

The ligands at the surface of the NCs not only passivate the surface but also modify their energy levels. This tunable tool opened the doors to band engineering in a NC layer. For example, it allows positioning the NC energy levels with respect to the chemical potential in the contacts of a device. This enables NC-based devices an improved control of charge transport and charge extraction. As the NC/ligands system is complex and thus difficult to model with ab initio calculations, we combined DFT and ETBM simulations along with electrostatic calculations. This project has been carried out in collaboration with Jing Li and Benoît Slénard from CEA for the DFT calculations, and with Emmanuel Lhuillier from INSP for experimental measurements. While this model is not mature enough for comparison with experimental measurements, we still unveiled some theoretical insights.

We present the possibility to describe ligands as point dipoles by showing the convergence of electrostatic calculations with DFT simulations. We looked at the edge effects on cubic NCs, and show that the resulting variations of potential is removed by dielectric screening in the core of the NC. Finally, we computed the energy shift due to ligands on cubic and octahedra NCs composed of thousands of atoms. This model still needs improvement such as the inclusion of the edge effect and a consistent determination of the NC-dipole distance. The work was still in progress at the time when this thesis has been written.

General conclusion

Conclusion

This dissertation focuses on the study of the optoelectronic properties of the active materials used in IR sensors in the form of NC layers. Different numerical tools were used and sometimes modified, especially TB_Sim for TB calculations. The latter allowed us to carry out a study of the electronic structure, and optical properties from bulk to NC for various semiconductors. We focused on PbS and HgTe which together cover all the IR spectrum.

Specifically, we unveiled in Chapter 2, a transition of topological nature from HgTe bulk to HgTe NC, which we predict for a NC diameter of about 26 nm. In Chapter 3, we relate this transition to a strong modification of optical properties.

PbS is a widely studied material in bulk, NC, and NC layers. Therefore, this is an ideal system to validate new models and gain new knowledge. In Chapter 2, we confirmed the p-like nature around the bandgap energy of the PbS electronic structure, which confers to this material high stability against trap states. In Chapter 3, we compared the optical properties calculated by TB with experimental works found in the literature. For the bulk, although a good agreement was found, some discrepancies remain. It allowed a discussion of the TB limits and also how an experimental error could propagate. In addition, we investigate the effect of confinement on the optical properties by the presence of discrete peaks that we could attribute to specific electronic transitions.

Then we extend the results of NCs to NC layers with EMA (Chapter 4). As previously, we focused on PbS and HgTe. This study was led in conjunction with SE measurements performed by the group of Emmanuel Lhuillier. We show how the NC properties such as size, shape, and surface chemistry impact the layer parameters and thus its optical properties. These were then injected into electromagnetism simulations of standard diode stack to predict photonic device performance. This methodology was then applied to other semiconductors that allowed a systematic comparison. In the SWIR, the lead chalcogenides present stronger optical properties compared to its potential substitute, namely InAs. Although the intrinsic optical properties of InP NC are comparable with NC CdSe, under NC layers CdSe outperforms its counterpart. In addition, we assess the performances of NCs-based IR photodiode in terms of EQE, emphasizing the interest of NCs in active imaging applications.

Finally, in Chapter 6, we developed a model to investigate and predict the effect of surface chemistry on the NC electronic structure. From a fundamental point of view, it allowed us to look at the edge effects due to a faceted object that is a NC, to show that electronic rearrangements could cancel potential variations inside a NC, and to consider the effect of the shape and the size on the drop of potential

due to passivating ligands. In the future, this model ambitions to be a tool for understanding but also predicting the variation of electronic structure with any ligands, which would allow band-alignment engineering.

Perspectives

Over these last 20 years, IR sensors based on solution-processed semiconductor NCs progressed drastically in various aspects. Advances in synthesis recipes, understanding and control of the electronic structure, optimization of the surface chemistry, and deposition methods take the NC-based photodetectors to almost commercial InGaAs level. Furthermore, colloidal NCs are directly integrated on top of the read-out circuit, removing the need for a flip-chip process. As a result, the NC-based sensors not only had smaller pixel pitches but also reduced costs of fabrication while allowing large-scale production. However, colloidal NCs are still not as mature as single-crystal technology which indicates the important potential of these materials in future technology and also points toward research efforts that are required. One of the main challenges is to better control the NC surface. This is logical since the presence of surfaces is the main difference between NC and single-crystal. The surfaces are as much a blessing as a curse for NCs. It's indeed from surfaces that derives numerous formidable properties such as a tunable band gap with the size. However, the surfaces present uncoordinated atoms contrary to their bulk counterparts, which can lead to trap states. This is especially those trap states that are responsible for higher dark current and smaller response time. Thus, passivating the undercoordinated sites by ligands while preserving the electronic transport properties into the layers is of fundamental importance. It could be useful to extend the capping ligand chemistry, especially for large PbS NCs mandatory in IR applications that present (100) surfaces with weak affinity for the current ligands and thus poor stability. Furthermore, scaling up the synthesis protocols while preserving good reproducibility is needed to meet industrial needs. This could be possible by the development of a large-scale continuous flow process. Another great challenge is the replacement of toxic heavy metals (Hg and Pb) currently used in IR detection with less toxic elements.

From the theoretical point of view, we developed a model to extract the physical properties of NC layers such as the NC volume fraction. It would be interesting to combine SE with TGA measurements to assess this model in greater detail. Furthermore, we know that this model does not describe correctly the interface NC-ligand, thus including this contribution to the dielectric response of the NC could be interesting. The last Chapter of the manuscript presents an unfinished model to estimate the effect of ligands on the layer work function. We pointed out different challenges that need to be tackled in the future such as including edge effects, describing the NC-ligand interface as a bond polarization, and extending the results to an assembly of NCs. The ligands also affect the coupling between NCs, and thus the transport properties inside the NC layer. Therefore, it would be interesting to have a model that includes, electronic, optical, and transport properties. It would for instance allow to choose the right ligand according to the application and the device structure. Finally, the recent advancements in machine learning could be implemented to increase the predictive power and reduce numerous trial and error procedures.

Appendix A

Appendix

A.1 Bond polarization model

This model serves to take into account the dielectric screening due to the application of an external electric field. The model or part of it can be found in [27, 203]. In this thesis, it has been used for NCs capped by ligands modeled as point dipoles (see Chapter 6). We assume the electrons of a dielectric system tightly bond to their ionic core. However, when an external electric field \mathbf{E}_0 is applied, the electrons move inducing electronic charge variation δn whose the electric field $\delta \mathbf{E}$ tends to oppose to \mathbf{E}_0 . As a result, the energy potential of an electron in a dielectric system under \mathbf{E}_0 can be divided into two contributions:

$$V = V_0 + \delta V \quad (\text{A.1})$$

where V_0 is the energy potential due to \mathbf{E}_0 , and δV the energy potential from the field $\delta \mathbf{E}$, often named depolarization field.

If we consider a NC of N atoms, δV can be written as:

$$\delta V = v \delta n \quad (\text{A.2})$$

where v is the Coulombic N by N matrix, with matrix elements: $v_{ij} = \frac{1}{|\mathbf{r}_i - \mathbf{r}_j|}$, and δV and δn are column matrices of length N .

Then, the charge transfer δn can be related to the electron potential energy V by:

$$\delta n = \chi V \quad (\text{A.3})$$

where χ is a $N * N$ matrix that represents the polarization of the bonds. From electrostatic considerations, the energy potential V can be related to V_0 by:

$$V = \epsilon^{-1} V_0 \quad (\text{A.4})$$

where $\epsilon = I - v\chi$ corresponds to the permittivity of the dielectric with I the identity matrix. Therefore, the remaining unknown to obtain V is the χ matrix.

Analytical formula of χ The latter can be simplified under some assumptions. Since for any potential V , the total variation of charge gives zero ($\sum_{i=1}^N \delta n_i = 0$), from eq. A.3, we have:

$$\sum_{j=1}^N \chi_{ij} = \sum_{i=1}^N \chi_{ij} = 0. \quad (\text{A.5})$$

Furthermore, we consider small charge variations and thus assume a bond polarizability model where $\chi_{ij} = 0$ for i, j second nearest neighbors or beyond. And since, binary semiconductors such as PbS present one type of bond, we note $\chi_{ij} = \chi_b$, with χ_b the polarization of the bond. Therefore, we can also write the on-site term according to χ_b as: $\chi_{i,i} = -n_b(i)\chi_b$, with $n_b(i)$ the number of nearest neighbors of the atom i . The last assumption is to assume that χ_b can be deduced from the bulk static dielectric constant, including the electronic and ionic response.

To extract an analytical formula of χ_b , we are considering a layer of dielectric made of $2N + 1$ planes (001), and with a total thickness of $2Na_0$, where a_0 is the inter-layer distance (see Figure A.1). An external electric field E_0 in the (001) direction induced charge transfer between planes (see eq. A.3), where V and δn are two column matrix of dimension $2N + 1$ and χ a matrix of dimension $(2N + 1)^2$. We know from classical electrostatic that the screened electric field \mathbf{E} due to \mathbf{E}_0 writes:

$$\mathbf{E} = \frac{\mathbf{E}_0}{\epsilon_b} \quad (\text{A.6})$$

and since the potential varies linearly along (001) direction, the potential in the layer i writes:

$$V_i = \frac{\mathbf{E}_0 a_0}{\epsilon_b}. \quad (\text{A.7})$$

Furthermore, we consider the charge transfer δn_i of the plane N_i in a cell of surface a_0^2 . Since there is one bond per surface area a_0^2 between two planes, the off-diagonal elements of χ write:

$$\chi_{i,j} = \chi_b. \quad (\text{A.8})$$

Therefore, combining the eqs. A.8 and A.5, the diagonal elements write:

$$\begin{aligned} \chi_{i,i} &= -2\chi_b \text{ for inner planes} \\ &= -\chi_b \text{ for surface planes} \end{aligned} \quad (\text{A.9})$$

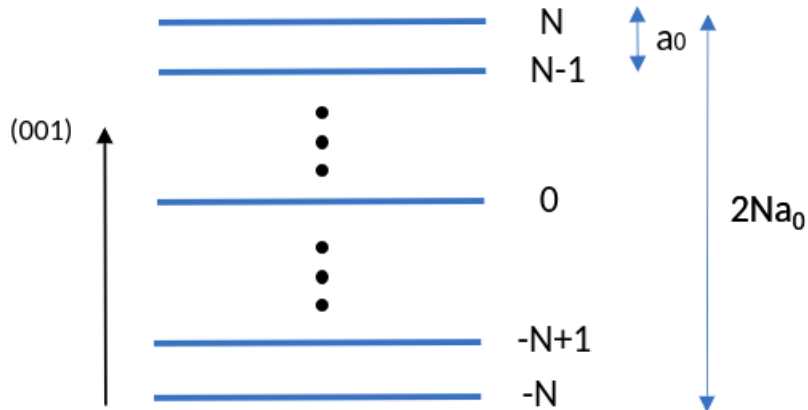


Figure A.1: Illustration of an atomic layer in the (001) direction.

Then feeding the eq. A.3, with the eqs. A.8, A.9, and A.7, we can obtain the charge transfer for the planes. We make the distinction between the inner planes

and the surface planes which are the upper plane denoted N and the lower denoted $-N$ (see Figure A.1).

For the inner plane:

$$\begin{aligned}\delta n_i &= -2(\chi_b)V_i + \chi_b V_{i+1} + \chi_b V_{i-1} \\ &= \frac{E_0 a_0 \chi_b}{\epsilon_b} [-2i + (i+1) + (i-1)] \\ &= 0\end{aligned}\tag{A.10}$$

For the upper plane:

$$\begin{aligned}\delta n_N &= -\chi_b V_N + \chi_b V_{N-1} \\ &= \frac{E_0 a_0 \chi_b}{\epsilon_b} [-N + N - 1] \\ &= \frac{-\chi_b E_0 a_0}{\epsilon_b}\end{aligned}\tag{A.11}$$

For the lower plane:

$$\begin{aligned}\delta n_{-N} &= -\chi_b V_{-N} + \chi_b V_{-N+1} \\ &= \frac{E_0 a_0 \chi_b}{\epsilon_b} [N - N + 1] \\ &= \frac{\chi_b E_0 a_0}{\epsilon_b}\end{aligned}\tag{A.12}$$

As a result, the transfer of charge accumulates on the surface letting the upper and lower planes with a charge Q :

$$Q = \frac{\chi_b e^2 E_0 a_0^3}{\epsilon_b}.\tag{A.13}$$

In addition, using the Gauss theorem with a surface surrounding one of the two planes, we can write:

$$\int \mathbf{E} \cdot d\mathbf{S} = 4\pi Q\tag{A.14}$$

where \mathbf{E} is the sum of the external field \mathbf{E}_0 and the screened field \mathbf{E} (see eq. A.6). Combining the eqs. A.13 and A.14, it finally gives:

$$\begin{aligned}\epsilon_b - 1 &= \frac{4\pi\chi_b}{a_0} \\ \implies \chi_b &= \frac{a_0}{4\pi} [\epsilon_b - 1].\end{aligned}\tag{A.15}$$

In Chapter 6, we choose the static permittivity of bulk PbS $\epsilon_b = 170$.

A.2 DFT, drop of potential

Here are given the drops of potential obtained by DFT for PbS slabs passivated by ligands (see Chapter 6 for details).

Ligand	Configuration	ΔV (eV)
Clean surface	-	0.00
F	-	-1.85
Cl	-	-3.02
Br	-	-2.66
I	-	-1.97
BT	-	0.40
1,2-BDT	Bidentate <100>	0.29
	Monodentate	0.14
1,3-BDT	Bidentate <100>	0.14
	Monodentate	-0.17
1,2-EDT	Bidentate <100>	-0.99
	Monodentate	-0.76
MPA	Thiolate	-1.56
	Carboxylate	-1.12

Table A.1: Drop of potential (ΔV) extracted by DFT for (100) PbS slabs passivated by various ligands.

Ligand	Configuration	ΔV (eV)
Clean surface	-	0.00
F	-	-1.43
Cl	-	-2.10
Br	-	-1.97
I	-	-1.44
BT	-	0.44
1,2-BDT	Bidentate	-0.39
	Monodentate	0.25
1,3-BDT	Bidentate	-0.10
	Monodentate	-0.50
1,2-EDT	Bidentate	0.17
	Monodentate	-1.02
MPA	Thiolate	-2.24
	Carboxylate	-1.09

Table A.2: Drop of potential (ΔV) extracted for (111) PbS slabs passivated by various ligands.

Bibliography

- [1] Jun Ohta. *Smart CMOS image sensors and applications*. CRC press, 2020.
- [2] J. S. Steckel, E. Josse, A. G. Pattantyus-Abraham, M. Bidaud, B. Mortini, H. Bilgen, O. Arnaud, S. Allegret-Maret, F. Saguin, L. Mazet, S. Lhostis, T. Berger, K. Haxaire, L. L. Chapelon, L. Parmigiani, P. Gouraud, M. Brihoum, P. Bar, M. Guillermet, S. Favreau, R. Duru, J. Fantuz, S. Ricq, D. Ney, I. Hammad, D. Roy, A. Arnaud, B. Vianne, G. Nayak, N. Virollet, V. Farys, P. Malinge, A. Tournier, F. Lalanne, A. Crocherie, J. Galvier, S. Rabary, O. Noblanc, H. Wehbe-Alause, S. Acharya, A. Singh, J. Meitzner, D. Aher, H. Yang, J. Romero, B. Chen, C. Hsu, K. C. Cheng, Y. Chang, M. Sarmiento, C. Grange, E. Mazaleyrat, and K. Rochereau. 1.62 μ m Global Shutter Quantum Dot Image Sensor Optimized for Near and Shortwave Infrared. In *2021 IEEE Int. Electron Devices Meet.*, pages 23.4.1–23.4.4. IEEE, dec 2021.
- [3] Peter Y. Zavalij Vitalij K. Pecharsky. *Fundamentals of Powder Diffraction and Structural Characterization of Materials*. Springer Science+Business Media, New-York, 2005.
- [4] Sehrish Gull, M Haris Jamil, Xiuwen Zhang, Hoi sing Kwok, and Guijun Li. Stokes Shift in Inorganic Lead Halide Perovskites: Current Status and Perspective. *ChemistryOpen*, 11(3), 2022.
- [5] Williams, David B. and C. Barry Carter. *Transmission electron microscopy*. Springer, 2008.
- [6] Louis Daudon. Thermogravimétrie. 33(0):0–22, 2011.
- [7] Peter Reiss, Marie Carrière, Christophe Lincheneau, Louis Vaure, and Sudarsan Tamang. Synthesis of Semiconductor Nanocrystals, Focusing on Non-toxic and Earth-Abundant Materials. *Chem. Rev.*, 116(18):10731–10819, 2016.
- [8] Haobo Wu and Zhijun Ning. Tutorial: Lead sulfide colloidal quantum dot infrared photodetector. *J. Appl. Phys.*, 133(4):41101, jan 2023.
- [9] Jianbing Zhang, Ryan W. Crisp, Jianbo Gao, Daniel M. Kroupa, Matthew C. Beard, and Joseph M. Luther. Synthetic Conditions for High-Accuracy Size Control of PbS Quantum Dots. *J. Phys. Chem. Lett.*, 6(10):1830–1833, 2015.
- [10] Ludovico Cademartiri, Jacopo Bertolotti, Riccardo Sapienza, Diederik S. Wiersma, Georg Von Freymann, and Geoffrey A. Ozin. Multigram scale, solventless, and diffusion-controlled route to highly monodisperse PbS nanocrystals. *J. Phys. Chem. B*, 110(2):671–673, 2006.

- [11] Jianbing Zhang, Jianbo Gao, Elisa M. Miller, Joseph M. Luther, and Matthew C. Beard. Diffusion-controlled synthesis of PbS and PbSe quantum dots with in situ halide passivation for quantum dot solar cells. *ACS Nano*, 8(1):614–622, 2014.
- [12] Mark P Hendricks, Michael P Campos, Gregory T Cleveland, Ilan Jen-La Plante, and Jonathan S Owen. A tunable library of substituted thiourea precursors to metal sulfide nanocrystals. *Science*, 348(6240):1226–1230, jun 2015.
- [13] Yao Liu, Markelle Gibbs, James Puthussery, Steven Gaik, Rachelle Ihly, Hugh W. Hillhouse, and Matt Law. Dependence of carrier mobility on nanocrystal size and ligand length in pbse nanocrystal solids. *Nano Lett.*, 10(5):1960–1969, 2010.
- [14] Pralay K. Santra, Axel F. Palmstrom, Jukka T. Tanskanen, Nuoya Yang, and Stacey F. Bent. Improving performance in colloidal quantum dot solar cells by tuning band alignment through surface dipole moments. *J. Phys. Chem. C*, 119(6):2996–3005, 2015.
- [15] Changming Fang, Marijn A. Van Huis, Daniël Vanmaekelbergh, and Henny W. Zandbergen. Energetics of polar and nonpolar facets of PbSe nanocrystals from theory and experiment. *ACS Nano*, 4(1):211–218, 2010.
- [16] Clive R. Bealing, William J. Baumgardner, Joshua J. Choi, Tobias Hanrath, and Richard G. Hennig. Predicting nanocrystal shape through consideration of surface-ligand interactions. *ACS Nano*, 6(3):2118–2127, 2012.
- [17] Hyekeyoung Choi, Jae Hyeon Ko, Yong Hyun Kim, and Sohee Jeong. Steric-hindrance-driven shape transition in PbS quantum dots: Understanding size-dependent stability. *J. Am. Chem. Soc.*, 135(14):5278–5281, 2013.
- [18] Yang Liu, Guozheng Shi, Zeke Liu, and Wanli Ma. Toward printable solar cells based on PbX colloidal quantum dot inks. *Nanoscale Horizons*, 6(1):8–23, 2021.
- [19] Younghoon Kim, Fanglin Che, Jea Woong Jo, Jongmin Choi, F. Pelayo García de Arquer, Oleksandr Voznyy, Bin Sun, Junghwan Kim, Min Jae Choi, Rafael Quintero-Bermudez, Fengjia Fan, Chih Shan Tan, Eva Bladt, Grant Walters, Andrew H. Proppe, Chengqin Zou, Haifeng Yuan, Sara Bals, Johan Hofkens, Maarten B.J. Roeffaers, Sjoerd Hoogland, and Edward H. Sargent. A Facet-Specific Quantum Dot Passivation Strategy for Colloid Management and Efficient Infrared Photovoltaics. *Adv. Mater.*, 31(17):1–8, 2019.
- [20] Mohan Yuan, Xia Wang, Xiao Chen, Jungang He, Kanghua Li, Boxiang Song, Huicheng Hu, Liang Gao, Xinzheng Lan, Chao Chen, and Jiang Tang. Phase-Transfer Exchange Lead Chalcogenide Colloidal Quantum Dots: Ink Preparation, Film Assembly, and Solar Cell Construction. *Small*, 18(2):1–17, 2022.
- [21] Iwan Moreels, Karel Lambert, Dries Smeets, David De Muynck, Tom Nollet, José C. Martins, Frank Vanhaecke, André Vantomme, Christophe Delerue,

- Guy Allan, and Zeger Hens. Size-dependent optical properties of colloidal PbS quantum dots. *ACS Nano*, 3(10):3023–3030, 2009.
- [22] G. Alan Harcourt. Tables for the identification of ore minerals by x-ray powder patterns. *J. Mineral. Soc. Am.*, 1942.
- [23] Mengfan Gu, Yongjie Wang, Fan Yang, Kunyuan Lu, Ye Xue, Tian Wu, Honghua Fang, Sijie Zhou, Yannan Zhang, Xufeng Ling, Yalong Xu, Fangchao Li, Jianyu Yuan, Maria Antonietta Loi, Zeke Liu, and Wanli Ma. Stable PbS quantum dot ink for efficient solar cells by solution-phase ligand engineering. *J. Mater. Chem. A*, 7(26):15951–15959, 2019.
- [24] Min Jae Choi, F. Pelayo García de Arquer, Andrew H. Proppe, Ali Seifitokaldani, Jongmin Choi, Junghwan Kim, Se Woong Baek, Mengxia Liu, Bin Sun, Margherita Biondi, Benjamin Scheffel, Grant Walters, Dae Hyun Nam, Jea Woong Jo, Olivier Ouellette, Oleksandr Voznyy, Sjoerd Hoogland, Shana O. Kelley, Yeon Sik Jung, and Edward H. Sargent. Cascade surface modification of colloidal quantum dot inks enables efficient bulk homojunction photovoltaics. *Nat. Commun.*, 11(1):1–9, 2020.
- [25] Martin. *Electronic Structure: Basic Theory and Practical Methods*, volume 21. 2006.
- [26] Gabriel Mugny. Simulation et modèles prédictifs pour les nanodispositifs avancés à canaux à base de matériaux alternatifs. 2017.
- [27] Christophe Delerue. *Nanostructure- Theory and Modeling*. 2003.
- [28] G. Allan and C. Delerue. Confinement effects in PbSe quantum wells and nanocrystals. *Phys. Rev. B - Condens. Matter Mater. Phys.*, 70(24):1–9, 2004.
- [29] Bilal Chehaibou, Eva Izquierdo, Audrey Chu, Claire Abadie, Mariarosa Cavallo, Adrien Khalili, Tung Huu Dang, Charlie Gréboval, Xiang Zhen Xu, Sandrine Ithurria, Grégory Vincent, Bruno Gallas, Gabriel Mugny, Arthur Arnaud, Emmanuel Lhuillier, and Christophe Delerue. The complex optical index of PbS nanocrystal thin films and their use for short wave infrared sensor design. *Nanoscale*, 14(7):2711–2721, 2022.
- [30] Jorick Maes, Nicolo Castro, Kim De Nolf, Willem Walravens, Benjamin Abécassis, and Zeger Hens. Size and concentration determination of colloidal nanocrystals by small-angle x-ray scattering. *Chem. Mater.*, 30(12):3952–3962, 2018.
- [31] Alexander N. Poddubny, Valentina M. Litvyak, Mikhail O. Nestoklon, Roman V. Cherbunin, Valerii V. Golubkov, Petr A. Onushchenko, Anastasiya N. Babkina, Alexei A. Onushchenko, and Serguei V. Goupalov. Role of Valley Anisotropy in Optical Absorption of Monodisperse PbS Nanocrystals. *J. Phys. Chem. C*, 121(49):27766–27773, 2017.
- [32] Mark C Weidman, Megan E Beck, Rachel S Hoffman, Ferry Prins, and William A Tisdale. Monodisperse, air-stable PbS nanocrystals via precursor stoichiometry control. *ACS Nano*, 8(6):6363–6371, 2014.

- [33] Philippe B. Green, Ziqi Li, and Mark W.B. Wilson. PbS Nanocrystals Made with Excess PbCl₂ Have an Intrinsic Shell that Reduces Their Stokes Shift. *J. Phys. Chem. Lett.*, 10(19):5897–5901, 2019.
- [34] Hossein Beygi, Seyed Abdolkarim Sajjadi, Abolfazl Babakhani, Jeff F. Young, and Frank C.J.M. van Veggel. Surface chemistry of as-synthesized and air-oxidized PbS quantum dots. *Appl. Surf. Sci.*, 457(June):1–10, 2018.
- [35] Roberto Grisorio, Doriana Debellis, Gian Paolo Suranna, Giuseppe Gigli, and Carlo Giansante. The Dynamic Organic/Inorganic Interface of Colloidal PbS Quantum Dots. *Angew. Chemie - Int. Ed.*, 55(23):6628–6633, 2016.
- [36] Guy Allan and Christophe Delerue. Tight-binding calculations of the optical properties of HgTe nanocrystals. *Phys. Rev. B - Condens. Matter Mater. Phys.*, 86(16):1–6, 2012.
- [37] Esther Groeneveld, Christophe Delerue, Guy Allan, Yann Michel Niquet, and Celso De Mello Donegá. Size dependence of the exciton transitions in colloidal CdTe quantum dots. *J. Phys. Chem. C*, 116(43):23160–23167, 2012.
- [38] Margaret H. Hudson, Menglu Chen, Vladislav Kamysbayev, Eric M. Janke, Xinzhen Lan, Guy Allan, Christophe Delerue, Byeongdu Lee, Philippe Guyot-Sionnest, and Dmitri V. Talapin. Conduction Band Fine Structure in Colloidal HgTe Quantum Dots. *ACS Nano*, 12(9):9397–9404, 2018.
- [39] Haozhi Zhang and Philippe Guyot-Sionnest. Shape-Controlled HgTe Colloidal Quantum Dots and Reduced Spin-Orbit Splitting in the Tetrahedral Shape. *J. Phys. Chem. Lett.*, 11(16):6860–6866, 2020.
- [40] Bilal Chehaibou, Claire Abadie, Yoann Prado, Xiang Zhen Xu, Grégory Vincent, Bruno Gallas, Gabriel Mugny, Arthur Arnaud, Emmanuel Lhuillier, and Christophe Delerue. Modeling HgTe Complex Optical Index from Bulk to Nanocrystal Layers. *J. Phys. Chem. C*, jul 2023.
- [41] S. E. Kohn, P. Y. Yu, Y. Petroff, Y. R. Shen, Y. Tsang, and M. L. Cohen. Electronic band structure and optical properties of PbTe, PbSe, and PbS. *Phys. Rev. B*, 8(4):1477–1488, 1973.
- [42] Sadao Adachi. *Optical Constants of Crystalline and Amorphous Semiconductors: numerical data and graphical information*. 2013.
- [43] Iwan Moreels, Guy Allan, Bram De Geyter, Ludger Wirtz, Christophe Delerue, and Zeger Hens. Dielectric function of colloidal lead chalcogenide quantum dots obtained by a Kramers-Krönig analysis of the absorbance spectrum. *Phys. Rev. B - Condens. Matter Mater. Phys.*, 81(23):1–7, 2010.
- [44] D. J. Chadi, John P. Walter, Marvin L. Cohen, Y. Petroff, and M. Balkanski. Reflectivities and electronic band structures of CdTe and HgTe. *Phys. Rev. B*, 5(8):3058–3064, 1972.
- [45] W. Szuszkiewicz, A. M. Witowski, and M. Grynberg. The Dynamic Dielectric Function in HgSe and HgTe. *Phys. Status Solidi*, 87(2):637–645, 1978.

-
- [46] Herbert Wormeester and Thomas W.H. Oates. *Ellipsometry at the Nanoscale*. 2013.
- [47] Chia-Hao M. Chuang, Patrick R. Brown, Vladimir Bulović, and Mounqi G. Bawendi. Improved performance and stability in quantum dot solar cells through band alignment engineering. *Nat. Mater.*, 13(8):796–801, aug 2014.
- [48] Zhenyu Yang, Oleksandr Voznyy, Mengxia Liu, Mingjian Yuan, Alexander H. Ip, Osman S. Ahmed, Larissa Levina, Sachin Kinge, Sjoerd Hoogland, and Edward H. Sargent. All-Quantum-Dot Infrared Light-Emitting Diodes. *ACS Nano*, 9(12):12327–12333, dec 2015.
- [49] Hisao Ishii, Kiyoshi Sugiyama, Eisuke Ito, and Kazuhiko Seki. Energy Level Alignment and Interfacial Electronic Structures at Organic/Metal and Organic/Organic Interfaces. *Adv. Mater.*, 11(8):605–625, jun 1999.
- [50] M. G. Helander, M. T. Greiner, Z. B. Wang, and Z. H. Lu. Pitfalls in measuring work function using photoelectron spectroscopy. *Appl. Surf. Sci.*, 256(8):2602–2605, 2010.
- [51] David Cahen and Antoine Kahn. Electron energetics at surfaces and interfaces: Concepts and experiments. *Adv. Mater.*, 15(4):271–277, 2003.
- [52] Shenyuan Yang, David Prendergast, and Jeffrey B. Neaton. Tuning semiconductor band edge energies for solar photocatalysis via surface ligand passivation. *Nano Lett.*, 12(1):383–388, 2012.
- [53] Daniel M. Kroupa, Márton Vörös, Nicholas P. Brawand, Brett W. McNichols, Elisa M. Miller, Jing Gu, Arthur J. Nozik, Alan Sellinger, Giulia Galli, and Matthew C. Beard. Tuning colloidal quantum dot band edge positions through solution-phase surface chemistry modification. *Nat. Commun.*, 8(May):2–9, 2017.
- [54] Abiseka Akash Ganesan, Arjan J. Houtepen, and Ryan W. Crisp. Quantum dot solar cells: Small beginnings have large impacts. *Appl. Sci.*, 8(10), 2018.
- [55] Hao Zhang, Jaeyoung Jang, Wenyong Liu, and Dmitri V. Talapin. Colloidal nanocrystals with inorganic halide, pseudohalide, and halometallate ligands. *ACS Nano*, 8(7):7359–7369, 2014.
- [56] J. C. Slater and G. F. Koster. Simplified LCAO Method for the Periodic Potential Problem. *Phys. Rev.*, 94(6):1498–1524, jun 1954.
- [57] J Al-Khalili. Book of optics. *Nature*, 518(7538):164–165, 2015.
- [58] H. Figgemeier, M. Benecke, K. Hofmann, R. Oelmaier, A. Sieck, J. Wendler, and J. Ziegler. SWIR detectors for night vision at AIM. *Infrared Technol. Appl. XL*, 9070(June 2014):907008, 2014.
- [59] Kelsey M Judd, Michael Thornton, and Austin Richards. Automotive sensing: assessing the impact of fog on LWIR, MWIR, SWIR, visible, and lidar performance. (May 2019):50, 2019.

- [60] Jessica A. Carr, Tulio A. Valdez, Oliver T. Bruns, and Mounqi G. Bawendi. Using the shortwave infrared to image middle ear pathologies. *Proc. Natl. Acad. Sci. U. S. A.*, 113(36):9989–9994, 2016.
- [61] Dimitris Manolakis, Michael Pieper, Eric Truslow, Ronald Lockwood, Andrew Weisner, John Jacobson, and Thomas Cooley. Longwave infrared hyperspectral imaging: Principles, progress, and challenges. *IEEE Geosci. Remote Sens. Mag.*, 7(2):72–100, 2019.
- [62] Chao Xie and Feng Yan. Flexible Photodetectors Based on Novel Functional Materials. *Small*, 13(43):1–36, 2017.
- [63] Maksym Yarema, Olesya Yarema, Weyde M.M. Lin, Sebastian Volk, Nuri Yazdani, Deniz Bozyigit, and Vanessa Wood. Upscaling Colloidal Nanocrystal Hot-Injection Syntheses via Reactor Underpressure. *Chem. Mater.*, 29(2):796–803, 2017.
- [64] Sudarsan TaMang, Sunghee Lee, Hyekyoung Choi, and Sohee Jeong. Tuning size and size distribution of colloidal InAs nanocrystals via continuous supply of prenucleation clusters on nanocrystal seeds. *Chem. Mater.*, 28(22):8119–8122, 2016.
- [65] Bertille Martinez, Julien Ramade, Clément Livache, Nicolas Goubet, Audrey Chu, Charlie Gréboval, Junling Qu, William L. Watkins, Loïc Becerra, Erwan Dandeu, Jean Louis Fave, Christophe Méthivier, Emmanuelle Lacaze, and Emmanuel Lhuillier. HgTe Nanocrystal Inks for Extended Short-Wave Infrared Detection. *Adv. Opt. Mater.*, 7(15):1–8, 2019.
- [66] Vanessa Wood and Vladimir Bulović. Colloidal quantum dot light-emitting devices. *Nano Rev.*, 1(1):5202, 2010.
- [67] Cherie R. Kagan, Efrat Lifshitz, Edward H. Sargent, and Dmitri V. Talapin. Building devices from colloidal quantum dots. *Science*, 353(6302), 2016.
- [68] Stijn Goossens, Gerasimos Konstantatos, and Antonios Oikonomou. Colloidal Quantum Dot Image Sensors: Technology and Marketplace Opportunities. *Inf. Disp. (1975)*, 37(6):18–23, 2021.
- [69] Charlie Gréboval, Audrey Chu, Nicolas Goubet, Clément Livache, Sandrine Ithurria, and Emmanuel Lhuillier. Mercury Chalcogenide Quantum Dots: Material Perspective for Device Integration. *Chem. Rev.*, 121(7):3627–3700, 2021.
- [70] Zhixu Wu, Yingdong Ou, Mengqiang Cai, Yuhao Wang, Rongxin Tang, and Yong Xia. Short-Wave Infrared Photodetectors and Imaging Sensors Based on Lead Chalcogenide Colloidal Quantum Dots. *Adv. Opt. Mater.*, 11(1):1–32, 2023.
- [71] CBea Murray, David J Norris, and Mounqi G Bawendi. Synthesis and characterization of nearly monodisperse CdE (E= sulfur, selenium, tellurium) semiconductor nanocrystallites. *J. Am. Chem. Soc.*, 115(19):8706–8715, 1993.

- [72] Michael P. Campos, Mark P. Hendricks, Alexander N. Beecher, Willem Walravens, Robert A. Swain, Gregory T. Cleveland, Zeger Hens, Matthew Y. Sfeir, and Jonathan S. Owen. A Library of Selenourea Precursors to PbSe Nanocrystals with Size Distributions near the Homogeneous Limit. *J. Am. Chem. Soc.*, 139(6):2296–2305, 2017.
- [73] James E Murphy, Matthew C Beard, Andrew G Norman, S Phillip Ahrenkiel, Justin C Johnson, Pingrong Yu, Olga I Mičić, Randy J Ellingson, and Arthur J Nozik. PbTe colloidal nanocrystals: Synthesis, characterization, and multiple exciton generation. *J. Am. Chem. Soc.*, 128(10):3241–3247, 2006.
- [74] Sean Keuleyan, Emmanuel Lhuillier, and Philippe Guyot-Sionnest. Synthesis of Colloidal HgTe Quantum Dots for Narrow Mid-IR Emission and Detection. *J. Am. Chem. Soc.*, 133(41):16422–16424, oct 2011.
- [75] Ranjana Yadav, Yongju Kwon, Céline Rivaux, Christine Saint-Pierre, Wai Li Ling, and Peter Reiss. Narrow Near-Infrared Emission from InP QDs Synthesized with Indium(I) Halides and Aminophosphine. *J. Am. Chem. Soc.*, (2), 2022.
- [76] Tianshuo Zhao, Nuri Oh, Davit Jishkariani, Mingliang Zhang, Han Wang, Na Li, Jennifer D. Lee, Chenjie Zeng, Manisha Muduli, Hak Jong Choi, Dong Su, Christopher B. Murray, and Cherie R. Kagan. General Synthetic Route to High-Quality Colloidal III-V Semiconductor Quantum Dots Based on Pnictogen Chlorides. *J. Am. Chem. Soc.*, 141(38):15145–15152, 2019.
- [77] Haipeng Lu, Gerard M. Carroll, Nathan R. Neale, and Matthew C. Beard. Infrared quantum dots: Progress, challenges, and opportunities. *ACS Nano*, 13(2):939–953, 2019.
- [78] Tom Nakotte, Simon G. Munyan, John W. Murphy, Steven A. Hawks, Shin Young Kang, Jinkyu Han, and Anna M. Hiszpanski. Colloidal quantum dot based infrared detectors: extending to the mid-infrared and moving from the lab to the field. *J. Mater. Chem. C*, 10(3):790–804, 2022.
- [79] Iwan Moreels, Karel Lambert, Dries Smeets, David De Muynck, Tom Nollet, José C. Martins, Frank Vanhaecke, André Vantomme, Christophe Delerue, Guy Allan, and Zeger Hens. Size-Dependent Optical Properties of Colloidal PbS Quantum Dots. *ACS Nano*, 3(10):3023–3030, oct 2009.
- [80] Iñigo Ramiro, Onur Özdemir, Sotirios Christodoulou, Shuchi Gupta, Mariona Dalmasas, Iacopo Torre, and Gerasimos Konstantatos. Mid- And Long-Wave Infrared Optoelectronics via Intraband Transitions in PbS Colloidal Quantum Dots. *Nano Lett.*, 20(2):1003–1008, 2020.
- [81] Nicolas Goubet, Amardeep Jagtap, Clément Livache, Bertille Martinez, Hervé Portalès, Xiang Zhen Xu, Ricardo P.S.M. Lobo, Benoit Dubertret, and Emmanuel Lhuillier. Terahertz HgTe Nanocrystals: Beyond Confinement. *J. Am. Chem. Soc.*, 140(15):5033–5036, 2018.

- [82] Pawel E. Malinowski, Epimitheas Georgitzikis, Jorick Maes, Ioanna Vamvaka, Fortunato Frazzica, Jan Van Olmen, Piet De Moor, Paul Heremans, Zeger Hens, and David Cheyns. Thin-film quantum dot photodiode for monolithic infrared image sensors. *Sensors*, 17(12), 2017.
- [83] S Manda, R Matsumoto, S Saito, S Maruyama, H Minari, T Hirano, T Takachi, N Fujii, Y Yamamoto, Y Zaizen, and Others. High-definition Visible-SWIR InGaAs Image Sensor using Cu-Cu Bonding of III-V to Silicon Wafer. In *2019 IEEE Int. Electron Devices Meet.* IEEE, 2019.
- [84] Adrian Romero Campelo. *Quantum dots : concept and application for image sensors*. PhD thesis, Universidad de Sevilla, 2021.
- [85] Gaoqi Cao, Fang Wang, Meng Peng, Xiumei Shao, Bo Yang, Weida Hu, Xue Li, Jing Chen, Yabin Shan, Peisong Wu, Laigui Hu, Ran Liu, Haimei Gong, Chunxiao Cong, and Zhi Jun Qiu. Multicolor Broadband and Fast Photodetector Based on InGaAs–Insulator–Graphene Hybrid Heterostructure. *Adv. Electron. Mater.*, 6(3), mar 2020.
- [86] Clément Livache, Bertille Martinez, Nicolas Goubet, Julien Ramade, and Emmanuel Lhuillier. Road map for nanocrystal based infrared photodetectors. *Front. Chem.*, 6(NOV):1–11, 2018.
- [87] Oleksandr Voznyy, Larissa Levina, James Z. Fan, Mikhail Askerka, Ankit Jain, Min Jae Choi, Olivier Ouellette, Petar Todorović, Laxmi K. Sagar, and Edward H. Sargent. Machine Learning Accelerates Discovery of Optimal Colloidal Quantum Dot Synthesis. *ACS Nano*, 13(10):11122–11128, 2019.
- [88] Nick Reilly, Michael Wehrung, Ryan Andrew O’Dell, and Liangfeng Sun. Ultrasmall colloidal PbS quantum dots. *Mater. Chem. Phys.*, 147(1-2):1–4, 2014.
- [89] Iwan Moreels, Yolanda Justo, Bram De Geyter, Katrien Haestraete, José C. Martins, and Zeger Hens. Size-Tunable, Bright, and Stable PbS Quantum Dots: A Surface Chemistry Study. *ACS Nano*, 5(3):2004–2012, 2012.
- [90] Margaret A. Hines and Gregory D. Scholes. Colloidal PbS Nanocrystals with Size-Tunable Near-Infrared Emission: Observation of Post-Synthesis Self-Narrowing of the Particle Size Distribution. *Adv. Mater.*, 15(21):1844–1849, 2003.
- [91] Soon Gu Kwon and Taeghwan Hyeon. Formation mechanisms of uniform nanocrystals via hot-injection and heat-up methods. *Small*, 7(19):2685–2702, 2011.
- [92] Clemens Burda, Xiaobo Chen, Radha Narayanan, and Mostafa A. El-Sayed. *Chemistry and properties of nanocrystals of different shapes*, volume 105. 2005.
- [93] Nguyen T.K. Thanh, N. Maclean, and S. Mahiddine. Mechanisms of nucleation and growth of nanoparticles in solution. *Chem. Rev.*, 114(15):7610–7630, 2014.
- [94] Jonathan De Roo. Chemical Considerations for Colloidal Nanocrystal Synthesis †. *Chem. Mater.*, 34(13):5766–5779, 2022.

- [95] Wenran Wang, Meng Zhang, Zhenxiao Pan, Gill M. Biesold, Shuang Liang, Huashang Rao, Zhiqun Lin, and Xinhua Zhong. Colloidal Inorganic Ligand-Capped Nanocrystals: Fundamentals, Status, and Insights into Advanced Functional Nanodevices. *Chem. Rev.*, 122(3):4091–4162, 2022.
- [96] Steven H Simon. *The Oxford solid state basics*. OUP Oxford, 2013.
- [97] Bernard Dennis Cullity. *Elements of X-ray Diffraction*. Addison-Wesley Publishing, 1956.
- [98] Zeger Hens and Iwan Moreels. Light absorption by colloidal semiconductor quantum dots. *J. Mater. Chem.*, 22(21):10406–10415, 2012.
- [99] M LEGRAND. Spectrophotometrie d’absorption dans l’ultraviolet, le visible et l’infrarouge. *Tech. l’ingénieur*, 1982.
- [100] Bernard Humbert, Manuel Dossot, and Cnrs-univ De Lorraine. l’ infrarouge Spectrométrie d’ absorption dans l’ infrarouge. *Tech. l’ingénieur*, 33(0):0–29, 2012.
- [101] Jai Singh. *Optical Properties of Condensed Matter and Applications - Wiley Series in Materials for Electronic - amp - Optoelectronic Applications*. 2006.
- [102] A. Franceschetti and S. T. Pantelides. Excited-state relaxations and Franck-Condon shift in Si quantum dots. *Phys. Rev. B - Condens. Matter Mater. Phys.*, 68(3):333131–333134, 2003.
- [103] Zhonghua Yu, Jingbo Li, Donald B. O’Connor, Lin Wang Wang, and Paul F. Barbara. Large resonant Stokes shift in CdS nanocrystals. *J. Phys. Chem. B*, 107(24):5670–5674, 2003.
- [104] D. O. Demchenko and Lin Wang Wang. Optical transitions and nature of Stokes shift in spherical CdS quantum dots. *Phys. Rev. B - Condens. Matter Mater. Phys.*, 73(15):1–5, 2006.
- [105] Yun Liu, Donghun Kim, Owen P. Morris, David Zhitomirsky, and Jeffrey C. Grossman. Origins of the Stokes Shift in PbS Quantum Dots: Impact of Polydispersity, Ligands, and Defects. *ACS Nano*, 12(3):2838–2845, 2018.
- [106] Oleksandr Voznyy, Larissa Levina, Fengjia Fan, Grant Walters, James Z. Fan, Amirreza Kiani, Alexander H. Ip, Susanna M. Thon, Andrew H. Proppe, Mengxia Liu, and Edward H. Sargent. Origins of Stokes Shift in PbS Nanocrystals. *Nano Lett.*, 17(12):7191–7195, 2017.
- [107] Jonathan S. Steckel, Brian K.H. Yen, David C. Oertel, and Mounqi G. Bawendi. On the mechanism of lead chalcogenide nanocrystal formation. *J. Am. Chem. Soc.*, 128(40):13032–13033, 2006.
- [108] Victor K. LaMer and Robert H Dinegar. Theory, Production and Mechanism of Formation of Monodispersed Hydrosols. *J. Am. Chem. Soc.*, 72(11):4847–4854, nov 1950.

- [109] Tadao Sugimoto. Underlying mechanisms in size control of uniform nanoparticles. *J. Colloid Interface Sci.*, 309(1):106–118, 2007.
- [110] Sofie Abe, Richard Karel Čapek, Bram De Geyter, and Zeger Hens. Tuning the postfocused size of colloidal nanocrystals by the reaction rate: From theory to application. *ACS Nano*, 6(1):42–53, 2012.
- [111] Michael P Campos, Jonathan De Roo, Matthew W Greenberg, Brandon Makana McMurtry, Mark Hendricks, Ellie Bennett, Natalie Saenz, Matthew Sfeir, Benjamin Abecassis, Sanjit Ghose, and Jonathan Owen. Growth Kinetics Determine the Polydispersity and Size of PbS and PbSe Nanocrystals. *Chem. Sci.*, 2022.
- [112] Benjamin Abécassis, Matthew W. Greenberg, Vivekananda Bal, Brandon M. McMurtry, Michael P. Campos, Lilian Guillemeney, Benoit Mahler, Sylvain Prevost, Lewis Sharpnack, Mark P. Hendricks, Daniel DeRosha, Ellie Bennett, Natalie Saenz, Baron Peters, and Jonathan S. Owen. Persistent nucleation and size dependent attachment kinetics produce monodisperse PbS nanocrystals. *Chem. Sci.*, 13(17):4977–4983, 2022.
- [113] Gerasimos Konstantatos, Ian Howard, Armin Fischer, Sjoerd Hoogland, Jason Clifford, Ethan Klem, Larissa Levina, and Edward H. Sargent. Ultrasensitive solution-cast quantum dot photodetectors. *Nature*, 442(7099):180–183, 2006.
- [114] Krisztina Szendrei, Fabrizio Cordella, Maksym V. Kovalenko, Michaela Böberl, Günther Hesser, Maksym Yarema, Dorota Jarzab, Oleksandr V. Mikhnenko, Agnieszka Gocalinska, Michele Saba, Francesco Quochi, Andrea Mura, Giovanni Bongiovanni, Paul W.M. Blom, Wolfgang Heiss, and Maria Antonietta Loi. Solution-processable near-IR photodetectors based on electron transfer from PbS nanocrystals to fullerene derivatives. *Adv. Mater.*, 21(6):683–687, 2009.
- [115] Mengxia Liu, Oleksandr Voznyy, Randy Sabatini, F. Pelayo García De Arquer, Rahim Munir, Ahmed Hesham Balawi, Xinzheng Lan, Fengjia Fan, Grant Walters, Ahmad R. Kirmani, Sjoerd Hoogland, Frédéric Laquai, Aram Amassian, and Edward H. Sargent. Hybrid organic-inorganic inks flatten the energy landscape in colloidal quantum dot solids. *Nat. Mater.*, 16(2):258–263, 2017.
- [116] Junfeng Xu, Haowei Wang, Shengyi Yang, Guoqiang Ni, and Bingsuo Zou. High-sensitivity broadband colloidal quantum dot heterojunction photodetector for night-sky radiation. *J. Alloys Compd.*, 764:446–451, 2018.
- [117] Samuel W. Winslow, Yun Liu, James W. Swan, and William A. Tisdale. Quantification of a PbCl_xShell on the Surface of PbS Nanocrystals. *ACS Mater. Lett.*, 1(2):209–216, 2019.
- [118] Simon Kahmann and Maria A. Loi. Trap states in lead chalcogenide colloidal quantum dots - Origin, impact, and remedies. *Appl. Phys. Rev.*, 7(4), 2020.
- [119] Michael A. Boles, Daishun Ling, Taeghwan Hyeon, and Dmitri V. Talapin. The surface science of nanocrystals. *Nat. Mater.*, 15(2):141–153, feb 2016.

- [120] M. L.H. Green. A new approach to the formal classification of covalent compounds of the elements. *J. Organomet. Chem.*, 500(1-2):127–148, 1995.
- [121] Malcolm L.H. Green and Gerard Parkin. Application of the covalent bond classification method for the teaching of inorganic chemistry. *J. Chem. Educ.*, 91(6):807–816, 2014.
- [122] Jonathan Owen. The coordination chemistry of nanocrystal surfaces. *Science*, 347(6222):615–616, 2015.
- [123] J. De Roo, K. De Keukeleere, Z. Hens, and I. Van Driessche. From ligands to binding motifs and beyond; The enhanced versatility of nanocrystal surfaces. *Dalt. Trans.*, 45(34):13277–13283, 2016.
- [124] Oleksandr Voznyy, David Zhitomirsky, Philipp Stadler, Zhijun Ning, Sjoerd Hoogland, and Edward H Sargent. ARTICLE A Charge-Orbital Balance Picture of Doping in Colloidal Quantum Dot. (9):8448–8455, 2012.
- [125] Melody L. Kessler and Jillian L. Dempsey. Mapping the Topology of PbS Nanocrystals through Displacement Isotherms of Surface-Bound Metal Oleate Complexes. *ACS Appl. Mater. Interfaces*, 2020.
- [126] Danylo Zherebetsky, Marcus Scheele, Yingjie Zhang, Noah Bronstein, Christopher Thompson, David Britt, Miquel Salmeron, Paul Alivisatos, and Lin Wang Wang. Hydroxylation of the surface of PbS nanocrystals passivated with oleic acid. *Science*, 344(6190):1380–1384, 2014.
- [127] Kenji Kimura, Kaoru Nakajima, Yoshikazu Fujii, and Michi hiko Manami. Observation of the PbSe(111) surface using high-resolution Rutherford backscattering spectroscopy. *Surf. Sci.*, 318(3):363–367, 1994.
- [128] Iwan Moreels, Bernd Fritzing, José C. Martins, and Zeger Hens. Surface chemistry of colloidal PbSe nanocrystals. *J. Am. Chem. Soc.*, 130(45):15081–15086, 2008.
- [129] Haley D. Hill, Jill E. Millstone, Matthew J. Banholzer, and Chad A. Mirkin. The role radius of curvature plays in thiolated oligonucleotide loading on gold nanoparticles. *ACS Nano*, 3(2):418–424, 2009.
- [130] Danylo Zherebetsky, Marcus Scheele, Yingjie Zhang, Noah Bronstein, Christopher Thompson, David Britt, Miquel Salmeron, Paul Alivisatos, David Britt, Miquel Sahneron, and Paul Alrvisatos. Hydroxylation of the surface with oleic acid PbS nanocrystals nanocrystals passivated PbS passivated. *Science*, 344(6190), 2014.
- [131] Nicholas C. Anderson, Mark P. Hendricks, Joshua J. Choi, and Jonathan S. Owen. Ligand exchange and the stoichiometry of metal chalcogenide nanocrystals: Spectroscopic observation of facile metal-carboxylate displacement and binding. *J. Am. Chem. Soc.*, 135(49):18536–18548, 2013.
- [132] Yannan Zhang, Yuanyuan Kan, Ke Gao, Mengfan Gu, Yao Shi, Xuliang Zhang, Ye Xue, Xuning Zhang, Zeke Liu, Yuan Zhang, Jianyu Yuan, Wanli

- Ma, and Alex K.Y. Jen. Hybrid Quantum Dot/Organic Heterojunction: A Route to Improve Open-Circuit Voltage in PbS Colloidal Quantum Dot Solar Cells. *ACS Energy Lett.*, 5(7):2335–2342, 2020.
- [133] Hong Il Kim, Se Woong Baek, Hyung Jin Cheon, Seung Un Ryu, Seungjin Lee, Min Jae Choi, Kyoungwon Choi, Margherita Biondi, Sjoerd Hoogland, F. P.García de Arquer, Soon Ki Kwon, Yun Hi Kim, Taiho Park, and Edward H. Sargent. A Tuned Alternating D–A Copolymer Hole-Transport Layer Enables Colloidal Quantum Dot Solar Cells with Superior Fill Factor and Efficiency. *Adv. Mater.*, 32(48):1–7, 2020.
- [134] Zhijun Ning, Haopeng Dong, Qiong Zhang, Oleksandr Voznyy, and Edward H. Sargent. Solar cells based on inks of n-type colloidal quantum dots. *ACS Nano*, 8(10):10321–10327, 2014.
- [135] Lei Wang, Yinglin Wang, Yuwen Jia, Xinlu Liu, Ting Liu, Ting Fu, Jinhuan Li, Binbin Weng, Xintong Zhang, and Yichun Liu. Manipulation of Phase-Transfer Ligand-Exchange Dynamics of PbS Quantum Dots for Efficient Infrared Photovoltaics. *J. Phys. Chem. C*, 123(50):30137–30144, 2019.
- [136] James Z. Fan, Nigel T. Andersen, Margherita Biondi, Petar Todorović, Bin Sun, Olivier Ouellette, Jehad Abed, Laxmi K. Sagar, Min Jae Choi, Sjoerd Hoogland, F. Pelayo García de Arquer, and Edward H. Sargent. Mixed Lead Halide Passivation of Quantum Dots. *Adv. Mater.*, 31(48):1–8, 2019.
- [137] Jongmin Choi, Min Jae Choi, Junghwan Kim, Filip Dinic, Petar Todorovic, Bin Sun, Mingyang Wei, Se Woong Baek, Sjoerd Hoogland, F. Pelayo García de Arquer, Oleksandr Voznyy, and Edward H. Sargent. Stabilizing Surface Passivation Enables Stable Operation of Colloidal Quantum Dot Photovoltaic Devices at Maximum Power Point in an Air Ambient. *Adv. Mater.*, 32(7):1–7, 2020.
- [138] Dmitry N. Dirin, Sébastien Dreyfuss, Maryna I. Bodnarchuk, Georgian Nedelcu, Paris Papagiorgis, Grigorios Itskos, and Maksym V. Kovalenko. Lead halide perovskites and other metal halide complexes as inorganic capping ligands for colloidal nanocrystals. *J. Am. Chem. Soc.*, 136(18):6550–6553, 2014.
- [139] Dmytro Bederak, Nataliia Sukharevska, Simon Kahmann, Mustapha Abdu-Aguye, Herman Duim, Dmitry N. Dirin, Maksym V. Kovalenko, Giuseppe Portale, and Maria A. Loi. On the Colloidal Stability of PbS Quantum Dots Capped with Methylammonium Lead Iodide Ligands. *ACS Appl. Mater. Interfaces*, 12(47):52959–52966, 2020.
- [140] Dmytro Bederak, Daniel M. Balazs, Nataliia V. Sukharevska, Artem G. Shulga, Mustapha Abdu-Aguye, Dmitry N. Dirin, Maksym V. Kovalenko, and Maria A. Loi. Comparing Halide Ligands in PbS Colloidal Quantum Dots for Field-Effect Transistors and Solar Cells. *ACS Appl. Nano Mater.*, 1(12):6882–6889, 2018.
- [141] Chase C. Reinhart and Erik Johansson. Colloidally Prepared 3-Mercaptopropionic Acid Capped Lead Sulfide Quantum Dots. *Chem. Mater.*, 27(21):7313–7320, 2015.

- [142] Zhenyu Yang, Alyf Janmohamed, Xinzheng Lan, F. Pelayo García De Arquer, Oleksandr Voznyy, Emre Yassitepe, Gi Hwan Kim, Zhijun Ning, Xiwen Gong, Riccardo Comin, and Edward H. Sargent. Colloidal Quantum Dot Photovoltaics Enhanced by Perovskite Shelling. *Nano Lett.*, 15(11):7539–7543, 2015.
- [143] Benoît Sklénard, Gabriel Mugny, Bilal Chehaibou, Christophe Delerue, Arthur Arnaud, and Jing Li. Size and Solvation Effects on Electronic and Optical Properties of PbS Quantum Dots. *J. Phys. Chem. Lett.*, 13(39):9044–9050, 2022.
- [144] Nir Yaacobi-Gross, Michal Soreni-Harari, Marina Zimin, Shifi Kababya, Asher Schmidt, and Nir Tessler. Molecular control of quantum-dot internal electric field and its application to CdSe-based solar cells. *Nat. Mater.*, 10(12):974–979, 2011.
- [145] Xiaoliang Zhang, Ute B. Cappel, Donglin Jia, Qisen Zhou, Juan Du, Tamara Sloboda, Sebastian Svanström, Fredrik O.L. Johansson, Andreas Lindblad, Erika Giangrisostomi, Ruslan Ovsyannikov, Jianhua Liu, Håkan Rensmo, James M. Gardner, and Erik M.J. Johansson. Probing and Controlling Surface Passivation of PbS Quantum Dot Solid for Improved Performance of Infrared Absorbing Solar Cells. *Chem. Mater.*, 31(11):4081–4091, 2019.
- [146] Daniel M. Balazs, Dmitry N. Dirin, Hong Hua Fang, Loredana Protesescu, Gert H. Ten Brink, Bart J. Kooi, Maksym V. Kovalenko, and Maria Antonietta Loi. Counterion-Mediated Ligand Exchange for PbS Colloidal Quantum Dot Superlattices. *ACS Nano*, 9(12):11951–11959, 2015.
- [147] Michèle Desouter-Lecomte, Yves Justum, and Xavier Chapuisat. *Introduction à la théorie quantique*. 2017.
- [148] Claude Cohen-Tannoudji, Bernard Diu, and Frank Laloe. *Quantum Mechanics, Volume 2*. 1986.
- [149] P. Hohenberg and W. Kohn. Inhomogeneous Electron Gas. *Phys. Rev.*, 136(3B):B864–B871, nov 1964.
- [150] W. Kohn and L. J. Sham. Self-Consistent Equations Including Exchange and Correlation Effects. *Phys. Rev.*, 140(4A):A1133–A1138, nov 1965.
- [151] Jochen Heyd, Gustavo E. Scuseria, and Matthias Ernzerhof. Hybrid functionals based on a screened Coulomb potential. *J. Chem. Phys.*, 118(18):8207–8215, 2003.
- [152] Takao Kotani, Mark Van Schilfgaarde, and Sergey V. Faleev. Quasiparticle self-consistent GW method: A basis for the independent-particle approximation. *Phys. Rev. B - Condens. Matter Mater. Phys.*, 76(16), 2007.
- [153] Tie Cheng Li and Pei Qing Tong. Time-dependent density-functional theory for multicomponent systems. *Phys. Rev. A*, 34(1):529–532, 1986.
- [154] Harrison. *Quantum Wells, Wires and Dots*, volume 133. 2016.

- [155] Volker Heine. The Pseudopotential Concept. *Solid State Phys. - Adv. Res. Appl.*, 24(C):1–36, 1970.
- [156] HEINE V Cohen, L. The Fitting of Pseudopotentials to Experimental Data and Their Subsequent Application. *Solid State Phys. - Adv. Res. Appl.*, 24(C):38–228, 1970.
- [157] J. C. Slater. Wave functions in a periodic potential. *Phys. Rev.*, 51(10):846–851, 1937.
- [158] Conyers Herring. A new method for calculating wave functions in crystals. *Phys. Rev.*, 57(12):1169–1177, 1940.
- [159] James C. Phillips and Leonard Kleinman. New method for calculating wave functions in crystals and molecules. *Phys. Rev.*, 116(2):287–294, 1959.
- [160] Walter A Harrison. *Electronic structure and the properties of solids: the physics of the chemical bond*. Courier Corporation, 2012.
- [161] C. Delerue, M. Lannoo, and G. Allan. *Tight binding for complex semiconductor systems*, volume 227. 2001.
- [162] Felix Bloch. Über die quantenmechanik der elektronen in kristallgittern. *Zeitschrift für Phys.*, 52(7-8):555–600, 1929.
- [163] M. V. Wolkin, J. Jorne, P. M. Fauchet, G. Allan, and C. Delerue. Electronic states and luminescence in porous silicon quantum dots: The role of oxygen. *Phys. Rev. Lett.*, 82(1):197–200, 1999.
- [164] G. Allan, Y. M. Niquet, and C. Delerue. Quantum confinement energies in zinc-blende III-V and group IV semiconductors. *Appl. Phys. Lett.*, 77(5):639–641, 2000.
- [165] C. Delerue, G. Allan, and M. Lannoo. Theoretical aspects of the luminescence of porous silicon. *Phys. Rev. B*, 48(15):11024–11036, 1993.
- [166] Richard Dalven. Electronic Structure of PbS, PbSe, and PbTe. pages 179–224, 1974.
- [167] Su Huai Wei and Alex Zunger. Electronic and structural anomalies in lead chalcogenides. *Phys. Rev. B - Condens. Matter Mater. Phys.*, 55(20):13605–13610, 1997.
- [168] Kerstin Hummer, Andreas Grüneis, and Georg Kresse. Structural and electronic properties of lead chalcogenides from first principles. *Phys. Rev. B - Condens. Matter Mater. Phys.*, 75(19):1–9, 2007.
- [169] Jean Marc Jancu, Reinhard Scholz, Fabio Beltram, and Franco Bassani. Empirical tight-binding calculation for cubic semiconductors: General method and material parameters. *Phys. Rev. B - Condens. Matter Mater. Phys.*, 57(11):6493–6507, 1998.

- [170] A. N. Poddubny, M. O. Nestoklon, and S. V. Goupalov. Anomalous suppression of valley splittings in lead salt nanocrystals without inversion center. *Phys. Rev. B - Condens. Matter Mater. Phys.*, 86(3):2–7, 2012.
- [171] T. E. Thompson, Paul R. Aron, B. S. Chandrasekhar, and D. N. Langenberg. Magnetostriction and Magnetoelastic Quantum Oscillations in p-PbTe. *Phys. Rev. B*, 4(2):518–536, jul 1971.
- [172] A. Svane, N. E. Christensen, M. Cardona, A. N. Chantis, M. Van Schilfhaarde, and T. Kotani. Quasiparticle self-consistent GW calculations for PbS, PbSe, and PbTe: Band structure and pressure coefficients. *Phys. Rev. B - Condens. Matter Mater. Phys.*, 81(24):1–10, 2010.
- [173] J. M. An, A. Franceschetti, S. V. Dudiy, and Alex Zunger. The peculiar electronic structure of PbSe quantum dots. *Nano Lett.*, 6(12):2728–2735, 2006.
- [174] Ivan D. Avdeev, Mikhail O. Nestoklon, and Serguei V. Goupalov. Exciton Fine Structure in Lead Chalcogenide Quantum Dots: Valley Mixing and Crucial Role of Intervalley Electron-Hole Exchange. *Nano Lett.*, 20(12):8897–8902, 2020.
- [175] Abhijeet Paul and Gerhard Klimeck. Atomistic study of electronic structure of PbSe nanowires. *Appl. Phys. Lett.*, 98(21):98–101, 2011.
- [176] H. Preier. Recent advances in lead-chalcogenide diode lasers. *Appl. Phys.*, 20(3):189–206, 1979.
- [177] Sarah Brittman, Adam E. Colbert, Todd H. Brintlinger, Paul D. Cunningham, Michael H. Stewart, William B. Heuer, Rhonda M. Stroud, Joseph G. Tischler, and Janice E. Boercker. Effects of a Lead Chloride Shell on Lead Sulfide Quantum Dots. *J. Phys. Chem. Lett.*, 10(8):1914–1918, 2019.
- [178] S. H. Groves, R. N. Brown, and C. R. Pidgeon. Interband magnetoreflexion and band structure of HgTe. *Phys. Rev.*, 161(3):779–793, 1967.
- [179] Jeremy W. Nicklas and John W. Wilkins. Accurate electronic properties for (Hg,Cd)Te systems using hybrid density functional theory. *Phys. Rev. B - Condens. Matter Mater. Phys.*, 84(12):6–8, 2011.
- [180] P. Man and D. S. Pan. Infrared absorption in HgTe. *Phys. Rev. B*, 44(16):8745–8758, 1991.
- [181] A. Svane, N. E. Christensen, M. Cardona, A. N. Chantis, M. Van Schilfhaarde, and T. Kotani. Quasiparticle band structures of β -HgS, HgSe, and HgTe. *Phys. Rev. B - Condens. Matter Mater. Phys.*, 84(20):1–6, 2011.
- [182] J. P. Laurenti, J. Camassel, A. Bouhemadou, B. Toulouse, R. Legros, and A. Lusson. Temperature dependence of the fundamental absorption edge of mercury cadmium telluride. *J. Appl. Phys.*, 67(10):6454–6460, 1990.
- [183] Nicolas Moghaddam, Charlie Gréboval, Junling Qu, Audrey Chu, Prachi Rastogi, Clément Livache, Adrien Khalili, Xiang Zhen Xu, Benoit Baptiste, Stefan Klotz, Guy Fishman, Francesco Capitani, Sandrine Ithurria, Sébastien

- Sauvage, and Emmanuel Lhuillier. The Strong Confinement Regime in HgTe Two-Dimensional Nanoplatelets. *J. Phys. Chem. C*, 124(42):23460–23468, 2020.
- [184] Y Niquet, C Delerue, G Allan, and M Lannoo. Method for tight-binding parametrization: Application to silicon nanostructures. *Phys. Rev. B - Condens. Matter Mater. Phys.*, 62(8):5109–5116, 2000.
- [185] Veronika Rinnerbauer, Kurt Hingerl, Maksym Kovalenko, and Wolfgang Heiss. Effect of quantum confinement on higher transitions in HgTe nanocrystals. *Appl. Phys. Lett.*, 89(19), 2006.
- [186] R. S. Kane, R. E. Cohen, and R. Silbey. Theoretical study of the electronic structure of PbS nanoclusters. *J. Phys. Chem.*, 100(19):7928–7932, 1996.
- [187] B. Andrei Bernevig, Taylor L. Hughes, and Shou-Cheng Zhang. Quantum Spin Hall Effect and Topological Phase Transition in HgTe Quantum Wells. *Science*, 314(5806):1757–1761, dec 2006.
- [188] Markus König, Steffen Wiedmann, Christoph Brune, Andreas Roth, Hartmut Buhmann, Laurens W Molenkamp, Xiao-liang Qi, and Shou-cheng Zhang. Quantum Spin Hall Insulator State in HgTe Quantum Wells. *Science*, 318(5851):766–770, nov 2007.
- [189] Natalia Malkova and Garnett W. Bryant. Negative-band-gap quantum dots: Gap collapse, intrinsic surface states, excitonic response, and excitonic insulator phase. *Phys. Rev. B - Condens. Matter Mater. Phys.*, 82(15):1–10, 2010.
- [190] Kittel. *Solid state physics*. 2014.
- [191] David J Griffiths. *Introduction to electrodynamics*. 2021.
- [192] Emmanuel Rosencher and Borge Vinter. *Optoelectronics*. Cambridge University Press, 2002.
- [193] Michel Lannoo, P. Tim Prins, Zeger Hens, Daniel Vanmaekelbergh, and Christophe Delerue. Universality of optical absorptance quantization in two-dimensional group-IV, III-V, II-VI, and IV-VI semiconductors. *Phys. Rev. B*, 105(3), 2022.
- [194] Titus Sandu. Optical matrix elements in tight-binding models with overlap. *Phys. Rev. B - Condens. Matter Mater. Phys.*, 72(12):1–6, 2005.
- [195] E. Clementi and D. L. Raimondi. Atomic screening constants from SCF functions. *J. Chem. Phys.*, 38(11):2686–2689, 1963.
- [196] E. Clementi, D. L. Raimondi, and W. P. Reinhardt. Atomic screening constants from SCF functions. II. Atoms with 37 to 86 electrons. *J. Chem. Phys.*, 47(4):1300–1307, 1967.
- [197] R. B. Schoolar Dixon and J. R. Optical Constants of Lead Sulfide in the Fundamental Absorption Edge Region. *Phys. Rev.*, 137(2), 1965.

- [198] Hideyuki Kanazawa and Sadao Adachi. Optical properties of PbS. *J. Appl. Phys.*, 83(11):5997–6001, 1998.
- [199] Arjan Jeroen Houtepen. *Charge injection and transport in quantum confined and disordered systems*. 2007.
- [200] Philippe Benjamin Green. *The Nucleation, Growth, and Surface of PbS Nanocrystals*. PhD thesis, 2021.
- [201] Monika Goyal. A model to determine variation in dielectric constant with size and composition in semiconducting nanosolids. *J. Comput. Electron.*, 21(6):1212–1219, 2022.
- [202] Haiming Lu and Xiangkang Meng. Correlation between band gap, dielectric constant, Young’s modulus and melting temperature of GaN nanocrystals and their size and shape dependences. *Sci. Rep.*, 5(August):1–8, 2015.
- [203] C. Delerue, G. Allan, and M. Lannoo. Concept of dielectric constant for nanosized systems. *Phys. Rev. B - Condens. Matter Mater. Phys.*, 68(11):3–6, 2003.
- [204] J. Baars and F. Sorger. Reststrahlen spectra of HgTe and $\text{Cd}_x\text{Hg}_{1-x}\text{Te}$. 10(1):875–878, 1972.
- [205] John G. Mavroides Dana H. Dickey. Reststrahlen reflection in HgTe. 2(June):213–215, 1964.
- [206] M. Grynberg, R. Le Toullec, and M. Balkanski. Dielectric function in HgTe between 8 and 300°K. *Phys. Rev. B*, 9(2):517–526, 1974.
- [207] Emmanuel Lhuillier, Marion Scarafagio, Patrick Hease, Brice Nadal, Hervé Aubin, Xiang Zhen Xu, Nicolas Lequeux, Gilles Patriarche, Sandrine Ithurria, and Benoit Dubertret. Infrared Photodetection Based on Colloidal Quantum-Dot Films with High Mobility and Optical Absorption up to THz. *Nano Lett.*, 16(2):1282–1286, 2016.
- [208] C Delerue, M Lannoo, and G Allan. Calculations of the electron-energy-loss spectra of silicon nanostructures and porous silicon. *Phys. Rev. B*, 56(23):15306, 1997.
- [209] Richard Karel Čapek, Iwan Moreels, Karel Lambert, David De Muynck, Qiang Zhao, André Van Tomme, Frank Vanhaecke, and Zeger Hens. Optical properties of zincblende cadmium selenide quantum dots. *J. Phys. Chem. C*, 114(14):6371–6376, 2010.
- [210] Sean E. Keuleyan, Philippe Guyot-Sionnest, Christophe Delerue, and Guy Allan. Mercury telluride colloidal quantum dots: Electronic structure, size-dependent spectra, and photocurrent detection up to 12 μm . *ACS Nano*, 8(8):8676–8682, 2014.
- [211] Prachi Rastogi, Audrey Chu, Tung Huu Dang, Yoann Prado, Charlie Gréboval, Junling Qu, Corentin Dabard, Adrien Khalili, Erwan Dandeu, Baptiste Fix,

- Xiang Zhen Xu, Sandrine Ithurria, Gregory Vincent, Bruno Gallas, and Emmanuel Lhuillier. Complex Optical Index of HgTe Nanocrystal Infrared Thin Films and Its Use for Short Wave Infrared Photodiode Design. *Adv. Opt. Mater.*, 9(10):2002066, 2021.
- [212] Gerald E. Jellison. Data Analysis for Spectroscopic Ellipsometry. *Handb. Ellipsom.*, 234:237–296, 2005.
- [213] N Ghellai, A Benmansour, and Chabane Sari N. Ellipsométrie spectroscopique. pages 22–27, 2011.
- [214] Mariuca Gartner, Mihai Stoica, Madalina Nicolescu, and Hermine Stroescu. The ellipsometry versatility in the study of sol-gel films. *J. Sol-Gel Sci. Technol.*, 98(1):1–23, 2021.
- [215] Tuck C. Choy. *Effective Medium Theory*. Oxford University Press, dec 2015.
- [216] Vadim A. Markel. Introduction to the Maxwell Garnett approximation: tutorial. *J. Opt. Soc. Am. A*, 33(7):1244, 2016.
- [217] Chao Liu, R. Lee Panetta, and Ping Yang. Inhomogeneity structure and the applicability of effective medium approximations in calculating light scattering by inhomogeneous particles. *J. Quant. Spectrosc. Radiat. Transf.*, 146:331–348, 2014.
- [218] Russell J. Gehr and Robert W. Boyd. Optical properties of nanostructured optical materials. *Chem. Mater.*, 8(8):1807–1819, 1996.
- [219] Aida Benchaabane, Zied Ben Hamed, Fayçal Kouki, Mohamed Abderrahmane Sanhoury, Kacem Zellama, Andreas Zeinert, and Habib Bouchriha. Performances of effective medium model in interpreting optical properties of polyvinylcarbazole:ZnSe nanocomposites. *J. Appl. Phys.*, 115(13), 2014.
- [220] J Cl Maxwell-Garnett. XII. Colours in metal glasses and in metallic films. *Philos. Trans. R. Soc. London. Ser. A, Contain. Pap. a Math. or Phys. Character*, 203(359-371):385–420, 1904.
- [221] Von D A G Bruggeman. Berechnung verschiedener physikalischer Konstanten von heterogenen Substanzen. I. Dielektrizitätskonstanten und Leitfähigkeiten der Mischkörper aus isotropen Substanzen. *Ann. Phys.*, 416(7):636–664, 1935.
- [222] G. A. Niklasson, C. G. Granqvist, and O. Hunderi. Effective medium models for the optical properties of inhomogeneous materials. *Appl. Opt.*, 20(1):26, 1981.
- [223] David J. Bergman. The dielectric constant of a composite material-A problem in classical physics. *Phys. Rep.*, 43(9):377–407, 1978.
- [224] Marcelo Alves-Santos, Rosa Di Felice, and Guido Goldoni. Dielectric functions of semiconductor nanoparticles from the optical absorption spectrum: The case of CdSe and CdS. *J. Phys. Chem. C*, 114(9):3776–3780, 2010.

- [225] Pingrong Yu, Matthew C. Beard, Randy J. Ellingson, Suzanne Fernere, Calvin Curtis, John Drexler, Fred Luiszer, and Arthur J. Nozik. Absorption cross-section and related optical properties of colloidal InAs quantum dots. *J. Phys. Chem. B*, 109(15):7084–7087, 2005.
- [226] C. A. Leatherdale, W. K. Woo, F. V. Mikulec, and M. G. Bawendi. On the absorption cross section of CdSe nanocrystal quantum dots. *J. Phys. Chem. B*, 106(31):7619–7622, 2002.
- [227] Iwan Moreels, Karel Lambert, David De Muynck, Frank Vanhaecke, Dirk Poelman, José C. Martins, Guy Allan, and Zeger Hens. Composition and size-dependent extinction coefficient of colloidal PbSe quantum dots. *Chem. Mater.*, 19(25):6101–6106, 2007.
- [228] Hee Chul Woo, Jin Woo Choi, Jae-Suk Lee, and Chang-Lyoul Lee. Determination of complex dielectric function of $\text{CH}_3\text{NH}_3\text{PbBr}_3$ perovskite cubic colloidal quantum dots by modified iterative matrix inversion method. *Opt. Express*, 27(15):20098, 2019.
- [229] Iwan Moreels, Yolanda Justo, Bram De Geyter, Katrien Haestraete, José C. Martins, and Zeger Hens. Quantum Dots: A Surface Chemistry Study. *ACS Nano*, 5(3):2004–2012, 2012.
- [230] C. S. Suchand Sandeep, Jon Mikel Azpiroz, Wiel H. Evers, Simon C. Boehme, Iwan Moreels, Sachin Kinge, Laurens D.A. Siebbeles, Ivan Infante, and Arjan J. Houtepen. Epitaxially connected PbSe quantum-dot films: Controlled neck formation and optoelectronic properties. *ACS Nano*, 8(11):11499–11511, 2014.
- [231] Dana B. Dement, Mayank Puri, and Vivian E. Ferry. Determining the Complex Refractive Index of Neat CdSe/CdS Quantum Dot Films. *J. Phys. Chem. C*, 122(37):21557–21568, 2018.
- [232] Ved Varun Agrawal, Neenu Varghese, G. U. Kulkarni, and C. N.R. Rao. Effects of changes in the interparticle separation induced by alkanethiols on the surface plasmon band and other properties of nanocrystalline gold films. *Langmuir*, 24(6):2494–2500, 2008.
- [233] Iwan Moreels, Yolanda Justo, Bram De Geyter, Katrien Haestraete, José C. Martins, and Zeger Hens. Size-Tunable, Bright, and Stable PbS Quantum Dots: A Surface Chemistry Study. *ACS Nano*, 5(3):2004–2012, mar 2011.
- [234] Ethan J.D. Klem, Harnik Shukla, Sean Hinds, Dean D. MacNeil, Larissa Levina, and Edward H. Sargent. Impact of dithiol treatment and air annealing on the conductivity, mobility, and hole density in PbS colloidal quantum dot solids. *Appl. Phys. Lett.*, 92(21):2006–2009, 2008.
- [235] David Zhitomirsky, Melissa Furukawa, Jiang Tang, Philipp Stadler, Sjoerd Hoogland, Oleksandr Voznyy, Huan Liu, and Edward H. Sargent. N-type colloidal-quantum-dot solids for photovoltaics. *Adv. Mater.*, 24(46):6181–6185, 2012.

- [236] Patrick R. Brown, Donghun Kim, Richard R. Lunt, Ni Zhao, Mounqi G. Bawendi, Jeffrey C. Grossman, and Vladimir Bulović. Energy level modification in lead sulfide quantum dot thin films through ligand exchange. *ACS Nano*, 8(6):5863–5872, 2014.
- [237] Mark C. Weidman, Kevin G. Yager, and William A. Tisdale. Interparticle spacing and structural ordering in superlattice pbs nanocrystal solids undergoing ligand exchange. *Chem. Mater.*, 27(2):474–482, 2015.
- [238] S. Torquato, T. M. Truskett, and P. G. Debenedetti. Is random close packing of spheres well defined? *Phys. Rev. Lett.*, 84(10):2064–2067, 2000.
- [239] C. B. Murray, C. R. Kagan, and M. G. Bawendi. Synthesis and Characterization of Monodisperse Nanocrystals and Close-Packed Nanocrystal Assemblies. *Annu. Rev. Mater. Sci.*, 30(1):545–610, aug 2000.
- [240] Benjamin T. Diroll, E. Ashley Gauding, Cherie R. Kagan, and Christopher B. Murray. Spectrally-Resolved Dielectric Functions of Solution-Cast Quantum Dot Thin Films. *Chem. Mater.*, 27(18):6463–6469, 2015.
- [241] Chia Hao M. Chuang, Patrick R. Brown, Vladimir Bulović, and Mounqi G. Bawendi. Improved performance and stability in quantum dot solar cells through band alignment engineering. *Nat. Mater.*, 13(8):796–801, 2014.
- [242] Maral Vafaie, James Z. Fan, Amin Morteza Najarian, Olivier Ouellette, Laxmi Kishore Sagar, Koen Bertens, Bin Sun, F. Pelayo García de Arquer, and Edward H. Sargent. Colloidal quantum dot photodetectors with 10-ns response time and 80% quantum efficiency at 1,550 nm. *Matter*, 4(3):1042–1053, mar 2021.
- [243] J-P Hugonin and Philippe Lalanne. Reticolo software for grating analysis, 2005.
- [244] Yu Bi, Santanu Pradhan, Shuchi Gupta, Mehmet Zafer Akgul, Alexandros Stavrinadis, and Gerasimos Konstantatos. Infrared Solution-Processed Quantum Dot Solar Cells Reaching External Quantum Efficiency of 80% at 1.35 μm and J_{sc} in Excess of 34 mA cm^{-2} . *Adv. Mater.*, 30(7), feb 2018.
- [245] Xinzheng Lan, Menglu Chen, Margaret H. Hudson, Vladislav Kamysbayev, Yuanyuan Wang, Philippe Guyot-Sionnest, and Dmitri V. Talapin. Quantum dot solids showing state-resolved band-like transport. *Nat. Mater.*, 19(3):323–329, 2020.
- [246] Bertille Martinez. *Etude des propriétés optoélectroniques de nanocristaux colloïdaux à faible bande interdite: application à la détection infrarouge*. PhD thesis, 2019.
- [247] Sang Soo Chee, Charlie Gréboval, Debora Vale Magalhaes, Julien Ramade, Audrey Chu, Junling Qu, Prachi Rastogi, Adrien Khalili, Tung Huu Dang, Corentin Dabard, Yoann Prado, Gilles Patriarche, Julien Chaste, Michael Rosticher, Sara Bals, Christophe Delerue, and Emmanuel Lhuillier. Correlating Structure and Detection Properties in HgTe Nanocrystal Films. *Nano Lett.*, 21(10):4145–4151, 2021.

- [248] Prachi Rastogi, Audrey Chu, Tung Huu Dang, Yoann Prado, Charlie Gréboval, Junling Qu, Corentin Dabard, Adrien Khalili, Erwan Dandeu, Baptiste Fix, Xiang Zhen Xu, Sandrine Ithurria, Gregory Vincent, Bruno Gallas, and Emmanuel Lhuillier. Complex Optical Index of HgTe Nanocrystal Infrared Thin Films and Its Use for Short Wave Infrared Photodiode Design. *Adv. Opt. Mater.*, 9(10):1–11, 2021.
- [249] Thomas C. Hales. A proof of the Kepler conjecture. *Ann. Math.*, 162(3):1065–1185, 2005.
- [250] Menglu Chen, Xinzheng Lan, Xin Tang, Yuanyuan Wang, Margaret H. Hudson, Dmitri V. Talapin, and Philippe Guyot-Sionnest. High Carrier Mobility in HgTe Quantum Dot Solids Improves Mid-IR Photodetectors. *ACS Photonics*, 6(9):2358–2365, 2019.
- [251] Gerard L G Sleijpen and Henk A Van der Vorst. A Jacobi – Davidson Iteration Problems. *SIAM Rev.*, 42(2):267–293, 2000.
- [252] Athmane Tadjine, Guy Allan, and Christophe Delerue. From lattice Hamiltonians to tunable band structures by lithographic design. *Phys. Rev. B*, 94(7):1–13, 2016.
- [253] Marion Dufour, Eva Izquierdo, Clément Livache, Bertille Martinez, Mathieu G. Silly, Thomas Pons, Emmanuel Lhuillier, Christophe Delerue, and Sandrine Ithurria. Doping as a Strategy to Tune Color of 2D Colloidal Nanoplatelets. *ACS Appl. Mater. Interfaces*, 11(10):10128–10134, 2019.
- [254] Leiping Duan, Long Hu, Xinwei Guan, Chun Ho Lin, Dewei Chu, Shujuan Huang, Xiaogang Liu, Jianyu Yuan, and Tom Wu. Quantum Dots for Photovoltaics: A Tale of Two Materials. *Adv. Energy Mater.*, 11(20):1–23, 2021.
- [255] Celso De Mello Donega, Serena Busatto, Mariska De Ruiter, Johann T.B.H. Jastrzebski, Wiebke Albrecht, Valerio Pinchetti, Sergio Brovelli, Sara Bals, and Marc Etienne Moret. Luminescent colloidal InSb quantum dots from in situ generated single-source precursor. *ACS Nano*, 14(10):13146–13160, 2020.
- [256] Taewan Kim, Seongmin Park, and Sohee Jeong. Diffusion dynamics controlled colloidal synthesis of highly monodisperse InAs nanocrystals. *Nat. Commun.*, 12(1), 2021.
- [257] Karan Surana, Pramod K. Singh, Hee Woo Rhee, and B. Bhattacharya. Synthesis, characterization and application of CdSe quantum dots. *J. Ind. Eng. Chem.*, 20(6):4188–4193, 2014.
- [258] Christian Kirchner, Tim Liedl, Stefan Kudera, Teresa Pellegrino, Almudena Muñoz Javier, Hermann E. Gaub, Sonja Stölzle, N. Fertig, and Wolfgang J. Parak. Cytotoxicity of colloidal CdSe and CdSe/ZnS nanoparticles. *Nano Lett.*, 5(2):331–338, 2005.
- [259] H Angus Macleod. *Thin-film optical filters*. CRC press, 2017.

- [260] Michal Soreni-Harari, Nir Yaacobi-Gross, Dov Steiner, Assaf Aharoni, Uri Banin, Oded Millo, and Nir Tessler. Tuning energetic levels in nanocrystal quantum dots through surface manipulations. *Nano Lett.*, 8(2):678–684, 2008.
- [261] Jacek Jasieniak, Marco Califano, and Scott E. Watkins. Size-dependent valence and conduction band-edge energies of semiconductor nanocrystals. *ACS Nano*, 5(7):5888–5902, 2011.
- [262] Ryan W. Crisp, Daniel M. Kroupa, Ashley R. Marshall, Elisa M. Miller, Jianbing Zhang, Matthew C. Beard, and Joseph M. Luther. Metal Halide Solid-State Surface Treatment for High Efficiency PbS and PbSe QD Solar Cells. *Sci. Rep.*, 5:1–6, 2015.
- [263] Liangfeng Sun, Joshua J Choi, David Stachnik, Adam C Bartnik, Byungryool Hyun, George G Malliaras, Tobias Hanrath, and Frank W Wise. Bright infrared quantum-dot light-emitting diodes through inter-dot spacing control. *Nat. Nanotechnol.*, 7(6):369–373, jun 2012.
- [264] Yixing Yang, Ying Zheng, Weiran Cao, Alexandre Titov, Jake Hyvonen, Jesse R. Manders, Jiangueng Xue, Paul H. Holloway, and Lei Qian. High-efficiency light-emitting devices based on quantum dots with tailored nanostructures. *Nat. Photonics*, 9(4):259–265, 2015.
- [265] Santanu Pradhan, Francesco Di Stasio, Yu Bi, Shuchi Gupta, Sotirios Christodoulou, Alexandros Stavrinadis, and Gerasimos Konstantatos. High-efficiency colloidal quantum dot infrared light-emitting diodes via engineering at the supra-nanocrystalline level. *Nat. Nanotechnol.*, 14(1):72–79, jan 2019.
- [266] Jung Hoon Song, Hyekyoung Choi, Hien Thu Pham, and Sohee Jeong. Energy level tuned indium arsenide colloidal quantum dot films for efficient photovoltaics. *Nat. Commun.*, 9(1):1–9, 2018.
- [267] Zhenwei Ren, Jiankun Sun, Hui Li, Peng Mao, Yuanzhi Wei, Xinhua Zhong, Jinsong Hu, Shiyong Yang, and Jizheng Wang. Bilayer PbS Quantum Dots for High-Performance Photodetectors. *Adv. Mater.*, 29(33):1702055, sep 2017.
- [268] Alan R. Lara-Canche, Vineetha Vinayakumar, Diana F. Garcia-Gutierrez, Eduardo Martinez-Guerra, and Domingo I. Garcia-Gutierrez. Energy band alignment engineering in nanostructured hybrid materials based on PbS QDs and reduced graphene oxide: Enhancing photodetector device performance. *J. Alloys Compd.*, 932:167707, jan 2023.
- [269] Georg Heimel, Lorenz Romaner, Egbert Zojer, and Jean-luc Bredas. The Interface Energetics of Self-Assembled Monolayers on Metals. *Acc. Chem. Res.*, 41(6):721–729, jun 2008.
- [270] Matthew T Frederick, Victor A Amin, Laura C Cass, and Emily A Weiss. A Molecule to Detect and Perturb the Confinement of Charge Carriers in Quantum Dots. *Nano Lett.*, 11(12):5455–5460, dec 2011.

- [271] Rolf Koole, Peter Liljeroth, Celso de Mello Donegá, Daniël Vanmaekelbergh, and Andries Meijerink. Electronic Coupling and Exciton Energy Transfer in CdTe Quantum-Dot Molecules. *J. Am. Chem. Soc.*, 128(32):10436–10441, aug 2006.
- [272] John P. Perdew, Kieron Burke, and Matthias Ernzerhof. Generalized gradient approximation made simple. *Phys. Rev. Lett.*, 77(18):3865–3868, 1996.
- [273] Christophe Krzeminski. Structure électronique et transport dans une jonction moléculaire. 2011.